Structural differences between granule cells and semilunar granule cells: role in differential post-traumatic plasticity of synaptic inputs.

Authors: Fatima S. Elgammal, Akshay Gupta, Archana Proddutur, Mille Swietek, Ogechukwu Chika-Nwosuh, Vijayalakshmi Santhakumar
Neurology and Neurosciences, New Jersey Medical School, University of Medicine and Dentistry of New Jersey, Newark, NJ

RATIONALE: Concussive brain trauma increase the risk for acquired epilepsy and memory dysfunction. In earlier studies, we identified that semilunar granule cells (SGCs), glutamatergic neurons in the inner molecular layer with axonal projections to CA3 (Williams et al., 2007), show enhanced excitability after brain injury. SGCs receive significantly greater inhibitory inputs than granule cells and demonstrate a post-traumatic decrease in the frequency of inhibitory synaptic inputs rather than an increase observed in granule cells (Gupta et al., 2012). Here, we examined whether differences in dendritic morphology contribute to the divergent intrinsic pattern and post-traumatic plasticity of synaptic inputs between the two cell types.

METHODS: in young adult rats was used to model brain injury. Whole-cell recordings from dentate neurons were obtained from acute hippocampal slices prepared 1 week after lateral fluid percussion injury (FPI) or sham-injury in young adult rats. Recorded neurons were filled with biocytin and processed for post-hoc cell identification. Neuronal reconstructions and morphometric analysis were performed on Neurolucida. Simulations were performed using NEURON.

RESULTS: In contrast to the differential post-injury changes in synaptic inhibition, both granule cells and SGCs showed an increase in the frequency spontaneous EPSCs one week after FPI. the frequency of sEPSCs in SGCs from sham-injured rats was significantly greater than in granule cells (sEPSC in Hz, GC median=1.65, IQR =0.88-3.68, n=3; SGC median=2.99, IQR=1.4-7.3, n=7). Molecular layer interneurons showed fewer spontaneous inhibitory inputs and a post-FPI increase in sIPSC frequency, indicating that location may not account for the differences in synaptic inputs between SGCs and granule cells. Morphometric analysis revealed a greater dendritic contraction angle in SGCs (in degrees, GC=59.1 ± 6.8, n=4; SGC=119.7 ±8.1, n=6, $p<0.05$, t-test). However, the total dendritic length was not different between the two cell types (in μm, GC=3206.9±377.4, n=5; SGC=2583.2±249.6, n=5). SGCs had more numerous first and second order branches and greater dendritic length in these low order, proximal branches than granule cells (dendritic length of first order branches in μm, GC=32.2±15.4, n=5; SGC=396.2±148.9, n=5; $p<0.05$, t-test). However, granule cells had greater dendritic length than SGCs at locations distal to the somata. Detailed morphological simulations of granule cells and SGCs incorporating identical active and passive properties suggest that the difference in morphology cannot fully explain the distinctive intrinsic physiology of SGCs.

CONCLUSIONS: These data reveal unique dendritic morphological characteristics of granule cells and SGCs that could contribute to the differences in their synaptic inputs and post-traumatic plasticity. However, our simulation studies indicate that, apart from the distinctive morphology, dissimilar channel distribution is likely to underlie differences in active properties between the two cell types.

Support: NJCBIR 09.003.BIR1 to VS and NJCBIR 11-3223-BIR-E-O to A.G

Print this Page

NEUROSCIENCE 2012

Presentation Abstract

Program#/Poster#: 769.02/W5

Presentation Title: Early changes in synaptic inputs to dentate molecular layer neurons following concussive brain injury.

Location: Hall F-J

Presentation time: Wednesday, Oct 17, 2012, 9:00 AM -10:00 AM

Authors: ***A. GUPTA**, A. PRODDUTUR, F. ELGAMMAL, V. SANTHAKUMAR; UMDNJ, Newark, NJ

Abstract: Closed head injury results in an early increase in excitability of the dentate gyrus one week after trauma. Alterations in both excitatory and inhibitory networks contribute to early post-injury dentate hyperexcitability. Since loss of hilar neurons is a typical feature of brain injury, studies have focused on granule cells and hilar neurons to determine if post-traumatic changes in intrinsic and synaptic physiology underlie the changes network excitability. Recently, we reported that semilunar granule cells (SGCs), a class of excitatory neurons in the molecular layer, demonstrate post-traumatic increase in intrinsic excitability not observed in other dentate glutamatergic neurons. We showed that granule cells and SGCs show marked differences in the effect of injury on synaptic and tonic inhibition. Since SGCs and molecular layer interneurons (MLI) contribute to feed-back and feed-forward inhibition in the dentate, we examined SGCs show post-traumatic changes in glutamatergic synaptic inputs and investigated whether early post-injury decreases synaptic inhibitory inputs is unique to SGCs or is common to other neurons in the molecular layer.
Whole-cell patch clamp recordings were obtained from SGCs and dentate MLI in hippocampal slices from juvenile male rats one week after lateral fluid percussion injury (FPI) and sham-injured controls (Gupta et al., 2012). Morphological reconstruction of biocytin-labeled neurons and intrinsic physiological characteristics were used to distinguish MLI from SGCs. Interneurons with somata in the molecular layer were classified as MLI and included morphologically identified MOPP, axo-axonic, and neurogliaform cells. We found that the frequency of excitatory

postsynaptic currents (sEPSCs) in SGCs was enhanced one week after FPI. Recordings in slices from control rats revealed that, compared to SGCs and granule cells, the frequency spontaneous inhibitory postsynaptic currents (sIPSCs) in MLI was significantly lower. There was a post-traumatic increase in sIPSC frequency in MLI, which parallels the early increase in granule cell sIPSC frequency, but contrasts with the decrease in sIPSC frequency in SGCs one week after FPI. Curiously, sIPSC frequency in MLI and SGCs was not different one week after FPI.
The early post-traumatic increase in SGC synaptic excitatory inputs observed here, could actively recruit hyperexcitable SGCs during network activity and contribute to post-traumatic dentate hyperexcitability. The distinctive early decrease in SGC synaptic inhibition after FPI suggests that interneuronal populations that innervate SGCs may be different from those synapsing with granule cells and MLI.

Disclosures: **A. Gupta:** None. **A. Proddutur:** None. **F. Elgammal:** None. **V. Santhakumar:** None.

Keyword(s): GABAERGIC

INTERNEURON

DENTATE GYRUS

Support: New Jersey Commission for Brain Injury Research Grant 09.003-BIR1 (to V.S.)

New Jersey Commission for Brain Injury Research Grant 11-3223-BIR-E-O (to A.G.)

[Authors]. [Abstract Title]. Program No. XXX.XX. 2012 Neuroscience Meeting Planner. New Orleans, LA: Society for Neuroscience, 2012. Online.

Toll-like receptor 4 signaling contributes to early increase in dentate excitability after concussive brain injury by NMDA receptor independent mechanisms

Ying Li [1]*, Akshata Korgaonkar [1*], Jianfeng Wang[1], Ellen Townes-Anderson[1], Stella Elkabes[2], Vijayalakshmi Santhakumar [1,3]

[1]Department of Neurology and Neurosciences, [2]Department of Neurological Surgery [3]Department of Pharmacology and Physiology, New Jersey Medical School, Rutgers University, Newark, New Jersey 07103.
*Authors Contributed Equally

Running title: Role if TLR4 in dentate hyperexcitability after FPI

Key words: Dentate gyrus, innate immunity, brain injury, epilepsy, TBI, trauma.

Word count for Abstract: x words; Introduction: x words; Discussion: x words

Number of figures: x Number of tables: 0 Number of pages: x

Author Contributions: Y.L, A.K and J.W performed experiments; Y.L and A.K analyzed data and prepared figures Y.L, A.K and V.S interpreted results of experiments; Y.L, A.K and V.S authored the manuscript; E.T.A and S.E provided guidance and technical expertise. Y.L, A.K, J.W, E.T.A and S.E edited and approved the manuscript. V.S: conception and design of research.

Acknowledgements: We thank Dr. Eldo Kuzhikandathil, UMDNJ for his extensive support with the western blotting studies Dr. Robert F. Heary for equipment and Ms. Archana Proddutur and Fatima S. Elgammal for their helpful comments and technical assistance. The project was supported by CURE Foundation and NJCBIR 09.003-BIR1 to V.S.

Correspondence:

Vijayalakshmi Santhakumar, PhD
Department of Neurology and Neuroscience,
UMDNJ-New Jersey Medical School
MSB-H-512, 185 S. Orange Ave. Newark, NJ 07103
E-mail: santhavi@umdnj.edu

Abbreviations:

FPI: Fluid percussion injury

NMDA: *N*-methyl-D-aspartate

NMDAR: NMDA receptor

TBI: Traumatic brain injury

TLR: Toll-like receptor

LPS-RS: Lipopolysaccharide from the photosynthetic bacterium *Rhodobacter sphaeroides*

Abstract (276/300 words)

Brain injury is a leading cause for development of temporal lobe epilepsy in young adults. Brain injury leads to cellular and synaptic changes in the hippocampus, including neuronal loss in the dentate hilus, microglial activation, and increased network excitability. Given the cellular damage during brain injury innate immune receptors such as toll-like receptors (TLRs) are likely to be activated by endogenous molecules released during cellular injury. Certain TLR subtypes, including TLR4 are expressed in neurons and have been implicated in regulation of neuronal survival and excitability. TLR4 expression and signaling is altered during sterile inflammation accompanying ischemia and epilepsy. Therefore, we examined the expression and functional role for TLR4 following concussive brain injury. Western blot analysis revealed an increase in the expression of TLR4 in the hippocampus of young adult rats within 4 hours after lateral fluid percussion injury (FPI). Expression of TLR4 in the injured hippocampus reached a maximum 24 hours after FPI but was not sustained 7 days after injury. Immunostaining studies identified that the post-injury increase in TLR4 expression is primarily neuronal with limited expression in astrocytes and microglia. In electrophysiological studies conducted 3 days and 1 week after FPI, LPS-RS, a specific antagonist of TLR4 receptors, selectively decreased afferent-evoked excitability in the dentate gyrus of head-injured but not in sham-operated controls. The ability of LPS-RS to selectively reduce excitability of the injured dentate gyrus persisted in the presence of NMDA receptor antagonists. These findings demonstrate that TLR4 signaling contributes to early enhancement of dentate excitability after brain injury through NMDAR-independent mechanisms and pave the way for determining how innate immune receptor signaling contributes to alterations in hippocampal function following closed head injury.

Introduction

Post-traumatic epilepsy as a result of civilian and combat-related brain injuries is a growing health issue due to long-term increases in the risk for epilepsy following even mild to moderate brain injury. In addition to neuronal damage, brain trauma results in release injury products from disrupted cells and extracellular matrix which can activate Toll-Like Receptors (TLRs), a class of innate immune pattern-recognition receptors. Certain TLR subtypes, namely TLR2, 4 and 8, are expressed in neurons and regulate neurite outgrowth, axonal reorganization, neurogenesis and cell death. Despite recent data implicating TLR signaling in hippocampal excitability in epilepsy (Maroso et al., 2010), whether brain injury alters the expression of TLRs in specific neuronal and glial cell-types and whether TLR signaling alters neuronal intrinsic and synaptic physiology is not known.

The immune system consists of both innate (cellular) and adaptive (humoral) components which are involved in responses to infection and autoimmune activation in the central nervous system. Toll-like receptors (TLRs) drive innate responses and recognize a few highly conserved structures called *pathogen-associated molecular patterns* (PAMPs) which are expressed by large groups of microorganisms. TLRs are highly conserved transmembrane receptors with a toll/interleukin-1 receptor homology domain. A major pathway for TLR signaling involves the myeloid differentiation primary response gene (MyD88) adapter molecule and a cascade that results in activation of the transcription factor nuclear factor-kappa B (NFkB) and gene induction (Owens et al., 2005). However, recent studies suggest that TLR4 signaling may also occur through MyD88-independent, pathways that involve TIR-domain-containing adapter-inducing interferon-β (TRIF) to activate Interferon regulatory factor 3 (IRF3) and produce interferon-β (Okun et al., 2011; Liu et al., 2012). Several TLRs are also expressed outside the immune system

including the CNS. Microglia, the resident innate immune cells are the principle cell type expressing TLRs in the brain (Kielian, 2006). Notably, certain TLR subtypes can be activated by several endogenous molecules including fibrinogen, fibronectin, heparin sulfate and mRNA (Kielian, 2006), the *damage-associated molecular patterns* (DAMPs) or alarmins that are likely released during cellular injury processes. Consistent with these observations, TLRs in the CNS are activated in autoimmune disorders, neuropathic pain, hypoxia, epilepsy and neurodegeneration (Owens et al., 2005; Tanga et al., 2005; Kielian, 2006), suggesting that specific classes of TLRs are likely to be activated after TBI.

There is increasing evidence for neuronal expression of TLRs (Ma et al., 2006; Tang et al., 2007). In adults, TLRs are expressed in neural progenitor cells in the subventricular zone and dentate gyrus and in cortical neurons (Rolls et al., 2007; Tang et al., 2007). It is intriguing that specific TLR subtypes are expressed in distinctive neuronal populations and even in specific subcellular locations (Kielian, 2006). Of particular interest is TLR4, which is expressed in central and peripheral neurons and in neural progenitor cells. TLR4 is present in several neuronal types including trigeminal sensory neurons, dorsal root ganglion neurons, and neuroblastoma cells (Wadachi and Hargreaves, 2006) and has been shown to induce apoptotic cell death and regulate neuronal differentiation (Rolls et al., 2007). It is unclear whether the same intracellular mechanisms that mediate immune and glial TLR4 signaling are responsible for neuronal TLR4 signaling (Liu et al., 2012). There is growing evidence that TLR4 modifies neuronal excitability (Maroso et al., 2010; Diogenes et al., 2011; Pascual et al., 2012). Recent studies have shown that TLR4-mediated increase in interleukin-1b leads to NMDAR phosphorylation and increase in neuronal calcium influx (Viviani et al., 2003; Balosso et al., 2008; Rodgers et al., 2009).

However, whether neuronal or glial TLR4 signaling contributes to TLR4-dependent increase in neuronal NMDA currents is not clear. TLR4 activation transiently enhances the frequency of EPSCs through a mechanism that involves metabotropic glutamate receptor activation and glial purinergic receptors (Pascual et al., 2012). Direct activation of TLR4 on trigeminal neurons has been shown to increase intracellular calcium influx through TRPV1 channels. These findings suggest that mechanisms of TLR4 signaling may have cellular, temporal and regional differences that remain to be elucidated.

TLR4, a member of the TLR family, is integral to mounting innate immune responses to microbes. Activation of TLR4 triggers signaling pathways which ultimately result in changes in gene expression and production of pro-inflammatory cytokines (Hallenbeck, 2002; Lambertsen et al., 2004). Recent studies have demonstrated the activation of TLR4 signaling in the hippocampus during ischemic reperfusion injury (Gao et al., 2009) and shown that mutations in TLR4 reduce edema and improve neurological outcome following ischemic reperfusion (Hua et al., 2007). TLR4 also been implicated in various neurological disorders including multiple sclerosis, stroke, amyotropic lateral sclerosis, Alzheimer's disease and Parkinson's disease (Okun et al., 2011). Notably, a recent study has identified both acute and chronic increases in the expression of TLR4 and its endogenous ligand HMGB1 in human and animal hippocampal tissue in chronic epilepsy and showed that TLR4 contributes to the pathological increase in hippocampal excitability in epilepsy (Rodgers et al., 2009; Maroso et al., 2010). TLR4 has also been implicated in phosphorylation of microtubule-associated protein tau, a pathological hallmark common to neurodegenerative disorders and chronic traumatic encephalopathy (Bhaskar et al., 2010). Taken together, the role of TLR4 in neuronal excitability, its involvement in epilepsy and potential role in long-term neurodegenerative pathology suggests that activation

TLR4 following brain trauma could contribute to the early post-traumatic increase in hippocampal excitability and prolonged neuro-cognitive disorders.

Experimental Procedures

All procedures were performed under protocols approved by the Institutional Animal Care and Use Committee of the University of Medicine and Dentistry of New Jersey, Newark, New Jersey.

Fluid percussion injury: Juvenile male Wisar rats (25-27 days old) were subject to the moderate (2-2.2 atm) lateral fluid percussion injury (FPI) or sham-injury using standard methods (Toth et al., 1997; Santhakumar et al., 2000; Santhakumar et al., 2003; Gupta et al., 2012). Briefly, the rats were placed in a stereotaxic frame under ketamine-xylazine anesthesia. A 3mm hole was drilled on the left side of the skull 3 mm antero-posterior and 3.5 mm lateral to the saggital suture keeping the dura intact. Two steel screws were screwed in to the skull and glued to support the cap. A Luer-Lok syringe hub was glued to the skull over the exposed dura and bonded to the skull with cyanoacrylate adhesive. One day later, animals were anesthetized with isoflurane and attached to a FPI device (Virginia Commonwealth University, VA). A pendulum was dropped to deliver a brief (20 ms) impact on the intact dura. For sham injury, the animals were anesthetized and attached to the fluid percussion device, but the pendulum was not dropped.

Protein Isolation and Western Blotting: Western blots of hippocampal tissue was performed as described previously (Tobon et al., 2012). Briefly, mice lacking the expression of TLR4 (*tlr4*$^{-/-}$, JAX labs), and rats at various time points after FPI or sham-injury (4 hours, 24 hours, 3 days, 7 days and 1 month) were quickly perfused with cold ACSF (4°C) under isoflurane anesthesia, fresh hippocampal tissue was isolated under a dissecting microscope and stored at -80°C until use. Tissue were homogenized with CelLytic MT cell lysis reagent supplemented with phenylmethylsulfonyl fluoride 1mM, Na fluoride 10 mM, Na Orthovanadate 1 mM, Phosphatase

inhibitor 10 ul/ml, Protease inhibitor 10 ul/ml (Sigma). Samples were cooled on ice for 10 min and centrifuged (15,000 x g) for 20 min at 4°C. The supernatant was transferred to a new tube. Protein concentration of the sample lysates was measured using BCA assay (Santa Cruz). Equal amounts of protein samples were diluted at a ratio of 1:1 in Laemmli sample buffer (Sigma) and separated on pre-cast gel (4-12% Tris-glycine, Bio-Rad). Protein was electro-transferred onto nitrocellulose membrane (Thermo Scientific) in a Tris-Glycine-Methanol buffer. The membrane was blocked for 1 h in 5% nonfat dry milk in 0.05% Tween-20 Tris-buffer solution (TBS) at room temperature (RT) on a slow shaker. The membrane was washed in TBS, incubated with primary antibody (TLR4: 1:500 in 5% BSA 0.05% Tween-20 TBS or β-actin: 1:5000 in 2.5% nonfat milk 0.05% Tween-20 TBS) overnight at 4 °C. TLR4 antibodies were obtained from Cell Signaling (Cat. 2219) and Santa Cruz (Cat. H-80) and β-actin from Sigma-Aldrich (Cat. A1978). This was followed by TBS wash and incubation in secondary antibody (HRP-conjugated goat anti-rabbit at 1:10000, Sigma or anti-mouse at 1:5000, Sigma) for 1 h at RT. Immunoreactivity was visualized and imaged on FluorChem using a chemiluminescent substrate Westdura (Thermo Scientific). Densitometry analyses were performed to quantify signals generated by Western blotting using ImageJ software (NIH). The density of each sample is normalized to its own density of β–actin.

Immunohistology: Immunosatining was performed on hippocampal sections (50 μm) obtained from rats and naïve adult *tlr4*$^{-/-}$ mice perfused with 4% paraformaldehyde in phosphate buffered saline (PBS) with Heparin (10 u/ml){Epstin, 1998 # }. Sections from rats were obtained 4hrs, 24 hrs and 1week after FPI and from age-matched sham-operated controls. Sections were then washed in PBS and blocked in 10% normal goat serum in 0.3% triton in PB for one hour. For TLR 4 staining, sections were incubated overnight in anti-TLR 4 antibody (1:500, SH-80 Rabbit

monoclonal; Santa Cruz) in 0.3% Triton and 2% normal goat serum in PBS at RT. Double staining for TLR4 and markers for neurons (NeuN), reactive astrocytes (GFAP) or microglia (IBA1) and TLR 4 was performed by sequentially incubating sections in anti-TLR 4 primary antibody for one hour followed by addition of anti-NeuN (1:1000, Mouse monoclonal antibody MAB377, Millipore) or anti-GFAP (1:500, Mouse monoclonal antibody MAB360, Millipore) or anti-IBA1 (1:300, mouse monoclonal antibody MABN92, Millipore) primary anitbodies and overnight incubation at RT. Sections were washed in PBS and immunostained with fluorescent secondary antibodies: goat anti-rabbit Alexa 594 (A11037, 1:500; Invitrogen) to reveal TLR4 and goat anti-mouse Alexa-488(A11029, 1:800; Invitrogen) to reveal NeuN, GFAP or IBA1. Sections were mounted on slides using Vectashield (Vector labs). Specificity of the anti-TLR4 antibody was confirmed by the lack of immunostaing in sections from *tlr4*$^{-/-}$ mice.

Sections were imaged using Olympus BX51 microscope. Quantification was performed in the dentate hilus of every 11th section along the septo-temporal extent of the hippocampus. Cell counts were performed using the optical fractionator of Stereo Investigator V.10.02 (MBF Bioscience, Williston, VT) on an Olympus BX51 microscope with a 100X objective. In each section, the hilus was outlined by a contour traced using a 10X objective. Sampling parameters were set at 100X: counting frame=50 μm by 50 μm, dissector height =30 μm, and top guard zone=5 μm. Approximately 25 sites per contour were selected using randomized systematic sampling protocols in Stereo Investigator (West et al., 1991; Gupta et al., 2012; Yu et al., 2013). In each section, an observer marked the outline of TLR4 positive somata in the hilus under epifluorescence illumination and a 100X oil objective and switched filters to visually examine the expression of NeuN subunit in the TLR4 labeled soma. Neurons were deemed co-labeled if the staining for NeuN shared the outline of the TLR4 soma had a greater intensity than the hilar

neuropil. For quantification of intensity of TLR4 staining, confocal images of the dentate gyrus were obtained using a Nikon A1R laser confocal microscope with a Nikon A1R laser confocal microscope with a 0.75 NA 20X air objective with identical camera setting and converted to RGB color mode. Two regions of interest (ROI) of identical dimensions were drawn in both the hilus and the dentate molecular layer using NIS Elements (Nikon Instruments). The average gray scale intensity of TLR4 staining for each ROI was determined using standard routines in NIS Elements (Yu et al., 2013). Image analyses were performed by an investigator blind to the treatment**.**

Electrophysiology: Three and seven days after FPI or sham-injury, rats were anesthetized with isoflurane and decapitated. Horizontal brain slices (400 μm) were prepared in ice-cold sucrose artificial CSF (sucrose-aCSF) containing (in μM) 85 NaCl, 75 sucrose, 24 $NaHCO_3$, 25 glucose, 4 $MgCl_2$, 2.5 KCl, 1.25 NaH_2PO_4, and 0.5 $CaCl_2$ using a Leica VT1200S Vibratome (Wetzlar, Germany). The slices were sagittally bisected and the slices from the left hemisphere (ipsilateral to the side of injury) were incubated at 32 ± 1°C for 30 minutes in a submerged holding chamber containing an equal volume of sucrose-aCSF and recording aCSF and subsequently held at RT. The recording aCSF contained (in mM) 126 NaCl, 2.5 KCl, 2 $CaCl_2$, 2 $MgCl_2$, 1.25 NaH_2PO_4, 26 $NaHCO_3$ and 10 D-glucose. All solutions were saturated with 95% O_2 and 5% CO_2 and maintained at a pH of 7.4 for 1–6 h. Slices were pretreated with either the TLR4 antagonist, LPS-RS (50 ng/ml) or vehicle (recording aCSF) for 2 hours before being transfer to an interface field recording (BSC2, Automate Scientific, Berkeley, CA) perfused with aCSF. Brain slices rested on a filter paper and were stabilized with platinum wire weights. The tissue was continuously superfused with humidified 95% O_2-5% CO_2 and the temperature of the perfusing solution was maintained at 34°C using a proportional control heating unit (PTC03, Automate Scientific). Field

recordings of evoked population spikes in the granule cell layer of the dentate gyrus were obtained using patch pipettes filled with recording aCSF. To evoke the field responses, constant current stimuli (0.5 - 4mA, 50 μs) were applied at 0.1 Hz through a bipolar 90 μm tungsten stimulating electrode placed in the perforant path, at the junction of the dorsal blade and the crest just outside the fissure where it was visualized as a fiber tract (Santhakumar et al., 2001; Gupta et al., 2012), and coupled to a high voltage stimulus isolator (A365R, WPI, Sarasota, FL). Recordings were obtained using an AxoPatch200B amplifier, filtered at 4 kHz using a Bessel filter, and digitized at 10 kHz with a DigiData 1440A analog–digital interface (Molecular Devices, Sunnyvale, CA). The field responses in the granule cell layer were measured at five predetermined points in each slice (Santhakumar et al., 2000; Yu et al., 2013), including the tips of the dorsal and the ventral blades, the middle of the dorsal and ventral blades and the middle of the crest, and the largest response was studied further. All salts were purchased from Sigma-Aldrich (St. Louis, MO).

Staistical analysis: Statistical analysis were performed using either IBM SPSS.20 or SigmaPlot 8.02 Quantitative data for western blot analysis (8 groups) were not normally distributed. Thus western blot data were compared using non-parametic tests (Kruskal-Wallis and Mann-Whitney U tests). One way ANOVA was used for analysis of cell counts and semi-quantitative analysis of TLR4 staining intensity. All independent samples were tested for normality and homogeneity of variance (Levene's test) in SPSS Levene's test using descriptive statistic. Post-hoc Tukey's test was used to assess statistical significance of between-group differences. Data from physiological experiments were compared using paired and unpaired Student's t-test or two-way repeated measures ANOVA as appropriate. Significance was set to $p < 0.05$. Data are shown as mean ± s.e.m.

Results

Early and transient increase in TLR 4 expression after FPI

Fluid percussion brain injury leads to immediate mechanical injury to neurons in the hippocampal dentate gyrus {Toth, 1997 #17} and dentate hilar cell death within hours of injury {Gupta, 2012 #4061}. Since neuronal injury and death likely to release substances known to activate the innate immune responses mediated by TLR4, we examined the time course of changes in TLR4 expression after FPI. Western blot assay was used to examine and quantify TLR4 protein levels in hippocampal tissue from FPI, Sham-injury rats at various time points after injury. First, we tested the specificity of TLR4 antibodies from Cell Signaling and Santa Cruz used in earlier studies (REF). As illustrated in Figure 1A, the TLR4 antibody from Cell Signaling (Cat 2219) labeled a single band at 95 kD, the molecular weight of TLR4, in hippocampal samples from both sham-operated control and FPI rats. In addition to the 95 kD band, the Cell Signaling antibody labeled a few bands with higher molecular weight which likely reflect glycosylation products. Antibody specificity was further confirmed by the complete absence of labeling in hippocampal tissue from mice lacking the TLR4 gene (Fig. 1, lane labeled as TLR4 KO). Similarly, the TLR4 antibody from Santa Cruz (Cat H-80) labeled a specific band at 95 kD and high molecular weight bands but failed to show the 95 kD band in mice lacking the TLR4 gene confirming antibody specificity (data not shown). Since, the Cell Signaling antibody was deemed to be better for Western analysis all subsequent quantitative Western blot analysis was conducted using the Cell Signaling (Cat 2219) antibody. Compared to the sparse TLR4 labeling in age-matched sham-controls, Western blots revealed a significant increase in TLR4 protein levels as early as 4 hours after FPI (Fig. 1A-B, TLR4 protein levels 4 hours after FPI was 121 ± 4 % of protein levels in sham group, n=6 rats each in both sham and FPI groups, $p<0.05$

by Kruskal-Wallis test followed by pairwise comparison by Mann-Whitney U tests). TLR4 expression showed a further increase 24 hours after FPI reaching 191 ± 15 % of the expression levels in age-matched sham controls (Fig. 1A-B, n=6 rats each in both sham and FPI groups, $p<0.05$ Kruskal-Wallis test followed by pairwise comparison by Mann-Whitney U tests). A significant elevation in TLR4 expression was maintained 3 days after FPI (Fig. 1 A-B, TLR4 protein levels 3 days after FPI: 135 ± 7 % of age-matched sham, n=6 rats each in both sham and FPI groups, $p<0.05$ by Kruskal-Wallis test followed by pairwise comparison by Mann-Whitney U tests). However, the small increase in TLR4 expression observed 7 days and 1 month after FPI failed to reach statistical significance (Fig. 1 A-B, TLR4 protein levels 7 days after FPI: 108± X % of the sham, 1 month after FPI: 105± X% of sham, n=6 rats all groups, $p>0.05$ by Kruskal-Wallis test followed by pairwise comparison by Mann-Whitney U tests). Remarkably, regardless of the time point after sham-injury, hippocampal tissue from sham-operated rats showed no difference in the levels of TLR4 expression from those observed in rats 4 hours after sham-injury (Fig. 1B, $p>0.05$ by Kruskal-Wallis test followed by pairwise comparison by Mann-Whitney U test) and in age-matched, naïve rats (data not shown) suggesting that the surgery did not lead to an increase in TLR4 expression in the absence of brain injury. These data demonstrate that concussive brain injury results in an early and transient up-regulation of TLR4 expression in hippocampus.

Since Western blot data identified an early enhancement of hippocampal TLR4 expression after FPI, we undertook immunostaining experiments to identify the regional distribution of post-injury alteration in TLR4 expression in the dentate gyrus. Consistent with data from Western blots, we found an increase in the expression of TLR4 in the dentate gyrus of rats sacrificed 4 hours (not shown) and 24 hours after brain injury compared to age-matched,

sham-operated controls (Fig. 2A-B). The absence of cellular labeling in hippocampal sections obtained from TLR4 knockout mice confirmed the specificity of the TLR4 antibody (Santa Cruz Cat H-80) for immunostaining studies (Fig.2C). Regionally, TLR4 expression appeared to be enhanced in all dentate layers (Fig. 2A-B). TLR4 labeling showed a prominent cellular pattern of expression in the dentate hilus. Additionally, the TLR4 immunostaining in the molecular layer and surrounding unstained spaces in the granule cell layer (Fig. 2A-B) suggest that granule cell dendrites and possibly, interneuronal axons may express TLR4. Semi-quantitative analysis of gray-scale images for fluorescence intensity in the molecular layer and dentate hilus showed that the intensity of TLR4 staining was significantly elevated in both the molecular layer and dentate hilus 24 hours after FPI (Fig. 2D, 43.01±6.48% increase in molecular layer; intensity in A.U, sham: 287.94±6.50 in 10 sections from 3 rats, FPI: 412.33±17.04 in 12 sections from 4 rats; 32.45±5.63% increase in the hilus; intensity in A.U, sham: 303.13±10.02 in 10 sections from 3 rats, FPI: 398.78±15.35 in 12 sections from 4 rats, $p<0.05$ by one way ANOVA followed by post-hoc Tukey's test). Similarly, the intensity of TLR4 labeling in the molecular layer and dentate hilus was enhanced 4 hr after FPI (36.96±8.62% increase in molecular layer; intensity in A.U, sham: 345.31±14.27 in 10 sections from 3 rats, FPI: 477.87±28.44 in 12 sections from 4 rats; 48.85±7.38% increase in the hilus; intensity in A.U, sham: 310.55±25.13 in 10 sections from 3 rats, FPI: 456.98±21.74 in 12 sections from 4 rats, $p<0.05$ by one way ANOVA followed by post-hoc Tukey's test). Curiously, although the increase in TLR4 levels in hippocampal tissue failed to reach statistical significance (Fig. 1B), the intensity of TLR4 labeling in the dentate molecular layer and hilus remained elevated even 1 week after FPI (66.85±9.40% increase in molecular layer; intensity in A.U, sham: 309.61±19.50 in 10 sections from 3 rats, FPI: 513.46±26.53 in 12 sections from 4 rats; 51.34±7.77% increase in the hilus; intensity in A.U,

sham: 330.13±21.85 in 10 sections from 3 rats, FPI: 496.27±24.51 in 12 sections from 4 rats, $p<0.05$ by one way ANOVA followed by post-hoc Tukey's test). It is possible that regional differences in the time course of post-injury TLR4 expression contributed to the lack of increase in TLR4 protein levels measured in the whole hippocampal tissue during Western analysis. However, the immunostaining data demonstrate that the post-traumatic increase in dentate TLR4 that occurs as early as 4 hours after injury persists up to one week after injury.

Expression and post-injury increase in TLR4 was predominantly neuronal.

Given the cellular expression pattern for TLR4, we undertook double immunolabeling studies to determine the cell-type specific expression of TLR4 in the dentate hilus. As illustrated in Figure 3, the intensity and cellular labeling of TLR4 was more apparent in sections from the injured rat compared to control. Double immunostaining revealed that several TLR4 positive neuronal profiles showed co-labeling for NeuN in hilar sections from both sham-operated controls and post-FPI rats sacrificed 24 hours after injury. However, not all NeuN positive profiles in the hilus were co-labeled withTLR4, suggesting cell-type specific expression of TLR4 among the diverse neuronal populations in the hilus. Streological quantification of the number of TLR4 positive profiles that expressed NeuN revealed a significant difference between sham-operated and FPI groups ($F_{(5, 15)}$ =24.92, $p<0.05$ and η^2=0.89 by one-way ANOVA). Pairwise comparison revealed that the number of NeuN cells co-labeled for TLR4 was increas:ed 4 and 24 hours after FPI (Fig. 3C, Estimated number of co-labeled cells in hilus/rat, 4 hours post-FPI: sham: 5998.67±532.78 based on 4 sections each from 3 rats, FPI: 15902.50±960.93 based on 3 sections each from 4 rats; 24 hours post-FPI: sham: 7888.00±412.28 based on 4 sections each from 3 rats, FPI: 25835.50±1065.88 based on 4 sections each from 4 rats, $p<0.05$ by post-hoc Tukey's test). Note that the increase in NeuN positive cells co-labeled for TLR4 occurred in spite

of a decrease in NeuN labeled dentate hilar neurons (% decrease in hilar neurons after FPI, 4 hours post-FPI: 165.10±16.01% of sham based on 4 sections from 3 sham rats and 4 sections from 4 post-FPI rats, 24 hours post-FPI: 227.52±13.51 % of sham based on 4 sections from 3 sham rats and 4 sections from 4 post-FPI rats, $p<0.05$ t-test). Although there was a trend towards an increase in the number of NeuN positive cells co-labeled for TLR4 one week after FPI, the difference failed to reach statistical significance (Fig 3C, Estimated number of co-labeled cells in hilus/rat, 1 week post-FPI: sham: 8415.33±894.87 based on 4 sections from 3 rats, FPI: 12068.75±1019.55 based on 4 sections from 4 rats, $p>0.05$ by post-hoc Tukey's test).

Previous studies have reported that TLR4 may be expressed in microglia and reactive astrocytes (REF). Since brain injury can recruit microglia and contribute to reactive astrocytosis (REF), we examined whether Iba1-positive microglia and GFAP-expressing reactive astrocytes express TLR4. Although we found cellular patterns of Iba1 and TLR4 expression in the dentate hilus in sections from both sham-controls and rats 24 hours after FPI, the expression patterns failed to overlap indicating the absence TLR4 expression in microglia (Fig. 4A-B, based on examination of 4 sections each from 3 sham rats and 4 sections each from 4 post-FPI rats). Consistent with earlier studies (REF), we found striking increases in GFAP-expressing astrocytes in the hilus 24 hours after FPI (Fig. 4C-D). However, there was limited overlap between the GFAP and TLR4 in both sham control and FPI rats (Fig. 4C-D, based on examination of 4 sections each from 3 sham rats and 4 sections each from 4 post-FPI rats). Sections obtained from rats 4 hours and 1 week after FPI and age-matched, sham-controls revealed qualitatively similar results with negligible co-labeling of TLR4 with either Iba1 or GFAP (data not shown).Taken together, our data indicate that the post-traumatic increase in TLR4 expression in the dentate gyrus is primarily in neurons.

TLR4 antagonist selectively decreases dentate excitability in injured rats

FPI cause hyperexcitablity of hippocampus {Lowenstein, 1992 #229}{Toth, 1997 #17}{Santhakumar, 2000 #7;Santhakumar, 2003 #948}{Gupta, 2012 #4061}. To determine if TLR4 mediated the hyperexcitability of hippocampus slices after FPI, field potential recordings were performed in the granule cell layer following perforant path stimulation. First, we assessed whether if TLR4 itself cause any change of excitability in granule cell of sham injury group. As shown in figure 5A &B, there was no detectable change in the amplitude of the granule cell population response to 4 mA stimulation intensity before and after the slices were incubated in the TLR4 antagonist LPS-RS (50 ug/ml) for 2 hours (Fig 5A, B, E, 0.24 ± 0.08mV vs. 0. 15 ± 0.05 mV, n=15 from 5 rats, ANOVA, $P>0.05$), suggesting TLR4 did not involve in excibability of granule cell population by stimulation of perforant path. Then the early post-traumatic changes in dentate excitability after FPI injury was tested. The amplitude of the granule cell population response at 3-5 days after FPI showed substantial increase compared with sham group (Fig. 5, at 4mV stimulation, 1.3 ± 0.3 mV FPI vs 0.08 ± 0.06 mV Sham group, n=8 from 3 rats, ANOVA, $p<0.05$), which is consistant with our previous result (Gupta et al, 2012). To examine if up-regulated TLR4 after FPI mediates injury-induced hyperexcitability in dentate gyrus of hippocampus, the hippocampal slices were incubated in either ACSF or ACSF containing TLR4 antagonist LPS-RS (50 ng/ml) for 2 hours. The amplitude of population response of hippocampal slices after FPI and sham injury group was compared before and after incubation. The amplitude of population response of hippocampal slices from rats after FPI was greatly reduced after incubation in LPS-RS (Fig. 5C,D,E, at 4mA stimulation intensity, 1.3 ± 0.3 mV before incubation vs 0.4 ± 0.1 mV after incubation in LPS-RS, n=15 from 5 rats, ANOVA, $p<0.05$). However, the amplitude of population response of slices after FPI was 1.4 ± 0.4 mV at

4 mA stimation intensity after incubation in ACSF. There was no significant difference in amplitude of population response of slices after FPI before and after incubation in ACSF (1.3 ± 0.3 mV before incubation vs 1.4 ± 0.4 mV after incubation in ACSF at 4 mA stimulation intensity, n=15 from 5 rats, ANOVA, P>0.05, data not shown), suggesting that the up-regulated TLR4 mediates increased excitability induced by FPI.

TLR4 antagonist decreases dentate excitability in the presence of APV

To examine if TLR4 mediates increased excitability through NMDA receptor, the slices from rats 3-5 days after sham or FPI injury were stimulated in the presence of selective NMDA receptor APV (50 uM) during recording. First, there was no significant change of the amplitude of pop spike with or withour APV (50 uM) (0.55 ± 0.15 mV without APV vs. 0.51 ±0.13 mV with APV at 4 mA stimulation intensity, n=12 from 5 rats, ANOVA, P>0.05, data not shown). And APV (50 uM) did not change hyperexcitablity of granule cells from rats after FPI (1.8 ± 0.3 mV without APV vs 1.7 ± 0.4 mV with APV, n=12 from 5 rats, ANOVA, p>0.05, data now shown). With APV in the perfusion solution, 4mA stimulation induced 0.51 ± 0.13 mV of population spike in sham slices incubated in ACSF (Fig. 6A,E, n=12 from 5 rats). After incubated in LPS-RS for 2 hours, the average amplitude of population spike was 0.45 ± 0.16 mV following 4 mA stimulation (Fig. 6B,E,n=12 from 5 rats). There was no significant difference in excitability of granule cells of sham rats after incubation in ACSF and ACSF containing LPS-RS (Fig. 6E, ANOVA, P>0.05). However, after incubated in LPS-RS (50). the amplitude of population spike of FPI slices was still significantly reduced (Fig. 6, 1.7 ± 0.4 mV in ACSF vs. 0.6 ± 0.2 mV in LPS-RS, ANOVA, n= 12 from 5 rats, p<0.05), suggesting TLR4 mediated hyperexcitability of granule cells after FPI was independent of NMDA receptors.

In our western blot experiment, TLR4 protein expression was significantly increased 3 days after FPI injury (Fig.1A,B). The TLR4 expression appeared increased but not significant at 7 days after FPI injury. In our previous study (Gupta et al, 2012), the exitablity of granule cells were increased 7 days after FPI injury. So we examined whether if TLR4 was involved in the hyperexcitability of granule cells 7 days after FPI injury. The amplitude of population spike after LPS-RS incubation was 51 ± 19 % of the amplitude of population spike after ACSF incubation (Fig. 6F, n=6 from 3 rats, ANOVA, $P<0.05$). In the FPI group 3 days after injury, the amplitude of population spike after LPS-RS incubation was 31±15% of the amplitude of population spike after ACSF incubation (Fig. 6F, n=6 from 3 rats, ANOVA, $P<0.05$). There was no significant difference of population spike amplitude between 3 days after FPI group and 7 days after FPI group (Fig. 6F, n=6 from 3 rats, ANOVA, $P>0.05$). The sham groups also showed no significant difference of amplitude of population spikes between 3 days after sham group and 7 days after sham group (Fig. 6F, n=6 from 3 rats, ANOVA, $P>0.05$). At 3 days after sham injury, the amplitude of population spikes after LPS-RS was 88 ± 17 % of the amplitude of population spike after ACSF. At 7 days after sham injury, the amplitude of population spikes after LPS-RS was 92 ± 18 % of the amplitude of population spike after ACSF.

Discussion

UNDER CONSTRUCTION

References

Balosso S, Maroso M, Sanchez-Alavez M, Ravizza T, Frasca A, Bartfai T, Vezzani A (2008) A novel non-transcriptional pathway mediates the proconvulsive effects of interleukin-1beta. Brain : a journal of neurology 131:3256-3265.

Bhaskar K, Konerth M, Kokiko-Cochran ON, Cardona A, Ransohoff RM, Lamb BT (2010) Regulation of tau pathology by the microglial fractalkine receptor. Neuron 68:19-31.

Diogenes A, Ferraz CC, Akopian AN, Henry MA, Hargreaves KM (2011) LPS sensitizes TRPV1 via activation of TLR4 in trigeminal sensory neurons. J Dent Res 90:759-764.

Gao Y, Fang X, Sun H, Wang Y, Yao LJ, Li JP, Tong Y, Zhang B, Liu Y (2009) Toll-like receptor 4-mediated myeloid differentiation factor 88-dependent signaling pathway is activated by cerebral ischemia-reperfusion in hippocampal CA1 region in mice. BiolPharmBull 32:1665-1671.

Gupta A, Elgammal FS, Proddutur A, Shah S, Santhakumar V (2012) Decrease in Tonic Inhibition Contributes to Increase in Dentate Semilunar Granule Cell. Journal of Neuroscience 32:2523-2537.

Hallenbeck JM (2002) The many faces of tumor necrosis factor in stroke. NatMed 8:1363-1368.

Hua F, Ma J, Ha T, Xia Y, Kelley J, Williams DL, Kao RL, Browder IW, Schweitzer JB, Kalbfleisch JH, Li C (2007) Activation of Toll-like receptor 4 signaling contributes to hippocampal neuronal death following global cerebral ischemia/reperfusion. JNeuroimmunol 190:101-111.

Kielian T (2006) Toll-like receptors in central nervous system glial inflammation and homeostasis. JNeurosciRes 83:711-730.

Lambertsen KL, Gregersen R, Meldgaard M, Clausen BH, Heibol EK, Ladeby R, Knudsen J, Frandsen A, Owens T, Finsen B (2004) A role for interferon-gamma in focal cerebral ischemia in mice. JNeuropatholExpNeurol 63:942-955.

Liu T, Gao YJ, Ji RR (2012) Emerging role of Toll-like receptors in the control of pain and itch. Neurosci Bull 28:131-144.

Ma Y, Li J, Chiu I, Wang Y, Sloane JA, Lu J, Kosaras B, Sidman RL, Volpe JJ, Vartanian T (2006) Toll-like receptor 8 functions as a negative regulator of neurite outgrowth and inducer of neuronal apoptosis. JCell Biol 175:209-215.

Maroso M, Balosso S, Ravizza T, Liu J, Aronica E, Iyer AM, Rossetti C, Molteni M, Casalgrandi M, Manfredi AA, Bianchi ME, Vezzani A (2010) Toll-like receptor 4 and high-mobility group box-1 are involved in ictogenesis and can be targeted to reduce seizures. NatMed 16:413-419.

Okun E, Griffioen KJ, Mattson MP (2011) Toll-like receptor signaling in neural plasticity and disease. Trends in neurosciences 34:269-281.

Owens T, Babcock AA, Millward JM, Toft-Hansen H (2005) Cytokine and chemokine inter-regulation in the inflamed or injured CNS. Brain ResBrain ResRev 48:178-184.

Pascual O, Ben Achour S, Rostaing P, Triller A, Bessis A (2012) Microglia activation triggers astrocyte-mediated modulation of excitatory neurotransmission. Proceedings of the National Academy of Sciences of the United States of America 109:E197-205.

Rodgers KM, Hutchinson MR, Northcutt A, Maier SF, Watkins LR, Barth DS (2009) The cortical innate immune response increases local neuronal excitability leading to seizures. Brain 132:2478-2486.

Rolls A, Shechter R, London A, Ziv Y, Ronen A, Levy R, Schwartz M (2007) Toll-like receptors modulate adult hippocampal neurogenesis. NatCell Biol 9:1081-1088.

Santhakumar V, Voipio J, Kaila K, Soltesz I (2003) Post-traumatic hyperexcitability is not caused by impaired buffering of extracellular potassium. J Neurosci 23:5865-5876.

Santhakumar V, Ratzliff AD, Jeng J, Toth K, Soltesz I (2001) Long-term hyperexcitability in the hippocampus after experimental head trauma. AnnNeurol 50:708-717.

Santhakumar V, Bender R, Frotscher M, Ross ST, Hollrigel GS, Toth Z, Soltesz I (2000) Granule cell hyperexcitability in the early post-traumatic rat dentate gyrus: the 'irritable mossy cell' hypothesis. J Physiol 524 Pt 1:117-134.

Tang SC, Arumugam TV, Xu X, Cheng A, Mughal MR, Jo DG, Lathia JD, Siler DA, Chigurupati S, Ouyang X, Magnus T, Camandola S, Mattson MP (2007) Pivotal role for neuronal Toll-like receptors in ischemic brain injury and functional deficits. ProcNatlAcadSciUSA 104:13798-13803.

Tanga FY, Nutile-McMenemy N, DeLeo JA (2005) The CNS role of Toll-like receptor 4 in innate neuroimmunity and painful neuropathy. ProcNatlAcadSciUSA 102:5856-5861.

Tobon KE, Chang D, Kuzhikandathil EV (2012) MicroRNA 142-3p mediates post-transcriptional regulation of D1 dopamine receptor expression. PLoS One 7:e49288.

Toth Z, Hollrigel GS, Gorcs T, Soltesz I (1997) Instantaneous perturbation of dentate interneuronal networks by a pressure wave-transient delivered to the neocortex. J Neurosci 17:8106-8117.

Viviani B, Bartesaghi S, Gardoni F, Vezzani A, Behrens MM, Bartfai T, Binaglia M, Corsini E, Di LM, Galli CL, Marinovich M (2003) Interleukin-1beta enhances NMDA receptor-mediated intracellular calcium increase through activation of the Src family of kinases. JNeurosci 23:8692-8700.

Wadachi R, Hargreaves KM (2006) Trigeminal nociceptors express TLR-4 and CD14: a mechanism for pain due to infection. JDentRes 85:49-53.

West MJ, Slomianka L, Gundersen HJG (1991) Unbiased Stereological Estimation of the Total Number of Neurons in the Subdivisions of the Rat Hippocampus Using the Optical Fractionator. Anatomical Record 231:482-497.

Yu J, Proddutur A, Elgammal FS, Ito T, Santhakumar V (2013) Status epilepticus enhances tonic GABA currents and depolarizes GABA reversal potential in dentate fast-spiking basket cells. J Neurophysiol.

Figure Legends

Fig. 1. Early increase in hippocampal TLR4 after FPI. A. Western blots of hippocampal tissue labeled with the Cell signaling (Cat # 2219) antibody against TLR4 show a single specific band at 95 KD (above). Note increase in intensity at various time points after FPI and absence of the band in TLR4 knockout. Beta-actin control for protein levels is shown below. B. Summary data shows TLR4 protein levels (normalized to β-actin levels in the samples). Data are presented as percent of TLR4 levels in controls 4 days after sham injury. Summary data demonstrate the TLR 4 levels at various time points. Error bars indicate s.e.m. * indicate $p<0.05$ by Kriskal Wallis and Mann Whitney U tests.

Figure 2. Post-traumatic increases in TLR4 expression in dentate gyrus. A-C. Gray scale images show fluorescence intensity of TLR4 labeling in dentate sections from a sham-operated rat (A), a rat 24 hrs post FPI (B) and a TLR4 knockout mouse (C). Note the increase in TLR4 staining after FPI and absence of staining in the knockout. GCL: granule cell layer; ML: molecular layer. Scale bar: 100 mm. D. Summary data shows semi-quantitative analysis of immunostaining intensity in molecular layer and dentate hilus of sections obtained from rats 24hrs after FPI and sham injury (Sham). Error bars indicate s.e.m. * indicate $p<0.05$ by one way ANOVA followed by Tukey's post hoc test.

Figure 3. Enhanced Neuronal expression of TLR4 after brain injury. A-B. Confocal images of sections obtained 24 hours after sham (A) or FPI (B) show immunostaining for NeuN (left),TLR4 (center) and merged images (right). Scale bar: 20 μm. C. Summary plots show that the number of TLR4 positive profiles in the hilus that co-label for NeuN is increased after FPI. Error bars indicate s.e.m. * indicate $p<0.05$ by one way ANOVA and Tukey's post hoc test.

Figure 4. Limited expression of TLR4 in glia. A-B. Confocal images of the dentate hilus from sections obtained 24 hours after sham-injury (A) and FPI (B) show labeling for Iba1, a microglial marker (left, arrows), and TLR4 (center, arrowheads). Merged image (right) shows the lack of co-labeling of cells stained for Iba1 and TLR4. C-D. Confocal images of the dentate hilus show immunostaining for GFAP (left) and TLR4 (center, arrowhead) and lack of co-labeling for GFAP and TLR4 in the merged image (right). Sections were obtained from 24 hrs after sham-injury (C) and FPI (D). Scale bar: 20 μm.**Figure 5. TLR4 antagonist selectively decreases dentate excitability in injured rats.** A-B. Granule cell population responses evoked by a 4 mA stimulus to the perforant path in a slice, before (A) and after (B) incubation in the TLR4 antagonist, LPS-RS (50 ng/ml for 2 hr). Slices were obtained from a sham-operated control rat. C-D. Dentate field responses in a slice obtained from a rat 7 days after FPI before (C) and after (D) LPS-RS treatment. Arrows indicate stimulus artifact. (E) Summary data demonstrate the effect of LPS-RS on the perforant path-evoked granule cell population spike amplitude in slices from sham-operated and FPI rats at various stimulation intensities. Error bars indicate s.e.m. * indicates $p<0.05$ by two-way repeated measures ANOVA.followed by and Tukey's post hoc test.

Figure 6. NMDA receptor antagonists fail to eliminate the post-injury decrease of dentate excitability by TLR4 antagonist. A-D. Representative granule cell population responses evoked by a 4 mA stimulus to the perforant path. Recordings were obtained in slices from rats 3 days after sham- (A,B) or FPI (C,D) in the presence of the NMDAR antagonist, APV (50 μm). Traces were obtained before (A,C) and after (B, D) incubation in LPS-Rs (50 ng/ml for 2 hr). Arrows indicate truncated stimulus artifact. (E) Summary data demonstrate the effect of LPS-RS on the afferent-evoked dentate population spike amplitude at various stimulation intensities in sections

obtained 3 days after FPI or sham -injury. (F) Summary plots of the dentate population spike amplitude after incubation in LPS-RS normalized to the amplitude in the same slice before incubation in LPS-RS show that LPS-RS selective decreases the amplitude of granule cell population responses both 3 and 7 days after FPI but not after sham-injury. Perforant path was stimulated by a 4 mA stimulus and recordings were obtained in APV (50 μm). N=6 slices each. Error bars indicate s.e.m. * indicates $p<0.05$ by two-way repeated measures ANOVA followed by and Tukey's post hoc test.

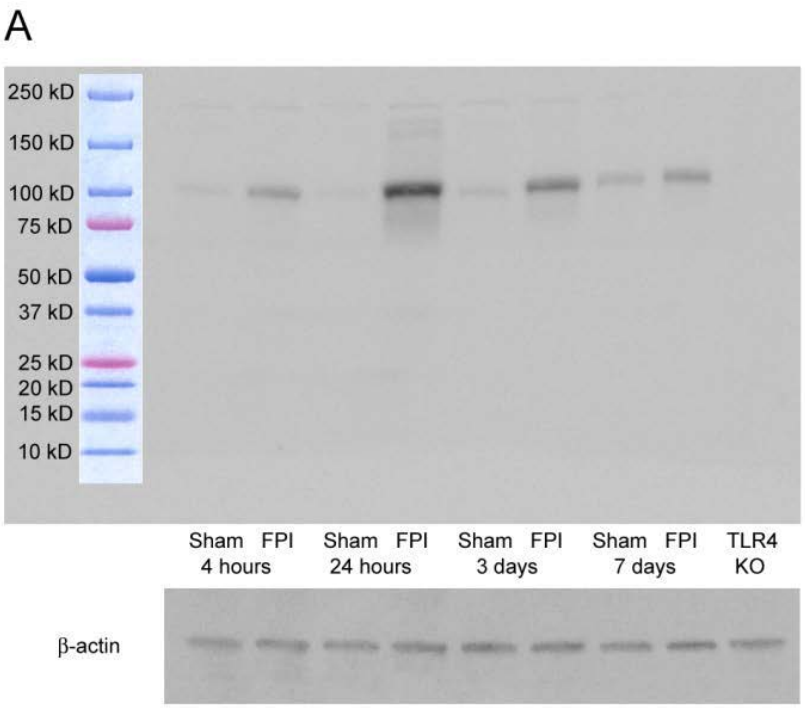

Li et al., Figure 1

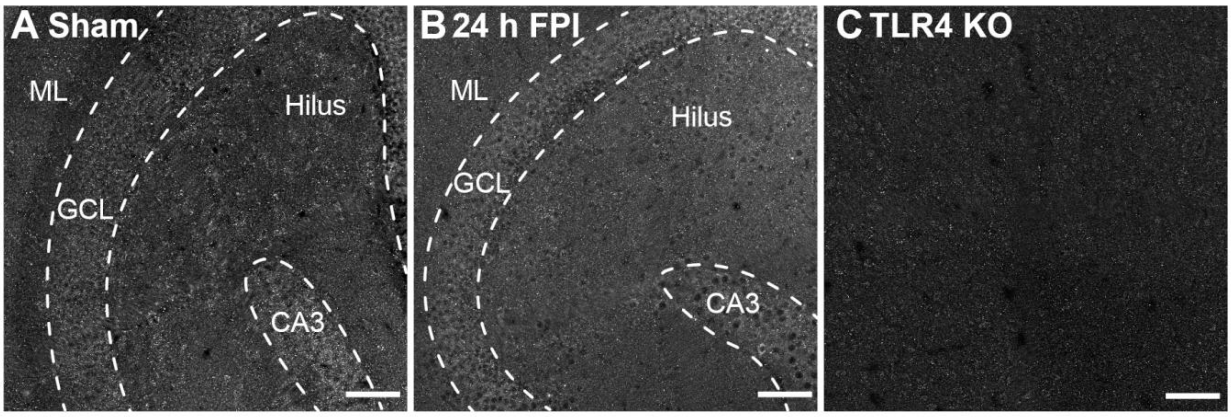

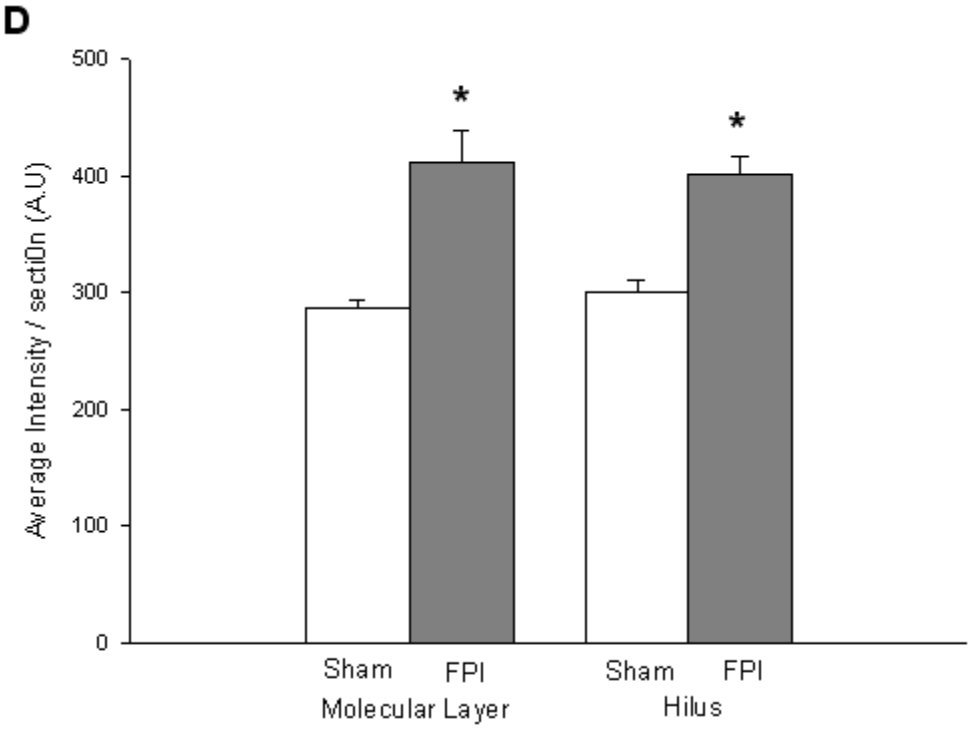

Li et al., Figure 2

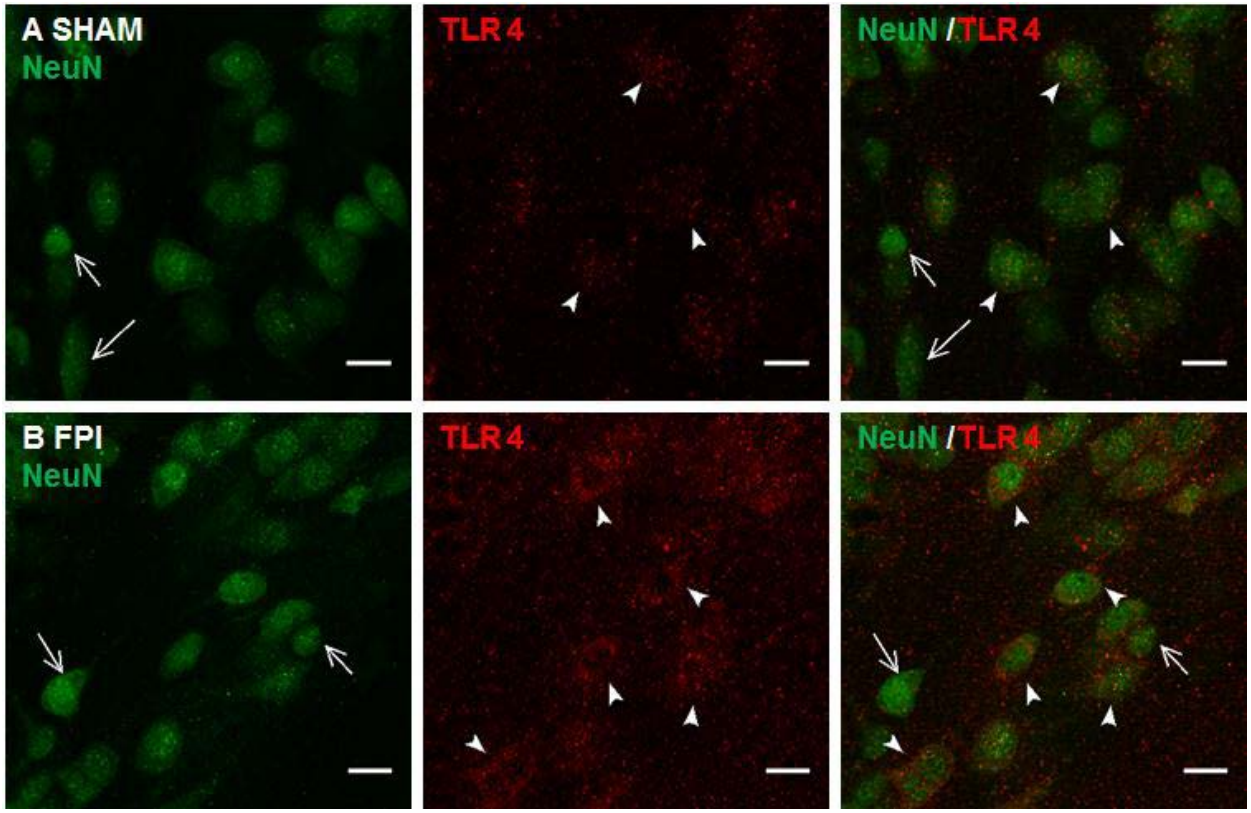

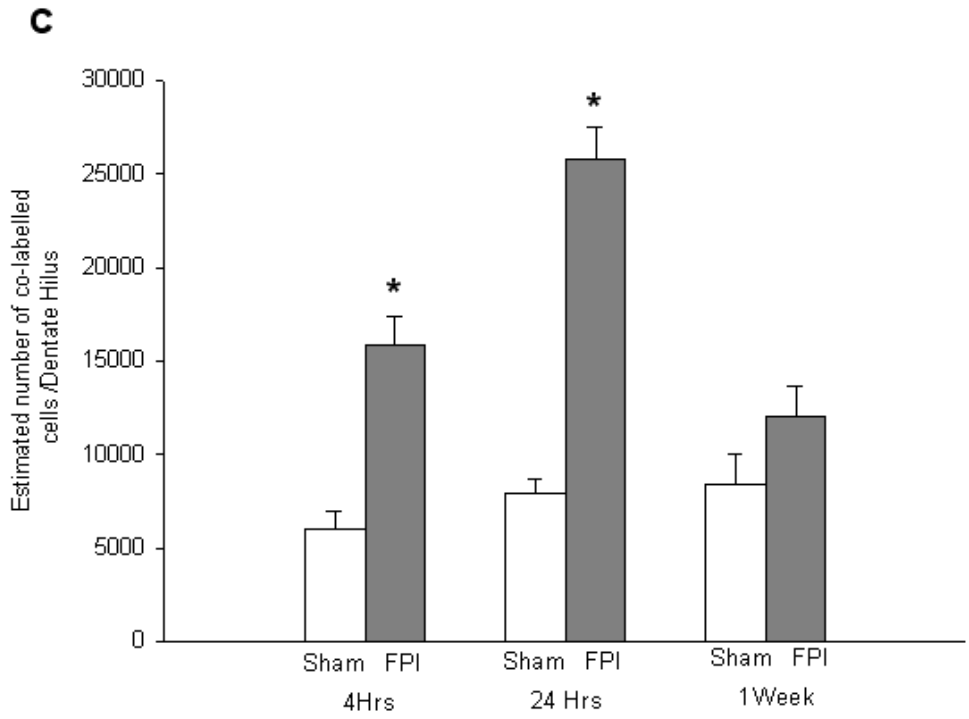

Li et al., Figure 3

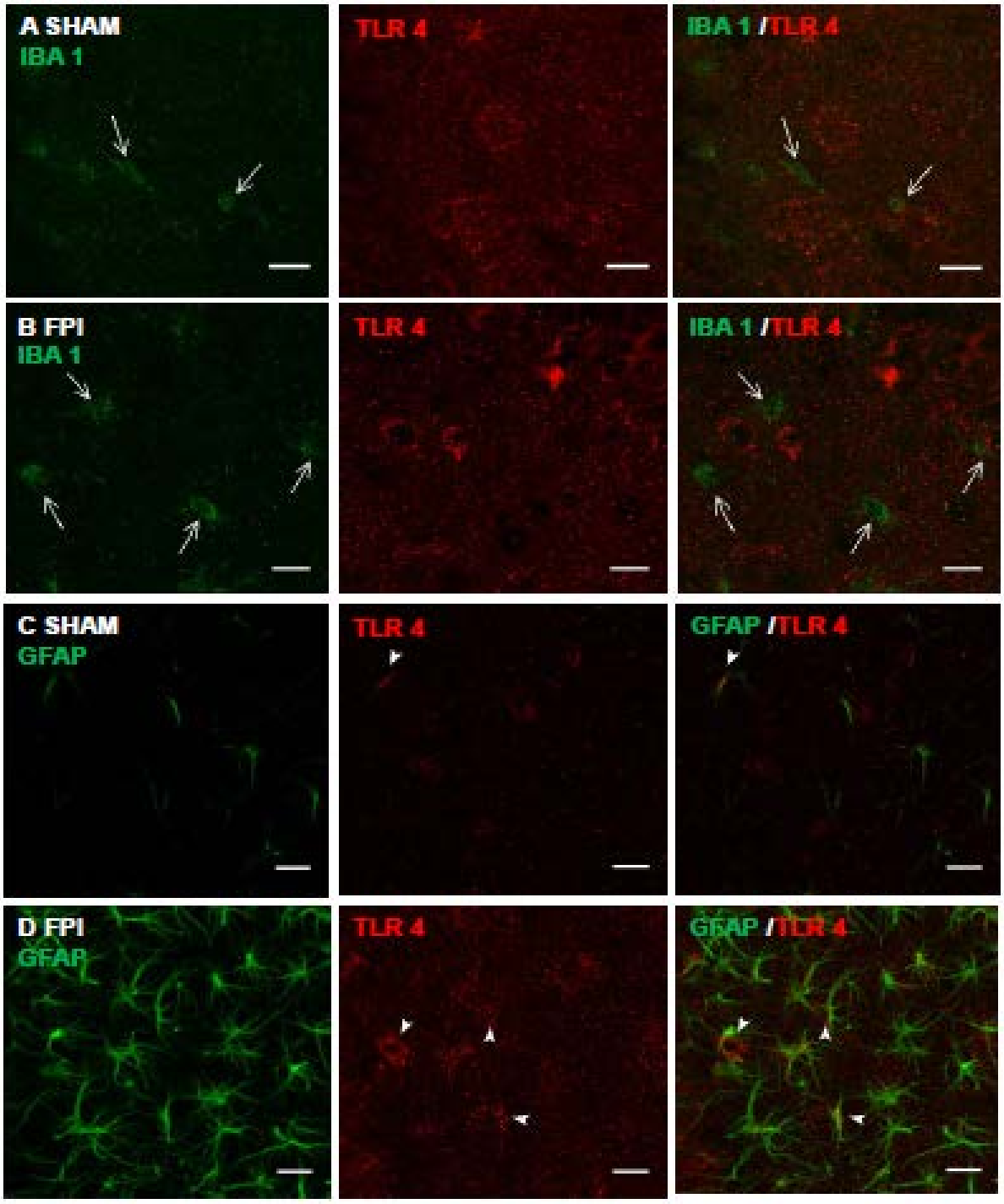

Li et al., Figure 4

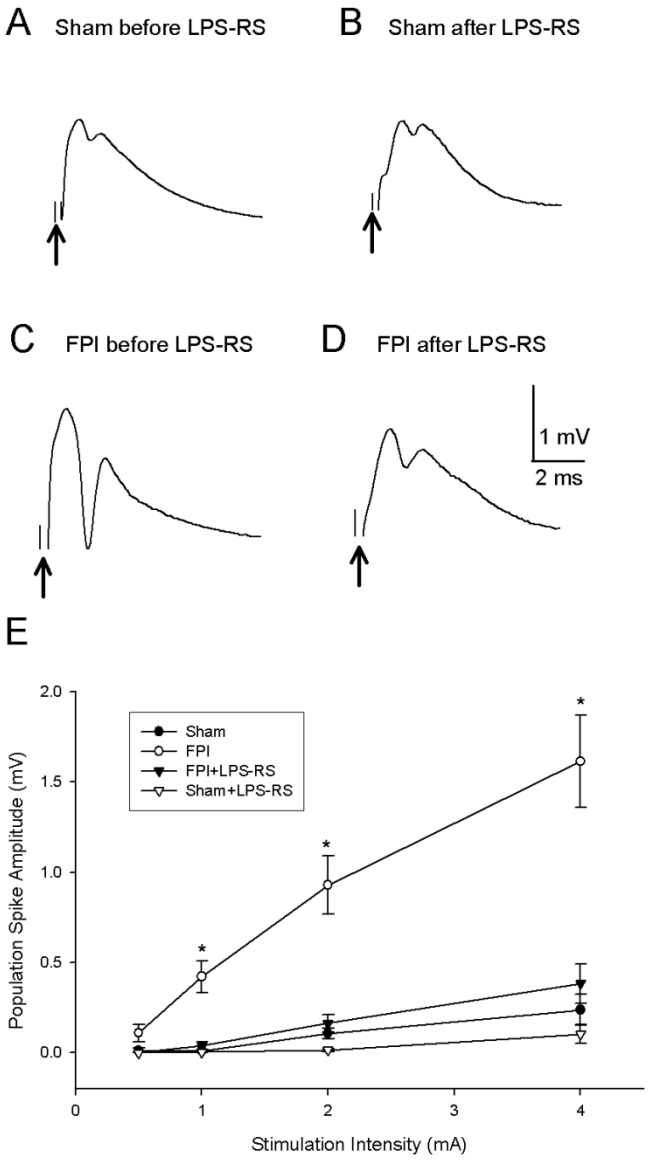

Li et al., Figure 5

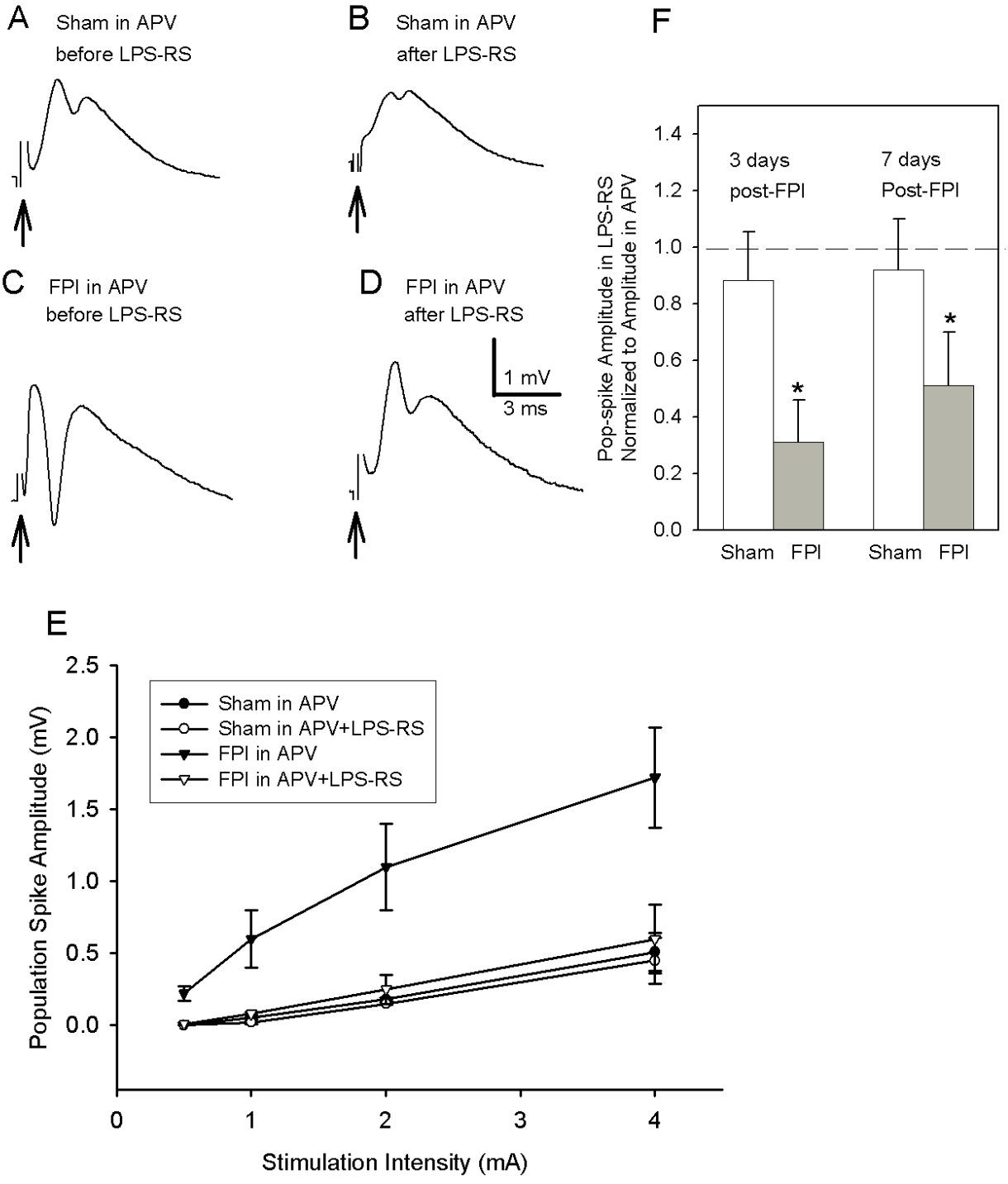

Li et al., Figure 6

Seizure-induced plasticity of fast-spiking basket cell GABA currents modulates frequency and coherence of gamma oscillation in network simulations

Archana Proddutur[1], Jiandong Yu[1], Fatima S. Elgammal[1] and Vijayalakshmi Santhakumar[1,2]

[1]Department of Neurology and Neurosciences, [2]Department of Pharmacology and Physiology, Rutgers New Jersey Medical School, Newark, New Jersey 07103

Running title: Basket cell extrasynaptic inhibition modulates network oscillations

Word Count for abstract: 348 **Body of the manuscript:** 7097

Figures: 5 Color Figures: 4 Tables: 0

Keywords: extrasynaptic inhibition, basket cell, epilepsy, high-gamma, dentate gyrus

Author Contributions: A.P performed all simulations J.Y performed physiological experiments; A.P analyzed data; A.P and V.S interpreted results of experiments; A.P and F.S.E prepared figures; A.P and V.S authored the manuscript; A.P, J.Y, F.S.E and V.S edited and approved the manuscript. A.P and V.S: conceived and designed research

Acknowledgements: This work is supported by NIH/NINDS NS069861 and NJCBIR 09.003-BIR1 to V.S.

Correspondence:
Vijayalakshmi Santhakumar, PhD
Department of Neurology and Neurosciences,
Rutgers New Jersey Medical School
MSB-H-512, 185 S. Orange Ave. Newark, NJ 07103
E-mail: santhavi@njms.rutgers.edu

Abstract

Gamma frequency oscillations are crucial for memory formation and retrieval. Networks of fast-spiking basket cells (FS-BCs) interconnected by fast, high amplitude GABA synapses and gap junctions are known to underlie development of gamma oscillations. Recent studies have identified that, apart from GABAergic synapses, FS-BCs in the hippocampal dentate gyrus have GABAergic currents mediated by extrasynaptic receptors. Moreover, following experimental seizures, FS-BC extrasynaptic (tonic) GABA currents are enhanced and GABA reversal potential (E_{GABA}) shifted to depolarizing potentials compared to controls. Here, we use homogeneous networks of biophysically realistic model FS-BCs to examine how the presence of extrasynaptic GABA conductance ($g_{GABA\text{-}extra}$) and seizure-induced changes in $g_{GABA\text{-}extra}$ and E_{GABA} influence network activity. Networks of FS-BCs interconnected by fast GABAergic synapses developed synchronous firing in the gamma frequency range. Systematic investigation of the effect of FS-BC interconnectivity on network synchrony revealed that the biologically realistic range of 30 to 40 connections between FS-BCs resulted in greater coherence at gamma frequency, when networks were activated by Poisson-distributed synaptic inputs rather than by heterogeneous current injections. Consistent with earlier studies, inclusion of gap junctions and distance-dependent conduction delay at synapses resulted in a modest enhancement of network coherence. In networks activated by heterogeneous current injections, increasing $g_{GABA\text{-}extra}$ modulated the frequency and coherence of network firing when E_{GABA} was shunting (-74 mV), but failed to alter network firing when E_{GABA} was depolarizing (-54 mV). When FS-BCs were activated by dendritic synaptic inputs, enhancing $g_{GABA\text{-}extra}$ reduced the frequency and coherence of FS-BC firing when E_{GABA} was shunting and increased firing frequency when E_{GABA} was depolarizing. Shifting E_{GABA} from shunting to depolarizing potentials consistently enhanced

firing by over 30 Hz shifting network firing to the high gamma frequency range (>80 Hz). Our demonstration that network oscillations are modulated by extrasynaptic inhibition in FS-BCs suggests that neuroactive compounds that act on extrasynaptic GABA receptors may impact memory formation by modulating hippocampal gamma oscillations. The simulation results indicate that the depolarized FS-BC GABA reversal, observed after experimental seizures, together with enhanced spillover extrasynaptic GABA currents are likely to promote generation of high gamma frequency activity associated with epileptic networks.

Lead paragraph

Among the rhythmic firing patterns observed in brain networks, gamma oscillations, which are involved in memory formation, are generated by a specific class of inhibitory neurons with robust interconnectivity through fast GABA synapses. Recently, we identified the presence of a tonic, slow form of GABA currents in these neurons and showed that experimentally-induced seizures increase the magnitude of tonic GABA currents and render GABA currents depolarizing. By simulating networks composed of biophysically accurate models of the specific inhibitory neuron involved in generation of gamma oscillations, we show that the presence of the tonic form of GABA currents can influence the robustness of gamma oscillations. Since tonic GABA currents are known to be altered by neuroactive compounds such as alcohol, steroids and anesthetics, our findings suggest a mechanism by which these agents may impact memory formation. Moreover, we find that the experimentally-detected, seizure-induced changes in GABA currents promote generation network activity at abnormally high gamma frequencies observed in epilepsy.

Introduction

Brain networks are characterized by the presence of oscillatory activity over a wide range of frequencies from the slow delta waves (0.5-3 Hz) to high frequency oscillations such as ripples (100-200 Hz) (Buzsaki et al., 2003; Buzsaki and Draguhn, 2004). Among the brain oscillations, the gamma frequency oscillations (30-80 Hz), which are present in several brain regions (Steriade et al., 1996; Csicsvari et al., 2003; Buzsaki, 2006), including hippocampal circuits, have been extensively investigated because of their proposed role as a reference signal in temporal encoding, contributions to binding of sensory feature and their role in memory formation and retrieval (Lisman and Idiart, 1995; Bartos et al., 2007; Montgomery and Buzsaki, 2007). Based on a large body of experimental and theoretical work, there is wide consensus that rhythmic activity of synaptically interconnected inhibitory neurons underlie hippocampal gamma oscillations (Wang and Buzsaki, 1996; Traub et al., 1998; Whittington et al., 2000; Bartos et al., 2002; Brunel and Wang, 2003). Indeed, hippocampal gamma oscillations, including those induced by agonists of metabotropic glutamate and muscarinic acetylcholine receptors *in vitro*, can be completely blocked by $GABA_A$ receptor ($GABA_AR$) antagonists, further indicating the critical role for inhibition in generation of gamma oscillations (Whittington et al., 1995; Fisahn et al., 1998; Mann et al., 2005). Among the diverse classes of inhibitory interneurons, the fast-spiking basket cells that express the calcium binding protein parvalbumin appear to be essential for the generation of gamma oscillations (Bartos et al., 2007). Parvalbumin positive basket cells are characterized by high mutual interconnectivity through fast synaptic inhibition and electrical coupling (Fukuda and Kosaka, 2000; Bartos et al., 2002; Galarreta and Hestrin, 2002; Hefft and Jonas, 2005). Additionally, parvalbumin basket cells have high intrinsic firing, low adaptation and an intrinsic resonance frequency which make them an optimal candidate to fire in phase with

gamma frequency oscillations (Pike et al., 2000; Hefft and Jonas, 2005). Fast-spiking basket cells (FS-BCs) innervate a large population of excitatory neurons which they can synchronize. Modeling studies have provided compelling evidence that homogeneous networks composed of integrate-and-fire neurons connected by synaptic inhibition can generate gamma frequency oscillations when activated by relatively homogeneous excitatory drive (Wang and Buzsaki, 1996). Subsequently, studies in networks of generic models of fast-spiking neurons connected to a biologically realistic number of local neighbors have demonstrated that incorporating the experimentally determined rapid synaptic decay kinetics between FS-BCs leads the network to synchronize in the gamma frequency range, even when in networks activated by heterogeneous non-synaptic excitatory drive (Bartos et al., 2002). Since network responses are strongly regulated by intrinsic neuronal properties (Bogaard et al., 2009), whether conclusions derived using generic models are robust to inclusion of biophysically realistic basket cell models remains to be examined.

One of the salient findings in simulation studies using homogeneous, synaptically connected inhibitory networks is that the frequency and coherence of network oscillations are regulated by the delay and decay kinetics of the GABA synapses (Bartos et al., 2002; Brunel and Wang, 2003; Bartos et al., 2007). Recently, we reported that, apart from the classical synaptic GABA currents, parvalbumin-positive, FS-BCs in the dentate gyrus express extrasynaptic (tonic) GABA currents (Yu et al., 2013). Extrasynaptic GABA currents are mediated by extra- and peri-synaptically located $GABA_A$Rs and can contribute to the decay kinetics of synaptic GABA receptors (Wei et al., 2003; Santhakumar et al., 2006; Glykys and Mody, 2007). Spillover of GABA from the synapse can activate extrasynaptic $GABA_A$Rs and lead to prolonged GABAergic inhibition. Since decay kinetics of synaptic inhibition regulate gamma oscillations

(Bartos et al., 2002), extrasynaptic GABA currents in FS-BCs are likely to modulate these rhythms. Consistent with this hypothesis, studies in hippocampal slices from mice lacking specific $GABA_AR$ subunits underlying extrasynaptic GABA currents have identified alterations in gamma rhythms (Mann and Mody, 2010). However, whether extrasynaptic GABA currents in FS-BCs modulate the coherence and frequency of network oscillation has not been examined. It is notable that extrasynaptic GABA currents in FS-BCs are enhanced following pilocarpine induced status epilepticus (Yu et al., 2013). The effect of extrasynaptic GABA currents on network oscillations may be of particular relevance to neurological disease, since previous studies have identified alterations in gamma oscillations in epilepsy and schizophrenia.

Apart from the kinetics of synaptic inhibition, the presence of shunting rather than hyperpolarizing reversal potential of synaptic GABA currents has also been shown to increase the frequency and reduce coherence of oscillations in homogeneous interneuronal networks (Vida et al., 2006). The increase in gamma frequency can be of clinical significance, since, unlike physiological gamma oscillations, high gamma oscillations at frequencies >80 Hz are associated with epileptic foci (Bragin et al., 2004; Worrell et al., 2004; Engel et al., 2009). Curiously, we found that the reversal potential for GABA currents (E_{GABA}) in FS-BCs is significantly depolarized following experimental status epilepticus (Yu et al., 2013) , raising the possibility that seizure-induced plasticity of FS-BC inhibition may contribute to increases in network oscillations frequencies. Here we use homogeneous networks of biophysically realistic, multi-compartmental model FS-BCs to examine how the presence of extrasynaptic GABA currents and the seizure-induced plasticity of GABA currents and E_{GABA} modify the frequency and coherence of network oscillations.

Material & Methods

Slice preparation and physiology

All procedures were performed under protocols approved by the University of Medicine and Dentistry of New Jersey, Newark, NJ, Institutional Animal Care and Use Committee. Young adult, male, Wistar rats between postnatal days 30-35 were were anesthetized with isoflurane and decapitated. Horizontal brain slices (300 µm) were prepared in ice-cold sucrose artificial CSF (sucrose-aCSF) containing (in mM) 85 NaCl, 75 sucrose, 24 $NaHCO_3$, 25 glucose, 4 $MgCl_2$, 2.5 KCl, 1.25 NaH_2PO_4, and 0.5 $CaCl_2$, using a Leica VT1200S Vibratome (Wetzlar, Germany). The slices were incubated at 32 ± 1°C for 30 minutes in a submerged holding chamber containing an equal volume of sucrose-aCSF and recording aCSF and subsequently held at room temperature (RT). The recording aCSF contained (in mM) 126 NaCl, 2.5 KCl, 2 $CaCl_2$, 2 $MgCl_2$, 1.25 NaH_2PO_4, 26 $NaHCO_3$ and 10 D-glucose. All solutions were saturated with 95% O_2 and 5% CO_2 and maintained at a pH of 7.4 for 1–6 h. Slices were transferred to a submerged recording chamber and perfused with oxygenated aCSF at 33 ± 1°C. Whole-cell current-clamp recordings from interneurons at the border of the hilus and granule cell layer were obtained under IR-DIC visualization using microelectrodes (5–7 MΩ) containing (in mM) 125 KCl, 10 K-gluconate, 10 HEPES, 2 $MgCl_2$, 0.2 EGTA, 2 Na-ATP, 0.5 Na-GTP and 10 PO Creatine titrated to a pH 7.25 with KOH. Biocytin (0.2%) was included in the internal solution for post-hoc cell identification (Gupta et al., 2012; Yu et al., 2013). Recordings were obtained using Axon Instruments MultiClamp 700B (Molecular Devices, Sunnyvale, CA). Data were low-pass filtered at 3 kHz, digitized using DigiData 1440A and acquired using pClamp10 at 10-kHz sampling frequency. Recorded neurons were held at -70 mV and the response to 1.5 sec positive and negative current injections were examined to determine active and passive characteristics. Cells

with non-adapting, high frequency firing for the entire duration of the current injection, and low input resistance (<150 MΩ), were classified as FS-BCs (Hefft and Jonas, 2005; Yu et al., 2013). Neurons with adapting firing, high input resistance (>150 MΩ), and sag during negative current injection were excluded from analysis. Post-hoc biocytin immunostaining and morphological analysis was used to definitively identify FS-BCs, on the basis of presence of axon terminals in the granule cell layer and immunostaining for parvalbumin (Yu et al., 2013). Following physiological recordings, slices were fixed in 0.1 M phosphate buffer containing 4% paraformaldehyde at 4°C for 2 days. Slices were incubated overnight at room temperature with anti-parvalbumin antibody (PV-28, 1.5:1000, polyclonal rabbit, Swant) in 0.3% Triton X-100 and 2% normal goat serum containing PBS. Immunoreactions were revealed using Alexa 488-conjugated secondary goat antibodies against rabbit IgG (1:250) and biocytin staining was revealed using Alexa 594-conjugated streptavidin (1:1000). Sections were visualized and imaged using a Nikon A1R laser confocal microscope with a 0.75 NA 20X air objective (Gupta et al., 2012; Yu et al., 2013).

Basket Cell Simulations.

Individual FS-BC models and FS-BC network simulations were implemented using the NEURON 7.0 simulation environment (Hines and Carnevale, 1997). The biophysically realistic FS-BC model was adapted from earlier studies (Santhakumar et al., 2005; Dyhrfjeld-Johnsen et al., 2007). The model FS-BC included a soma and 2 apical and basal dendrites each with 4 distinct compartments (Fig. 1B). Active and passive conductances were distributed as detailed previously (Santhakumar et al., 2005). Sodium and fast delayed rectifier potassium channels restricted to the soma and proximal dendrites. Reversal potential of a non-specific leak channel was set to -75mV to modify the basket cell resting membrane potential (-75 mV) to match

experimental data (Yu et al., 2013). Additionally, conductance of the non-specific leak channel was set to 0.18 mS/cm^2 in the soma and 0.12 mS/cm^2 in the dendrite to simulate the experimentally observed input resistance. Gap junctions were implemented as an intercellular conductance (Bartos et al., 2002). In an initial set of experiments (Fig. 2), total gap junctional conductance to the model FS-BC was systematically varied between 1 and 10^6 pS to determine the effect on cellular input resistance. Input resistance was measured in response to -100 pA current injection. Baseline extrasynaptic GABA conductance was modeled as a linear deterministic leak conductance with baseline, control GABA reversal potential (E_{GABA}) of -74 mV (Song et al., 2011; Yu et al., 2013). Extrasynaptic GABA conductance ($g_{GABA\text{-}extra}$) was distributed uniformly in all compartments and varied between 2 and 10 μS/cm^2, corresponding to a biologically relevant range of 10 to 60pA extrasynaptic GABA currents (Yu et al., 2013).

Network Simulations.

Structurally realistic FS-BC network models were simulated with 200 FS-BCs arranged on a virtual ring with 50 μm spacing between adjacent cells (Bartos et al., 2002; Vida et al., 2006). FS-BCs were connected by $GABA_A$ synapses located on the proximal apical dendrite as described previously (Santhakumar et al., 2005). Exp2Syn process was used to implement chemical synapses. Based on data from experimental studies, $GABA_A$ synapses between FS-BCs were simulated with a maximum synaptic conductance of 7.6 nS, rise and decay time constants of 0.16 and 1.8 ms, respectively, and a 0.8 ms synaptic delay (Bartos et al., 2002; Santhakumar et al., 2005). In an initial set of simulations, the number of synaptic connections between FS-BCs was systematically increased from 4 to 100 connections distributed among neighboring FS-BCs on either side. This pattern of connectivity is based on estimates obtained from anatomical data on the numbers and distribution of synaptic connections among dentate

basket cells (Sik et al., 1997; Bartos et al., 2001; Dyhrfjeld-Johnsen et al., 2007; Santhakumar, 2008). While all $GABA_A$ synapses included a synaptic delay of 0.8 ms, in some simulations an additional distance-dependent "conduction delay" was included. The conduction delay was calculated from the distance between pre- and postsynaptics cell along the circumference of the ring and an estimated conduction velocity of 0.25 m/s (Bartos et al., 2002). Additionally, in a subset of simulations each neuron was connected to 50 nearest neighbors by electrical synapses located in the dendritic compartments (Amitai et al., 2002). Consistent with experimental data on the single channel conductance of connexin 36 channels (Srinivas et al., 1999), conductance of a single electrical synapse was 10 pS. Unless otherwise stated, network simulations with extrasynaptic GABA currents included both baseline and "spillover" $g_{GABA\text{-}extra}$, modeled to simulate increases in $g_{GABA\text{-}extra}$ that accompany elevation in extracellular GABA levels during neuronal activity (Glykys and Mody, 2007). Spillover was modeled by including "spillover $g_{GABA\text{-}extra}$" associated with each inhibitory synaptic connection to the model FS-BC. The spillover $g_{GABA\text{-}extra}$ was modeled as two synapses with slow rise (7 ms) and decay time (200 ms) constants (Rossi et al., 2003) and 1.25pS and 0.125pS peak conductance. The peak conductance of the synaptic spill was further scaled by a factor reflecting the degree of enhancement of baseline extrasynaptic GABA currents (ratio of baseline $g_{GABA\text{-}extra}$ in a given simulation in $\mu S/cm^2$ to baseline $g_{GABA\text{-}extra}$ of 2 $\mu S/cm^2$). Networks were activated either by heterogeneous somatic current injections or by excitatory synaptic inputs. In networks activated by somatic current injections, the magnitude of the current injection in each FS-BC was varied by randomly selecting the peak amplitude from a Gaussian distribution of amplitudes with a peak of 500 pA and variance of 0.5. Additional variability was introduced by staggering the time of commencement of current injection over a 70 ms time window (-20 to 50 ms of simulation time).

In networks activated by synaptic inputs, each model FS-BC received an independent Poisson-distributed train of excitatory synaptic inputs at 200 Hz. Excitatory synapses were located in the apical distal dendrites. The peak AMPA synaptic conductance was 20 nS and kinetics were similar to those used in previous studies (Santhakumar et al., 2005; Yu et al., 2013). The effects of increasing $g_{GABA\text{-}extra}$ on the average frequency and coherence of firing of FS-BCs in the mutually connected networks were examined. Unless otherwise stated, E_{GABA} of synaptic and extrasynaptic GABA currents was set to -74 mV to simulate the experimentally determined GABA reversal in control FS-BCs (Yu et al., 2013). Reversal potential of synaptic and extrasynaptic GABA currents was set to -54 mV to simulate the depolarized GABA reversal in FS-BCs after experimental status epilepticus (Yu et al., 2013).

Analysis.

Firing frequency was quantified as the average of the reciprocal of inter-spike intervals during 200-400 ms of the simulation after establishment of stable network synchrony. Population coherence during 200-400 ms of the simulation was calculated as described previously (White et al., 1998; Santhakumar et al., 2005). Briefly, for a pair of discharging neurons, trains of square pulses were generated for each of the cells with each pulse of height unity being centered at the spike peak and the width being 20% of the mean firing period (interspike interval) of the faster cell in the pair. Next, the cross-correlation was calculated at zero time lag of these pulse trains, which is equivalent to calculating the shared area of the unit height pulses. Coherence was defined as the sum of the shared areas divided by the square root of the product of the total areas of each individual train (Santhakumar et al., 2005). The average coherence was calculated from the coherence values obtained for all cell pair combinations. Summary data in Figures 4 and 5 were generated from 3 independent runs with different randomization seeds. Physiological and

computational data are presented as mean±s.e.m. Where appropriate, two-way repeated measures ANOVA (SPSS) was used to compare data. Significance was set at $p<0.05$.

Results

Comparison of model and biological basket cell physiology.

The most salient intrinsic biophysical properties of FS-BCs include high frequency non-adapting firing and low input resistance (Hefft and Jonas, 2005; Zhang and Buckmaster, 2009). In order to directly compare the intrinsic properties of the model FS-BC to the biological neurons, we obtained physiological recordings from dentate basket cells. As illustrated in Figure 1, FS-BCs were identified by their morphological features including axon in the granule cell layer, immunoreactivity for parvalbumin (Fig. 1A) and characteristic high frequency, non-adapting firing pattern (Fig. 1C). We adapted the multi-compartmental basket cell model used in earlier studies (Santhakumar et al., 2005; Dyhrfjeld-Johnsen et al., 2007). The model FS-BC had two apical and 2 basal dendrites each with 4 compartments (Fig 1B). The resting membrane potential of the model FS-BC was set to –75 mV, consistent with that of biological FS-BCs (-74.0 ±1.9, n=10 cells) reported in our recent study (Yu et al., 2013). In response to positive current injections, the model FS-BC simulated the high frequency, non-adapting firing pattern observed in biological FS-BCs (Fig. 1 C, D). Comparison of the model FS-BC firing frequency in response to increasing positive current injections demonstrated that the firing in response to steady state current injections was similar in the model and biological FS-BCs (Fig. 1E, firing data in biological FS-BCs was obtained from n=12 cells). FS-BCs are known to have a low input resistance compared to other hippocampal interneurons. The input resistance (R_{in}) of the model FS-BC was set to 94.3 MΩ consistent with the range observed in biological FS-BCs (Fig. 1F; FS-BC R_{in}: 93.0±10.6 MΩ, n=12 cells, data previously reported in Yu et al., 2013). Since neuronal R_{in} can modify both responses to current injections and how synaptic and extrasynaptic conductances impact neuronal excitability, we measured the input resistance of model

interneurons in published studies examining the effects of GABAergic and gap junctional conductances on neuronal and network excitability. In contrast to the low <100 MΩ R_{in} in biological basket cells, model interneurons in seminal studies, which examined how biologically realistic GABA and gap junctional conductances influence gamma synchrony, exhibited R_{in} over 9000 MΩ (Bartos et al., 2002; Vida et al., 2006). Similarly, the model neurons in recent studies that examined the impact of $g_{GABA\text{-}extra}$ on interneuronal excitability had an R_{in} of >900 MΩ (Song et al., 2011). The use of biologically-based conductance values in model neurons with unrealistically high R_{in} is likely to lead to overestimation of the influence of the introduced conductance. Therefore, this study examined interneuronal networks of model FS-BCs with realistic passive membrane properties.

Effect of gap junctional and extrasynaptic GABA conductance on FS-BC input resistance

In addition to synaptic connections, FS-BC networks are interconnected by electrical synapses. A subset of our subsequent network simulation included gap junctions connections between 50 neighboring FS-BCs, each with a physiologically realistic single channel conductance of 10 pS (Srinivas et al., 1999). In order to determine whether inclusion of the gap junctional conductance altered FS-BC input resistance, we systematically increased the conductance of a single gap junction between a pair of FS-BCs and measured the input resistance. Regardless of whether gap junctions were located in the proximal or distal dendritic compartment, junctional conductances in the range of 1 to 100 pS did not decrease FS-BC input resistance (Fig. 2A). Additional increases in junctional conductance progressively reduced FS-BC input resistance to 90.3 MΩ at the 500 pS gap junctional conductance introduced in the model FS-BCs in our network simulations (Fig. 2A).

Next we introduced baseline $g_{GABA\text{-}extra}$ as a deterministic conductance. The magnitude of the specific membrane conductance was varied between 2 and 10 $\mu S/cm^2$, the conductance range that was estimated to simulated the biologically relevant range (10 to 60 pA) of extrasynaptic GABA currents (Yu et al., 2013). Varying the $g_{GABA\text{-}extra}$ across this entire range resulted in a <10% change in FS-BC membrane conductance (Fig. 2B). Moreover, including an additional 500 pS gap junctional conductance did not alter FS-BC membrane conductance beyond that resulting from the $g_{GABA\text{-}extra}$. Thus, the non-synaptic conductances introduced into model FS-BCs in the subsequent network simulation are not likely result in major changes in FS-BC passive membrane properties.

Effect of synaptic interconnectivity on network oscillations

We used networks of 200 FS-BCs connected in a virtual ring (Bartos et al., 2002; Vida et al., 2006) to examine how the degree of GABAergic synaptic interconnectivity affects network oscillations. We progressively increased the number of neighboring FS-BCs that each model neuron connected with from 4 to 100 (a range of 5 to 50% network connectivity). Synaptic conductance and kinetics were constrained by experimental data (Santhakumar et al., 2005) and held constant in all simulations. Individual FS-BCs in the network were activated by non-homogeneous current injections which were initiated at different time points to introduce asynchrony (see *Methods*). Increasing FS-BC connectivity lead to an initial decrease the firing frequency from 60.25±0.08 Hz with 4 connections to 43.65±0.13 Hz when each FS-BC was connected to 20 neighbors followed by an increase back to 61.14±0.28 Hz when FS-BCs contacted 30 or more neighbors (Fig. 3A, n= 3 runs). Notably, regardless of the connectivity, the network firing frequency remained within the gamma frequency range. Unlike frequency, coherence, which is a measure of synchronous network firing, was relatively low when FS-BCs

contacted 30 or less neighbors and increased considerably when 40 or more FS-BCs were connected (Fig. 3B).

Next, we examined whether the extent of GABAergic synaptic interconnectivity alters network synchrony when FS-BCs are activated by synaptic inputs. Perforant path AMPA synapses were located on the apical distal dendrites of FS-BCs and activated by Poisson-distributed spike trains at an average frequency of 200 Hz. Networks within the wide range of GABAergic synaptic interconnectivity (5 to 100 contacts) synchronized in the range of 60-80 Hz. Interestingly, while still within the gamma frequency range, the frequency at which synaptically activated networks synchronized was higher than that observed in networks activated by current injections (Fig. 3A). FS-BC networks activated by excitatory synaptic inputs synchronized with fewer FS-BC synaptic interconnections. The coherence of synaptically activated networks in which FS-BCs connected 20 or 30 neighbors showed considerably higher coherence than structurally similar networks activated by constant current injection in FS-BCs (Fig. 3B). Overall, coherence in synaptically activated networks remained relatively stable when 30 or more FS-BCs were interconnected by fast GABA synapses. The ability of the network to attain stable coherence when FS-BCs contact 30 or more neighbors is of particular interest since, based on morphological data (Sik et al., 1997; Bartos et al., 2001), basket cells in the dentate gyrus are estimated to contact approximately 35 neighboring basket cells (Dyhrfjeld-Johnsen et al., 2007; Santhakumar, 2008). Thus, it appears that the dentate basket cell networks may have an optimal connectivity to support coherent network oscillations.

Earlier studies using networks of generic fast-spiking model neurons have indicated that the presence of distance dependent axonal conduction delay and gap junctional coupling can modulate network coherence (Bartos et al., 2002; Bartos et al., 2007). In networks activated by

somatic current injection, inclusion of distance dependent conduction delay resulted in an increase in firing frequency (Fig. 3C) and coherence (Fig. 3D), particularly in networks with 30 interconnections. However, change in frequency and coherence in networks with higher interconnections was marginal (Fig. 3C-D). These simulation data suggest that conduction delay may tend to promote synchrony in networks with fewer interconnections. Similarly, inclusion of gap junctional connections from a model FS-BC to 50 neighbors lead to a small increase in both the firing frequency (Fig. 3C) and coherence (Fig. 3D) in networks with 30 or more connections. The limited effect of gap junctions on network coherence in our simulations differs from the more robust increase in coherence reported previously (Bartos et al., 2002). It is possible that the use of a single compartmental model with synapses and gap junctions located in the same somatic compartment (Bartos et al., 2002), rather than a biologically realistic dendritic distribution of gap junctions used in the current study, contributed to the difference in the magnitude of gap junctional modulation of gamma frequency coherence. In networks activated by dendritic perforant path synaptic inputs, inclusion of conduction delay and gap junctional coupling had negligible effect on either the firing frequency or coherence at all levels of FS-BC connectivity examined (data not shown). Therefore, we proceeded to use homogeneous FS-BC networks including distance-dependent axonal conduction delay and 30 or 40 synaptic connections between FS-BCs to investigate the effect of $g_{GABA\text{-}extra}$ on network firing and coherence.

Extrasynaptic GABA currents and depolarizing GABA reversal shift the frequency and reduce coherence of gamma oscillations.

Earlier simulation studies have demonstrated the crucial role played by synaptic inhibition in mediating synchronous gamma frequency oscillations (Wang and Buzsaki, 1996;

Bartos et al., 2002; Vida et al., 2006). Experimental data suggest that reduction in interneuronal extrasynaptic GABA currents can increase the frequency of charbachol-induced gamma oscillations *in vitro* through mechanisms involving NMDA receptors (Mann and Mody, 2010). However, whether the presence of extrasynaptic GABA currents in FS-BCs modulates the frequency and coherence of network oscillations has not been tested. This issue is particularly relevant to epilepsy, because FS-BC extrasynaptic GABA currents are enhanced following experimental status epilepticus (Yu et al., 2013). Therefore, we examined whether introducing baseline and spillover $g_{GABA\text{-}extra}$ in model FS-BCs modified network oscillations. FS-BCs were connected to 30 adjacent neighbors by synaptic GABA conductances and activated by heterogeneous current injection. Gap junctional connections were not included and GABA reversal was set to -74 mV, the experimentally determined value in control FS-BCs (Yu et al., 2013). Compared to the simulations without extrasynaptic GABA, introducing the normal biological level of baseline $g_{GABA\text{-}extra}$ (2 $\mu S/cm^2$) and corresponding spillover $g_{GABA\text{-}extra}$ (see *Methods*) led to a decrease in the average firing frequency (Fig. 4G, 59.43±1.01 Hz without $g_{GABA\text{-}extra}$ and 55.2±0.7 Hz with 2 $\mu S/cm^2$ baseline $g_{GABA\text{-}extra}$, $p<0.05$ by Student's t-test) and coherence (Fig. 4H, 0.42±0.6 without $g_{GABA\text{-}extra}$ and 0.30±0.4 with 2 $\mu S/cm^2$ baseline $g_{GABA\text{-}extra}$). Although increasing baseline $g_{GABA\text{-}extra}$ did not alter the network firing and coherence in the absence of spillover $g_{GABA\text{-}extra}$ (data not shown), parallel increases in baseline and spillover $g_{GABA\text{-}extra}$ resulted in progressive decrease in firing frequency and a biphasic change in coherence which peaked when $g_{GABA\text{-}extra}$ was 4 $\mu S/cm^2$ (Fig. 4A-B and G-H, $p< 0.05$ for effect of $g_{GABA\text{-}extra}$ on frequency and coherence by two way repeated measures ANOVA).

Apart from an increase in extrasynaptic GABA currents, FS-BCs E_{GABA} has been shown to shift to values more depolarized than the resting membrane potential after status epilepticus

(Yu et al., 2013). Earlier simulation studies have established that E_{GABA} modulates the firing frequency in homogeneous interneuronal networks (Vida et al., 2006; Bartos et al., 2007). We examined the effect of E_{GABA} on synaptically coupled networks of FS-BCs with a resting membrane potential of -75 mV without extrasynaptic inhibition. In networks activated by the same somatic current injection paradigm, altering synaptic GABA reversal from -74 mV (the value observed in control FS-BCs) to -54mV, the experimentally measured E_{GABA} in FS-BCs after status epilepticus, increased firing frequency by approximately 30 Hz (Fig. 4C,G, frequency in Hz: -74 mV E_{GABA}= 59.43±1.01, -54 mV E_{GABA} = 88.3±0.01, $p<0.05$ by Student's t-test) and decreased the coherence of FS-BC firing (Fig. 4D,H, coherence: -74 mV E_{GABA}= 0.42±0.6, -54 mV E_{GABA} = 0.2±0.0, $p<0.05$ by Student's t-test). Curiously, this increase in firing frequency occurred even though an E_{GABA} of -54 mV is negative to the model FS-BC firing threshold of -52 mV. Inclusion of $g_{GABA\text{-}extra}$ resulted in a little change in frequency (88.3±0.01 Hz without $g_{GABA\text{-}extra}$ and 88.4±0.02 Hz with 2 $\mu S/cm^2$ $g_{GABA\text{-}extra}$). Additionally, progressively increasing $g_{GABA\text{-}extra}$ caused a marginal decrease in network firing frequency (Fig. 4E-G, 88.4±0.02 Hz with 2 $\mu S/cm^2$ and 87.4±0.02 Hz with 10 $\mu S/cm^2$ $g_{GABA\text{-}extra}$). However, compared to networks with similar $g_{GABA\text{-}extra}$ and an E_{GABA} of -74 mV which fired at gamma frequencies (40-60 Hz), networks with -54 mV E_{GABA} showed marked increase in firing at 85-90 Hz (Fig. 4G, $p< 0.05$ for effect of E_{GABA} on frequency by two way repeated measures ANOVA). Moreover, the coherence of FS-BC firing was consistently lower in networks with -54 mV E_{GABA} (Fig. 4H, $p< 0.05$ for effect of E_{GABA} on coherence by two way repeated measures ANOVA). Qualitatively similar results were obtained in networks including gap junctional coupling and when model FS-BCs made synaptic connections with 40 adjacent neighbors (data not shown). Overall, when networks with shunting E_{GABA} are activated by heterogeneous current

injections, increases in FS-BC $g_{GABA\text{-}extra}$ within the biologically relevant range, resulted in progressive decrease in network firing and changes in coherence. However the average firing frequency remained within the gamma frequency range. In contrast to the effect of conductance, shifting E_{GABA} to a depolarized potential of -54 mV increased the average FS-BC firing frequency to >80Hz. Moreover, when E_{GABA} was -54 mV, increasing $g_{GABA\text{-}extra}$ did not further enhance firing or decrease the already low coherence. Together the simulation data from networks activated by heterogeneous current injections indicate that $g_{GABA\text{-}extra}$ can modulate gamma frequency oscillations under normal, physiological conditions of shunting inhibition. However, the depolarized E_{GABA} observed under pathological conditions reduces network coherence and shifts firing to higher frequencies regardless of the magnitude of $g_{GABA\text{-}extra}$.

Analyses of interneuronal networks activated by somatic current injections have greatly advanced our understanding of mechanisms underlying generation of network oscillations (Wang and Buzsaki, 1996; Bartos et al., 2002; Vida et al., 2006). However, biological networks are activated by synaptic excitatory inputs to the dendrites. Therefore we evaluated whether the modulation of network oscillations by extrasynaptic inhibition and E_{GABA} is altered when FS-BCs were activated by excitatory synaptic inputs to the distal dendrites. Networks of 200 FS-BCs connected to 30 nearest neighbors were activated by individual 200 Hz trains of Poisson-distributed, simulated perforant path synaptic inputs (Yu et al., 2013). Gap junctional connections were not included in the initial set of simulations. In synaptically activated networks, in the absence of $g_{GABA\text{-}extra}$ and with E_{GABA} set to -74 mV, FS-BCs fired with greater coherence and at a higher baseline frequency than corresponding simulations in networks activated by somatic current injections (Fig 3A-B, 4G-H, 5E-F). Introducing $g_{GABA\text{-}extra}$ resulted in a progressive decrease in both the frequency and coherence of FS-BC firing (Fig. 5A-B, E-F;

frequency in Hz: 73.6±0.0 8 without $g_{GABA\text{-}extra}$ 70.82±0.0 2 with 2 $\mu S/cm^2$ $g_{GABA\text{-}extra}$ and 54.1±0.1 with 10 $\mu S/cm^2$ $g_{GABA\text{-}extra}$; coherence: 0.62±0.0 2 without $g_{GABA\text{-}extra}$, 0.59±0.0 3 with 2 $\mu S/cm^2$ $g_{GABA\text{-}extra}$ and 0.47±0.0 4 with 10 $\mu S/cm^2$ $g_{GABA\text{-}extra}$, $p< 0.05$ for effect of $g_{GABA\text{-}extra}$ on frequency and coherence by two way repeated measures ANOVA). Although synaptically activated networks demonstrated greater firing frequency than networks activated by somatic current injection, both classes of networks synchronized in the gamma frequency range. Moreover, $g_{GABA\text{-}extra}$ decreased the firing frequency and coherence under both conditions. In additional simulations in which FS-BCs were connected to 50 adjacent neighbors by gap junctions, increasing $g_{GABA\text{-}extra}$ progressively reduced firing frequency and coherence (Fig. E-F). Similarly, even when FS-BCs were connected to 40 adjacent neighbors, $g_{GABA\text{-}extra}$ decreased firing frequency and coherence (Fig. E-F).

Next we examined how depolarizing E_{GABA} modulated synchrony in networks a without gap junctional connections activated by perforant path synaptic inputs. Networks of FS-BC with GABAergic synaptic connections to 30 adjacent FS-BCs simulated without $g_{GABA\text{-}extra}$ and with E_{GABA} set to -54 mV, fired at higher frequency but considerably lower coherence than similar networks with a -74 mV E_{GABA}. Unlike networks activated by somatic current injections, increasing $g_{GABA\text{-}extra}$ progressive enhanced the network firing frequency with little effect on coherence (Fig. 5C-D, E-F; frequency in Hz: 123.0±0.0 2 with 2 $\mu S/cm^2$ $g_{GABA\text{-}extra}$ and 129.4±0.0 2 with 10 $\mu S/cm^2$ $g_{GABA\text{-}extra}$; coherence: 0.21±0.0 with 2 $\mu S/cm^2$ $g_{GABA\text{-}extra}$ and 0.20±0.0 with 10 $\mu S/cm^2$ $g_{GABA\text{-}extra}$, $p< 0.05$ for effect of $g_{GABA\text{-}extra}$, E_{GABA} and interaction between $g_{GABA\text{-}extra}$ and E_{GABA} on frequency and coherence by Two way repeated measures ANOVA). When E_{GABA} was set to -54 mV, FS-BC firing frequency consistently remained over 120 Hz, in the range of high frequency oscillations. Even in simulations where gap junctional

connections were included or when FS-BCs were connected to 40 adjacent neighbors, increasing $g_{GABA\text{-}extra}$ steadily enhanced the network firing frequency in the range of high frequency oscillations in the presence of the depolarizing E_{GABA}.

Thus, simulations of networks activated by distal dendritic excitatory synaptic inputs demonstrate that $g_{GABA\text{-}extra}$ can modulate gamma frequency oscillations, reducing frequency and coherence when E_{GABA} is shunting and increasing firing frequency when E_{GABA} is depolarizing. Furthermore, irrespective of how the networks were activated, the depolarizing shift in FS-BC E_{GABA} enhanced firing by over 50 Hz shifting normal gamma frequency oscillations to the high frequency oscillations known to be associated with epilepsy.

Discussion

Networks of fast-spiking interneurons connected by fast GABA synapses are known to play a fundamental role in generation of gamma frequency oscillations in brain networks (Wang and Buzsaki, 1996; Whittington et al., 2000; Bartos et al., 2002; Bartos et al., 2007). Apart from the network structure which can sculpt spatial and temporal patterns of activity (Netoff et al., 2004; Percha et al., 2005; Morgan and Soltesz, 2008), recent reports have underscored the effect of intrinsic neuronal properties on network firing patterns (Bogaard et al., 2009; Skinner, 2012). Here we use homogeneous networks of biophysically realistic models of dentate fast-spiking basket cells to examine the effect of synaptic interconnectivity and extrasynaptic inhibition on network firing patterns. The simulation results demonstrate that networks activated by realistic synaptic current inputs develop more coherent network firing at higher gamma frequency ranges than networks in which model neurons are activated by somatic current injections. Networks with 30-40 synaptic connections, similar to the range of basket cell connectivity estimated based on experimental literature (Dyhrfjeld-Johnsen et al., 2007), develop highly coherent firing in the gamma frequency range. As identified in earlier studies (Bartos et al., 2002), gap junctional connectivity and axonal conduction delay have marginal effect on firing frequency but enhance coherence of network activity. In the presence of shunting GABA reversal, extrasynaptic GABA conductance reduced both frequency and coherence of gamma oscillations, demonstrating that modulation of basket cell tonic inhibition can impact network rhythms. A depolarizing shift in E_{GABA}, observed in basket cells one week after experimental status epilepticus (Yu et al., 2013), enhances network firing to high frequencies associated with epileptic networks and degrades network coherence. In synaptically activated networks, increases in extrasynaptic GABA currents, also a feature of basket cells following experimental status epilepticus (Yu et al.,

2013), further augments the firing frequency. These findings indicate that seizure-induced changes in basket cell GABA currents and reversal may undermine physiological gamma oscillations and contribute to the pathological high frequency oscillations observed in human and animal epilepsy (Bragin et al., 1999; Worrell et al., 2004; Worrell et al., 2008).

Motivation for use of biophysically realistic neuron models

Combinations of theoretical and experimental studies have provided convincing evidence that fast-spiking interneurons contribute to the generation of gamma frequency network oscillations. Recent studies have identified that intrinsic properties of the individual cells in a network can play a critical role in determining the spatiotemporal patterns of network activity (Bogaard et al., 2009). Thus, intrinsic properties of FS-BCs that underlie gamma frequency oscillations are likely to impact the emergent activity patterns in homogeneous interconnected networks. The membrane excitability properties of FS-BCs, described by the firing frequency-current input relationship (*f-I* curve), show a continuous *f-I* curve with low firing frequencies at threshold and a steep *f-I* slope (Fig. 1C) and are typical of type I neurons (Bogaard et al., 2009). Apart from developing synchronous chains and bursts of activity, networks of type I neurons can demonstrate asynchronous high frequency firing which is not observed in networks of type II neurons characterized by shallow *f-I* slope (Bogaard et al., 2009). Indeed, we find that FS-BC networks show synchronous bursting at gamma frequencies when E_{GABA} is shunting, and the activity pattern in structurally similar networks switches to low coherence high frequency firing when E_{GABA} is depolarizing. These finding suggest that, in addition to changes in connectivity patterns, alterations in synaptic reversal potential can also impact synchrony in networks of type I neurons.

While most existing studies adopt model FS-BC neurons with high frequency firing and realistic synaptic, extrasynaptic or gap junctional conductances (Bartos et al., 2002; Vida et al., 2006; Kochubey et al., 2011; Song et al., 2011), we observed that generic models adopt unrealistic high R_{in} which can alter membrane time constants and contribute to overestimation of the impact of the conductances under investigation. Indeed, our recent study found that the biphasic firing response generated by introducing depolarizing extrasynaptic GABA conductance in generic interneuronal models with high R_{in} (Song et al., 2011) was observed only when extremely high levels of extrasynaptic GABA conductance was introduced in biophysically realistic model FS-BCs (Yu et al., 2013). Since one of the salient features of FS-BCs is their low R_{in}, and as our goal was to study the effect of introducing biologically realistic levels of $g_{GABA\text{-}extra}$, we adopted biophysically accurate models of dentate FS-BCs in our study. Our simulations demonstrate that FS-BCs networks connected with fast GABA synapses with realistic synaptic parameters and connectivity show coherent firing in the gamma frequency range and confirm the findings of earlier studies using generic models of fast-spiking neurons (Bartos et al., 2002). However, we find that gap junctional conductances have a rather modest effect on firing coherence in networks of biophysically realistic model FS-BCs. We propose that the combination of natural FS-BC input resistance and dendritic location of the coupling in our multi-compartmental model neurons provides a more faithful representation of biology. While dendritic gap junctions are known to modulate network dynamics in the presence of active dendrites (Saraga et al., 2006), the restriction of sodium and fast delayed rectifier potassium conductances to the somatic compartment in our model FS-BC may have contributed to the limited effect of gap junctional conductances. Interestingly, despite the caveat that our model FS-BCs did not replicate the gamma frequency intrinsic resonance observed in hippocampal fast

spiking interneurons (Pike et al., 2000), FS-BC networks with fast GABA synapses and anatomically realistic connectivity patterns developed robust synchrony in the gamma frequency range. Moreover, even when we replaced somatic current injections with biologically motivated asynchronous dendritic synaptic inputs at 200 Hz to activate FS-BCs, network activity consistently synchronized in the gamma frequency range. These results are consistent recent simulation studies demonstrating that excitatory synaptic drive at frequencies between 20 and 200 Hz result in gamma oscillations in networks of fast-spiking interneurons (Kochubey et al., 2011). The network model developed here provides a powerful system to examination how the presence and plasticity of specific membrane conductances influence the ability of FS-BC networks to sustain gamma oscillations.

Modulation of gamma frequency oscillations by extrasynaptic inhibition.

Tonic GABA currents mediated by peri- and extrasynaptic GABA receptors are present in various interneuronal types including FS-BCs (Semyanov et al., 2003; Glykys et al., 2007; Krook-Magnuson et al., 2008; Olah et al., 2009; Mann and Mody, 2010; Yu et al., 2013). Extrasynaptic GABA receptors contribute to the baseline levels of noise and influence neuronal excitability and gain (Mitchell and Silver, 2003; Farrant and Nusser, 2005). Additionally, experimental studies have demonstrated that rodents lacking GABA receptor subtypes that underlie tonic GABA currents show changes in gamma frequency oscillations (Towers et al., 2004; Mann and Mody, 2010). It is known that both stochastic noise and synaptic parameters modulate network oscillations (Bartos et al., 2007; Stacey et al., 2009). In addition to their contribute to baseline noise, extrasynaptic GABA receptors contribute to the decay of synaptic receptors and slow spillover GABA conductances (Rossi et al., 2003; Mtchedlishvili and Kapur, 2006; Santhakumar et al., 2006; Glykys and Mody, 2007). Indeed, the decay of inhibitory

synaptic kinetics in FS-BCs is modulated by THIP (unpublished observations), an agonist selective for $GABA_AR$ δ subunits which mediate tonic GABA currents in FS-BCs (Yu et al., 2013). Our simulations showing that increases in spillover GABA conductances decrease the frequency and coherence of gamma frequency oscillations (Fig. 4 and 5) are consistent with the reduction frequency and coherence when synaptic decay kinetics are prolonged (Bartos et al., 2007). However, in light of our highly conservative assumption of low spillover conductance, it is possible that our simulations underestimate the magnitude of the effect of $g_{GABA\text{-}extra}$ on the frequency and coherence of network oscillations. Moreover, robust increases in synaptic inhibition during physiological and pathological neuronal activity are likely to be accompanied by enhancement of spillover GABA conductance which could further augment the impact of $g_{GABA\text{-}extra}$ on network oscillations. Our observation that systematic increases in the baseline $g_{GABA\text{-}extra}$ fail to modulate network oscillations in the absence of spillover conductance underscores the importance of synaptic kinetics in determining network oscillations. However, our simulation of baseline extrasynaptic GABA conductance as a deterministic leak conductance rather than stochastic noisy conductance precludes changes in baseline root-mean-square noise associated with increasing $g_{GABA\text{-}extra}$. Consequently, use of a deterministic leak conductance to simulate baseline tonic GABA conductance may have resulted in further underestimation of the impact of these conductances on network coherence.

The ability of $g_{GABA\text{-}extra}$ to modulate gamma oscillations can have considerable impact on the physiological and pharmacological modulation of gamma oscillations. Tonic GABA currents in FS-BCs are mediated by $GABA_ARs$ containing δ subunits (Yu et al., 2013). $GABA_ARs$ δ subunits are subject to modulation by several neuroactive compounds such as alcohol, neurosteroids and certain anesthetics (Stell et al., 2003; Mody et al., 2007; Brickley and Mody,

2012). Therefore, it is possible that certain neroactive compounds act, in part, by modulating network oscillations as a consequence of their effect on $g_{GABA\text{-}extra}$. Moreover, recent findings that tonic GABA currents mediated by δ subunit containing $GABA_A$Rs are modulated by $GABA_B$ receptor activation (Connelly et al., 2013; Tao et al., 2013), suggest that physiological modulation of tonic GABA currents could regulate the robustness of network oscillations. Overall, our results demonstrating that FS-BC $g_{GABA\text{-}extra}$, especially spillover GABA conductance, reduces the frequency and coherence of network oscillations suggests that gamma oscillations may be subject to physiological and pathological modulation of basket cell tonic inhibition.

Basket cell inhibitory plasticity impacts network oscillations: Implications for seizure disorders.

Since our simulations showed that extrasynaptic GABA conductance modulated network oscillations, we further investigated whether seizure-induced depolarization of FS-BC GABA reversal potential together with increase in extrasynaptic GABA conductance (Yu et al., 2013) alter network oscillations. In contrast to the absence of changes in network excitability (Yu et al., 2013) , simultaneous introduction of tonic GABA currents and depolarized GABA reversal resulted in a striking enhancement of firing frequency and decrease in coherence of FS-BC network oscillations. The shift in E_{GABA} of synaptic and extrasynaptic GABA currents resulted in over 30 Hz increase in FS-BC firing (Fig. 4 and 5) and resulted in network firing in the high frequency range (> 80 Hz) observed in epileptic foci (Bragin et al., 1999; Worrell et al., 2004; Worrell et al., 2008). Moreover, systematically increasing extrasynaptic GABA conductance further enhanced network firing frequency when E_{GABA} is depolarizing indicating that post-seizure increases in FS-BC $g_{GABA\text{-}extra}$ may further enhance the firing frequency. It is possible that

the pathologically depolarized inhibitory synaptic drive resulted in a net, depolarizing synaptic input frequency, albeit subthreshold, greater than the 200 Hz dendritic synaptic input frequency. Thus, the reduction in synchrony observed in interneuronal networks activated by excitatory synaptic inputs with frequencies over 200 Hz (Kochubey et al., 2011) could contribute mechanistically to the reduction in coherence observed in our networks simulated with depolarizing E_{GABA}. Simultaneously, it is notable that physiological gamma oscillations are compromised in the presence of seizure-induced changes in FS-BC GABA currents and likely contribute to the memory deficits associated with epilepsy (Chauviere et al., 2009; Narayanan et al., 2012; Rattka et al., 2013).

Taken together, our results demonstrate that homogeneous networks of biophysically realistic fast-spiking basket cells connected by fast GABA synapses develop robust synchrony in the gamma frequency range that are subject to modulation by extrasynaptic GABA conductances and changes in GABA reversal potential. The findings suggest that physiological and pharmacological enhancement of basket cell tonic inhibition and plasticity of FS-BC GABA currents following status epilepticus can compromise gamma frequency oscillations and contribute to impairment of memory formation and recall.

References

Amitai Y, Gibson JR, Beierlein M, Patrick SL, Ho AM, Connors BW, Golomb D (2002) The spatial dimensions of electrically coupled networks of interneurons in the neocortex. JNeurosci 22:4142-4152.

Bartos M, Vida I, Jonas P (2007) Synaptic mechanisms of synchronized gamma oscillations in inhibitory interneuron networks. NatRevNeurosci 8:45-56.

Bartos M, Vida I, Frotscher M, Geiger JR, Jonas P (2001) Rapid signaling at inhibitory synapses in a dentate gyrus interneuron network. The Journal of neuroscience : the official journal of the Society for Neuroscience 21:2687-2698.

Bartos M, Vida I, Frotscher M, Meyer A, Monyer H, Geiger JR, Jonas P (2002) Fast synaptic inhibition promotes synchronized gamma oscillations in hippocampal interneuron networks. Proceedings of the National Academy of Sciences of the United States of America 99:13222-13227.

Bogaard A, Parent J, Zochowski M, Booth V (2009) Interaction of cellular and network mechanisms in spatiotemporal pattern formation in neuronal networks. J Neurosci 29:1677-1687.

Bragin A, Engel J, Jr., Wilson CL, Fried I, Mathern GW (1999) Hippocampal and entorhinal cortex high-frequency oscillations (100--500 Hz) in human epileptic brain and in kainic acid--treated rats with chronic seizures. Epilepsia 40:127-137.

Bragin A, Wilson CL, Almajano J, Mody I, Engel J, Jr. (2004) High-frequency oscillations after status epilepticus: epileptogenesis and seizure genesis. Epilepsia 45:1017-1023.

Brickley SG, Mody I (2012) Extrasynaptic GABA(A) receptors: their function in the CNS and implications for disease. Neuron 73:23-34.

Brunel N, Wang XJ (2003) What determines the frequency of fast network oscillations with irregular neural discharges? I. Synaptic dynamics and excitation-inhibition balance. J Neurophysiol 90:415-430.

Buzsaki G (2006) Rhythms of the Brain. USA: Oxford University Press.

Buzsaki G, Draguhn A (2004) Neuronal oscillations in cortical networks. Science 304:1926-1929.

Buzsaki G, Buhl DL, Harris KD, Csicsvari J, Czeh B, Morozov A (2003) Hippocampal network patterns of activity in the mouse. Neuroscience 116:201-211.

Chauviere L, Rafrafi N, Thinus-Blanc C, Bartolomei F, Esclapez M, Bernard C (2009) Early deficits in spatial memory and theta rhythm in experimental temporal lobe epilepsy. J Neurosci 29:5402-5410.

Connelly WM, Fyson SJ, Errington AC, McCafferty CP, Cope DW, Di Giovanni G, Crunelli V (2013) GABAB Receptors Regulate Extrasynaptic GABAA Receptors. J Neurosci 33:3780-3785.

Csicsvari J, Jamieson B, Wise KD, Buzsaki G (2003) Mechanisms of gamma oscillations in the hippocampus of the behaving rat. Neuron 37:311-322.

Dyhrfjeld-Johnsen J, Santhakumar V, Morgan RJ, Huerta R, Tsimring L, Soltesz I (2007) Topological determinants of epileptogenesis in large-scale structural and functional models of the dentate gyrus derived from experimental data. JNeurophysiol 97:1566-1587.

Engel J, Jr., Bragin A, Staba R, Mody I (2009) High-frequency oscillations: what is normal and what is not? Epilepsia 50:598-604.

Farrant M, Nusser Z (2005) Variations on an inhibitory theme: phasic and tonic activation of GABA(A) receptors. Nat Rev Neurosci 6:215-229.

Fisahn A, Pike FG, Buhl EH, Paulsen O (1998) Cholinergic induction of network oscillations at 40 Hz in the hippocampus in vitro. Nature 394:186-189.

Fukuda T, Kosaka T (2000) Gap junctions linking the dendritic network of GABAergic interneurons in the hippocampus. J Neurosci 20:1519-1528.

Galarreta M, Hestrin S (2002) Electrical and chemical synapses among parvalbumin fast-spiking GABAergic interneurons in adult mouse neocortex. ProcNatlAcadSciUSA 99:12438-12443.

Glykys J, Mody I (2007) The main source of ambient GABA responsible for tonic inhibition in the mouse hippocampus. JPhysiol 582:1163-1178.

Glykys J, Peng Z, Chandra D, Homanics GE, Houser CR, Mody I (2007) A new naturally occurring GABA(A) receptor subunit partnership with high sensitivity to ethanol. NatNeurosci 10:40-48.

Gupta A, Elgammal FS, Proddutur A, Shah S, Santhakumar V (2012) Decrease in Tonic Inhibition Contributes to Increase in Dentate Semilunar Granule Cell. Journal of Neuroscience 32:2523-2537.

Hefft S, Jonas P (2005) Asynchronous GABA release generates long-lasting inhibition at a hippocampal interneuron-principal neuron synapse. NatNeurosci 8:1319-1328.

Hines ML, Carnevale NT (1997) The NEURON simulation environment. Neural Comput 9:1179-1209.

Kochubey S, Semyanov A, Savtchenko L (2011) Network with shunting synapses as a non-linear frequency modulator. Neural Netw 24:407-416.

Krook-Magnuson EI, Li P, Paluszkiewicz SM, Huntsman MM (2008) Tonically active inhibition selectively controls feedforward circuits in mouse barrel cortex. Journal of Neurophysiology 100:932-944.

Lisman JE, Idiart MA (1995) Storage of 7 +/- 2 short-term memories in oscillatory subcycles. Science 267:1512-1515.

Mann EO, Mody I (2010) Control of hippocampal gamma oscillation frequency by tonic inhibition and excitation of interneurons. Nature neuroscience 13:205-212.

Mann EO, Suckling JM, Hajos N, Greenfield SA, Paulsen O (2005) Perisomatic feedback inhibition underlies cholinergically induced fast network oscillations in the rat hippocampus in vitro. Neuron 45:105-117.

Mitchell SJ, Silver RA (2003) Shunting inhibition modulates neuronal gain during synaptic excitation. Neuron 38:433-445.

Mody I, Glykys J, Wei W (2007) A new meaning for "Gin & Tonic": tonic inhibition as the target for ethanol action in the brain. Alcohol 41:145-153.

Montgomery SM, Buzsaki G (2007) Gamma oscillations dynamically couple hippocampal CA3 and CA1 regions during memory task performance. Proc Natl Acad Sci U S A 104:14495-14500.

Morgan RJ, Soltesz I (2008) Nonrandom connectivity of the epileptic dentate gyrus predicts a major role for neuronal hubs in seizures. ProcNatlAcadSciUSA 105:6179-6184.

Mtchedlishvili Z, Kapur J (2006) High-affinity, slowly desensitizing GABAA receptors mediate tonic inhibition in hippocampal dentate granule cells. MolPharmacol 69:564-575.

Narayanan J, Duncan R, Greene J, Leach JP, Razvi S, McLean J, Evans JJ (2012) Accelerated long-term forgetting in temporal lobe epilepsy: verbal, nonverbal and autobiographical memory. Epilepsy Behav 25:622-630.

Netoff TI, Clewley R, Arno S, Keck T, White JA (2004) Epilepsy in small-world networks. JNeurosci 24:8075-8083.

Olah S, Fule M, Komlosi G, Varga C, Baldi R, Barzo P, Tamas G (2009) Regulation of cortical microcircuits by unitary GABA-mediated volume transmission. Nature 461:1278-1281.

Percha B, Dzakpasu R, Zochowski M, Parent J (2005) Transition from local to global phase synchrony in small world neural network and its possible implications for epilepsy. Phys Rev E Stat Nonlin Soft Matter Phys 72:031909.

Pike FG, Goddard RS, Suckling JM, Ganter P, Kasthuri N, Paulsen O (2000) Distinct frequency preferences of different types of rat hippocampal neurones in response to oscillatory input currents. J Physiol 529 Pt 1:205-213.

Rattka M, Brandt C, Loscher W (2013) The intrahippocampal kainate model of temporal lobe epilepsy revisited: epileptogenesis, behavioral and cognitive alterations, pharmacological response, and hippoccampal damage in epileptic rats. Epilepsy Res 103:135-152.

Rossi DJ, Hamann M, Attwell D (2003) Multiple modes of GABAergic inhibition of rat cerebellar granule cells. J Physiol 548:97-110.

Santhakumar V (2008) Modeling mossy cell loss and mossy fiber sprouting in epilepsy. In: Computational Neuroscience in Epilepsy (Soltesz I, Staley KJ, eds), pp 89-111: Academic Press.

Santhakumar V, Aradi I, Soltesz I (2005) Role of mossy fiber sprouting and mossy cell loss in hyperexcitability: a network model of the dentate gyrus incorporating cell types and axonal topography. JNeurophysiol 93:437-453.

Santhakumar V, Hanchar HJ, Wallner M, Olsen RW, Otis TS (2006) Contributions of the GABAA receptor alpha6 subunit to phasic and tonic inhibition revealed by a naturally occurring polymorphism in the alpha6 gene. JNeurosci 26:3357-3364.

Saraga F, Ng L, Skinner FK (2006) Distal gap junctions and active dendrites can tune network dynamics. JNeurophysiol 95:1669-1682.

Semyanov A, Walker MC, Kullmann DM (2003) GABA uptake regulates cortical excitability via cell type-specific tonic inhibition. Nat Neurosci 6:484-490.

Sik A, Penttonen M, Buzsaki G (1997) Interneurons in the hippocampal dentate gyrus: an in vivo intracellular study. European Journal of Neuroscience 9:573-588.

Skinner FK (2012) Cellular-based modeling of oscillatory dynamics in brain networks. Curr Opin Neurobiol 22:660-669.

Song I, Savtchenko L, Semyanov A (2011) Tonic excitation or inhibition is set by GABA(A) conductance in hippocampal interneurons. Nat Commun 2:376.

Srinivas M, Rozental R, Kojima T, Dermietzel R, Mehler M, Condorelli DF, Kessler JA, Spray DC (1999) Functional properties of channels formed by the neuronal gap junction protein connexin36. J Neurosci 19:9848-9855.

Stacey WC, Lazarewicz MT, Litt B (2009) Synaptic noise and physiological coupling generate high-frequency oscillations in a hippocampal computational model. J Neurophysiol 102:2342-2357.

Stell BM, Brickley SG, Tang CY, Farrant M, Mody I (2003) Neuroactive steroids reduce neuronal excitability by selectively enhancing tonic inhibition mediated by delta subunit-containing GABAA receptors. Proc Natl Acad Sci U S A 100:14439-14444.

Steriade M, Contreras D, Amzica F, Timofeev I (1996) Synchronization of fast (30-40 Hz) spontaneous oscillations in intrathalamic and thalamocortical networks. J Neurosci 16:2788-2808.

Tao W, Higgs MH, Spain WJ, Ransom CB (2013) Postsynaptic GABAB Receptors Enhance Extrasynaptic GABAA Receptor Function in Dentate Gyrus Granule Cells. J Neurosci 33:3738-3743.

Towers SK, Gloveli T, Traub RD, Driver JE, Engel D, Fradley R, Rosahl TW, Maubach K, Buhl EH, Whittington MA (2004) Alpha 5 subunit-containing GABAA receptors affect the dynamic range of mouse hippocampal kainate-induced gamma frequency oscillations in vitro. J Physiol 559:721-728.

Traub RD, Spruston N, Soltesz I, Konnerth A, Whittington MA, Jefferys GR (1998) Gamma-frequency oscillations: a neuronal population phenomenon, regulated by synaptic and intrinsic cellular processes, and inducing synaptic plasticity. ProgNeurobiol 55:563-575.

Vida I, Bartos M, Jonas P (2006) Shunting inhibition improves robustness of gamma oscillations in hippocampal interneuron networks by homogenizing firing rates. Neuron 49:107-117.

Wang XJ, Buzsaki G (1996) Gamma oscillation by synaptic inhibition in a hippocampal interneuronal network model. J Neurosci 16:6402-6413.

Wei W, Zhang N, Peng Z, Houser CR, Mody I (2003) Perisynaptic localization of delta subunit-containing GABA(A) receptors and their activation by GABA spillover in the mouse dentate gyrus. JNeurosci 23:10650-10661.

White JA, Chow CC, Ritt J, Soto-Trevino C, Kopell N (1998) Synchronization and oscillatory dynamics in heterogeneous, mutually inhibited neurons. J Comput Neurosci 5:5-16.

Whittington MA, Traub RD, Jefferys JG (1995) Synchronized oscillations in interneuron networks driven by metabotropic glutamate receptor activation. Nature 373:612-615.

Whittington MA, Traub RD, Kopell N, Ermentrout B, Buhl EH (2000) Inhibition-based rhythms: experimental and mathematical observations on network dynamics. International journal of psychophysiology : official journal of the International Organization of Psychophysiology 38:315-336.

Worrell GA, Parish L, Cranstoun SD, Jonas R, Baltuch G, Litt B (2004) High-frequency oscillations and seizure generation in neocortical epilepsy. Brain 127:1496-1506.

Worrell GA, Gardner AB, Stead SM, Hu S, Goerss S, Cascino GJ, Meyer FB, Marsh R, Litt B (2008) High-frequency oscillations in human temporal lobe: simultaneous microwire and clinical macroelectrode recordings. Brain 131:928-937.

Yu J, Proddutur A, Elgammal FS, Ito T, Santhakumar V (2013) Status epilepticus enhances tonic GABA currents and depolarizes GABA reversal potential in dentate fast-spiking basket cells. J Neurophysiol.

Zhang W, Buckmaster PS (2009) Dysfunction of the dentate basket cell circuit in a rat model of temporal lobe epilepsy. JNeurosci 29:7846-7856.

Figure legends

Figure 1: Structure and intrinsic properties of model fast-spiking basket cell. A. Projection of confocal image stacks of a fast-spiking basket cell (FS-BC) filled during recordings (red) and labeled for parvalbumin (PV in green) shows the typical morphology with and axon in granule cell layer (arrows). *Insets:* Confocal image of biocytin-filled (biocytin) soma (top in red) and labeling for PV (mid in green). Merged image showing PV and biocytin co-labeling in the soma (bottom). Scale bar, 50 μm. B. Schematic representation of the structure of the model FS-BC. C, D. Membrane voltage traces from the biological (C) and model FS-BC (D) illustrates the fast-spiking, non-adapting firing pattern during a +500 pA current injection and relatively low membrane hyperpolarization in response to a -50 pA current injection. E. Overlay of the firing rates of biological and model FS-BCs in response to increasing current injection. F. Plot compares the input resistance of biological and model FS-BCs.

Figure 2: Effect of gap junctions and extrasynaptic GABA conductance on model FS-BC input resistance of cell. A) Plot shows the input resistance of a model FS-BC in the presence of progressively increasing the gap junctional conductance between a FS-BC pair. Input resistance at the gap junctional conductance used in network simulations is indicated by the arrow. Dotted line represents FS-BC input resistance in the absence of gap junctions. B) Plot shows the % change in model FS-BC membrane conductance when the baseline extrasynaptic GABA conductance was increased in the physiologically relevant range. FS-BC pairs were simulated with and without 500 pS gap junction al conductance.

Figure 3: Impact of FS-BC synaptic interconnectivity on frequency and coherence of network firing. A-B) Effect of progressively increase in FS-BC interconnectivity on average firing frequency (A) and coherence (B) of activity in networks activated by heterogeneous

somatic current injections (Somatic I inj in red) and perforant path synaptic inputs (PP Inputs in blue). Legend in A applies to A and B. C-D. Data from networks activated by heterogeneous somatic current injections show the effect of including distance dependent axonal conduction delay and gap junctions (GJ) on the frequency (C) and coherence (D) of FS-BC network activity. Legend in C applies to C and D. Data are presented as mean±s.e.m of 3 independent runs.

Figure 4: Effect of extrasynaptic GABA conductance and GABA reversal on firing in FS-BC networks activated by heterogeneous somatic current injections. A-B. Spike rasters illustrate activity in FS-BC networks with 30 synaptic interconnections in which the GABA reversal potential was -74 mV. Networks were activated by a mean somatic current injection of 500 pA, the start time of which was randomly varied between -20 and 50 ms in each cell. Spike ratsters in networks simulated with an extrasynaptic GABA conductance of 2 $\mu S/cm^2$ (A) and 10 $\mu S/cm^2$ (B) are illustrated. C-D. Representative spike rasters show activity in FS-BC networks with 30 synaptic interconnections and GABA reversal potential set to -54 mV. Spike ratsters in networks simulated with an extrasynaptic GABA conductance of 2 $\mu S/cm^2$ (C) and 10 $\mu S/cm^2$ (D) are illustrated. E-F. Overlay of membrane potential traces from 10 randomly selected FS-BCs in networks with 30 synaptic connections, no gap junctions and no extrasynaptic GABA conductances show the firing in networks simulated with a GABA reversal potential of -74 mV and -54 mV (F). G-H. Data from networks activated by heterogeneous somatic current injections show the effect of FS-BC tonic GABA conductance on frequency (G) and coherence (H) of network activity. Legend in G applies to G and H. Summary data are presented as mean±s.e.m of 3 independent runs.

Figure 5: Extrasynaptic GABA conductance modulates firing and coherence in networks activated by excitatory synaptic inputs. A-D. Spike rasters of activity in FS-BC networks with

30 synaptic interconnections activated by perforant path synaptic inputs. Spike ratsters in networks simulated with a GABA reversal of -74 mV and extrasynaptic GABA conductance of 2 $\mu S/cm^2$ (A) and 10 $\mu S/cm^2$ (B) and GABA reversal of -54 mV and extrasynaptic GABA conductance of 2 $\mu S/cm^2$ (C) and 10 $\mu S/cm^2$ (D). E-F. Data from networks activated by synaptic inputs show the effect of FS-BC tonic GABA conductance on frequency (E) and coherence (F) of network activity. Legend applies to E and F. Summary data are presented as mean±s.e.m of 3 independent runs.

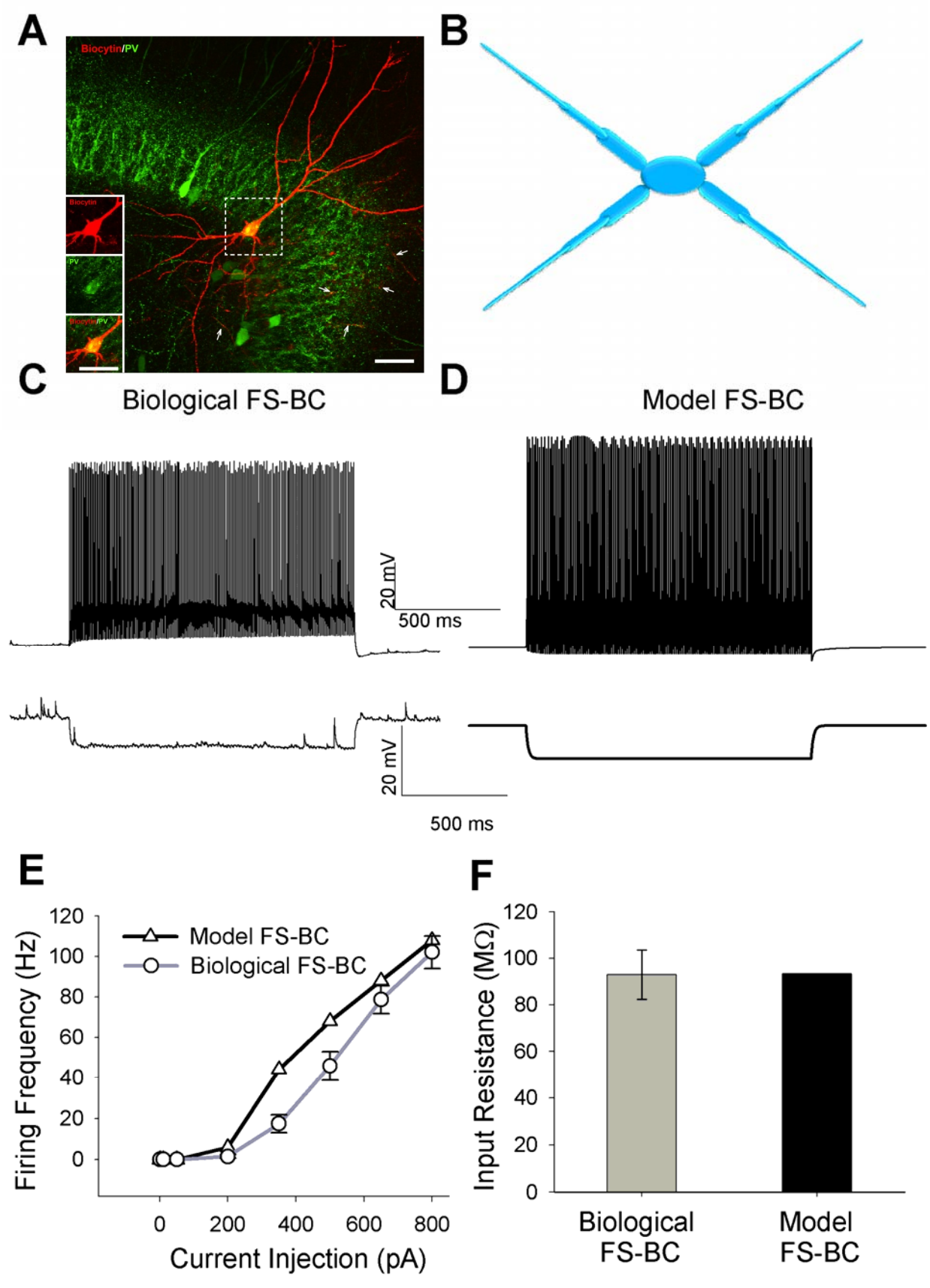

Proddutur et al. Figure 1

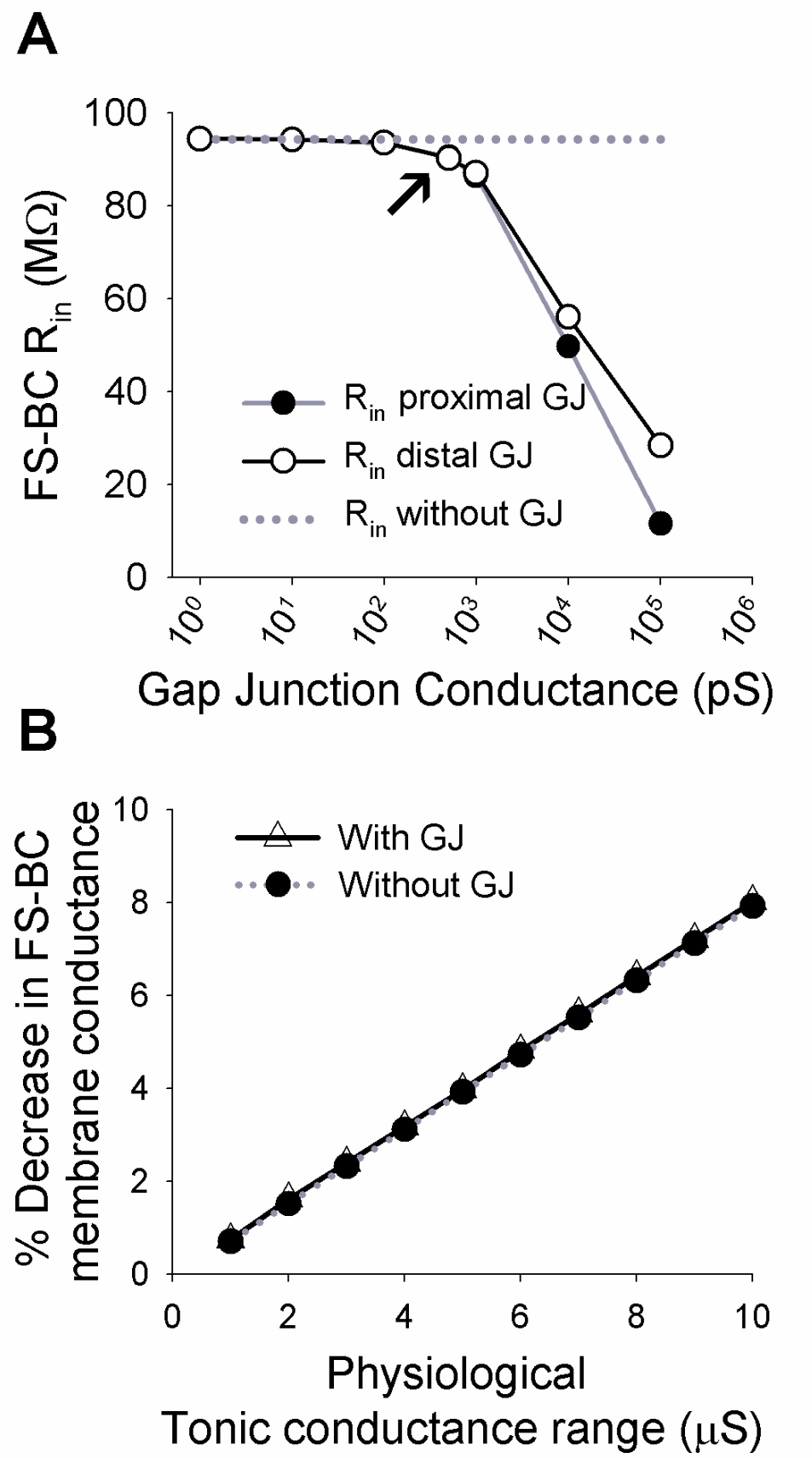

Proddutur et al. Figure 2

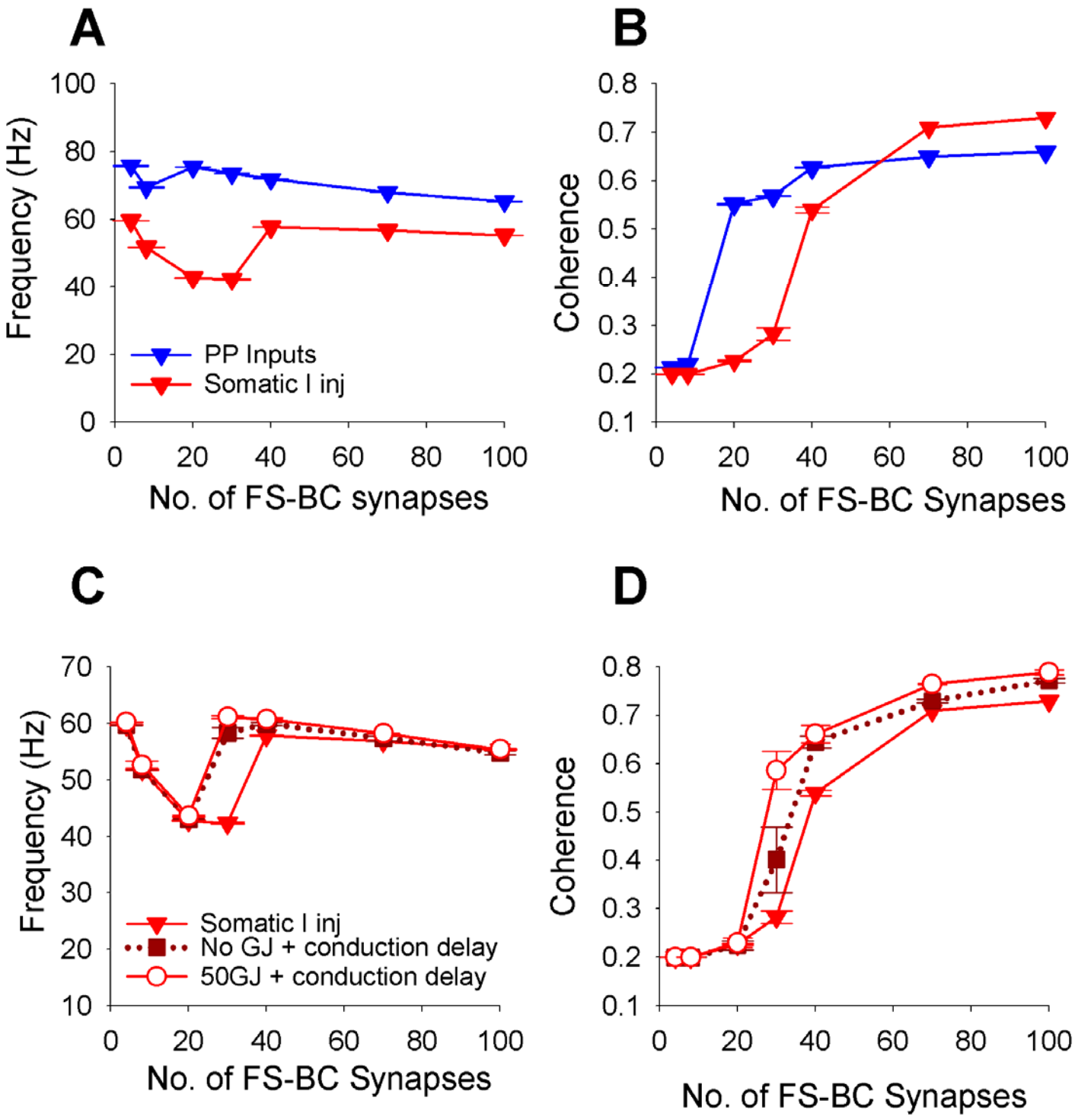

Proddutur et al. Figure 3

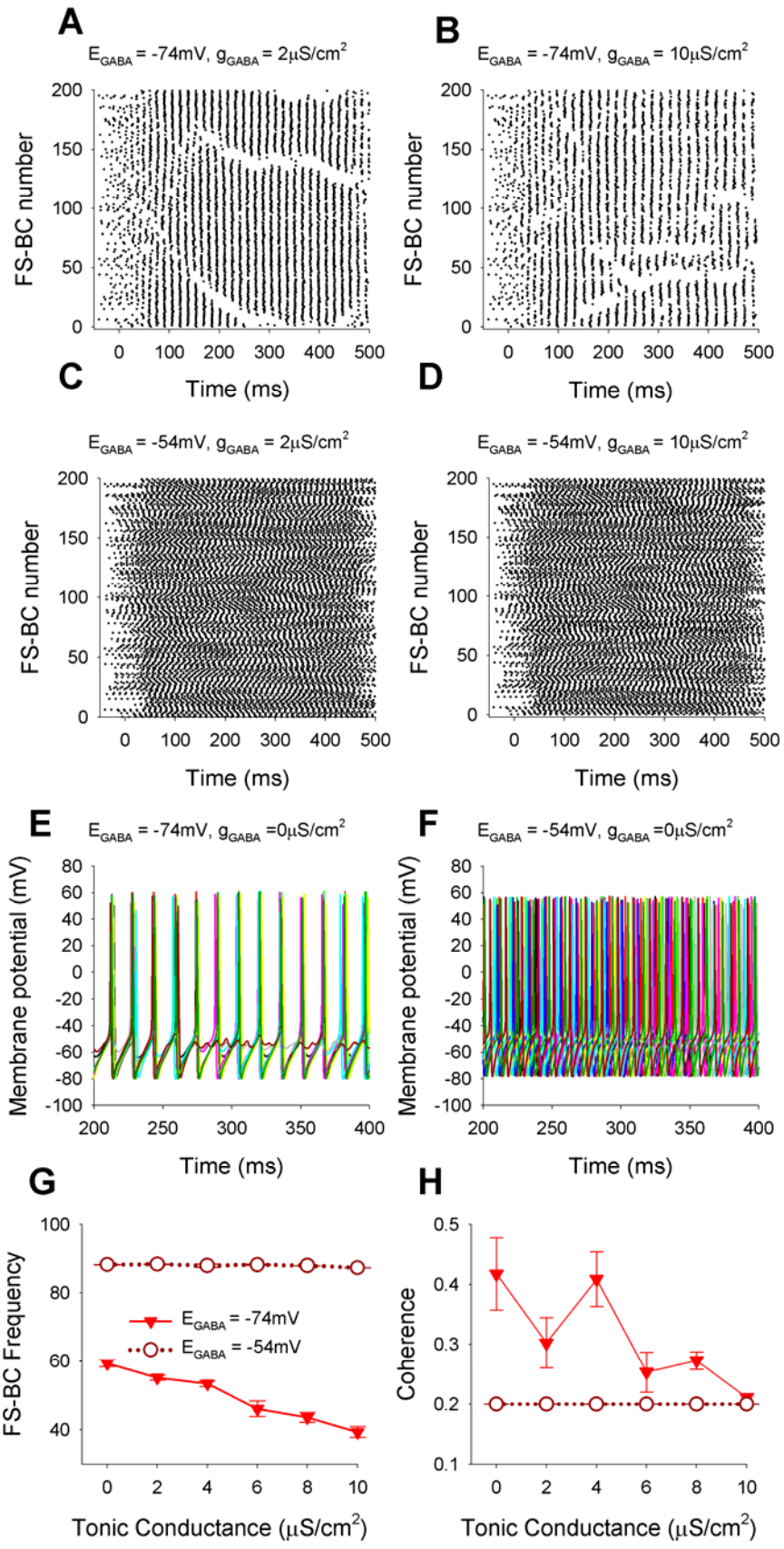

Proddutur et al. Figure 4

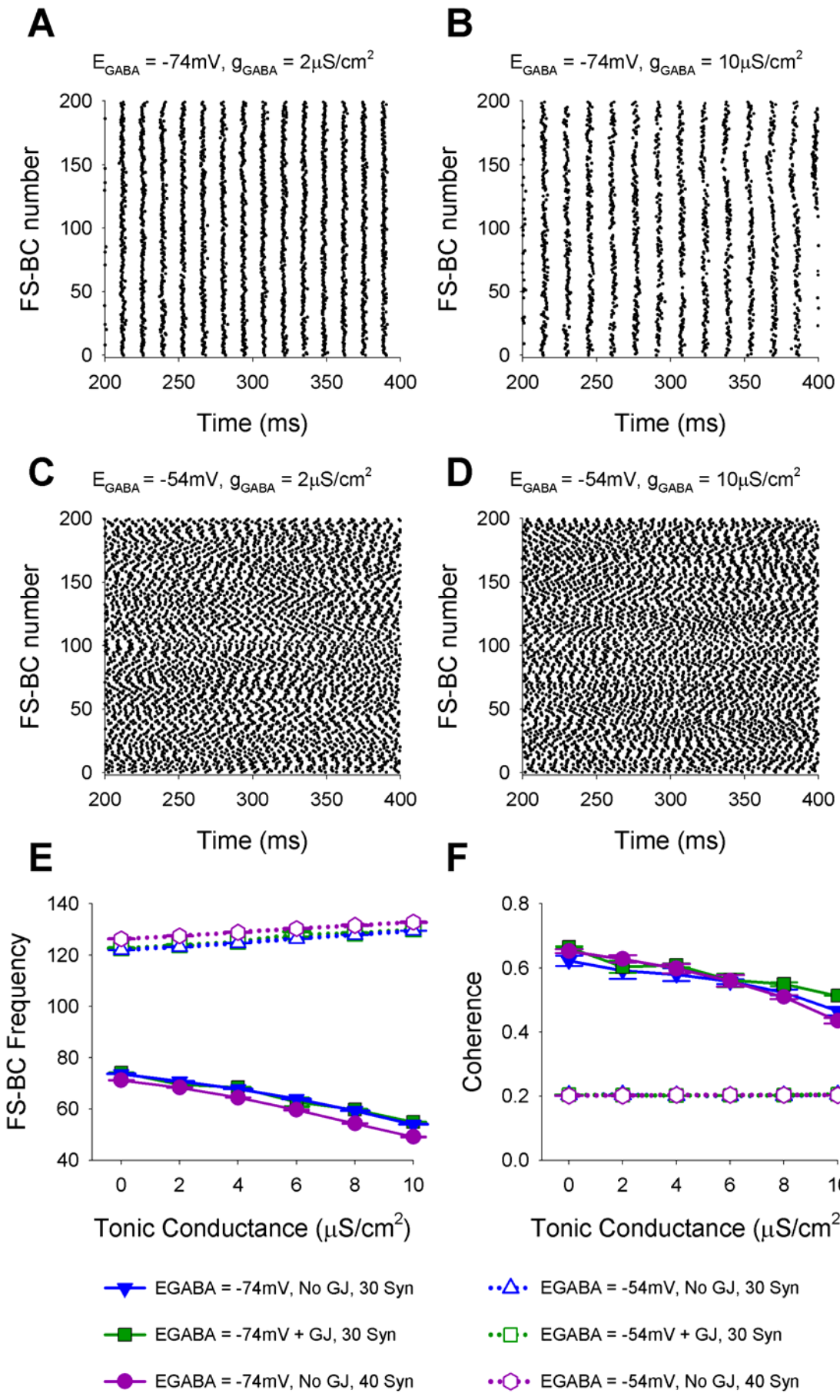

Proddutur et al. Figure 5

Distinct effect of impact rate on immediate and early neuropathology after brain injury

Eric J Neuberger BS[1*], Radia Abdul Wahab MS[3*], Archana Jayakumar MBS[1], Bryan J Pfister PhD[3], Vijayalakshmi Santhakumar MBBS, PhD[1,2]

[1]Department of Neurology and Neurosciences, [2]Department of Pharmacology and Physiology, Rutgers New Jersey Medical School, Newark, New Jersey 07103, [3]Department of Biomedical Engineering, New Jersey Institute of Technology, Newark, New Jersey 07102

*Authors Contributed Equally

Running title: Impact rate dependent neuropathology after TBI

Word Count for abstract**:** 249 Body of the manuscript: 3203 Figures: 5

Color Figures: 2 Tables: 0 References: 48 Pages: 25

Character count: Title: 75 Running title: 41

Correspondence:

Vijayalakshmi Santhakumar, PhD

Department of Neurology and Neuroscience,

Rutgers New Jersey Medical School

MSB-H-512, 185 S. Orange Ave. Newark, NJ 07103

E-mail: santhavi@njms.rutgers.edu

Abstract (248/250)

Traumatic brain injury (TBI) can occur from physical trauma from a wide spectrum of insults ranging from explosions in combat to falls in elderly. The kinematics of the trauma can vary in key features including the rate and magnitude of the insult. While the effect of peak injury pressure on neurological outcome has been examined in the fluid percussion injury (FPI) model, whether differences in the rate of rise of the injury waveform lead to distinct cellular and physiological changes in the injured brain is unknown. To determine the effect of injury rate on neurological outcome, we examined rats subject to FPI at fast- and standard-rates of rise to a constant peak pressure using a programmable FPI device. Immediate post-injury assessment identified fewer seizures and relatively brief loss of consciousness after fast-rate injuries than following standard-rate injuries at similar peak pressures. Compared to rats injured at standard-rates, fewer silver-stained injured neuronal profiles and degenerating neurons were observed in the dentate hilus of rats sustaining fast-rate FPI. One week post-injury, both fast- and standard-rate FPI resulted in hilar cell loss and enhanced perforant path-evoked granule cell field excitability compared to sham-controls. Notably, the extent of neuronal loss and increase in dentate excitability were not different between rats injured at fast- and standard rates. Our data indicate that reduced cellular damage and improved immediate neurological outcome after fast-rate primary concussive injuries obscure the severity of the subsequent cellular and neurophysiological pathology and may be unreliable as a predictor of prognosis.

Introduction

Traumatic brain injury (TBI) is a rapidly growing silent epidemic,[1, 2] leading to short and long-term neurological dysfunction including impaired learning, memory and reasoning, psychological disorders such as depression and anxiety,[3, 4] and increased risk for diseases such as epilepsy, Alzheimer's and Parkinson's disease.[5, 6] Brain injury is characterized by a cascade of cellular and circuit changes,[7-11] which culminate into lasting neurological sequelae.[12-14] Evidence from TBI models suggest that early post-traumatic anatomical and physiological changes contribute to in progressive neurological dysfunction.[8, 15, 16] The mechanical impact resulting in brain injury can differ in several physical attributes including the maximum pressure, rate of rise to maximum pressure and duration of the pressure wave. The proximate cause of TBI can range from relatively slow events like falls, which can be caused by low velocity impacts in the order of a few meters/sec,[17, 18] to the high velocity brief pressure increases in blasts.[19-22] Because brain tissue is viscoelastic,[23-25] tissue response has been shown to be sensitive to both the rate and magnitude of trauma.[25, 26] To date, studies on concussive brain injury using the FPI model have primarily focused on how the peak magnitude of the pressure waveform influences neuropathology.[27-29] However, little is known about how injury rate influences the early and long-term histological and physiological changes after brain injury.

Early neurological assessment paradigms, commonly used as indicators of prognosis in brain injured patients, use similar parameters to assess the severity regardless of the injury rate.[30, 31] While majority of practicing physicians believe that an accurate early neurological assessment is important for medical management of TBI patients, fewer are confident that these measures reliably predict prognosis.[32, 33] Curiously, whether differences in early and later cellular neuropathology following injuries at dissimilar rates contribute to inconsistencies between early

neurological assessment and subsequent prognosis has not been considered. A recently developed voice-coil-driven FPI (VC-FPI) device,[34] which allows for independent control of the magnitude and rate of the concussive waveform, enabled us to experimentally examine the effect of injury rate on the brain. Here we address the critical issue of how differences in impact rates affect measures of immediate neurological assessment and early cellular injury following concussive brain trauma at the same peak impact pressures. We further examine if the early cellular and neurological measures are reliable indicators of subsequent cellular and physiological pathology after primary concussive brain injury at different rates.

Material & Methods

Fluid percussion injury.

All procedures were performed under protocols approved by the Institutional Animal Care and Use Committee of the University of Medicine and Dentistry of New Jersey, Newark, New Jersey. Lateral fluid percussion injury (FPI) was performed using a uniquely programmable FPI device[34] that permits independent control of key variables defining the waveform (Fig. 1A). This prototype device utilizes a voice-coil actuator to generate a precise temporal forcing function under closed loop control with a proportional–integral–derivative motion controller and a linear encoder with a 1 μm resolution. The voice coil is coupled to a syringe filled with water that delivers the defined fluid percussion waveform. The device was programmed to deliver FPI waveforms at constant peak pressure (1.8-2.1 atm) and two distinct rates of pressure rise: (1) fast rate with a 3-5 ms rise to peak, and (2) standard rate with a 10-15 ms rise to peak, similar to the rise-rate observed in the pendulum-style FPI device (Fig. 1B). This peak pressure has been shown to result in moderate FPI at the standard rate using the pendulum-style FPI device.[7, 11, 35, 36] Young adult (postnatal days 24–26) male, Wistar rats (Charles River) underwent FPI or sham-injury as described previously.[7, 11, 28, 35-37] Briefly, under anesthesia, stereotaxic craniotomy was performed to expose the dura on the left parietal bone (-3mm from bregma and 3.5 mm lateral to sagittal suture) and anchor a Luer-Lok syringe hub to the skull.[7, 36] One day later, animals were attached to the VC-FPI device under isoflurane anesthesia and randomly selected rats underwent either fast-rate or standard-rate FPI at 1.8-2.1 atm. Sham-injured control animals underwent the craniotomy and were attached to the FPI device under anesthesia without delivery of the pressure wave.[36, 37] Immediately following injury, rats were monitored for occurrence of seizures, duration of apnea (time to first breath following injury), time to recovery

of response to toe pinch, recovery of righting reflex and mortality. Seizures were defined as the presence of Racine Stage 3 or higher seizures including forelimb or hind limb clonus or generalized tonic clonic seizures.

Histology and immunohistochemistry.

Gallyas silver stain[35, 38, 39] and Fluoro-Jade C staining were performed on 40 μm sections from animals perfused with 4% paraformaldehyde within 4 hours after injury. Only sections ipsilateral to the side of injury were examined. Sections processed for Gallyas stain were dehydrated in 50%, 75%, and 100% 1-propanol for 5 min each, incubated at 56°C in 0.8% sulfuric acid in 1-propanol for 16 hours and treated with 1% acetic acid for 5 min. Sections were then rehydrated and treated with 3% acetic acid and developed in a silicotungstate solution.[38, 39] Following development, sections were treated with 1% acetic acid for 30 min, dehydrated and mounted on slides. For Fluoro-Jade C staining, sections mounted on gelatinized slides were air dried, hydrated and incubated in 0.06% potassium permanganate before being stained with 0.001% Fluoro-Jade C in 0.1% acetic acid in the dark for 30 min.

For NeuN staining, rats were perfused 1 week after sham or head injury. Sections (50μm) were immunostained with anti-NeuN antibody (MAB377, 1:1000, mouse monoclonal, Millipore) and reacted with an appropriate secondary antibody to reveal staining.[40] Controls in which primary antibody was omitted were routinely included. Quantification was performed using randomized systematic sampling protocols selecting every tenth slice along the septo-temporal axis of the hippocampus on the injured side.[40] Cell counts were performed using the Optical Fractionator probe of Stereo Investigator V.10.02 (MBF Bioscience) using an Olympus BX51 microscope and a 100X oil objective. In each section, the hilus was outlined by a contour traced using a 10X

objective. Sampling parameters were set at 100X: counting frame, 50 X 50 μm; dissector height, 25 μm; and top guard zone, 4 μm. Approximately 30 sites per contour were sampled using randomized systematic sampling protocols. In each section, the number of labeled cells was estimated based on planimetric volume calculations in Stereo Investigator.[40-42] Data are plotted as number of stained neurons per section.

***In vitro* electrophysiology.**

One week (7–10 days) after FPI or sham injury,[8, 36] rats were decapitated under isoflurane anesthesia. Horizontal brain slices (400 μm) were prepared in ice-cold sucrose artificial CSF (sucrose-aCSF) containing the following (in mM): 85 NaCl, 75 sucrose, 24 $NaHCO_3$, 25 glucose, 4 $MgCl_2$, 2.5 KCl, 1.25 NaH_2PO_4, and 0.5 $CaCl_2$ using a Leica VT1200S Vibratome. Slices ipsilateral to the side of injury were incubated at 32 ± 1°C for 30 min in a submerged holding chamber and subsequently held at room temperature.[36] The recording aCSF contained the following (in mM): 126 NaCl, 2.5 KCl, 2 $CaCl_2$, 2 $MgCl_2$, 1.25 NaH_2PO_4, 26 $NaHCO_3$, and 10 D-glucose. All solutions were saturated with 95% O_2 and 5% CO_2 and maintained at a pH of 7.4 for 1–6 h. Field recordings were performed in an interface recording chamber (BSC2, Automate Scientific) perfused with aCSF at 34°C. Recordings in the granule cell layer of the dentate gyrus were obtained using patch pipettes filled with recording aCSF. Responses were evoked by constant current stimuli (0.5–6 mA, 50 μs) delivered at 0.1 Hz through a bipolar 90 μm tungsten stimulating electrode placed in the perforant path at the junction of the dorsal blade and the crest as previously described.[7, 8, 36] Recordings were obtained using an AxoPatch200B amplifier and digitized at 10 kHz with a DigiData 1440A (Molecular Devices) and population spike amplitude and numbers were measured as described previously.[7, 35]

Analysis and statistics.

Statistical analysis of behavioral data was performed using Mann-Whitney *U* test as appropriate. The Bonferroni method was use to correct for multiple comparisons. Categorical data was analyzed using chi-square test. One-way ANOVA on ranks (Kruskal-Wallis test) followed by pairwise multiple comparison by Dunn's Method was used to test for statistical differences in histological outcome between experimental groups. Two-way repeated-measure ANOVA was used to compare field recording data between experimental groups. Statistical analysis was performed on SigmaPlot 12.3. Significance was set to $p < 0.05$. Data are shown as mean ± SEM and median and interquartile range (IQR) where appropriate.

Results

Differential immediate behavioral response to fast and standard-rate FPI.

Previous studies using pendulum FPI devices have shown distinctive immediate behavioral changes such as seizures and transient apnea following moderate concussive brain injury.[28, 35] First, we examined the immediate neurobehavioral responses after fast- and standard-rate FPI at similar peak pressures. While sham-controls showed no apnea (data not shown), rats injured using both fast and standard waveform demonstrated apnea. The difference in duration of post-traumatic apnea following fast- and standard-rate FPI did not reach statistical significance (Fig. 2A, apnea in sec, fast-FPI: 19.1±2.4, median = 16.0, IQR = 12.0-24.3, n = 16; standard-FPI: 24.9±4.0, median = 17.0, IQR = 12.8-36.0, n = 16, $p>0.05$ by Mann-Whitney U test). Although the duration of apnea was not different, few rats exposed to fast-rate FPI demonstrated post injury seizures (0 of 16 rats subject to fast-rate FPI) while a majority of the rats exposed to standard rate FPI developed stage 3 or higher seizures (13 of 18 rats subject to fast-rate FPI). The difference in the percent of rats that developed seizures following fast- and standard rate injuries was statistically significant (percent of rats that developed seizures, sham: 0, n = 7; fast-FPI: 0, n = 16; standard-FPI: 72.2, n = 18, $p<0.05$ for sham versus standard, $p<0.05$ for fast versus standard and $p>0.05$ for sham versus fast by Chi-Square test). Injury using a standard rate of rise to peak pressure resulted in 22.2% mortality in the rats (4 of 18 rats: 2 rats died from post-injury apnea and 2 rats died following continuous post-traumatic seizures). However, none of the rats exposed to fast-rate FPI at identical peak pressures died following injury indicating a significantly lower mortality following fast-rate injury (percent mortality within 1 hour after FPI, sham: 0, n = 7; fast-FPI: 0, n = 16; standard-FPI: 22.2, n = 18, $p<0.05$ for sham versus standard, $p<0.05$ for fast versus standard and $p>0.05$ for sham versus fast by Chi-Square test; data from

animals used for immediate histological assessment). Similar results were obtained in animals used for histological and physiological studies one week after FPI (percent mortality within 1 hour after FPI, sham: 0, n = 14; fast-FPI: 0, n = 16; standard-FPI: 22.7, n = 22, $p<0.05$ for sham versus standard, $p<0.05$ for fast versus standard and $p>0.05$ for sham versus fast by Chi-Square test). Moreover, although rats injured using either waveform showed increase in latency of response to toe-pinch and recovery of righting reflex compared to controls, rats subject to fast-rate FPI exhibited a significantly faster recovery of response to toe-pinch than rats that underwent standard-rate FPI (Fig. 2B, latency to recovery of toe-pinch in sec in rats examined at the 1 week time point, sham: 4.6±0.4, median = 4.0, IQR = 4.0-5.5, n = 5; fast-FPI: 17.0±1.1, median = 16.0, IQR = 15.0-19.5, n = 5; standard-FPI: 70.4±12.7, median = 73.0, IQR = 41.5-98.0, n = 5, $p<0.05$ for all pairwise comparisons by Mann-Whitney U test corrected for multiple comparisons using Bonferroni method). Similarly, rats that sustained fast-rate FPI exhibited earlier return of righting reflex compared to rats injured at standard-rate FPI (Fig. 2C, return of righting reflex in sec in rats examined at the 1 week time point, sham: 26.0±1.7, median = 25.0, IQR = 22.5-30.0, n = 5; fast-FPI: 115.80±33.5, median = 89.0, IQR = 63.0-182.0, n = 5; standard-FPI: 332.4±41.9, median = 287.0, IQR = 262.0-425.5, n = 5, $p<0.05$ for all pairwise comparisons by Mann-Whitney U test corrected for multiple comparisons using Bonferroni method). Together the immediate neurobehavioral data suggest that even when peak injury pressures are similar, the fast-rate injuries result in less severe early neurological deficits compared to standard-rate injuries.

Injury rate modifies the extent of early hilar neuronal injury.

Next, we examined whether the injury rate-specific difference in immediate neurobehavioral outcome was associated with differences in cellular responses to injury at fast and standard rates.

Previous studies have shown that moderate injuries at standard-rate, using the pendulum-style FPI device, lead to instantaneous mechanical injury[35] and early degeneration[36] of neurons in the hilus of the dentate gyrus. Similar to earlier studies,[35] sections from sham-control rats treated with the Gallyas silver stain[35, 38] revealed negligible hilar staining, in contrast to the dense staining of hilar neuronal somata and dendrites following standard-rate injury (Fig.3A,C). Importantly, the somatic silver staining following fast-rate FPI was relatively sparse, indicating reduced mechanical damage to dentate neurons than after standard-rate FPI at similar peak pressures (Fig.3A-C, *n* = 3-4 sections from 3 rats each). To confirm our findings and quantify whether the differences in neuronal injury translated to dissimilar early degeneration of neurons following FPI at different rates, a second investigator subjected an additional group of rats to injuries at fast and standard rates for examination of early post-injury neuronal degeneration. Fluoro-Jade C staining performed 4 hours FPI revealed few labeled neurons in sham-controls and several degenerating hilar neurons in rats exposed to both fast- and standard-rate FPI (Fig.3D-F). Notably, stereological quantification revealed significantly fewer Fluoro-Jade-immunoreactive dentate hilar neurons in rats subject to fast-rate FPI compared to rats injured at standard-rates (Fig. 3G, estimated number of degenerating hilar neurons per section, sham: 1.13±0.40, median = 1.00, IQR = 0.0-2.0, *n* = 8 sections from 2 rats; fast-FPI: 12.31±2.29, median = 9.5, IQR = 4-21, *n* = 16 sections from 3 rats; standard FPI: 75.58±9.2, median = 65.0, IQR = 38.0-91.0, *n* = 19 sections from 3 rats, $p<0.05$, $H = 33.575$, $df = 2$ by Kruskal-Wallis One Way ANOVA on Ranks). Pairwise multiple comparison by Dunn's Method showed a statistically significant difference in degenerating neurons between sham and standard-rate FPI and between standard- and fast-rate FPI. However, the difference in the number of degenerating neuron per section between sham and fast-rate FPI failed to reach statistical significance.

Collectively, the immediate post-injury behavioral assessment and early cellular damage demonstrate that even when peak pressures are the same, the rate of impact influences the immediate cellular pathology and neurological assessment measures. Moreover, the rate-specific differences in early neurobehavioral assessment and cellular damage suggest that rats exposed to fast-rate FPI may have a milder injury and thus show improved neurological prognosis compared to rats receiving standard-rate FPI at identical peak pressure.

Absence of rate-specific difference in dentate cell loss and excitability one week after FPI

Given the difference in early neuronal degeneration following FPI at fast and standard rates, we examined whether rate-specific differences in hilar neuronal loss were observed one week after FPI, a time point at which the cellular and physiological changes in the dentate gyrus have been extensively characterized after FPI using pendulum-style devices.[7, 8, 11, 35, 36] In sections obtained from rats perfused 1 week after injury, NeuN staining for neuronal nuclei revealed fewer NeuN immunoreactive neurons in the dentate hilus following both fast- and standard-rate FPI than in sham-controls (Fig 4A). Stereological cell counts revealed a significant decrease in hilar neurons after both fast- and standard-rate FPI (Fig 4A-C, NeuN-positive hilar neurons per section, sham: 523.3±44.0, median = 476.0, IQR = 358.8-549.0, n = 24 sections from 3 rats; fast-FPI: 372.4±32.1, median = 335.5, IQR = 288.3-457.5, n = 18 sections from 3 rats; standard-FPI: 322.1±27.4, median = 287.0, IQR = 216.0-411.0, n = 23 sections from 3 rats, $p<0.05$, $H = 14.029$, $df=2$ by Kruskal-Wallis One Way ANOVA on Ranks). Pairwise multiple comparison by Dunn's Method showed that the difference in the number of surviving NeuN-positive neurons between sham and standard-rate FPI and between sham and fast-rate FPI were statistically significant. In contrast to the rate dependent effect on neuronal injury observed 4 hours after FPI, the difference in the number of NeuN-labeled neurons was not different between fast- and

standard-rate FPI one week after injury. Given the disparity between hilar neuronal degeneration following fast- and standard-rate FPI at 4 hours, this could suggest recovery of some mechanically injured neurons following standard-rate FPI.[35] However, since Fluoro-Jade labels irrevocably degenerating neurons, our data likely indicate a greater progression of hilar cell loss within hours to a week following fast-rate FPI.

Several groups have consistently demonstrated an increase in dentate network excitability and altered inhibition one week after FPI using the pendulum-style device.[7, 8, 11, 35, 36] The hilar neuronal loss and increase in dentate excitability have been suggested to predict development of long-term neurological complications such as post-traumatic epilepsy.[11, 35] Therefore, we examined the granule cell population response to afferent activation in order to assess the effect of injury-rate on neurophysiological outcomes one week after FPI. As illustrated in Figure 5A, while the granule cell population response evoked by perforant path stimulation at 4 mA rarely showed population spikes in sham-control rats, afferent activation reliably elicited population spikes in granule cells one week after fast- and standard-rate FPI. Summary data demonstrate that the afferent-evoked granule cell population spike amplitude in rats injured at either rate, while significantly enhanced from sham-controls, was not different between slices from rats injured with fast-rate or standard-rate FPI (Fig. 5B, sham: n = 13 slices from 5 rats; fast-FPI: n = 12 slices from 6 rats, standard-FPI: n = 12 slices from 6 rats, significance determined by two-way repeated-measures ANOVA followed by post-hoc Tukey's test). Earlier studies have identified that brain injury with the pendulum-style FPI device enhances excitability of the dentate excitatory network, measured in the presence of $GABA_A$ receptor ($GABA_AR$) antagonists.[7] To determine whether injuries at fast- and standard-rates differentially impacted the excitability of the dentate excitatory network we examined the perforant path-evoked granule

cell field responses in slices which were perfused with SR95531 (10 μM, gabazine) a $GABA_AR$ antagonist. Once again, the amplitude of the first population spike in response to afferent activation was greater in slices from head-injured rats compared with sham-controls (Fig. 5C). Additionally, the slices from rats subject to FPI showed an increase in the number of afferent-evoked population spikes (Fig. 5C). However, neither the amplitude of the first population spike nor the number of population spikes in response to perforant path stimulation (inset in Fig. 5D, top panel) were different between slices from rats exposed to fast- and standard-rate FPI (Fig. 5D, sham: n = 13 slices from 5 rats; fast-FPI: n = 12 slices from 6 rats, standard-FPI: n = 12 slices from 6 rats, significance determined by two-way repeated-measures ANOVA followed by post-hoc Tukey's test). Together, our studies on fast- and standard-rate FPI at similar peak impact pressures indicate that although the superior neurobehavioral outcome and reduced cellular injury measures within hours following fast-rate injury suggest that fast-rate trauma leads to a milder TBI than slower rate injury, the extent of cell loss and physiological dysfunction after fast-rate injury are comparable to moderate TBI within a week after injury.

Discussion

The use of a novel programmable VC-FPI device allowed us to examine a fundamental question concerning how differences in the rate of delivery of a concussive wave alters neurological outcome following brain injury. We demonstrate, for the first time, that even when peak injury pressures are similar, the rate of rise to peak impact pressure modifies the immediate cellular injury. Although both the early behavioral assessment and neuronal degeneration within 4 hours after injury suggest that fast-rate injuries lead to reduced neurological damage compared to slower-rate injuries, studies performed one week after injury demonstrate similar extent of dentate hilar cell loss and increase in network excitability following fast- and slower-rate injuries. Our findings suggest that a better immediate neurological outcome following fast injury may mask the severity of neuropathology at later time points. Since strategies for evaluation of injury severity rely primarily on early clinical measures,[31] our data suggest the need to consider the effect of injury rate in shaping the cellular and physiological response at later time points while managing patients sustaining fast-rate and slower-rate concussive injuries.

TBI can result from a wide spectrum of injuries ranging from falls that occur at relatively slow impact velocities[18], to sports injuries and traffic accidents which represent higher rate impacts to,[43, 44] at the other end of the spectrum, the extremely rapid waves generated by blasts.[20, 21] Fast-rate TBI following exposure to explosive blasts is the signature injury of the recent wars[30] and a growing issue facing veterans. The primary impact waves of blast TBI have a faster rise to peak pressure than non-blast concussive TBI.[18-21, 45] Most contemporary studies use inherently different devices such as explosions or blast tubes to generate fast-rate injuries,[46-49] or FPI devices[6, 28] to deliver standard fixed concussive waveforms. The inability to independently control rate and magnitude in the pendulum-style FPI device and use of different devices to

model injuries at different rates renders it difficult to directly compare rate-specific changes in neuropathology without differences in peak pressure and device-dependent confounding factors. The prototype voice coil driven FPI device[34] enabled us to overcome these technical obstacles and demonstrate that, even at constant peak pressures, the rate of fluid percussion directly affects the immediate neurological response. Despite the limitation that the fast-rate FPI waveform generated by our programmable FPI device was slower than the typical blast waveform,[21, 30] our study presents the first demonstration that injury rate can modify the ability of early neurological measures to predict the subsequent neuropathology. Another potential caveat is that while the peak pressures are similar, the fast injury waveform in the current study had a shorter duration than the standard wave. Thus the impulse, a measure of energy transfer determined as the area under the pressure curve, in fast-rate FPI is lower than in standard-rate FPI. However, real world high-rate injuries such as blast waves usually have a brief duration compared to the standard concussive waveform modeled by the pendulum-style FPI device.[21, 30] Moreover, although it might be expected that the fast-rate, low impulse injury would lead to a milder TBI, it is notable that fast-rate FPI produced comparable cellular and physiological pathology at one week as standard-rate, higher-impact injuries. Our finding that both fast- and standard-rate FPI result in similar dentate hilar cell loss and alterations in network excitability one week after FPI, notwithstanding a dramatically milder neurobehavioral assessment immediately after fast-rate FPI have important implications for assessment of blast and non-blast TBI. The Glasgow Coma Scale, or a modified version, is widely used to assess severity of neurological injury and predict prognosis following TBI.[30, 31, 50] Our data indicate that post-injury criteria, which seem to reliably predict prognosis following increasing magnitudes of impact at similar rates[27-29] may need to consider the effect of impact rate for fast-rate injuries such as blast-TBI.

Our histological studies four hours after injury demonstrate that the immediate cellular injury and degeneration is considerably milder following fast-rate FPI than after standard-rate FPI. What are the mechanisms that could account for the subsequent absence of rate-specific difference in hilar cell loss and network excitability one week after injury? Structural characteristics of cytoskeletal elements in somato-dendritic compartments may underlie the difference in mechanical damage induced by fast- and slower-rate FPI. It is possible that axons which have distinctive cytoskeletal components[51] may be more vulnerable to injury during fast-rate TBI. Consistent with this possibility, diffuse axonal injury takes a longer time to manifest[52, 53] compared to considerable early somato-dendritic injury evident in silver-stained sections from rats exposed to standard-rate injury. Additionally, high-rate TBI is typically associated with extensive white matter injury.[54, 55] An equally possible alternative is that fast-rate injuries lead to greater progressive excitotoxic cell death[56-58] leading to increased network excitability. While the exact mechanisms remain to be elucidated, it is evident that the progression of neuropathology following fast-rate FPI is different than after slower-rate TBI. The observed divergence between early post-injury assessment and subsequent cellular and physiological outcome following fast- and standard-rate FPI suggest that early behavioral measures used to predict prognosis following slower-rate TBI may underestimate the severity of long-term neurological outcome following fast-rate, blast-related TBI.

References

1. Congeni J. Management of the adolescent concussion victim. Adolescent medicine: state of the art reviews. 2009 Apr;20(1):41-56, viii.

2. Vaishnavi S, Rao V, Fann JR. Neuropsychiatric problems after traumatic brain injury: unraveling the silent epidemic. Psychosomatics. 2009 May-Jun;50(3):198-205.

3. Iverson GL, Brooks BL, Collins MW, Lovell MR. Tracking neuropsychological recovery following concussion in sport. Brain injury : [BI]. 2006 Mar;20(3):245-52.

4. Stroke NIoNDa. Traumatic brain injury: hope through research. In: Health NIo, editor. Bethesda (MD)2002.

5. Engel J, Pedley TA. Epilepsy : a comprehensive textbook. Philadelphia: Lippincott-Raven; 1998.

6. Garga N, Lowenstein DH. Posttraumatic epilepsy: a major problem in desperate need of major advances. Epilepsy Curr. 2006 Jan-Feb;6(1):1-5.

7. Santhakumar V, Bender R, Frotscher M, et al. Granule cell hyperexcitability in the early post-traumatic rat dentate gyrus: the 'irritable mossy cell' hypothesis. J Physiol. 2000 Apr 1;524 Pt 1:117-34.

8. Santhakumar V, Ratzliff AD, Jeng J, Toth Z, Soltesz I. Long-term hyperexcitability in the hippocampus after experimental head trauma. Annals of neurology. 2001 Dec;50(6):708-17.

9. Winter CD, Pringle AK, Clough GF, Church MK. Raised parenchymal interleukin-6 levels correlate with improved outcome after traumatic brain injury. Brain. 2004 Feb;127(Pt 2):315-20.

10. Cohen AS, Pfister BJ, Schwarzbach E, Grady MS, Goforth PB, Satin LS. Injury-induced alterations in CNS electrophysiology. Prog Brain Res. 2007;161:143-69.

11. Lowenstein DH, Thomas MJ, Smith DH, McIntosh TK. Selective vulnerability of dentate hilar neurons following traumatic brain injury: a potential mechanistic link between head trauma and disorders of the hippocampus. The Journal of neuroscience : the official journal of the Society for Neuroscience. 1992 Dec;12(12):4846-53.

12. Herman ST. Epilepsy after brain insult: targeting epileptogenesis. Neurology. 2002 Nov 12;59(9 Suppl 5):S21-6.

13. Creed JA, DiLeonardi AM, Fox DP, Tessler AR, Raghupathi R. Concussive brain trauma in the mouse results in acute cognitive deficits and sustained impairment of axonal function. Journal of neurotrauma. 2011 Apr;28(4):547-63.

14. Hicks RR, Smith DH, Lowenstein DH, Saint Marie R, McIntosh TK. Mild experimental brain injury in the rat induces cognitive deficits associated with regional neuronal loss in the hippocampus. Journal of neurotrauma. 1993 Winter;10(4):405-14.

15. Kharatishvili I, Nissinen JP, McIntosh TK, Pitkanen A. A model of posttraumatic epilepsy induced by lateral fluid-percussion brain injury in rats. Neuroscience. 2006 Jun 30;140(2):685-97.

16. D'Ambrosio R, Fairbanks JP, Fender JS, Born DE, Doyle DL, Miller JW. Post-traumatic epilepsy following fluid percussion injury in the rat. Brain. 2004 Feb;127(Pt 2):304-14.

17. Zhang J, Yoganandan N, Pintar FA, Gennarelli TA. Role of translational and rotational accelerations on brain strain in lateral head impact. Biomedical sciences instrumentation. 2006;42:501-6.

18. Wright AD, Laing AC. The influence of headform orientation and flooring systems on impact dynamics during simulated fall-related head impacts. Medical engineering & physics. 2012 Oct;34(8):1071-8.

19. Chavko M, Koller WA, Prusaczyk WK, McCarron RM. Measurement of blast wave by a miniature fiber optic pressure transducer in the rat brain. Journal of neuroscience methods. 2007 Jan 30;159(2):277-81.

20. Shridharani JK, Wood GW, Panzer MB, et al. Porcine head response to blast. Frontiers in neurology. 2012;3:70.

21. Zhang J, Pintar FA, Yoganandan N, Gennarelli TA, Son SF. Experimental study of blast-induced traumatic brain injury using a physical head model. Stapp car crash journal. 2009 Nov;53:215-27.

22. Graham DI, Raghupathi R, Saatman KE, Meaney D, McIntosh TK. Tissue tears in the white matter after lateral fluid percussion brain injury in the rat: relevance to human brain injury. Acta Neuropathol(Berl). 2000;99(2):117-24.

23. Prange MT, Margulies SS. Regional, directional, and age-dependent properties of the brain undergoing large deformation. Journal of biomechanical engineering. 2002 Apr;124(2):244-52.

24. Vappou J, Breton E, Choquet P, Goetz C, Willinger R, Constantinesco A. Magnetic resonance elastography compared with rotational rheometry for in vitro brain tissue viscoelasticity measurement. Magma. 2007 Dec;20(5-6):273-8.

25. Rashid B, Destrade M, Gilchrist MD. Mechanical characterization of brain tissue in compression at dynamic strain rates. Journal of the mechanical behavior of biomedical materials. 2012 Jun;10:23-38.

26. Morrison B, 3rd, Cater HL, Wang CC, et al. A tissue level tolerance criterion for living brain developed with an in vitro model of traumatic mechanical loading. Stapp car crash journal. 2003 Oct;47:93-105.

27. Povlishock JT, Hayes RL, Michel ME, McIntosh TK. Workshop on animal models of traumatic brain injury. Journal of neurotrauma. 1994 Dec;11(6):723-32.

28. Dixon CE, Lyeth BG, Povlishock JT, et al. A fluid percussion model of experimental brain injury in the rat. Journal of neurosurgery. 1987 Jul;67(1):110-9.

29. Huh JW, Widing AG, Raghupathi R. Differential effects of injury severity on cognition and cellular pathology after contusive brain trauma in the immature rat. Journal of neurotrauma. 2011 Feb;28(2):245-57.

30. Elder GA, Cristian A. Blast-related mild traumatic brain injury: mechanisms of injury and impact on clinical care. Mt Sinai J Med. 2009 Apr;76(2):111-8.

31. Saatman KE, Duhaime AC, Bullock R, et al. Classification of traumatic brain injury for targeted therapies. Journal of neurotrauma. 2008 Jul;25(7):719-38.

32. Steyerberg EW, Mushkudiani N, Perel P, et al. Predicting outcome after traumatic brain injury: development and international validation of prognostic scores based on admission characteristics. PLoS Med. 2008 Aug 5;5(8):e165; discussion e.

33. Collaborators MCT, Perel P, Arango M, et al. Predicting outcome after traumatic brain injury: practical prognostic models based on large cohort of international patients. BMJ. 2008 Feb 23;336(7641):425-9.

34. Abdul-Wahab R SB, Mina S, Sampath S, Santhakumar V, Pfister BJ. Precisely controllable traumatic brain injury devices for rodent models. . Bioengineering Conference (NEBEC), 2011 IEEE 37th Annual Northeast, 1-22011.

35. Toth Z, Hollrigel GS, Gorcs T, Soltesz I. Instantaneous perturbation of dentate interneuronal networks by a pressure wave-transient delivered to the neocortex. The Journal of neuroscience : the official journal of the Society for Neuroscience. 1997 Nov 1;17(21):8106-17.

36. Gupta A, Elgammal FS, Proddutur A, Shah S, Santhakumar V. Decrease in tonic inhibition contributes to increase in dentate semilunar granule cell excitability after brain injury. The Journal of neuroscience : the official journal of the Society for Neuroscience. 2012 Feb 15;32(7):2523-37.

37. Santhakumar V, Voipio J, Kaila K, Soltesz I. Post-traumatic hyperexcitability is not caused by impaired buffering of extracellular potassium. The Journal of neuroscience : the official journal of the Society for Neuroscience. 2003 Jul 2;23(13):5865-76.

38. Gallyas F, Guldner FH, Zoltay G, Wolff JR. Golgi-like demonstration of "dark" neurons with an argyrophil III method for experimental neuropathology. Acta neuropathologica. 1990;79(6):620-8.

39. van den Pol AN, Gallyas F. Trauma-induced Golgi-like staining of neurons: a new approach to neuronal organization and response to injury. J Comp Neurol. 1990 Jun 22;296(4):654-73.

40. Yu J, Proddutur A, Elgammal FS, Ito T, Santhakumar V. Status epilepticus enhances tonic GABA currents and depolarizes GABA reversal potential in dentate fast-spiking basket cells. J Neurophysiol. 2013 Jan 16.

41. West MJ, Slomianka L, Gundersen HJ. Unbiased stereological estimation of the total number of neurons in thesubdivisions of the rat hippocampus using the optical fractionator. Anat Rec. 1991 Dec;231(4):482-97.

42. West MJ. New stereological methods for counting neurons. Neurobiol Aging. 1993 Jul-Aug;14(4):275-85.

43. Zhang J, Yoganandan N, Pintar FA. Dynamic biomechanics of the human head in lateral impacts. Annals of advances in automotive medicine / Annual Scientific Conference

Association for the Advancement of Automotive Medicine Association for the Advancement of Automotive Medicine Scientific Conference. 2009 Oct;53:249-56.

44. Zhang J, Yoganandan N, Pintar FA, Gennarelli TA. Brain strains in vehicle impact tests. Annual proceedings / Association for the Advancement of Automotive Medicine Association for the Advancement of Automotive Medicine. 2006;50:1-12.

45. Cernak I, Noble-Haeusslein LJ. Traumatic brain injury: an overview of pathobiology with emphasis on military populations. J Cereb Blood Flow Metab. 2010 Feb;30(2):255-66.

46. Risling M, Plantman S, Angeria M, et al. Mechanisms of blast induced brain injuries, experimental studies in rats. Neuroimage. 2011 Jan;54 Suppl 1:S89-97.

47. Rubovitch V, Ten-Bosch M, Zohar O, et al. A mouse model of blast-induced mild traumatic brain injury. Experimental neurology. 2011 Dec;232(2):280-9.

48. Skotak M, Wang F, Alai A, et al. Rat injury model under controlled field-relevant primary blast conditions: Acute response to a wide range of peak overpressures. Journal of neurotrauma. 2013 Jan 30.

49. Cernak I, Wang Z, Jiang J, Bian X, Savic J. Ultrastructural and functional characteristics of blast injury-induced neurotrauma. The Journal of trauma. 2001 Apr;50(4):695-706.

50. Sternbach GL. The Glasgow coma scale. J Emerg Med. 2000 Jul;19(1):67-71.

51. Stiess M, Bradke F. Neuronal polarization: the cytoskeleton leads the way. Developmental neurobiology. 2011 Jun;71(6):430-44.

52. Carbonell WS, Grady MS. Regional and temporal characterization of neuronal, glial, and axonal response after traumatic brain injury in the mouse. Acta neuropathologica. 1999 Oct;98(4):396-406.

53. Leonard JR, Grady MS, Lee ME, Paz JC, Westrum LE. Fluid percussion injury causes disruption of the septohippocampal pathway in the rat. Experimental neurology. 1997 Feb;143(2):177-87.

54. Jorge RE, Acion L, White T, et al. White matter abnormalities in veterans with mild traumatic brain injury. The American journal of psychiatry. 2012 Dec 1;169(12):1284-91.

55. Koliatsos VE, Cernak I, Xu L, et al. A mouse model of blast injury to brain: initial pathological, neuropathological, and behavioral characterization. Journal of neuropathology and experimental neurology. 2011 May;70(5):399-416.

56. Manev H, Favaron M, Guidotti A, Costa E. Delayed increase of Ca2+ influx elicited by glutamate: role in neuronal death. Mol Pharmacol. 1989 Jul;36(1):106-12.

57. Palmer AM, Marion DW, Botscheller ML, Swedlow PE, Styren SD, DeKosky ST. Traumatic brain injury-induced excitotoxicity assessed in a controlled cortical impact model. Journal of neurochemistry. 1993 Dec;61(6):2015-24.

58. Yi JH, Hazell AS. Excitotoxic mechanisms and the role of astrocytic glutamate transporters in traumatic brain injury. Neurochem Int. 2006 Apr;48(5):394-403.

Acknowledgements: We thank Mat Long, Bogumila Swietek, Akshata Korgaonkar and Fatima S. Elgammal for their helpful comments and technical assistance and Drs. Stella Elkabes and Robert F. Heary for equipment and technical support. The project was supported by NJCBIR multi-investigator grant: CBIR11PJT003 to B.J.P and V.S and NJCBIR 09.003-BIR1 and NIH/NINDS NS069861 to V.S.

Author Contributions: E.J.N, R.A.W and A.J performed experiments; E.J.N and R.A.W analyzed data; B.J.P and V.S interpreted results of experiments; E.J.N prepared figures; E.J.N and V.S authored the manuscript; R.A.W, A.J, B.J.P edited and approved the manuscript. B.J.P and V.S: conception and design of research.

Figure legends

Figure 1. Schematic of the VC-FPI device and representative FPI waveforms.

A. Schematic of the programmable VC-FPI device that independently controls key variables defining the waveform and can generate high-rate blast-like injuries. The system utilizes a voice coil actuator to generate a precise temporal forcing function under closed loop controlled with a proportional–integral–derivative (PID) motion controller and linear encoder with a 1 μm resolution. The voice coil is coupled to a syringe filled with water that delivers the fluid percussion injury. In this study, the device was programmed to alter the rates of pressure rise, keeping the pressure peak consistent. B. Representative fast- and standard-rate pressure waveforms obtained during animal injuries using the VC-FPI device are overlaid on a trace from the pendulum-style FPI device (Virginia Commonwealth University, VA) for comparison.

Figure 2. Injury rate impacts immediate post-injury behavior.

A. Summary plot of the average duration of apnea immediately following fast- and standard-rate FPI. B-C. Summary histograms shows the duration of recovery of response to toe pinch (B) and time to recovery of righting reflex (C) following injuries. * denotes significance compared to sham by Mann-Whitney U test following Bonferroni correction for multiple comparisons. # denotes significance compared to fast-rate FPI by Mann-Whitney U test following Bonferroni correction for multiple comparisons.

Figure 3. Differential early dentate neuronal injury and degeneration after fast- and standard-rate FPI within 4 hours after injury.

A-C. Representative sections from the dentate gyrus of rats fixed 4 hours after sham-, fast-rate and standard-rate FPI and stained with the Gallyas silver stain to reveal neurons with mechanical

injury. Note the lack of staining in controls (A), the sparse staining after fast-rate FPI (B) and presence of numerous darkly stained cells in the dentate hilus and also a subset of the darkly stained cells in the granule cell layer (GCL) after standard-rate FPI (C). D-F. Fluoro-Jade C stained hippocampal sections from rats perfused 4-6 hours after FPI show few labeled hilar neurons in the sham-control (D), several labeled neurons following fast-rate FPI (E) and numerous degenerating neurons in the dentate hilus after standard-rate FPI (F). G. Summary histogram of stereological counts of Fluoro-Jade C-labeled hilar neurons in animals subject to the injury paradigms. * denotes significance by one-way ANOVA for ranks followed by post-hoc pairwise comparison by Dunn's method.

Figure 4. Dentate hilar neuronal loss 1 week after fast- and standard-rate FPI.

A-C. Representative NeuN stained hippocampal sections from rats perfused 1 week after injury show significantly more neurons in the hilus of sham-controls (A) compared to rats exposed to either fast- (B) or standard-rate FPI (C). D. Summary data compare stereological counts of NeuN-labeled neurons in sections from sham-controls and rats subject to fast- and standard-rate FPI. GCL, Granule Cell Layer. * denotes significance and N.S indicates not significant by one-way ANOVA for ranks followed by post-hoc pairwise comparison by Dunn's method.

Figure 5. Absence of rate-specific difference in dentate excitability one week after FPI.

A. Representative dentate granule cell field responses evoked by a 4mA stimulus to the perforant path. Recordings were performed in control aCSF. B. Summary plot of afferent evoked population spike amplitude in aCSF. C. Dentate population responses evoked by perforant path stimulation at 4mA in the $GABA_A$ receptor antagonist SR95531 (10μM). D. Summary plot of perforant path-evoked granule cell population spike amplitude in SR95531 (10 μM). Inset in top

panel shows summary histogram of number of population spikes. *denotes significance by multi-way repeated measure ANOVA.

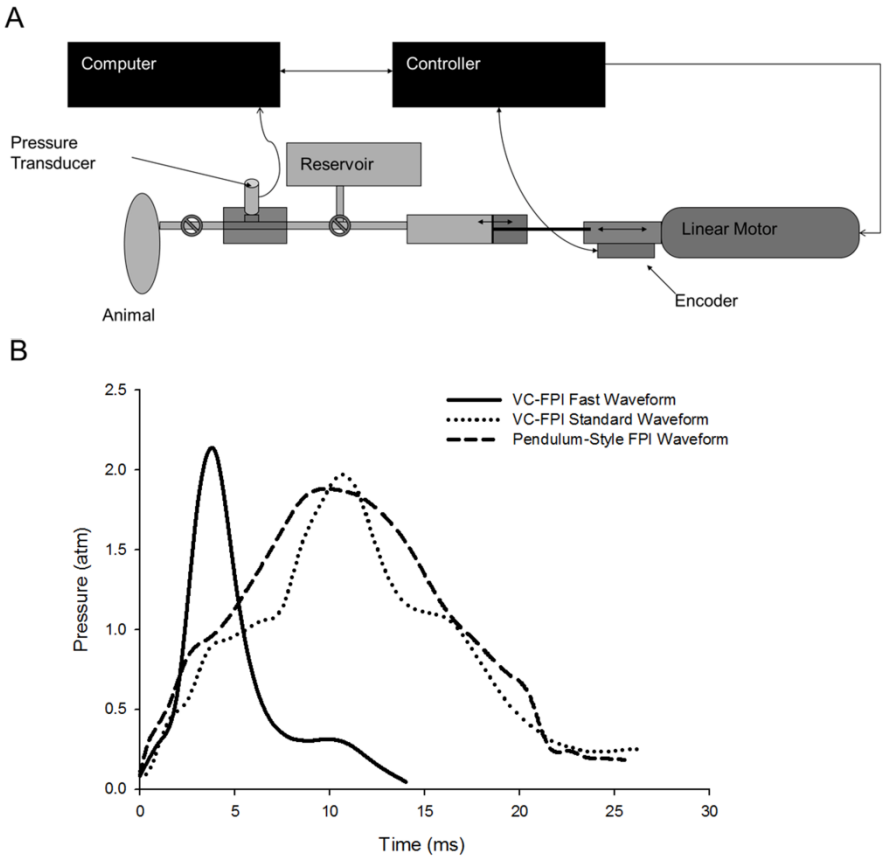
A
Computer
Controller
Pressure
Transducer
Reservoir
Linear Motor
Encoder
Animal
B
VC-FPI Fast Waveform
VC-FPI Standard Waveform
Pendulum-Style FPI Waveform
Pressure (atm)
Time (ms)
0.0
0.5
1.0
1.5
2.0
2.5
0
5
10
15
20
25
30

Figure 1

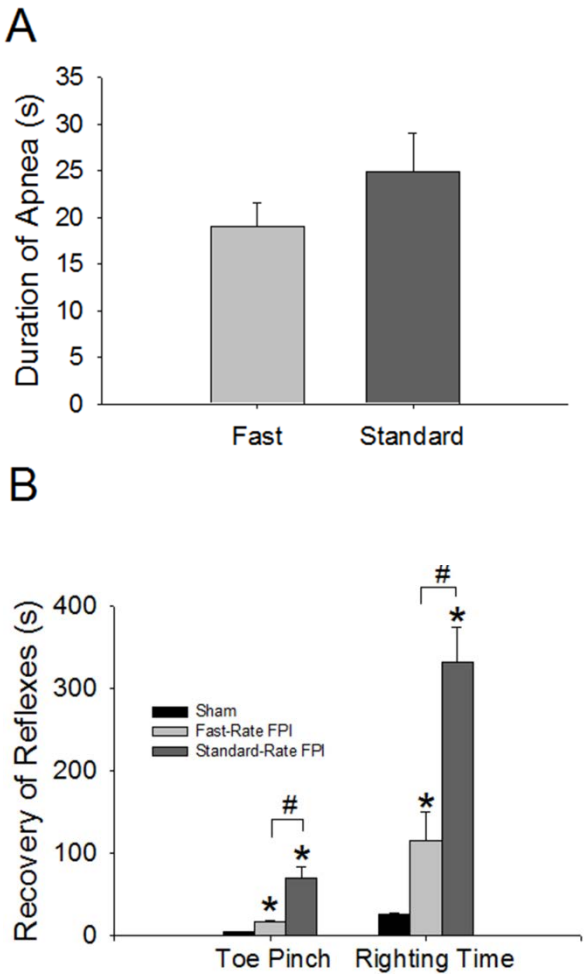
A
Duration of Apnea (s)
35
30
25
20
15
10
5
0
Fast
Standard
B
Recovery of Reflexes (s)
400
300
200
100
0
Sham
Fast-Rate FPI
Standard-Rate FPI
#
*
#
*
*
*
Toe Pinch
Righting Time

Figure 2

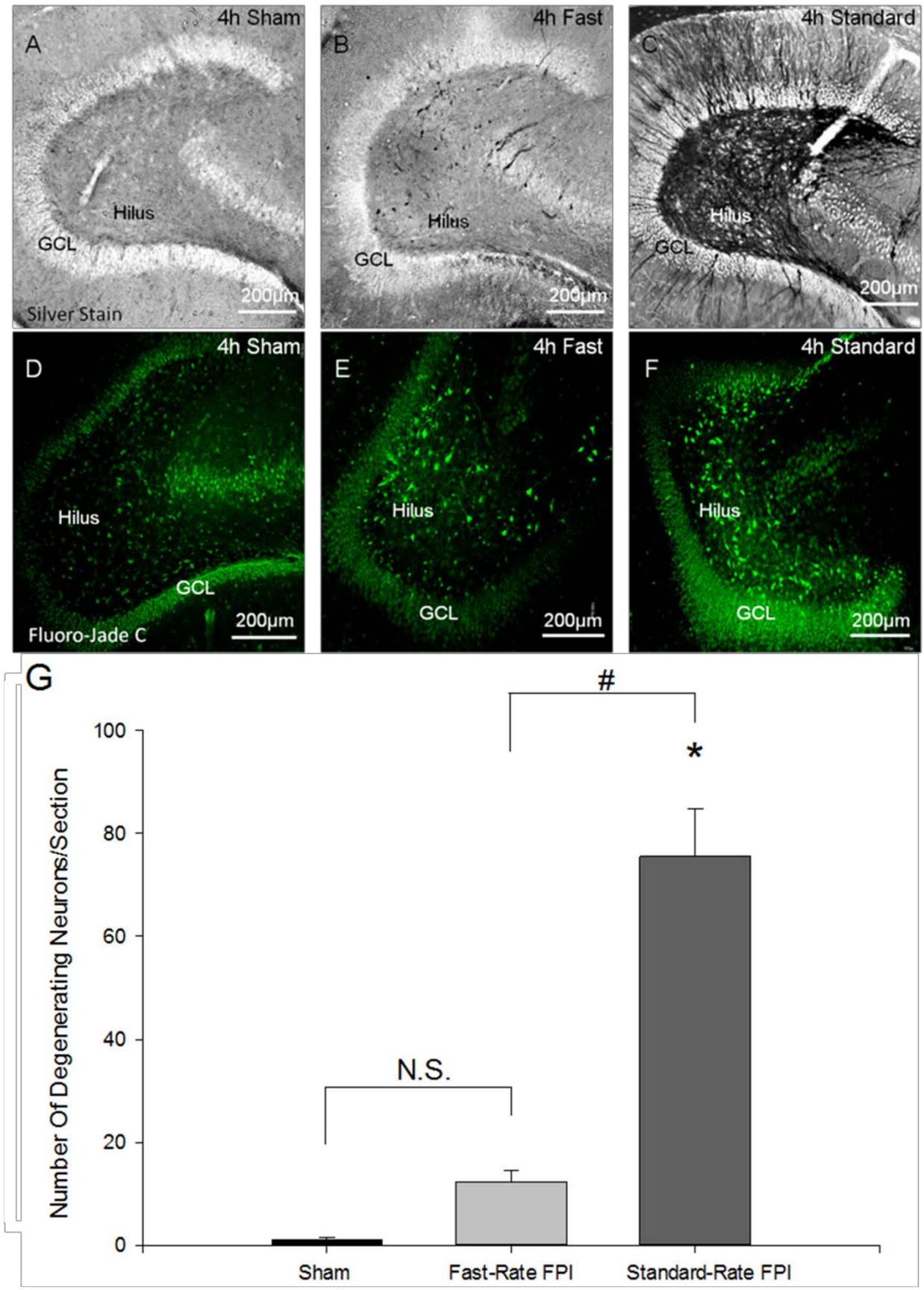
A
4h Sham
Hilus
GCL
Silver Stain
200μm
B
4h Fast
Hilus
GCL
200μm
C
4h Standard
Hilus
GCL
200μm
D
4h Sham
Hilus
GCL
Fluoro-Jade C
200μm
E
4h Fast
Hilus
GCL
200μm
F
4h Standard
Hilus
GCL
200μm
G
Number Of Degenerating Neurons/Section
100
80
60
40
20
0
#
*
N.S.
Sham
Fast-Rate FPI
Standard-Rate FPI

Figure 3

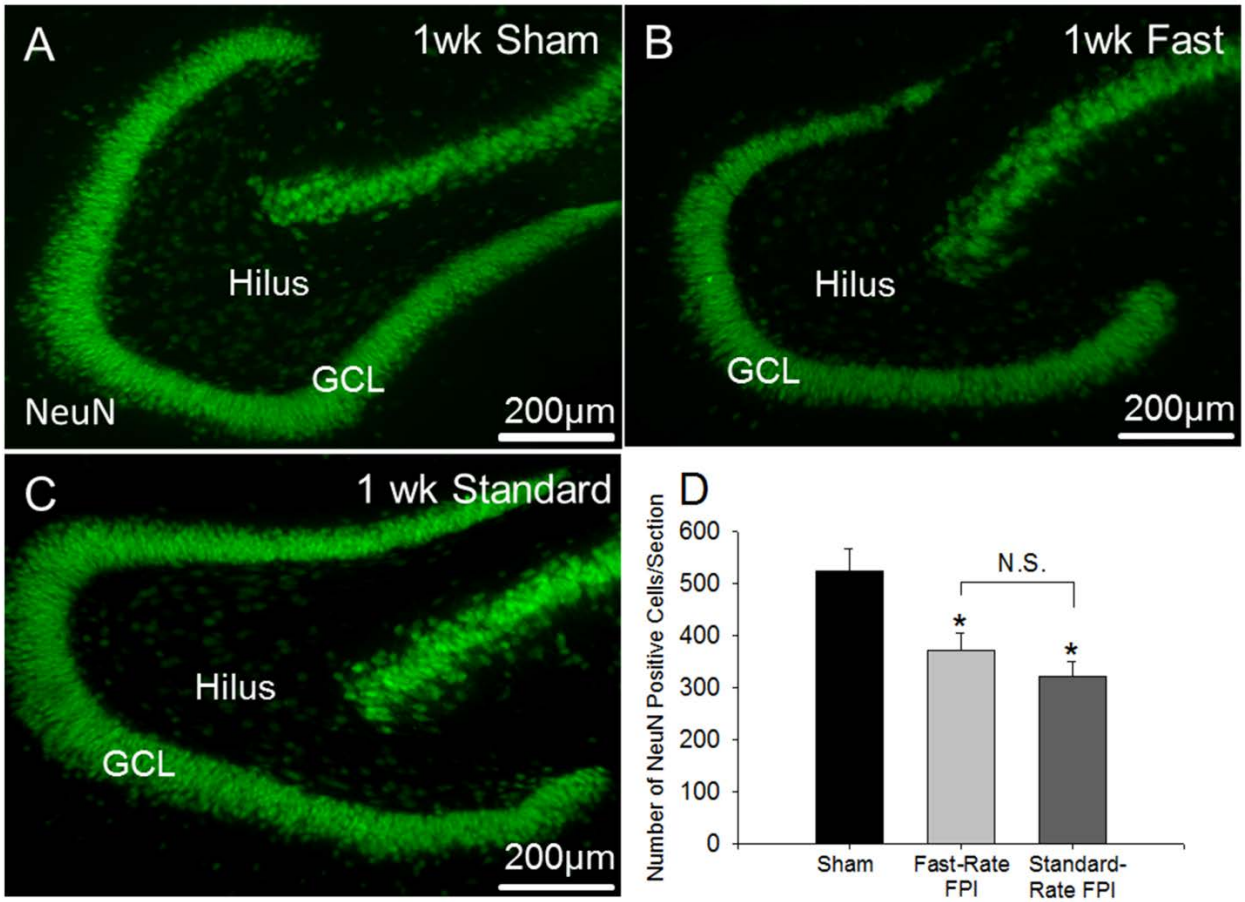
A
1wk Sham
Hilus
GCL
NeuN
200μm
B
1wk Fast
Hilus
GCL
200μm
C
1 wk Standard
Hilus
GCL
200μm
D
Number of NeuN Positive Cells/Section
600
500
400
300
200
100
0
N.S.
*
*
Sham
Fast-Rate FPI
Standard-Rate FPI

Figure 4

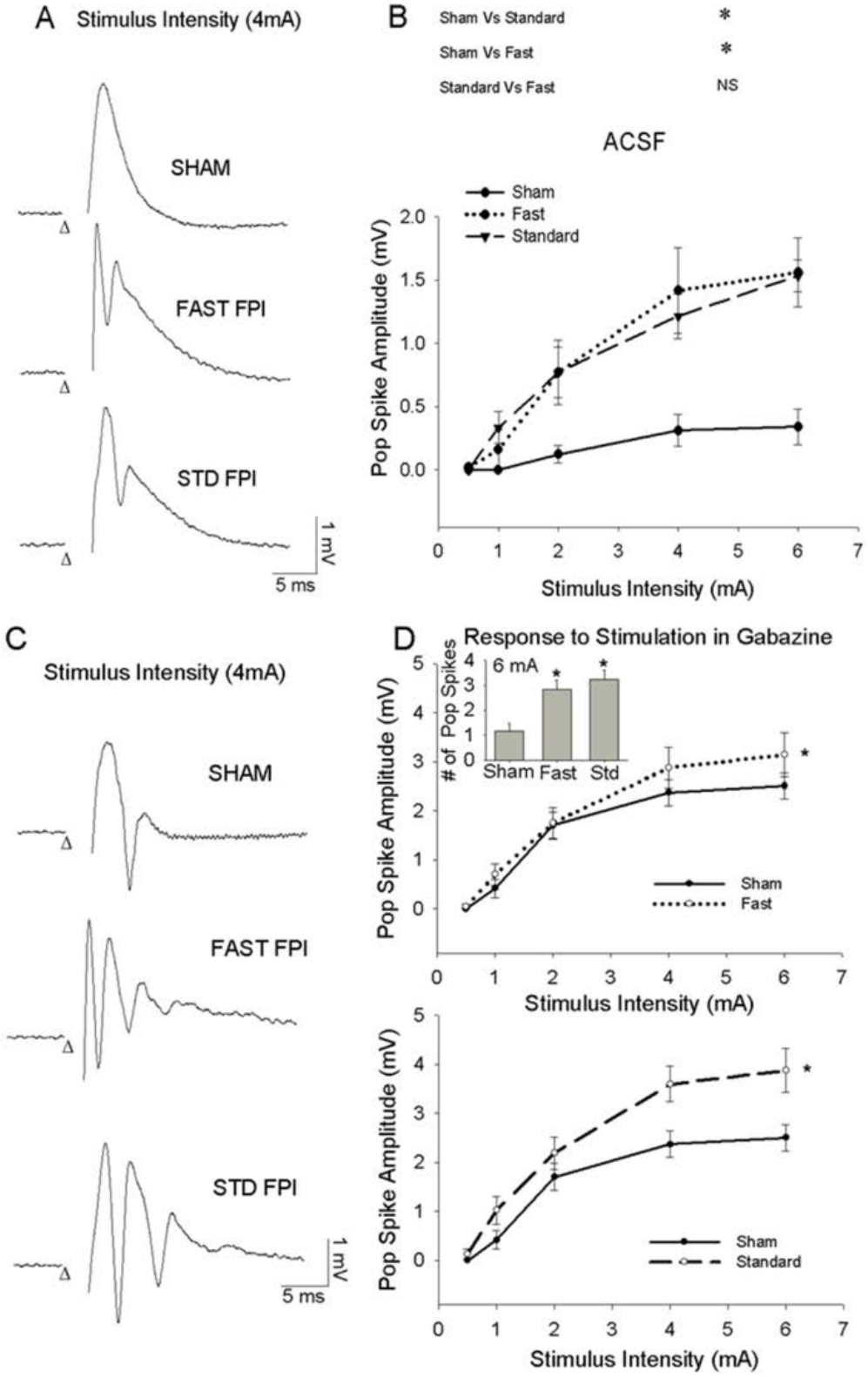
A
Stimulus Intensity (4mA)
SHAM
FAST FPI
STD FPI
1 mV
5 ms
B
Sham Vs Standard *
Sham Vs Fast *
Standard Vs Fast NS
ACSF
Sham
Fast
Standard
Pop Spike Amplitude (mV)
Stimulus Intensity (mA)
C
Stimulus Intensity (4mA)
SHAM
FAST FPI
STD FPI
1 mV
5 ms
D
Response to Stimulation in Gabazine
6 mA
# of Pop Spikes
Sham Fast Std
Sham
Fast
Standard
Pop Spike Amplitude (mV)
Stimulus Intensity (mA)

Figure 5

J Neurophysiol 109: 000–000, 2013.
First published January 16, 2013; doi:10.1152/jn.00891.2012.

Status epilepticus enhances tonic GABA currents and depolarizes GABA reversal potential in dentate fast-spiking basket cells

AQ: 1

Jiandong Yu,[1]* Archana Proddutur,[1]* Fatima S. Elgammal,[1] Takahiro Ito,[1] and Vijayalakshmi Santhakumar[1,2]

[1]*Department of Neurology and Neurosciences, New Jersey Medical School, University of Medicine and Dentistry of New Jersey, Newark, New Jersey; and* [2]*Department of Pharmacology and Physiology, New Jersey Medical School, University of Medicine and Dentistry of New Jersey, Newark, New Jersey*

Submitted 8 October 2012; accepted in final form 11 January 2013

AQ: 2

Yu J, Proddutur A, Elgammal FS, Ito T, Santhakumar V. Status epilepticus enhances tonic GABA currents and depolarizes GABA reversal potential in dentate fast-spiking basket cells. *J Neurophysiol* 109: 000–000, 2013. First published January 16, 2013; doi:10.1152/jn.00891.2012.—Temporal lobe epilepsy is associated with loss of interneurons and inhibitory dysfunction in the dentate gyrus. While status epilepticus (SE) leads to changes in granule cell inhibition, whether dentate basket cells critical for regulating granule cell feedforward and feedback inhibition express tonic GABA currents (I_{GABA}) and undergo changes in inhibition after SE is not known. We find that interneurons immunoreactive for parvalbumin in the hilar-subgranular region express $GABA_A$ receptor ($GABA_AR$) δ-subunits, which are known to underlie tonic I_{GABA}. Dentate fast-spiking basket cells (FS-BCs) demonstrate baseline tonic I_{GABA} blocked by $GABA_AR$ antagonists. In morphologically and physiologically identified FS-BCs, tonic I_{GABA} is enhanced 1 wk after pilocarpine-induced SE, despite simultaneous reduction in spontaneous inhibitory postsynaptic current (sIPSC) frequency. Amplitude of tonic I_{GABA} in control and post-SE FS-BCs is enhanced by 4,5,6,7-tetrahydroisoxazolo[5,4-*c*]pyridin-3-ol (THIP), demonstrating the contribution of $GABA_AR$ δ-subunits. Whereas FS-BC resting membrane potential is unchanged after SE, perforated-patch recordings from FS-BCs show that the reversal potential for GABA currents (E_{GABA}) is depolarized after SE. In model FS-BCs, increasing tonic GABA conductance decreased excitability when E_{GABA} was shunting and increased excitability when E_{GABA} was depolarizing. Although simulated focal afferent activation evoked seizurelike activity in model dentate networks with FS-BC tonic GABA conductance and shunting E_{GABA}, excitability of identical networks with depolarizing FS-BC E_{GABA} showed lower activity levels. Thus, together, post-SE changes in tonic I_{GABA} and E_{GABA} maintain homeostasis of FS-BC activity and limit increases in dentate excitability. These findings have implications for normal FS-BC function and can inform studies examining comorbidities and therapeutics following SE.

interneuron; epilepsy; tonic inhibition

AQ: 3

ACQUIRED TEMPORAL LOBE EPILEPSY occurring as a consequence of unprovoked seizures is marked by neuropathological changes in the dentate gyrus (Margerison and Corsellis 1966). Alterations in granule cell inhibition, resulting from loss or dysfunction of GABAergic interneurons, have been proposed to contribute to development of epilepsy (Cossart et al. 2005; Coulter 2001). The early period within a week after status epilepticus (SE) is characterized by enhanced entorhinal input to the dentate gyrus (Bragin et al. 2004; Kobayashi et al. 2003) and is associated with changes in granule cell GABA currents (I_{GABA}) (Kobayashi and Buckmaster 2003; Zhan and Nadler 2009) and GABA reversal potential (E_{GABA}) (Pathak et al. 2007). The cellular and synaptic changes that occur prior to development of spontaneous seizures have been the focus of several studies because of their potential to contribute to the epileptogenic process rather than being a side effect of epilepsy (Brooks-Kayal et al. 1998; Kobayashi et al. 2003; Pathak et al. 2007). SE leads to loss and structural reorganization of interneurons and alterations in their excitatory inputs (Zhang and Buckmaster 2009; Zhang et al. 2009). Although interneuronal inhibition underlies generation of brain rhythms and regulates network activity levels (Buzsaki 2006), whether interneuronal inhibition shows early changes after SE remains untested.

Fast-spiking basket cells (FS-BCs), a class of interneurons with perisomatic projections, are critical for maintaining the low excitability and sparse firing of dentate granule cells and contribute to feedforward and feedback dentate inhibition (Ewell and Jones 2010; Kraushaar and Jonas 2000). Dentate FS-BCs express the calcium-binding protein parvalbumin (PV), have a characteristic high-frequency nonadapting firing pattern (Harney and Jones 2002; Hefft and Jonas 2005), and are interconnected through high-fidelity GABAergic synapses (Bartos et al. 2001). Apart from synaptic $GABA_A$ receptors ($GABA_ARs$), granule cells and certain interneurons express extra- and perisynaptic high-affinity $GABA_ARs$ that contribute to "tonic" I_{GABA} (Farrant and Nusser 2005; Scimemi et al. 2005). $GABA_ARs$ containing δ-subunits contribute to tonic I_{GABA} in dentate granule cells and molecular layer interneurons (Glykys et al. 2007; Mtchedlishvili and Kapur 2006; Wei et al. 2003). Previous studies have shown that nonprincipal neurons in the dentate hilus express $GABA_AR$ δ-subunits (Peng et al. 2004); however, whether dentate FS-BCs express tonic I_{GABA} is not known. Since tonic I_{GABA} regulates neuronal excitability and can undergo activity-dependent changes during synaptic GABA spillover (Glykys and Mody 2007), the presence of tonic I_{GABA} in FS-BCs will impact their function during network activity. Moreover, FS-BC tonic I_{GABA} may be altered after SE, as has been observed in granule cells (Zhan and Nadler 2009; Zhang et al. 2007).

GABAergic inhibition is hyperpolarizing when E_{GABA} is negative to neuronal resting membrane potential (RMP) and shunting when E_{GABA} is close to RMP. Hippocampal and dentate interneuronal E_{GABA} has been shown to lie positive to RMP, contributing to shunting inhibition (Banke and McBain AQ: 9

*J. Yu and A. Proddutur contributed equally to this work.

Address for reprint requests and other correspondence: V. Santhakumar, Dept. of Neurology and Neurosciences, UMDNJ-New Jersey Medical School, MSB-H-512, 185 S. Orange Ave. Newark, NJ 07103 (e-mail: santhavi@umdnj.edu).

AQ: 9

2006; Vida et al. 2006). Curiously, whether SE alters interneuronal E_{GABA}, as was demonstrated in granule cells (Pathak et al. 2007), is not known. Interactions between GABA conductance (g_{GABA}) and E_{GABA} determine the net effect of tonic I_{GABA} on neuronal excitability (Song et al. 2011). Therefore, we examined whether dentate FS-BCs express tonic I_{GABA} and whether FS-BC tonic I_{GABA} and E_{GABA} are altered 1 wk after SE. Using single-cell models and large-scale network simulations, we characterized how the experimentally identified post-SE changes in FS-BC tonic inhibition influence FS-BC and dentate network activity.

MATERIALS AND METHODS

Pilocarpine status epilepticus. All procedures were performed under protocols approved by the University of Medicine and Dentistry of New Jersey Institutional Animal Care and Use Committee. Pilocarpine injection was performed as previously reported (Zhang et al. 2009). Young adult male Wistar rats between postnatal days 25 and 27 were injected with scopolamine methyl nitrate (1 mg/kg sc) 30 min before pilocarpine injection. SE was induced by injection of pilocarpine (300 mg/kg ip). After 1 h and 30 min of continuous stage 3 or greater seizures (Racine scale), diazepam (10 mg/kg ip) was administered and repeated as needed to terminate seizures. Control rats received scopolamine pretreatment followed by saline injection (ip) and diazepam after 2 h. Animals were video monitored (continuous video recording for 8 h on the day before experimentation with a PC333HR high-resolution camera coupled to a 4 Channel H.264 Pentaplex Digital Video Recorder) to rule out occurrence of spontaneous seizures. Unless otherwise stated, all anatomical and physiological studies were conducted on seizure-free rats 6–8 days after pilocarpine-SE and in age-matched, saline-injected control rats.

Slice preparation. One week (6–8 days) after saline injection or pilocarpine-induced SE, rats were anesthetized with isoflurane and decapitated. Horizontal brain slices (300 μm for patch clamp and 400 μm for field experiments) were prepared in ice-cold sucrose-artificial cerebrospinal fluid (sucrose-aCSF) containing (in mM) 85 NaCl, 75 sucrose, 24 $NaHCO_3$, 25 glucose, 4 $MgCl_2$, 2.5 KCl, 1.25 NaH_2PO_4, and 0.5 $CaCl_2$ with a Leica VT1200S Vibratome (Wetzlar, Germany). The slices were sagittally bisected and incubated at 32 ± 1°C for 30 min in a submerged holding chamber containing an equal volume of sucrose-aCSF and recording aCSF and subsequently held at room temperature (RT). The recording aCSF contained (in mM) 126 NaCl, 2.5 KCl, 2 $CaCl_2$, 2 $MgCl_2$, 1.25 NaH_2PO_4, 26 $NaHCO_3$, and 10 D-glucose. All solutions were saturated with 95% O_2-5% CO_2 and maintained at a pH of 7.4 for 1–6 h.

In vitro electrophysiology. For patch-clamp recordings, slices (300 μm) were transferred to a submerged recording chamber and perfused with oxygenated aCSF at 33 ± 1°C. Whole cell voltage- and current-clamp recordings from interneurons at the border of the hilus and granule cell layer were performed with IR-DIC visualization techniques with a Nikon Eclipse FN-1 microscope, using a ×40 water-immersion objective. Recordings were obtained with Axon Instruments MultiClamp 700B (Molecular Devices, Sunnyvale, CA). Data were low-pass filtered at 3 kHz, digitized with DigiData 1440A, and acquired with pCLAMP 10 at 10-kHz sampling frequency. Tonic and synaptic I_{GABA} were recorded in perfusing aCSF containing the glutamate receptor antagonist kynurenic acid (KyA, 3 mM; Tocris, Ellisville, MO). No additional GABA was included in the recording solution. Except in experiments presented in Fig. 5*D*, GABA transporter antagonists were not included in the recording solution. Recordings were obtained with microelectrodes (5–7 MΩ) containing (in mM) 125 KCl, 10 K-gluconate, 10 HEPES, 2 $MgCl_2$, 0.2 EGTA, 2 Na-ATP, 0.5 Na-GTP, and 10 phosphocreatine titrated to a pH of 7.25 with KOH. Biocytin (0.2%) was included in the internal solution for post hoc cell identification (Santhakumar et al. 2010). Recorded neurons were initially held at −70 mV, and the responses to 1.5-s positive and negative current injections were examined to determine active and passive characteristics. Cells with nonadapting, high-frequency firing for the entire duration of the current injection and low input resistance (R_{in}) (<150 MΩ) were classified as FS-BCs (Hefft and Jonas 2005). Neurons with adapting firing, high R_{in} (>150 MΩ), and sag during negative current injection were considered non-fast-spiking interneurons (non-FS-INs) (Hefft and Jonas 2005). Post hoc biocytin immunostaining and morphological analysis were used to definitively identify FS-BCs included in this study, on the basis of presence of axon terminals in the granule cell layer. After current-clamp recordings, cells were held in voltage clamp at −70 mV for analysis of GABA currents. Tonic I_{GABA}, steady-state currents blocked by the $GABA_AR$ antagonist SR95531 (10 μM), was measured as described previously (Gupta et al. 2012) with custom macros in IGOR Pro 7.0 software (WaveMetrics, Lake Oswego, OR). Briefly, the magnitude of tonic I_{GABA} was calculated by plotting all-point histograms of relevant 30-s segments of data. These data were fit to Gaussian equations, constraining fits to values two bins more negative than the peak. This ensured that the tail of higher-amplitude values [representing spontaneous inhibitory postsynaptic currents (sIPSCs)] did not influence the fit (Santhakumar et al. 2006, 2010). Recordings were discontinued if series resistance increased by >20%. Cell capacitance was measured with the automated function in Multiclamp 700B. In some experiments, 4,5,6,7-tetrahydroisoxazolo[5,4-*c*]pyridin-3-ol (THIP, 1 μM), a selective $GABA_AR$ agonist with a preference for δ-subunit-containing $GABA_ARs$ (Brown et al. 2002), or the GABA transporter-1 uptake inhibitor 1-[2-[[(diphenylmethylene)imino]oxy]ethyl]-1,2,5,6-tetrahydro-3-pyridinecarboxylic acid hydrochloride (NO-711, 10 μM) was included in the external solution. Individual sIPSCs were detected with custom software in IGOR Pro 7.0 (Gupta et al. 2012; Santhakumar et al. 2010). Events were visualized, and any "noise" that spuriously met trigger specifications was rejected. Cumulative probability plots of sIPSC parameters were constructed with IGOR Pro by pooling an equal number of sIPSCs from each cell.

Gramicidin-perforated-patch recordings were performed to prevent alteration of the intracellular chloride concentration by the pipette solution (Ebihara et al. 1995). Intracellular solution contained (mM) 135 KCl, 0.5 $CaCl_2$, 5 Na_2EGTA, 10 HEPES, 2 $MgCl_2$, and 2 Mg ATP, with 0.2% biocytin, pH set to 7.2 with KOH and gramicidin D (100 μg/μl with 1% DMSO final concentration). Electrode tips were filled with gramicidin-free internal solution and back-filled with the solution containing gramicidin D. On formation of a tight seal, responses to positive and negative current injections were recorded in cell-attached mode for physiological identification. A cocktail containing tetrodotoxin (TTX, 1 μM), 6,7-dinitroquinoxaline-2,3-dione (DNQX, 20 μM), and D-(−)-2-amino-5-phosphonopentanoic acid (APV, 50 μM) (Tocris), to block Na^+ channels, AMPA receptors, and NMDA receptors, was used to isolate I_{GABA}. Perforated-patch recordings were obtained after series resistance had stabilized between 80 and 100 MΩ, ~40 min after patch formation. Series resistance was monitored at 2-min intervals, and data were rejected when resistance suddenly decreased, indicating rupture of the perforated patch. In some initial experiments Alexa Fluor 488 (50–100 μM) was included in the pipette to confirm that the change in resistance was a reliable and adequate indicator of patch rupture. A Picospritzer (PMI-100, Dagan) was used to apply GABA (100 μM, containing blockers of synaptic transmission mentioned above) at 10 psi from a pipette resting 10–20 μm above the slice at the position of the recorded soma. Voltage ramps −130 to +10 mV over 200 ms applied from a holding potential of −60 mV in the absence and presence of GABA were used to determine E_{GABA}. The membrane voltage at which the current traces, obtained in the presence and absence of GABA, crossed was measured as the apparent E_{GABA} (Billups and Attwell 2002). RMP was measured as the potential at which holding current = 0 pA. All measurements were corrected for a liquid junction potential and

AQ: 4

voltage drop across series resistance. In a subset of cells, E_{GABA} was also estimated by systematically varying the steady-state holding potential and estimating the reversal potential of GABA-evoked currents (Verheugen et al. 1999). After rupture of the patch, cells were filled and processed for biocytin immunostaining and morphological identification. Cells in which the access after patch rupture was inadequate were repatched with a gramicidin-free internal solution for biocytin fill. Tight-seal cell-attached recordings were obtained from FS-BCs with electrodes containing the gramicidin-free KCl-based internal solution in standard aCSF. Recordings were obtained in current-clamp mode with zero current injection. At the end of the recordings, the patch was ruptured to gain whole cell access for physiological identification and biocytin filling for post hoc morphological identification.

Field recordings were performed in an interface recording chamber (BSC2, AutoMate Scientific, Berkeley, CA) perfused with aCSF. Brain slices (400 μm) rested on filter paper and were stabilized with platinum wire weights. The tissue was continuously superfused with humidified 95% O_2-5% CO_2, and the temperature of the perfusing solution was maintained at 34°C with a proportional control heating unit (PTC03, AutoMate Scientific). Field recordings of evoked population spikes in the granule cell layer of the dentate gyrus were obtained with patch pipettes filled with recording aCSF. To evoke the field responses, constant-current stimuli (0.5–4 mA, 50 μs) were applied at 0.1 Hz through a bipolar 90-μm tungsten stimulating electrode placed in the perforant path, at the junction of the dorsal blade and the crest just outside the fissure where it was visualized as a fiber tract (Gupta et al. 2012; Santhakumar et al. 2001), and coupled to a high-voltage stimulus isolator (A365R, WPI, Sarasota, FL). Recordings were obtained with an AxoPatch200B amplifier, filtered at 4 kHz with a Bessel filter, and digitized at 10 kHz with a DigiData 1440A analog-digital interface (Molecular Devices). The field responses in the granule cell layer were measured at five predetermined points in each slice (Santhakumar et al. 2000), including the tips of the dorsal and the ventral blades, the middle of the dorsal and ventral blades, and the middle of the crest, and the largest response was studied further. All salts were purchased from Sigma-Aldrich (St. Louis, MO).

Anatomical methods. NeuN staining was performed on sections from rats perfused with 4% paraformaldehyde 1 wk after pilocarpine-induced SE and from age-matched, saline-injected control rats. Sections (40 μm) were incubated overnight at RT with anti-NeuN antibody (MAB377, 1:10,000, mouse monoclonal; Millipore) in 0.3% Triton X-100 and 2% normal goat serum (NGS) in phosphate-buffered saline (PBS). Sections were reacted with Alexa Fluor 594-conjugated goat anti-mouse secondary to reveal staining. Quantification was performed on every 11th section along the septo-temporal extent of the hippocampus. Cell counts were performed with the optical fractionator of Stereo Investigator V.10.02 (MBF Bioscience, Williston, VT) on an Olympus BX51 microscope with a ×100 oil objective. In each section, the hilus was outlined by a contour traced with a ×10 objective. Sampling parameters were set at 100×: counting frame = 50 μm × 50 μm, dissector height = 30 μm, and top guard zone = 5 μm. Approximately 25 sites per contour were selected with randomized systematic sampling protocols in Stereo Investigator (West et al. 1991).

Immunohistological studies were performed in rats perfused 1 wk after SE and in age-matched control rats. Sections were selected at random from the entire septo-temporal extent of the hippocampus. Sections were processed for antigen retrieval in a water bath (Peng et al. 2004). Briefly, free-floating sections were incubated in 0.05 M sodium citrate solution, pH 6.0 at RT (30 min), and subsequently heated in a water bath at 90°C for 30 min. Sections were allowed to cool at RT for 30 min and rinsed in PBS. Sections were processed for double immunofluorescence labeling for $GABA_AR$ δ-subunit or KCC2 and PV. After antigen retrieval, sections were blocked with 10% NGS and 0.3% Triton X-100 in PBS at RT for 1 h and incubated in a solution containing rabbit anti-δ (1:200; 868-GDN, Phospho-Solutions) and monoclonal mouse anti-PV (1.5:1,000; 235, Swant) in PBS with 0.3% Triton X-100 and 2% NGS at RT for 24 h. Sections were rinsed in PBS and incubated at 4°C for 24 h in a mixture of goat anti-rabbit IgG conjugated to Alexa Fluor 488 (1:250) to reveal $GABA_AR$ δ-subunit and goat anti-mouse labeled with Alexa Fluor 594 (1:500) to reveal PV. Similar procedures were used to examine double labeling for KCC2 and PV with polyclonal rabbit anti-KCC2 (1:200; Millipore) and monoclonal mouse anti-PV (1.5:1,000; 235, Swant) and appropriate secondary antibodies. Sections were rinsed in PBS and mounted with Vectashield (Vector Labs). Controls in which primary antibody was omitted were routinely included. Additionally, sections from mice lacking the $GABA_AR$ δ-subunit (*Gabrd*$^{-/-}$ mice, a generous gift from Dr. Jamie Maguire, Tufts University) were used to confirm specificity of the $GABA_AR$ δ-subunit primary antibody. Double labeling was quantified in the granule cell layer and 100 μm of the subgranular region of the hilus. The region of interest (ROI) was outlined by a contour traced with a ×10 objective. Sampling parameters were set at 100×: counting frame = 100 μm × 60 μm, dissector height = 30 μm, and guard zones = 5 μm. In each section, an observer marked the outline of PV-positive (PV+) somata in the ROI under epifluorescence illumination and a ×100 oil objective and switched filters to visually examine the expression of $GABA_AR$ δ-subunit in the PV-labeled soma. Neurons were deemed colabeled if the staining for $GABA_AR$ δ-subunit shared the outline of the PV-labeled soma and had a greater intensity than the hilar neuropil. The percentage of PV-labeled cells that were colabeled for $GABA_AR$ δ-subunit was determined. Single-plane confocal images for illustration were obtained with a Nikon A1R laser confocal microscope with a ×60 water objective and identical camera settings. Semiquantitative analysis of $GABA_AR$ δ-subunit and KCC2 fluorescence intensity in PV+ neurons was performed on images from an equal number of randomly selected PV+ neurons in the hilar-granule cell layer border from each section. Images were obtained with a Nikon A1R laser confocal microscope with a 1.2 NA ×60 water objective with identical camera settings and converted to RGB color mode. An ROI was traced around PV+ neurons (in the red channel), and the average grayscale intensity of $GABA_AR$ δ-subunit was determined in the green channel (δ-subunit). For estimation of KCC2 fluorescence intensity in PV+ neurons, the ROI was confined to the periphery of the PV-labeled profile in order to assess membrane expression of KCC2. Image analysis was performed with ImageJ v1.43u (National Institutes of Health) by an investigator blind to the treatment.

After physiological recordings, slices were fixed in 0.1 M phosphate buffer containing 4% paraformaldehyde at 4°C for 2 days. For post hoc immunohistochemistry, thick slices (300 μm) were incubated overnight at RT with anti-PV antibody (PV-28, 1.5:1,000, polyclonal rabbit, Swant) in 0.3% Triton X-100- and 2% NGS-containing PBS. Immunoreactions were revealed with Alexa Fluor 488-conjugated secondary goat antibodies against rabbit IgG (1:250), and biocytin staining was revealed with Alexa Fluor 594-conjugated streptavidin (1:1,000). Sections were visualized and imaged with a Nikon A1R laser confocal microscope with a 1.2 NA ×60 water objective. As a result of prolonged recordings and use of high-chloride internal solution, few cells showed somatic labeling for PV. When present, the expression of PV in the soma or dendrites was used as an added confirmation of cell identity. Cell reconstructions and morphological analyses were performed with Neurolucida V.10.02 (MBF Bioscience) and confocal image stacks.

Computational modeling. Single FS-BC models and dentate network simulations were implemented with the NEURON 7.0 simulation environment (Hines and Carnevale 1997). The biophysically realistic FS-BC model was adapted from earlier studies (Dyhrfjeld-Johnsen et al. 2007; Santhakumar et al. 2005) and included a soma and two apical and basal dendrites each with four distinct compartments (a total of 17 compartments). Active and passive conductances were distributed as detailed previously (Santhakumar et al. 2005).

Sodium and fast delayed-rectifier potassium channels were restricted to the soma and proximal dendrites. Reversal potential of a nonspecific leak channel was set to −75 mV to modify the basket cell RMP to match the data from perforated-patch recordings in the present study. Conductance of the nonspecific leak channel was not altered. Tonic g_{GABA} was modeled as a linear deterministic leak conductance with reversal (E_{GABA}) based on experimental data: −74 mV or −54 mV. Tonic g_{GABA} was distributed uniformly in all compartments and varied from 0 to 0.1 mS/cm^2. In some simulations, tonic g_{GABA} was restricted to the soma and proximal dendrite to determine whether the distribution of tonic g_{GABA} altered the magnitude of tonic I_{GABA} or R_{in} in model FS-BCs. In simulations performed to examine the biologically relevant range of tonic g_{GABA} (see Fig. 10*B*), FS-BCs were simulated with a somatic voltage clamp and E_{GABA} was set to 0 mV to model symmetrical chloride of our physiological recordings. Model FS-BCs were voltage clamped at −70 mV, tonic g_{GABA} was varied between 0 and 5 mS/cm^2, and tonic I_{GABA} was measured as the difference in baseline current in the presence and absence of tonic g_{GABA}. R_{in} was measured in response to −100-pA current injection. To examine the effect of tonic I_{GABA} on neuronal excitability, model FS-BCs were activated by identical 200-Hz Poisson-distributed trains of excitatory synaptic inputs to the apical distal dendrites. Excitatory synaptic parameters were based on AMPA conductances in previous studies (Santhakumar et al. 2005), with the synaptic AMPA conductance (g_{AMPA}) set at 3 nS to simulate low activity levels and g_{AMPA} = 20 nS to simulate high activity levels. The effect of increasing tonic g_{GABA} on evoked firing of the model FS-BC was examined with E_{GABA} set at −74 mV (control) and −54 mV (after SE).

The large-scale, topologically and biophysically constrained model network used in this study was adapted from the 500-cell network described by Santhakumar et al. (2005) and expanded to include 1,000 granule cells, 30 mossy cells, 12 basket cells, and 12 hilar interneurons. The multicompartmental single-cell models, distribution and magnitude of active and passive properties, and synaptic conductances were based on Santhakumar et al. (2005) and were derived from anatomical and physiological data in the literature. The networks were topographically constrained, incorporating the axon distribution of the cell types, and simulated by distributing the neurons in a ring structure to avoid edge effects. Enhanced excitability in the early post-SE condition was modeled by including mossy fiber sprouting, simulated by adding synaptic connections from granule cells to the proximal dendrites of granule cells. Since the simulations were designed to test early stages of network excitability (1 wk after SE), the degree of mossy fiber sprouting in the model was set at 20% of the maximal sprouting observed in the pilocarpine model of epilepsy (Dyhrfjeld-Johnsen et al. 2007). In a second set of simulations, both sprouting and hilar neuronal loss were simulated with 20% sprouting as detailed above and a corresponding deletion of 20% of randomly selected hilar mossy cells and dendritically projecting interneurons as described in earlier studies (Santhakumar 2008; Santhakumar et al. 2005). Network models were simulated with 2.5-Hz spontaneous activity in all 1,000 granule cells during the entire duration of the simulation (3,500 ms). Spontaneous activity was simulated as independent Poisson-distributed spike trains to the perforant path input (Dyhrfjeld-Johnsen et al. 2007). A single, synchronous synaptic input to 100 granule cells and 2 local basket cells (at t = 2,001 ms) was used to simulate focally evoked network firing. The basket cell models (and only basket cell models) included tonic g_{GABA} (described above in the single-cell model) distributed uniformly and in all compartments. In networks simulated with control GABA reversal, E_{GABA} of both tonic and synaptic GABA currents in all model FS-BCs was set to −74 mV. Similarly, networks with the post-SE depolarized GABA reversal were simulated with E_{GABA} for tonic and synaptic GABA currents in basket cells set to −54 mV. In a subset of simulations including sprouting and hilar cell loss (see Fig. 11*E*), E_{GABA} of synaptic and tonic g_{GABA} were set to different values. The E_{GABA} at GABA synapses on other neurons was not altered. Simulations included "synaptic spillover," modeled to simulate increases in tonic g_{GABA} that accompany increases in extracellular GABA levels during neuronal activity (Glykys and Mody 2007). Spillover was modeled by including three "spillover GABA conductances" with progressively decreasing amplitudes associated with each inhibitory synaptic connection to model FS-BCs. The spillover GABA conductances were modeled as synapses with slower rise (7 ms) and decay time (200 ms) constants (Rossi et al. 2003) and had 20%, 10%, and 5% of the peak conductance of the primary synapse. The effect of basket cell g_{GABA} and E_{GABA} on the average frequency of granule cell spontaneous activity and evoked activity were quantified during 1,000–2,000 ms and 2,001–3,500 ms, respectively. In initial simulations, instantiation of the network connections was randomized within preset topological constraints. Each set of simulations was run multiple times, and summary data are presented as means ± SE. In some simulations the random seed of the network connectivity was set to a specific value, and the effect of tonic g_{GABA} and E_{GABA} on dentate excitability was compared in structurally identical networks.

Analysis and statistics. Statistical analysis was performed by paired and unpaired Student's *t*-test (Microsoft Excel 2007) or Kolmogorov-Smirnov (K-S) test (in IGOR Pro 7.0) for data that were not distributed normally or univariate and multivariate repeated-measures ANOVA (Systat) for experiments involving repeated measurements from the same sample. Significance was set to $P < 0.05$. Data are shown as mean ± SE or median and interquartile range (IQR) where appropriate.

RESULTS

Early dentate cell loss and enhanced excitability in young adult rats after status epilepticus. A single episode of SE following injection of pilocarpine leads to development of recurrent spontaneous seizures and has been used to model acquired epilepsy. In adult rats, pilocarpine-induced SE replicates the characteristic hippocampal cell loss and network reorganization observed in epileptic patients. The presence and extent of cell loss in younger rats may be variable (Raol et al. 2003). Therefore, we performed NeuN staining for neuronal nuclei in tissue from control rats and those subjected to SE to examine whether SE in the young adult rats (postnatal days 25–27) used in the present study resulted in dentate hilar cell loss. As illustrated in Fig. 1, comparison of sections prepared 1 wk after pilocarpine-induced SE (post-SE) and from age-matched saline-injected control rats revealed a significant decrease in NeuN-stained neurons in the dentate hilus after SE (Fig. 1, *A* and *B*; control: 377.5 ± 40.4 hilar neurons counted/section, a total of 4,251 cells counted in 15 sections from 3 rats; post-SE: 225.7 ± 18.8 hilar neurons counted/section, based on 2,789 cells counted in 15 sections from 3 rats; 40.2 ± 5.0% decrease, $P < 0.05$, Student's *t*-test) consistent with observations in previous studies (Kobayashi et al. 2003; Mello et al. 1993; Zhang et al. 2012). Additionally, hippocampal sections from rats 1 wk after SE but not control rats had degenerating neurons stained by Fluoro-Jade C in CA1 and CA3 (data not shown), as observed in previous studies (Ekstrand et al. 2011). These data demonstrate that the young adult rats used in the present study show hilar cell loss within a week after SE. Previous studies have identified changes in dentate excitability and granule cell inhibition 1–2 wk after SE and prior to onset of epileptic seizures (Pathak et al. 2007). We examined the population spike (Fig. 1*C*) of dentate granule cells in response to perforant path stimulation to determine whether dentate network excitability was altered 1 wk after SE. Field recordings showed that the amplitude of the afferent-evoked granule cell population spike was enhanced 1 wk

F1

AQ: 7

COLOR

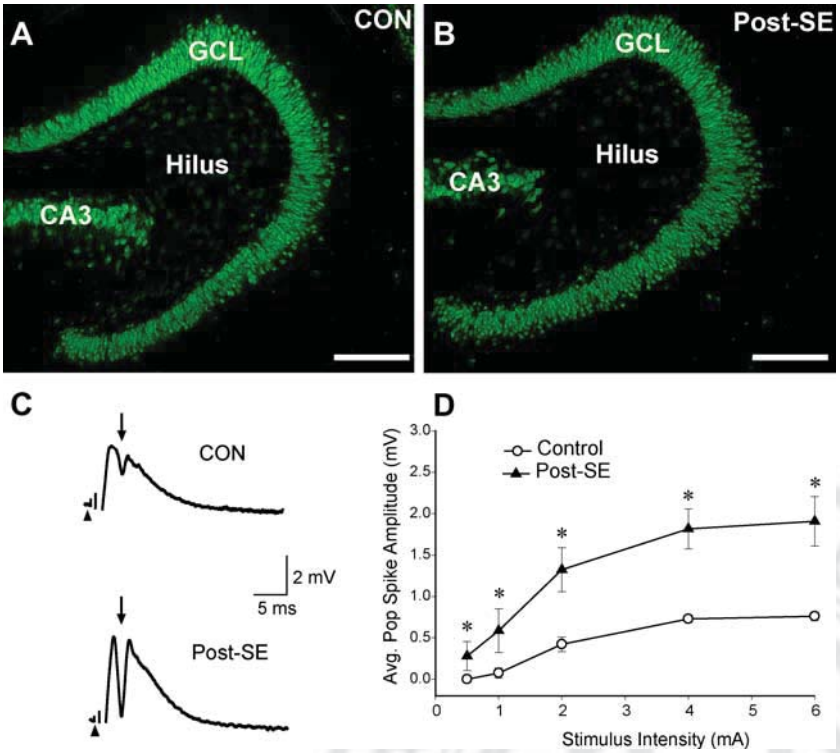

Fig. 1. Early changes in dentate network function after pilocarpine-induced status epilepticus (SE). *A* and *B*: photomicrographs of NeuN-stained sections obtained from rats perfused 1 wk after saline injection or pilocarpine-induced SE demonstrate the presence of numerous NeuN-stained hilar neurons in the section from the control (*A*) and fewer hilar NeuN-stained neurons in a level-matched post-SE section (*B*). GCL, granule cell layer. Scale bars, 200 μm. *C*: representative traces of granule cell field responses evoked by perforant path stimulation in slices from control (*top*) and 1 wk after SE (*bottom*) illustrate the larger population spike amplitude in the post-SE dentate. Traces are an average of 4 trials in response to a 4-mA stimulus to the perforant path. Arrowheads indicate the location of the truncated stimulus artifact, and arrows point to the population spike. *D*: summary data demonstrate the post-SE increase in dentate-evoked excitability at various stimulation intensities. Error bars indicate SE. $^*P < 0.05$ by repeated-measures ANOVA.

after SE compared with age-matched control rats (Fig. 1*C*). Summary data demonstrate the post-SE increase in dentate population spike amplitude at various stimulation intensities [Fig. 1*D*; control: $n = 8$ slices from 4 rats, post-SE: $n = 13$ slices from 6 rats; $F_{(1,19)} = 8.93$, $P < 0.05$ by univariate repeated-measures ANOVA]. Even when the population spike amplitude was normalized by the simultaneously recorded field excitatory postsynaptic potential (fEPSP) slope, to account for differences in effective excitatory synaptic drive in response to stimulation, the fEPSP-normalized population spike amplitude was significantly greater in slices from post-SE rats [$F(_{1,19}) = 4.8$, $P < 0.05$ by repeated-measures ANOVA]. Since identifying early SE-induced changes in dentate inhibition can provide mechanistic insights into dentate physiology in the latent period leading up to spontaneous seizures, we focused on inhibitory plasticity of perisomatically projecting PV-expressing basket cells 1 wk after SE.

$GABA_AR$ δ-subunits are expressed in parvalbumin-positive dentate interneurons. In dentate granule cells, SE leads to alterations in synaptic and extrasynaptic $GABA_AR$ expression and in synaptic and tonic I_{GABA} (Mtchedlishvili and Kapur 2006; Peng et al. 2004; Zhan and Nadler 2009; Zhang et al. 2007). Hippocampal and dentate interneurons appear to express $GABA_ARs$ underlying tonic I_{GABA} and demonstrate tonic I_{GABA} (Glykys et al. 2007; Semyanov et al. 2003; Song et al. 2011). Studies in mice have revealed that $GABA_AR$ δ-subunits, known to underlie tonic I_{GABA}, are expressed in presumed interneurons in the hilar-granule cell layer border (Peng et al. 2004). However, whether perisomatically projecting basket cells, which express PV and are critical for rapid and precise inhibition (Freund 2003; Hefft and Jonas 2005), express $GABA_AR$ δ-subunits has not been determined. Confocal images of hippocampal sections, obtained from rats 1 wk after saline injection or pilocarpine-induced SE and immunostained for PV and $GABA_AR$ δ-subunits, showed that PV-labeled neurons in the hilar-granule cell layer border (Fig. 2, *A–D*, *right*) consistently demonstrated somatic labeling for $GABA_AR$ δ-subunits (Fig. 2, *A* and *C*, *center*). The intense $GABA_AR$ δ-subunit labeling of granule cell dendrites made it difficult to isolate $GABA_AR$ δ-subunit labeling of PV+ dendrites in the molecular layer. However, PV+ dendrites in the hilus of both the control (Fig. 2*B*) and post-SE (Fig. 2*D*) rats showed distinct colabeling for $GABA_AR$ δ-subunit, consistent with somato-dendritic staining for $GABA_AR$ δ-subunit observed in other neuronal types (Olah et al. 2009; Zhang et al. 2007). Absence of immunostaining in sections from *Gabrd*$^{-/-}$ mice lacking the $GABA_AR$ δ-subunit was used to confirm specificity of the $GABA_AR$ δ-subunit primary antibody (data not shown). As illustrated by the summary plots, 99.1 ± 0.9% of the 115 PV+ neurons from control rats (18 slices from 3 rats) and 97.1 ± 2.9% of the 120 PV+ neurons from post-SE rats (18 slices from 3 rats) in the hilar-granule cell layer border (see MATERIALS AND METHODS) were colabeled for $GABA_AR$ δ-subunit (Fig. 2*E*). The proportion of PV+ neurons labeled for the $GABA_AR$ δ-subunit was not altered after SE (Fig. 2*F*; $P > 0.05$ by Student's *t*-test). However, quantification of the fluorescence intensity for $GABA_AR$ δ-subunit expression in PV-labeled neurons from control and post-SE rats revealed a significant increase in expression of $GABA_AR$ δ-subunit after SE (Fig. 2*F*; grayscale intensity in arbitrary units: control 14.7 ± 5.7, $n = 65$ cells from 3 rats; post-SE 24.2 ± 15.8, $n = 70$ cells from 3 rats, $P < 0.05$ by Student's *t*-test). These data demonstrate expression and post-SE enhancement of $GABA_AR$ δ-subunits in PV+ interneurons in the hilar-granule cell layer border.

Expression of tonic GABA currents in dentate fast-spiking basket cells. In light of our immunostaining data demonstrating the expression of $GABA_AR$ δ-subunits in PV+ interneurons (Fig. 2), we examined whether PV+ basket cells express functional tonic I_{GABA}. Dentate PV+ basket cells can be distinguished from the other interneurons in the hilar-granule cell

tapraid4/z9k-neurop/z9k-neurop/z9k00713/z9k1866d13z | xppws | S=1 | 2/12/13 | 7:01 | MS: JN-00891-2012 | Ini: 04/sa/ss

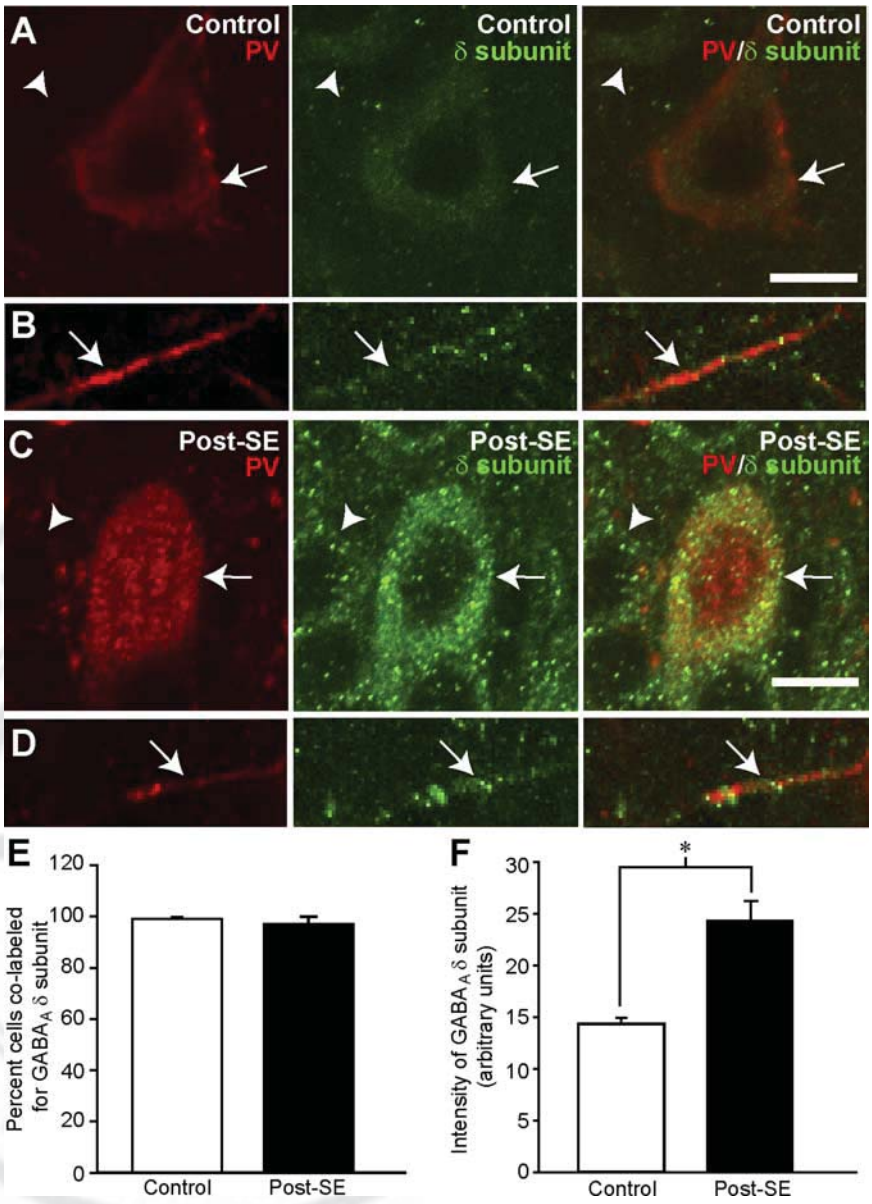

COLOR

Fig. 2. $GABA_A$ receptor ($GABA_AR$) δ-subunit expression in parvalbumin (PV) interneurons. *A–D*: confocal images from a slice labeled for PV (*left*) and $GABA_AR$ δ-subunit (*center*). Merged images (*right*) show colabeling of PV and $GABA_AR$ δ-subunit in soma (*A*) and a hilar dendrite (*B*) from a control rat and soma (*C*) and a hilar dendrite (*D*) from a post-SE rat. Arrows indicate colabeled cells, and arrowheads point to cells expressing $GABA_AR$ δ-subunit not labeled for PV. Scale bars (10 μm) in *A* and *C* apply to *A–D*. *E*: summary data show % of PV+ neurons in the hilar-GCL border colabeled for $GABA_AR$ δ-subunit. *F*: histogram of fluorescence intensity for $GABA_AR$ δ-subunit staining in the somata of PV+ neurons from control and post-SE rats.

layer border on the basis of their characteristic morphological and physiological properties. Previous studies have established that dentate PV+ basket cells have axon collaterals largely localized in the granule cell layer, whereas axons of CCK- and somatostatin-expressing interneurons project to the molecular layer (Buckmaster et al. 2002; Hefft and Jonas 2005). Thus the distinctive axonal distribution in the granule cell layer can be used to morphologically identify PV+ interneurons. Apart from morphology, the typical high-frequency, nonadapting firing during depolarizing current injections has been used as a physiological marker of PV+ basket cells (Harney and Jones 2002; Hefft and Jonas 2005; Zhang and Buckmaster 2009). Figure 3*A* illustrates a reconstructed FS-BC with the axon in the granule cell layer. The cell was filled during physiological recordings and processed for post hoc biocytin immunostaining. The FS-BC reconstructed in Fig. 3*A*, *top*, demonstrated characteristic high-frequency, nonadapting firing in response to a 500-pA depolarizing current injection, with low R_{in} and numerous synaptic events during −100-pA hyperpolarizing current injection (Fig. 3*A*, *bottom*, and *insets* in Figs. 4*B* and 5*A*). Additionally, colabeling of the dendrites of the recorded neuron for parvalbumin (Fig. 3*A*, *inset*) confirm the identity of the cell as a PV+ FS-BC. Although our routine immunostaining identified PV labeling in dendrites of biocytin-filled FS-BCs, most FS-BCs did not show somatic labeling for PV. It is likely that the combination of high-chloride internal solution and long-duration recording contributed to the difficulty in detecting somatic PV labeling. Consequently, all FS-BCs in the present study were identified on the basis of a combination of fast-spiking, nonadapting physiology, the presence of axon collaterals in the granule cell layer, and dendritic PV labeling. In addition to FS-BCs, we recorded from non-FS-INs with somata in the hilar-granule cell layer border and axon collaterals distributed in the molecular layer (Fig. 3*B*, *top*). Physiological recordings from the same cell (Fig. 3B, *bottom*) illustrate the adapting firing pattern during positive current injection (+200 pA) and the presence of depolarizing sag and high R_{in} in response to negative current injections (−100 pA).

COLOR

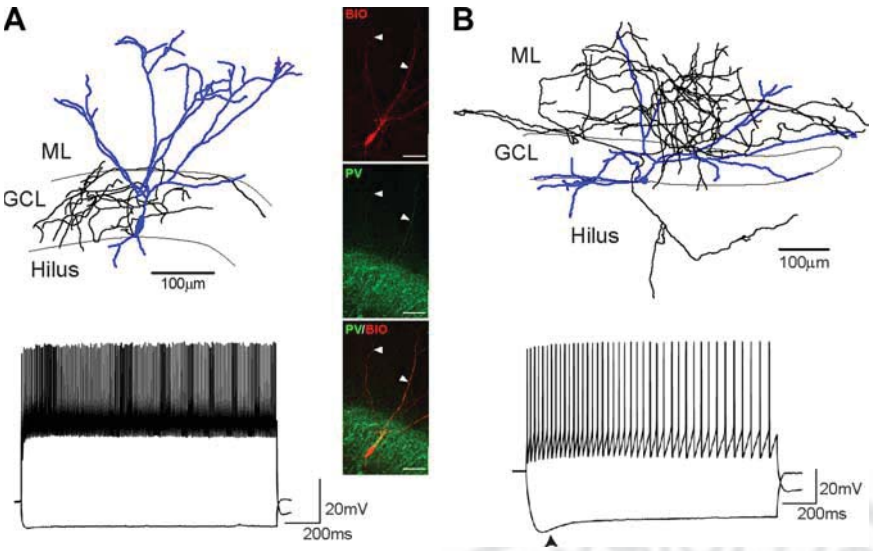

Fig. 3. Morphological and physiological characterization of dentate interneurons projecting to granule cell somata and dendrites. *A*, *top*: reconstruction of a fast-spiking basket cell (FS-BC) filled during recordings shows the typical morphology with soma and dendrites in blue and axon in GCL in black. ML, molecular layer. *Bottom*: membrane voltage traces from the same cell illustrate the fast-spiking, nonadapting firing pattern during a +500 pA current injection and relatively low membrane hyperpolarization in response to a −100 pA current injection. Scale bar, 50 μm. *Inset*: confocal image of biocytin-filled (BIO) soma and dendrites (arrowheads) of the cell in *A* (*top*) and labeling for PV in the dendrites (*middle*); *bottom*: merged image showing PV colabeling in the biocytin-filled dendrites (arrowheads). Scale bar, 100 μm. *B*, *top*: Neurolucida reconstruction of a non-fast-spiking interneuron (non-FS-IN) with axon in the ML. *Bottom*: membrane voltage traces from the same cell show the typical adapting firing during a +200 pA current injection and membrane hyperpolarization and depolarizing sag (arrowhead) during a −100-pA current injection. Note the difference in membrane hyperpolarization in response to −100-pA current injections between the FS-BC (*A*) and non-FS-IN (*B*).

Although the RMPs of FS-BCs and non-FS-INs were not different (RMP in mV: FS-BC −74.0 ± 1.9 in $n = 10$ cells; non-FS-IN −72.3 ± 2.4 in $n = 12$ cells, $P > 0.05$ by Student's *t*-test), the frequency of FS-BC firing in response to a +800-pA current injection was significantly greater (frequency in Hz: FS-BC 112.1 ± 7.9 in $n = 12$ cells; non-FS-IN 52.0 ± 5.7 in $n = 8$ cells, $P < 0.05$ by Student's *t*-test) and the R_{in} lower (R_{in} in MΩ: FS-BC 93.0 ± 10.6 in $n = 12$ cells; non-FS-IN 233.3 ± 6.8 in $n = 8$ cells, $P < 0.05$ by Student's *t*-test) than in non-FS-IN. Together, these morphological and physiological characteristics are consistent with earlier studies (Harney and Jones 2002) and were used to reliably distinguish FS-BCs from a potentially diverse set of non-FS-INs projecting to the molecular layer.

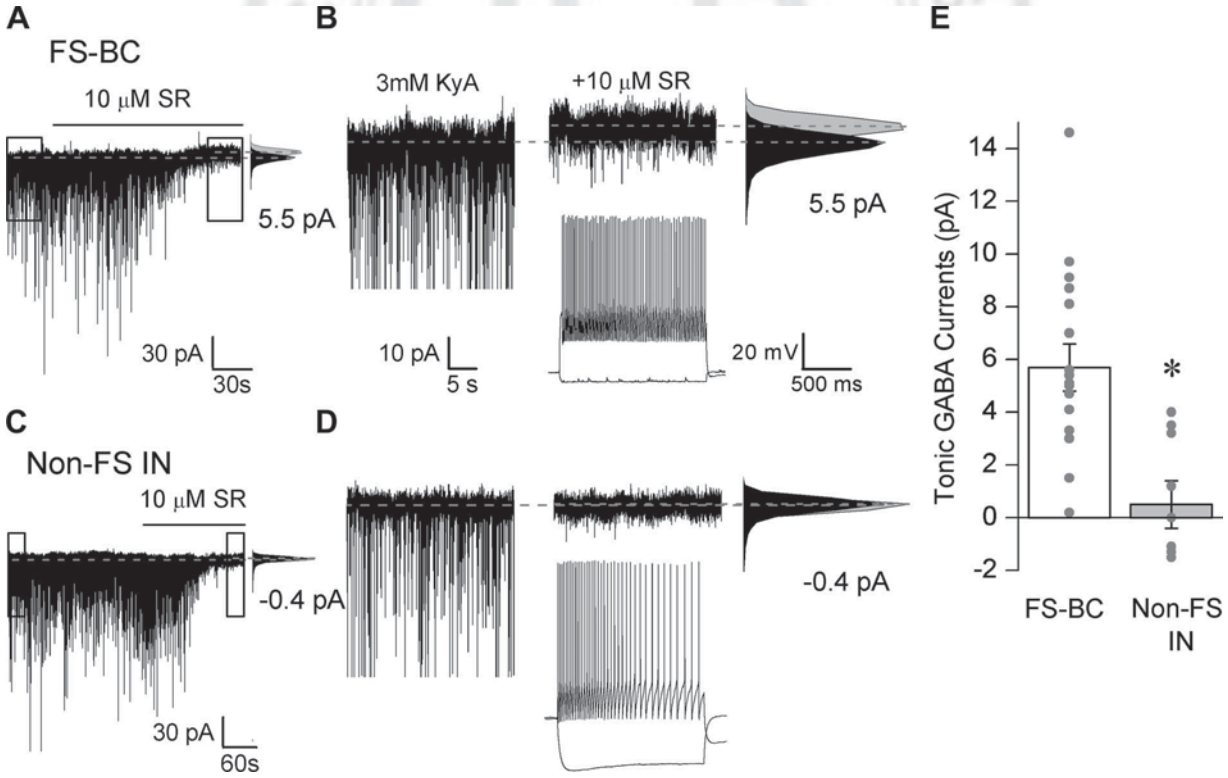

Fig. 4. Expression of tonic GABA currents (I_{GABA}) in dentate FS-BCs. *A*: representative voltage-clamp recordings ($V_{hold} = -70$ mV) from a FS-BC in the hilar-GCL border illustrates the presence of tonic I_{GABA} blocked by SR95531 (gabazine, 10 μM). *B*: expanded 30-s traces of the boxed area in *A*. Gaussian fits to all-points histograms derived from the illustrated recording periods in control conditions, in the presence of 3 mM kynurenic acid (KyA), and after the addition of gabazine used to determine tonic current amplitude are shown on *right*. Dashed lines indicate Gaussian means, and the difference currents are noted. *Inset*: membrane voltage trace from the same cell shows fast-spiking firing. *C*: representative voltage-clamp recordings ($V_{hold} = -70$ mV) from a non-FS-IN in the hilar-GCL border illustrates lack of tonic I_{GABA} on blocking $GABA_AR$ with SR95531 (10 μM). *D*: expanded 30-s traces of the boxed area in *C*. Gaussian fits to all-points histograms used to determine tonic current amplitude are presented on *right*. *Inset*: membrane voltage trace from the cell in *C* and *D* shows adapting firing. *E*: summary data of tonic I_{GABA} amplitude in 3 mM kynurenic acid in FS-BCs and non-FS-IN. Individual data points are represented by gray dots. *$P < 0.05$ by unpaired Student's *t*-test.

tapraid4/z9k-neurop/z9k00713/z9k1866d13z | xppws | S=1 | 2/12/13 | 7:01 | MS: JN-00891-2012 | Ini: 04/sa/ss

We examined interneurons in the hilar-granule cell layer border for the presence of tonic I_{GABA}. Recordings were performed in the presence of the glutamate receptor antagonist KyA (3 mM), and tonic I_{GABA} was measured as the baseline current blocked by the $GABA_AR$ antagonist SR95531 (gabazine, 10 μM). Recordings were obtained at physiological temperature and in the absence of added GABA or GABA transporter inhibitors. As illustrated by representative recordings from an FS-BC in Fig. 4*A* and the magnified 30-s segments of the boxed areas in Fig. 4*A* (Fig. 4*B*), SR95531 caused a small but significant shift in the baseline current, indicating the presence of tonic I_{GABA} in FS-BCs ($P < 0.05$, paired Student's *t*-test). In contrast, non-FS-INs lacked tonic I_{GABA} and showed little shift in baseline after addition of SR95531 (Fig. 4, *C* and *D*; $P > 0.05$, paired Student's *t*-test). On average the magnitude of tonic I_{GABA} in morphologically and physiologically identified FS-BCs was significantly greater than in non-FS-INs (Fig. 4*E*; tonic I_{GABA} in pA: FS-BC 5.7 $\pm$ 0.9, $n = 17$; non-FS-IN: 0.5 $\pm$ 0.9, $n = 9$; $P < 0.05$ by Student's *t*-test). Thus, consistent with the anatomical data showing colabeling of $GABA_AR$ δ-subunits with PV+ interneurons (Fig. 2), our physiological data demonstrate that dentate FS-BCs express tonic I_{GABA}. Additionally, the results demonstrate that the magnitude of tonic I_{GABA} in FS-BCs is greater than in non-FS-INs.

Status epilepticus enhances FS-BC tonic I_{GABA}. Since our immunostaining data (Fig. 2) indicate that the expression of $GABA_AR$ δ-subunits in PV+ interneurons is enhanced 1 wk after SE, we examined whether FS-BC tonic I_{GABA} are increased after SE. In recordings from FS-BCs in control rats, THIP (1 μM), a preferential agonist of $GABA_ARs$ containing δ-subunits (Brown et al. 2002), enhanced tonic I_{GABA}, confirming the contribution of $GABA_AR$ δ-subunits (Fig. 5, *A* and *C*; tonic I_{GABA} in pA: 5.3 $\pm$ 2.0 in KyA and 11.5 $\pm$ 2.7 in THIP, $n = 7$ cells, $P < 0.05$, paired Student's *t*-test). Similarly, THIP enhanced tonic I_{GABA} in FS-BCs from post-SE rats (Fig. 5, *B* and *C*; tonic I_{GABA} in pA: 14.0 $\pm$ 2.1 in KyA and 21.9 $\pm$ 2.1 in THIP, $n = 7$ cells, $P < 0.05$, paired Student's *t*-test). Importantly, the magnitude of FS-BC tonic I_{GABA}, both in KyA and in THIP, was significantly greater in post-SE rats compared with control rats (Fig. 5, *A–C*; $P < 0.05$, *t*-test). Application of THIP (1 μM) caused a significantly greater increase in baseline currents in FS-BCs from post-SE rats (baseline current increase in THIP in pA: control FS-BCs: 6.0 $\pm$ 1.4, $n = 8$ cells; post-SE FS-BCs 10.8 $\pm$ 1.6, $n = 10$ cells, $P < 0.05$ by Student's *t*-test), confirming that increases in membrane expression of $GABA_AR$ δ-subunits contribute to post-SE increase in FS-BC tonic I_{GABA}. To eliminate the possibility that THIP, like GABA, may alter $GABA_AR$ antagonist binding (Bianchi and Macdonald 2001) and confound estimation of tonic I_{GABA}, we also measured tonic I_{GABA} in control aCSF in the presence of KyA and without perfusion of THIP. When normalized to cell membrane capacitance, to eliminate confounding effects due to differences in cell size, tonic I_{GABA} in FS-BCs from post-SE rats was greater than those from control rats (Fig. 5*D*; tonic I_{GABA} current density in pA/pF: control 0.10 $\pm$ 0.02, $n = 11$ cells; post-SE 0.23 $\pm$ 0.05, $n = 7$ cells, $P < 0.05$, Student's *t*-test). Moreover, FS-BC tonic I_{GABA} measured in the presence of the GABA transporter antagonist NO-711 (10 μM), to abolish potential post-SE differences in GABA transporter function, was also enhanced after SE (Fig. 5*E*; tonic I_{GABA} in pA: control 14.7 $\pm$ 2.6, $n = 6$ cells; post-SE 24.6 $\pm$ 3.1, $n = 6$ cells, $P < 0.05$, Student's *t*-test). Comparison of the intrinsic properties measured during whole cell recordings revealed no change in either R_{in} or RMP between FS-BCs from control and post-SE rats (R_{in} in MΩ: control 93.0 $\pm$ 10.6, $n = 12$ cells; post-SE 97.6 $\pm$ 11.2, $n = 9$ cells, $P > 0.05$, Student's *t*-test; RMP in mV: control −74.0 $\pm$ 1.9, $n = 10$ cells; post-SE −75.0 $\pm$ 2.4, $n = 10$ cells, $P > 0.05$, Student's *t*-test). R_{in} was measured in response to a −100-pA current injection. Our measurements of FS-BC tonic I_{GABA} demonstrate, unequivocally, that tonic I_{GABA} is present in FS-BCs and is enhanced after SE. Our results indicate that SE-induced increases in the expression of $GABA_ARs$ with δ-subunits likely contribute to increases in FS-BC tonic I_{GABA} after SE.

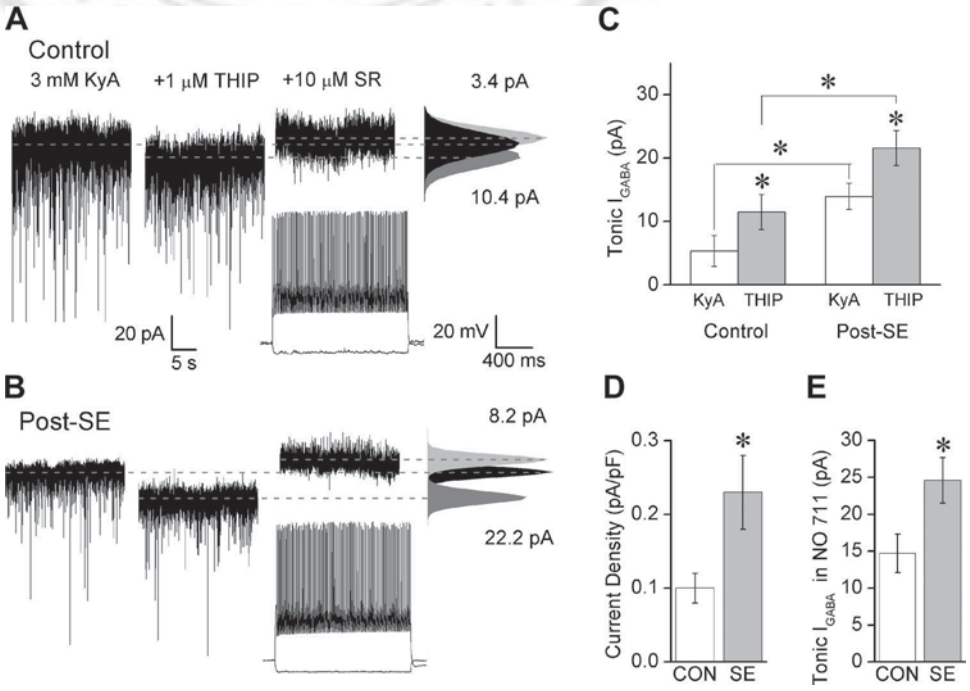

Fig. 5. Tonic I_{GABA} in dentate FS-BCs are enhanced after SE. *A* and *B*: segments (30 s) of representative voltage-clamp recordings (V_{hold} = −70 mV) from control (*A*) and post-SE (*B*) FS-BCs illustrate the enhancement of tonic I_{GABA} by addition of 4,5,6,7-tetrahydroisoxazolo[5,4-*c*]pyridin-3-ol (THIP, 1 μM). Tonic I_{GABA} was measured as the current blocked by SR95531 (10 μM). Panels on *right* show Gaussian fits to all-points histograms of the 30-s recording periods in 3 mM kynurenic acid, after the addition of THIP (1 μM), and in SR95531. Dashed lines indicate Gaussian means, and the difference currents are noted. *Insets*: membrane voltage traces show fast-spiking firing of the respective cells. *C*: summary of the magnitude of FS-BC tonic I_{GABA} in 3 mM kynurenic acid and after perfusion of THIP (1 μM) in controls and after SE. *D*: histogram presents baseline tonic I_{GABA} recorded in 3 mM kynurenic acid normalized to the cell membrane capacitance. *E*: tonic I_{GABA} in control and post-SE FS-BCs measured with the GABA transporter antagonist NO-711 (10 μM) in the presence of 3 mM kynurenic acid. *$P < 0.05$ by paired and unpaired Student's *t*-test.

tapraid4/z9k-neurop/z9k00713/z9k1866d13z | xppws | S=1 | 2/12/13 | 7:01 | MS: JN-00891-2012 | Ini: 04/sa/ss

Spillover of synaptically released GABA into the extrasynaptic space is known to contribute to tonic I_{GABA} (Glykys and Mody 2007). Therefore, one possibility is that the post-SE enhancement of tonic I_{GABA} reflects post-SE increases in synaptic GABA release. Previous studies have demonstrated that in granule cells the frequency of sIPSCs is decreased after SE (Kobayashi and Buckmaster 2003), discounting the possible contribution of enhanced GABA spillover from inhibitory synapses to granule cells. To examine whether increases in synaptic GABA release to FS-BCs could contribute to the observed enhancement of tonic I_{GABA} after SE, we analyzed the frequency of sIPSCs in cells examined for changes in tonic I_{GABA} (in Fig. 5). As illustrated by representative traces (Fig. 6, *A* and *B*), there was a considerable decrease in the frequency of sIPSCs in FS-BCs from post-SE rats (Fig. 6*B*; sIPSC frequency in Hz: control median = 7.0, IQR = 3.7–13.7, mean ± SE = 10.9 ± 0.5, n = 10 cells; post-SE median = 5.0, IQR = 2.6–10.6, mean ± SE = 8.9 ± 0.6, n = 7 cells, $P < 0.05$, K-S test). Additionally, FS-BC sIPSC amplitude was reduced (in pA: control median = 17.7, IQR = 10.6–34.2, mean ± SE 30.3 ± 1.6, n = 10 cells; post-SE median = 14.7, IQR = 8.4–26.2, mean ± SE = 22.5 ± 1.1, n = 7 cells, $P < 0.05$, K-S test) and decay increased (in ms: control median = 3.65, IQR = 2.9–6.1, mean ± SE = 5.4 ± 0.2, n = 10 cells; post-SE median = 4.8, IQR = 3.3–8.5, mean ± SE = 6.3 ± 0.3, n = 7 cells, $P < 0.05$, K-S test) after SE. However, sIPSC charge transfer showed a small but statistically significant decrease after SE (Fig. 6*C*; charge transfer in pA·ms: control median = 83.66, IQR = 52.3–150.2, mean ± SE = 133.24 ± 6.1, n = 10 cells; post-SE median = 75.5, IQR = 48.2–140.8, mean ± SE = 111.138 ± 4.7, n = 7 cells, $P < 0.05$, K-S test). Additionally, THIP (1 μM) caused a small but statistically significant decrease in sIPSC amplitude in both control and post-SE FS-BCs (in pA: control median = 17.7, IQR = 10.6–34.2, mean ± SE = 30.3 ± 1.6, n = 10 cells; THIP median = 15.5, IQR = 8.9–28.8, mean ± SE = 26.1 ± 1.2, n = 10 cells, $P < 0.05$, K-S test; post-SE median = 14.7, IQR = 8.4–26.2, mean ± SE = 22.5 ± 1.1; THIP median = 14.1, IQR = 7.6–23.05, mean ± SE = 17.9 ± 0.7, n = 7 cells, $P < 0.05$, K-S test). Together, the reductions in both FS-BC and granule cell sIPSC frequency after SE argue against the possibility that synaptic spillover underlies post-SE increase in tonic I_{GABA}.

Depolarizing shift in FS-BC E_{GABA} after status epilepticus. The ability of $GABA_AR$ activation to inhibit neuronal excitability depends on a combination of hyperpolarization, when E_{GABA} is negative to neuronal RMP (hyperpolarizing driving force), and shunting inhibition resulting from $GABA_AR$ conductance. E_{GABA} depends on the electrochemical gradients for Cl^- and, to a lesser extent, HCO_3^- ions and can be positive to neuronal RMP during development when intracellular chloride is relatively high (Ben-Ari 2001). Developmental changes in chloride transporters are instrumental in maintaining a hyperpolarizing E_{GABA} in adult neurons (Rivera et al. 2005). However, there may be cell type-specific differences in chloride regulation (Banke and McBain 2006). Remarkably, pilocarpine-induced SE contributes to a depolarizing shift in dentate granule cell E_{GABA} 1 wk after SE (Pathak et al. 2007). Since the net effect of the observed increase in FS-BC tonic I_{GABA} on FS-BC and dentate excitability is likely to depend on whether E_{GABA} is positive or negative to the RMP, we examined whether FS-BC RMP and E_{GABA} are altered after SE.

To avoid perturbations of the intracellular chloride concentration, we used gramicidin-perforated-patch recordings (Billups and Attwell 2002; Pathak et al. 2007) and measured the RMP and reversal potential of GABA-evoked currents in parallel within the same FS-BC. Upon establishment of adequate access (see MATERIALS AND METHODS), we first determined the neuronal firing pattern in response to depolarizing current injections before perfusion of TTX (1 μM) to block action potential generation. Next, in the absence of added GABA, we recorded FS-BCs current responses to −130 to +10 mV voltage ramps from a holding potential of −60 mV (Fig. 7*A*). The potential at which the holding current was 0 pA was measured as the RMP (Fig. 7*A*). In interleaved recordings preformed at 40-s intervals, voltage ramps were repeated

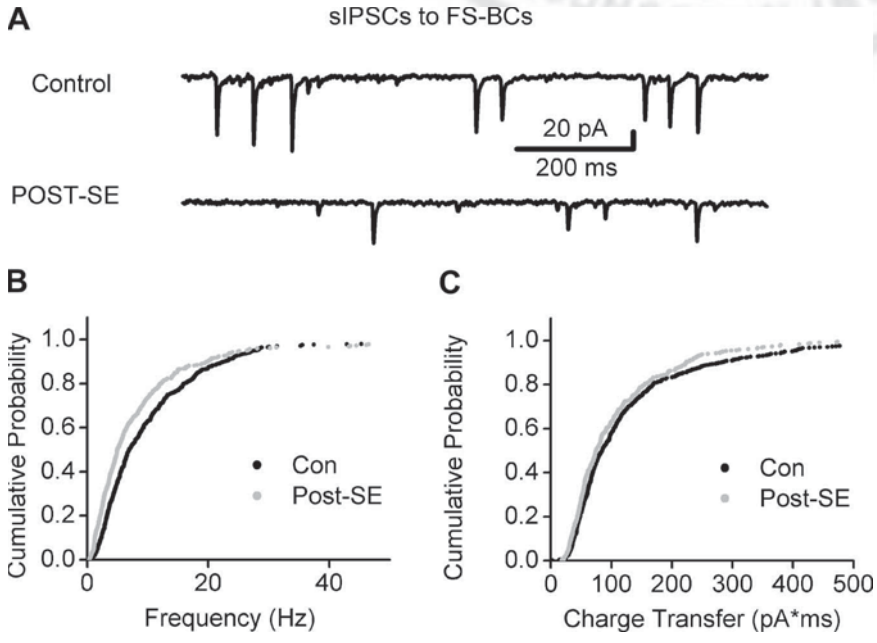

Fig. 6. Decrease in FS-BC spontaneous inhibitory postsynaptic current (sIPSC) frequency after SE. *A*: representative traces of voltage-clamp recordings from control (*top*) and post-SE (*bottom*) FS-BCs show the higher sIPSC frequency in the control FS-BC. Note the decrease in sIPSC frequency in the recording from the post-SE FS-BC. *B* and *C*: cumulative probability plot of the sIPSC instantaneous frequency (*B*) and charge transfer (*C*) in control and post-SE FS-BCs measured with symmetrical chloride from a holding potential of −70 mV in kynurenic acid (3 mM). The same number of individual events was selected from each cell to develop the cumulative probability distribution (control: n = 10 cells; post-SE: n = 7 cells).

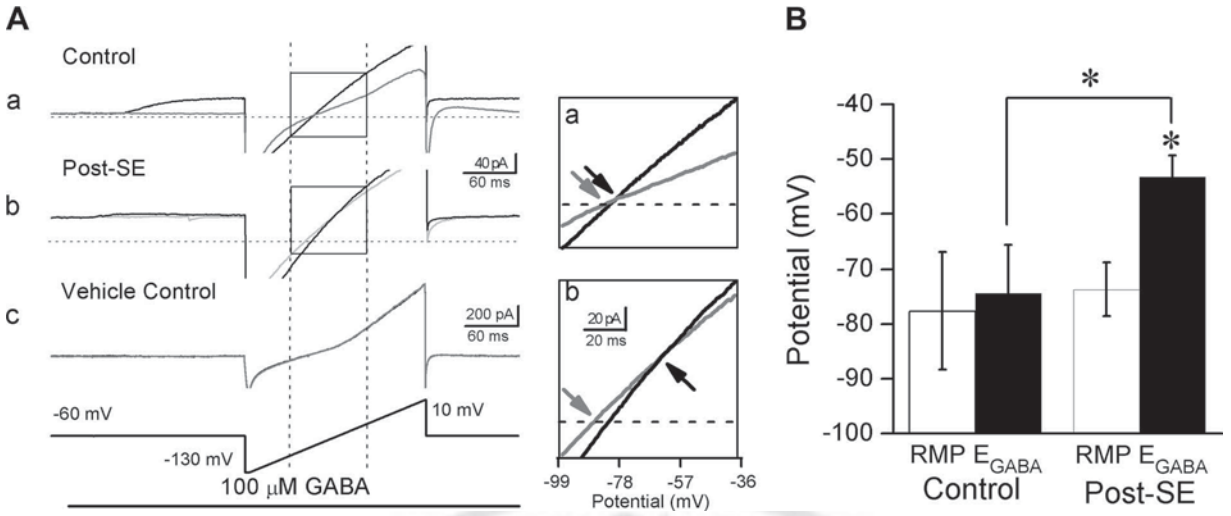

Fig. 7. FS-BC GABA reversal potential (E_{GABA}) is depolarized after status epilepticus. *A*: gramicidin-perforated-patch recordings show current traces from control (*a*) and post-SE (*b*) FS-BCs recorded during depolarizing ramps (*bottom*) in the absence of GABA (gray) and during pressure application of 100 μM GABA (black). Horizontal dashed line represents holding current (I_{hold}) = 0 pA at which resting membrane potential (RMP) was determined (gray arrows in *insets*). The ramp potential at which the current traces without GABA and with GABA crossed represents E_{GABA} (black arrow in *inset*). Vertical dashed lines intersecting the command potential schematic show the range of command voltage in the boxed area. *Insets*: expanded traces of boxed regions illustrate the FS-BC RMP (gray arrow) and E_{GABA} (black arrow) in control (*a*) and post-SE (*b*) FS-BCs. *c*: Representative traces from a control experiment showing overlapping current traces in response to depolarizing ramps in the absence of (gray) and during pressure application of the vehicle (black). *B*: summary plot of FS-BC RMP and E_{GABA}. *$P < 0.05$ by paired and unpaired Student's *t*-test.

during local pressure application of GABA (100 μM). The potential at which the currents generated during the voltage ramp in the absence and the presence of GABA crossed was measured as E_{GABA}. As shown in Fig. 7*Aa*, *inset*, RMP in control FS-BCs was not different from the potential at which the current traces obtained in the presence and absence of GABA crossed (in mV: E_{GABA} -74.2 ± 8.8, RMP -77.6 ± 10.7, in $n = 6$ cells, $P > 0.05$ by paired Student's *t*-test). These data suggest that $GABA_AR$ activation likely contributes to shunting inhibition in control FS-BCs. In control experiments, we found no difference between E_{GABA} measured with voltage ramp and voltage step protocols in the same cell (in mV: E_{GABA} with voltage ramp -77.28 ± 2.89, E_{GABA} with voltage step -80.0 ± 3.68, in $n = 4$ cells, $P > 0.05$ by paired Student's *t*-test), indicating that the voltage ramp protocol can be used to reliably estimate E_{GABA}. In contrast to control rats, E_{GABA} measured in FS-BCs from post-SE rats was significantly more depolarized than RMP (Fig. 7*Ab*; in mV: E_{GABA} -53.3 ± 4.0, RMP -73.7 ± 4.9 in $n = 7$ cells, $P < 0.05$ by paired Student's *t*-test). Overlapping interleaved traces from control experiments performed under identical conditions in the absence and during pressure application of vehicle without GABA confirmed the absence of pressure artifacts under our recording conditions (Fig. 7*Ac*). While the difference in RMP between control and post-SE FS-BCs was not statistically significant (Fig. 7*B*; FS-BC RMP in mV: control -77.6 ± 10.7, $n = 6$; post-SE -73.7 ± 4.9, $n = 7$, $P > 0.05$ by Student's *t*-test), there was a clear depolarizing shift in FS-BC E_{GABA} after SE (Fig. 7*B*; FS-BC E_{GABA} in mV: control -74.2 ± 8.8, $n = 6$; post-SE -53.3 ± 4.0, $n = 7$, $P < 0.05$ by Student's *t*-test).

We directly tested whether activation of GABA receptors leads to membrane depolarization in FS-BCs from post-SE rats. Although cell-attached recordings from FS-BCs showed spontaneous firing when external potassium was elevated to 3 mM and above (not shown), as observed by Fricker et al. (1999), few interneurons fired spontaneously under our recording conditions with 2.5 mM external potassium. To avoid confounding effects due to changes in RMP, cell-attached recordings from FS-BCs were obtained in standard aCSF containing 2.5 mM potassium. Cell-attached recordings showed that while pressure application of the $GABA_AR$ agonist muscimol (50 μM) caused little change in membrane potential in control FS-BCs, it consistently depolarized FS-BCs from post-SE rats (Fig. 8; maximum membrane potential change in muscimol in mV: control 0.3 ± 1.3, $n = 5$; post-SE 7.6 ± 2.1, $n = 8$, $P < 0.05$ by Student's *t*-test). Together, comparison of RMP and E_{GABA} in FS-BCs from control and post-SE rats under identical experimental conditions suggests that activation of extrasynaptic $GABA_ARs$ may be shunting under control conditions and result in depolarizing currents after SE. F8

Previous studies have identified that FS-BC synaptic E_{GABA} undergoes a developmental hyperpolarizing shift and have suggested that increases in the expression of the potassium-chloride cotransporter KCC2 (Sauer and Bartos 2010) may underlie this effect. Since changes in expression of KCC2 have been shown contribute to post-SE alterations in granule cell E_{GABA} (Pathak et al. 2007), we examined FS-BCs for post-SE changes in KCC2 expression. Examination of sections immunostained for PV and KCC2 revealed the presence of KCC2 localized to the periphery of PV+ profiles in both control and post-SE rats (Fig. 9). Quantification of the fluorescence intensity for KCC2 subunit expression in PV+ neurons identified a significant post-SE decrease in KCC2 along the margins of PV+ profiles in the hilar-granule cell layer border (grayscale intensity in arbitrary units: control 15.7 ± 2.6, $n = 29$ cells from 15 sections in 3 rats; post-SE 9.8 ± 1.1, $n = 36$ cells from 15 sections in 3 rats, $P < 0.05$ by Student's *t*-test). The observed decrease in KCC2 expression in PV+ neurons likely contributes to the depolarizing shift in FS-BC E_{GABA} after SE. F9

Impact of tonic g_{GABA} and E_{GABA} on FS-BC excitability: isolated basket cell simulations. How do the presence and post-SE changes in tonic g_{GABA}, together with the depolarized E_{GABA}, modify FS-BC excitability? Given the concurrent changes in

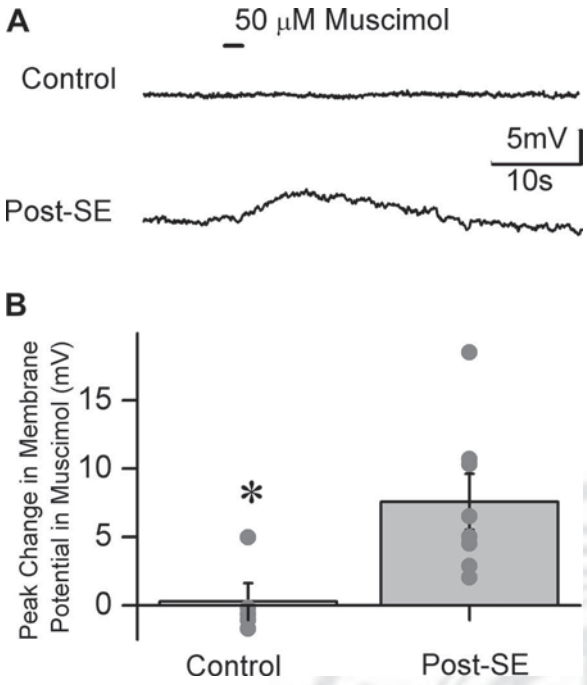

Fig. 8. GABA agonists depolarize FS-BCs 1 wk after SE. *A*: cell-attached recordings show membrane voltage traces from control (*top*) and post-SE (*bottom*) FS-BC recorded during pressure application of 50 μM muscimol (black bar). *B*: summary plot of the maximum change in FS-BC membrane potential in response to muscimol application. Individual data points are represented by gray dots. *$P < 0.05$ by unpaired Student's *t*-test.

conductance and reversal of tonic I_{GABA}, and potential confounding SE-induced changes in the intrinsic physiology of FS-BCs (unpublished observations) that are as yet unknown, it is difficult to isolate how alterations in FS-BC tonic I_{GABA}, both singly and when coupled with depolarized E_{GABA}, modify network activity in biological experiments. Therefore, we adopted computational modeling to determine how systematic changes in FS-BC tonic g_{GABA}, in the presence and absence of the observed depolarizing shift in GABA reversal, influence FS-BC and dentate network excitability. A recent study conducted with generic single compartmental models showed that when E_{GABA} is depolarizing, tonic g_{GABA} increases neuronal excitability only in a narrow range of g_{GABA}. With additional increases in tonic g_{GABA}, the shunting effect of the conductance overwhelms the depolarizing currents, resulting in net inhibition (Song et al. 2011). To systematically examine how post-SE changes in tonic g_{GABA} and E_{GABA} influence FS-BC excitability, we implemented biophysically realistic multicompartmental simulations of FS-BCs (Santhakumar et al. 2005). As illustrated in Fig. 10*A*, the model FS-BC fired at a frequency of 100 Hz in response to a 800-pA current injection, simulating the experimentally determined characteristic high-frequency firing and low R_{in} of biological dentate FS-BCs (for detailed comparison of the active and passive properties of the model FS-BC and biological basket cells see Table 3 in Santhakumar et al. 2005). To determine the magnitude of tonic g_{GABA} that generates the biologically observed tonic I_{GABA}, we simulated voltage-clamp recordings in model FS-BCs and examined how increases in tonic g_{GABA} influence the magnitude of tonic I_{GABA} and R_{in}. Systematically increasing tonic g_{GABA} from 5 nS/cm^2 resulted in negligible tonic I_{GABA} and no change in R_{in} in the model FS-BC up to a conductance of 0.5 μS/cm^2. Tonic g_{GABA} of 1 μS/cm^2 resulted in 10-pA tonic I_{GABA}, comparable to experimentally observed tonic I_{GABA} with g_{GABA} contributing to <0.5% of the model FS-BC resting conductance. Increasing tonic g_{GABA} to 10 μS/cm^2 resulted in 60-pA tonic I_{GABA}, a 3.3-MΩ decrease in R_{in} (Fig. 10*B*), and a 2.7% decrease in FS-BC membrane conductance. When tonic g_{GABA} was increased to 50 μS/cm^2 and above, tonic I_{GABA} was >250 pA and R_{in} decreased by >10 MΩ, which is well outside the range observed in our experimental data (Fig. 5). The effect of tonic g_{GABA} on tonic I_{GABA} and R_{in} in model FS-BCs was unchanged even when the g_{GABA} was restricted to the soma and proximal dendritic compartments (Fig. 10*B*). Since our experimental estimation of ~5-pA tonic I_{GABA} in control FS-BCs is *1*) without added GABA, *2*) in continuously perfused slices, and *3*) at physiological temperature, it is likely an underestimation. Note also that in the presence of the GABA transporter antagonist tonic I_{GABA} in FS-BCs is >10 pA, despite the presumably low activity levels in slices perfused with glutamate receptor antagonists (Fig. 5*E*). Therefore, we expect that tonic g_{GABA} between 1 and 10 μS/cm^2 (corresponding to 10- to 60-pA tonic I_{GABA}) in our simulations represents the range of biologically realistic tonic I_{GABA} levels during neuronal activity.

Next, we examined the effect of tonic I_{GABA} on the excitability of model FS-BCs during excitatory synaptic inputs. Model FS-BCs received 200-Hz Poisson-distributed excitatory inputs to their distal dendrites, to simulate perforant path AMPA-mediated synaptic inputs. The rise and decay of the AMPA synapse was constrained by experimental data as described previously (Santhakumar et al. 2005). g_{AMPA} was set either at 3 nS to simulate low excitatory inputs that lead to minimal FS-BC firing (Fig. 10, *C* and *D*) or at 20 nS, which resulted in model FS-BC firing at >30 Hz in the absence of tonic g_{GABA} (Fig. 10*E*). Model FS-BCs received identical input trains in each simulation. In the first set of simulations, the reversal potential for the tonic g_{GABA} was set to −74 mV, the experimentally determined E_{GABA} in control FS-BCs. Tonic g_{GABA} was simulated as a uniformly distributed leak conductance in the range of 5 nS/cm^2 to 5 mS/cm^2. This wide range of tonic g_{GABA} encompassed the biologically relevant range of 1–10 μS/cm^2, and extended to include conductance values that resulted in biphasic changes in neuronal excitability similar to those described in previous studies (Song et al. 2011). Tonic g_{GABA} in the range of 1 μS/cm^2 to 1 mS/cm^2 decreased model FS-BC firing during both low (3 nS)- and high (20 nS)-conductance excitatory inputs and abolished firing at g_{GABA} over 75 μS/cm^2 and 0.3 mS/cm^2, respectively (Fig. 10, *C–E*). Since RMP of the model FS-BC was −70 mV, the decrease in excitability when E_{GABA} was −74 mV is consistent with shunting inhibition. When E_{GABA} was set to −54 mV, the experimentally determined E_{GABA} in post-SE FS-BCs, increasing tonic g_{GABA} led to an initial increase in model FS-BC firing when tonic g_{GABA} was over 1 μS/cm^2, which reached a maximum when tonic g_{GABA} was 1 mS/cm^2. FS-BC firing declined with further increase in tonic g_{GABA} and was eventually completely suppressed (Fig. 10, *C–E*). Model FS-BC firing during excitatory synaptic inputs delivered in the presence of depolarizing E_{GABA} (−54 mV) and 1 μS/cm^2 to 1 mS/cm^2 tonic g_{GABA} increased even though E_{GABA} was more hyperpolarized than the model FS-BC action potential threshold (−40.5 mV). The simulation results are consistent with recent studies demonstrating that, in the presence of a depolarizing E_{GABA}, progressively increasing tonic g_{GABA} leads to an initial neuronal depolarization followed by shunting inhibition with

tapraid4/z9k-neurop/z9k-neurop/z9k00713/z9k1866d13z | xppws | S=1 | 2/12/13 | 7:01 | MS: JN-00891-2012 | Ini: 04/sa/ss

COLOR

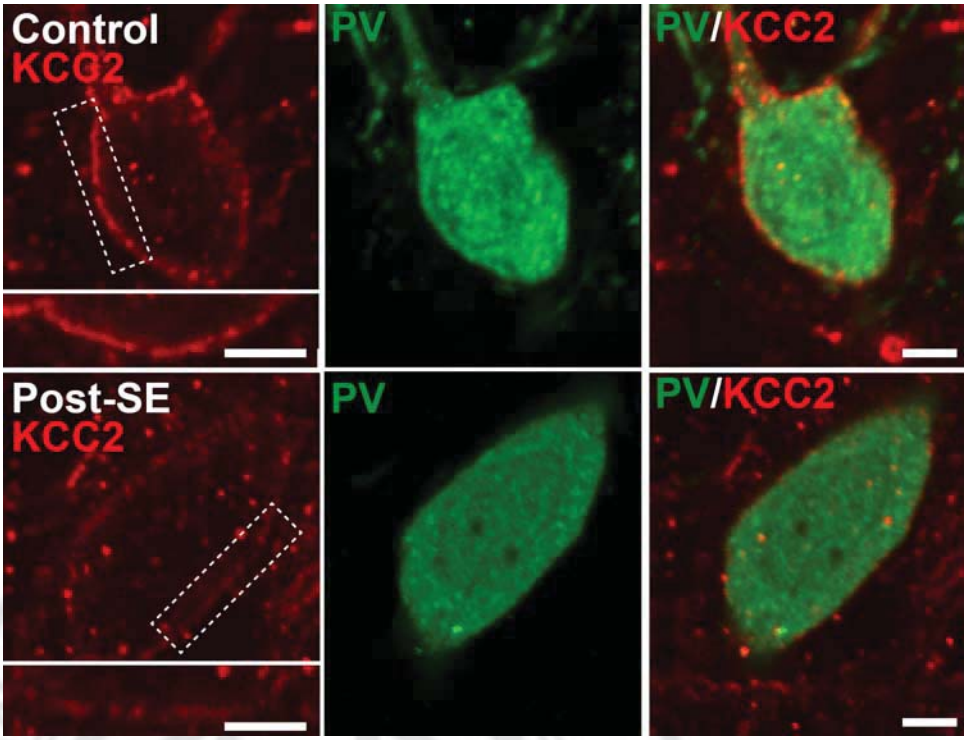

Fig. 9. SE decreases expression of KCC2 in PV interneurons. Confocal images from sections labeled for KCC2 (*left*) and PV (*center*) are shown. Merged images (*right*) show colabeling of KCC2 particularly in the periphery of the PV-positive neurons from a control (*top*) and a post-SE (*bottom*) rat. Boxed areas are shown at higher magnification in *insets*. Images were obtained with identical camera settings. Scale bars, 10 μm.

further increases (Song et al. 2011). However, our simulations demonstrate that in the biologically relevant range of 1–10 μS/cm^2 tonic g_{GABA}, the experimentally observed post-SE E_{GABA} (−54 mV) reverses the decrease in excitability mediated by tonic I_{GABA}.

In additional simulations, we restricted tonic g_{GABA} to the somatic and proximal dendritic compartments to examine whether dendritic tonic g_{GABA} influenced neuronal excitability by local modulation of synaptic inputs. In simulations performed without tonic g_{GABA} in the distal dendritic compartments where the excitatory synapses were located, both the range of tonic g_{GABA} values that modulated model FS-BC excitability and the biphasic nature of the changes were indistinguishable from simulations that included tonic g_{GABA} in all compartments (not shown). These simulations results suggest that local dendritic modulation of synaptic inputs does not underlie the effect of tonic g_{GABA} on model FS-BC excitability. Thus the isolated FS-BC simulations predict that post-SE increases in tonic g_{GABA} in the biologically relevant range would, in the absence of concomitant changes in E_{GABA} (at E_{GABA} = −74 mV), decrease FS-BC excitability during both low and moderate excitatory synaptic drive (Fig. 10*C*, *left*, and Fig. 10, *D* and *E*). Alternatively, a depolarizing shift in E_{GABA}, when not accompanied by changes in tonic g_{GABA}, would enhance FS-BC excitability (Fig. 10*C*, compare *left* and *right* at each tonic g_{GABA}; Fig. 10, *D* and *E*, compare firing at identical tonic g_{GABA} levels). However, the combined effect of the concurrent increase in tonic g_{GABA} and depolarized E_{GABA} is to maintain the control levels of FS-BC excitability during low levels of excitatory synaptic drive (Fig. 10*D*).

Effect of seizure-induced FS-BC GABAergic plasticity on dentate excitability: dentate network simulations. Our experimental data have demonstrated two distinct SE-induced changes in the inhibitory tone of dentate FS-BCs, namely, an increase in tonic I_{GABA} and a positive shift in the driving force for I_{GABA} after SE. Since both tonic I_{GABA} and E_{GABA} are also altered in granule cells after SE (Pathak et al. 2007; Zhan and Nadler 2009; Zhang et al. 2007), we adopted computational simulations to determine how seizure-induced plasticity in FS-BCs tonic inhibition affects dentate network excitability independent of, and in the absence of, other confounding changes. First, we examined whether the post-SE changes in FS-BC E_{GABA} altered dentate excitability in the absence of tonic g_{GABA}. The 1,000+ dentate neuronal network based on Santhakumar et al. (2005) was simulated as a ring and included 20% sprouting (see MATERIALS AND METHODS). The network included two major interneuronal populations, FS-BCs and hilar dendritically projecting HIPP cells. Since simulating post-SE hilar neuronal loss by removing HIPP cells from the network would disproportionately enhance the role of FS-BCs, the first set of simulations were performed without introducing hilar neuronal loss. Networks received 2.5-Hz spontaneous activity for the entire duration of the simulation. A single synchronous input to 100 adjacent granule cells was used to simulate focal perforant path-evoked network activity. In the absence of tonic g_{GABA}, changing model FS-BC E_{GABA} (of inhibitory synaptic inputs to model FS-BCs from other FS-BCs and hilar interneurons) from −74 mV to −54 mV did not change either the spontaneous background activity level or average granule cell firing in response to synchronous activation (Fig. 11, A_1 and B_1). This is consistent with the ability of the inhibitory synaptic conductance to provide shunting inhibition even when E_{GABA} is more depolarized than RMP (Song et al. 2011; Vida et al. 2006). F11

Next, we introduced tonic g_{GABA} with activity-dependent synaptic spillover conductance (see MATERIALS AND METHODS) in model FS-BCs. In one group of simulations, E_{GABA} for both tonic and synaptic g_{GABA} was set to −74 mV as observed in controls. Tonic I_{GABA} was increased between 3 μS/cm^2, contributing to 18-pA tonic I_{GABA} similar to levels observed in

tapraid4/z9k-neurop/z9k00713/z9k1866d13z | xppws | S=1 | 2/12/13 | 7:01 | MS: JN-00891-2012 | Ini: 04/sa/ss

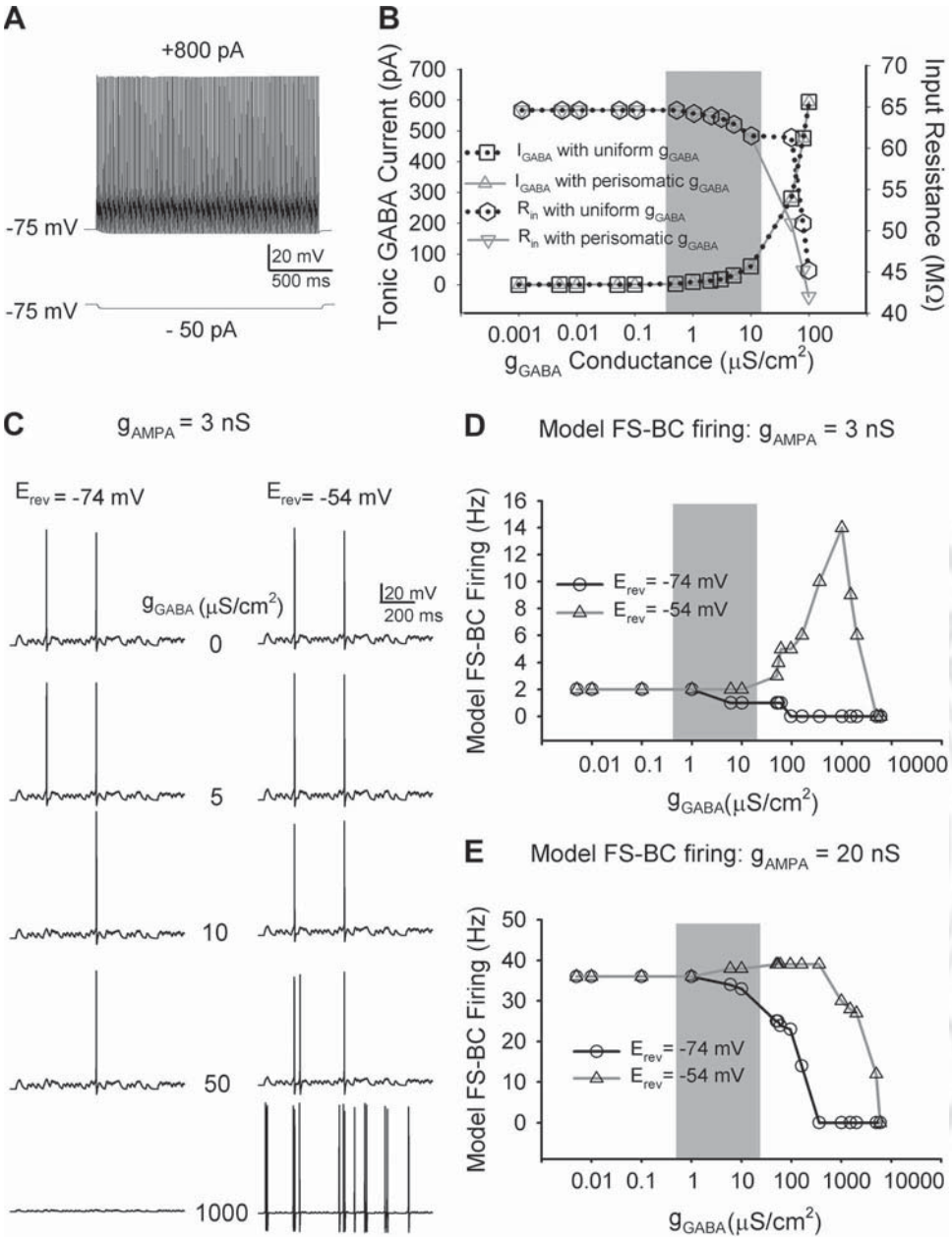

Fig. 10. Effect of GABA reversal and tonic GABA conductance (g_{GABA}) on model FS-BC excitability. *A*: responses of biophysically realistic multicompartmental model FS-BC to depolarizing and hyperpolarizing current injections illustrate nonadapting firing and low input resistance (R_{in}). *B*: summary plot shows tonic I_{GABA} and R_{in} in model FS-BCs as a function of tonic g_{GABA}. In simulations with perisomatic g_{GABA}, tonic GABA channels were distributed only in the soma and proximal dendrite. Simulations incorporated voltage-clamp recording conditions with symmetrical chloride and V_{hold} = −70 mV. Shaded region represents biologically relevant tonic I_{GABA} and g_{GABA} range. *C*: membrane voltage traces illustrate firing in FS-BC simulations during 200 Hz during identical Poisson-distributed excitatory inputs when tonic g_{GABA} is systematically increased from 0 to 1 mS/cm^2. Peak amplitude of input synaptic conductance (g_{AMPA}) was 3 nS. Simulations were performed with control (−74 mV, *left*) and post-SE (−54 mV, *right*) E_{GABA} values (E_{rev}). *D*: summary plot of FS-BC firing evoked by 200-Hz excitatory synaptic inputs (3 nS peak conductance) in the presence of increasing tonic g_{GABA} in FS-BC with E_{GABA} set at −74 and −54 mV. *E*: summary data show effect of E_{GABA} on FS-BC firing during excitatory synaptic activation at 200 Hz at increasing FS-BC tonic g_{GABA}. Peak conductance of synaptic inputs was 20 nS.

post-SE FS-BC, and 10 μS/cm^2. Tonic g_{GABA} in model FS-BCs did not alter the background spontaneous activity (Fig. 11, *A* and *C*). Strikingly, while increasing FS-BC tonic g_{GABA} did not alter overall network excitability in response to focal afferent activation in some network instantiation (summarized in Fig. 11*D* as "low activity"), it significantly increased average granule cell firing and resulted in self-sustained, recurrent, seizurelike activity in a subset of simulated networks [Fig. 11*A*, summarized in Fig. 11*D*; between-subject analysis for effect of network structure: $F_{(1,11)} = 356.9$, $P < 0.05$ by univariate repeated-measures ANOVA]. Importantly, these results suggest that in the presence of a permissive network structure shunting tonic g_{GABA} augments network excitability, leading to seizurelike activity patterns (Fig. 11*A*). When the reversal potential of model FS-BC synaptic and tonic GABA currents was set to −54 mV, the background spontaneous activity was unchanged (Fig. 11, *B* and *C*). Notably, unlike simulations with shunting E_{GABA}, networks simulated with depolarizing E_{GABA} showed no increase in evoked granule cell activity at all tonic g_{GABA} levels tested [Fig. 11, *B* and *D*; between-subject analysis for effect of E_{GABA}: $F_{(1,11)} = 345.3$, $P < 0.05$ by univariate repeated-measures ANOVA; interaction between network structure and E_{GABA}: $F_{(1,11)} = 355.2$, $P < 0.05$ by multivariate repeated-measures ANOVA]. To isolate the impact of FS-BC tonic g_{GABA} and E_{GABA} from network structural features, we set the randomization seed to a constant value to simulate structurally identical networks. Spike raster plots from simulations of structurally identical networks (illustrated in Fig. 11*A*) showed that when FS-BC E_{GABA} was −74 mV model networks had higher granule cell firing and recurrent network activity compared with networks with depolarizing (−54 mV) FS-BC E_{GABA} at all tonic g_{GABA} values tested. Next, we performed simulations on structurally identical networks (generated by 4 different predetermined randomization

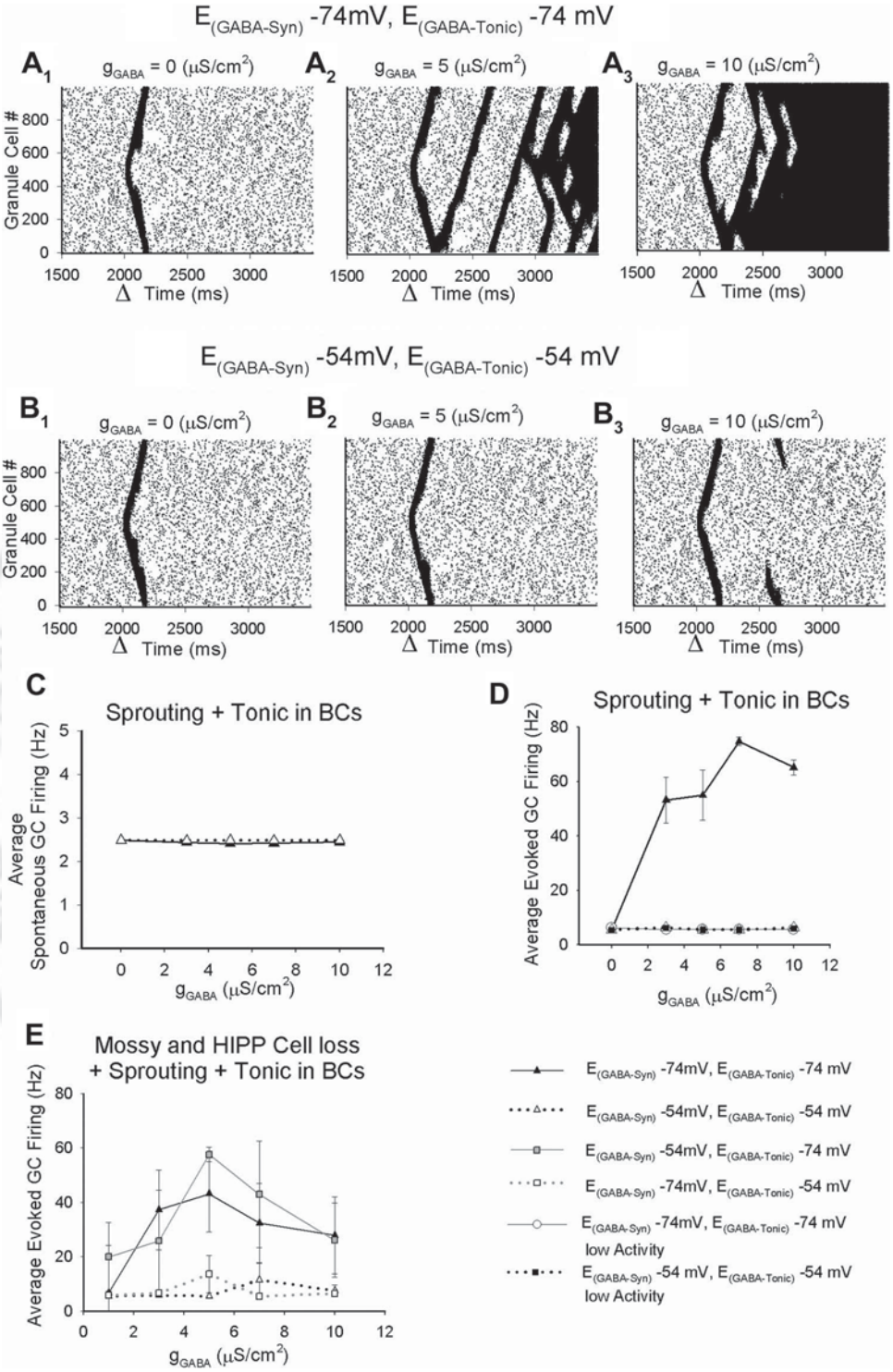

Fig. 11. Basket cell (BC) tonic GABAergic inhibition regulates dentate network excitability. *A*: granule cell (GC) spike rasters show the action potential firing of each of the 1,000 GCs. Each action potential is represented by a dot corresponding to the active cell (GC number on *y*-axis) at a certain simulation time (*x*-axis). Dentate networks were simulated as a ring with 20% sprouting. Network activity was established with Poisson-distributed suprathreshold inputs to granule cell dendrites at 2.5 Hz. A single synchronous suprathreshold activation of 100 GCs at the time marked by the arrowhead in each plot was used to simulate focal afferent activation. Spike rasters illustrate simulations performed with model FS-BC E_{GABA} at −74 mV, in the absence of tonic g_{GABA} (A_1), with g_{GABA} = 5 μS/cm^2 corresponding to a 30-pA FS-BC tonic I_{GABA} (A_2), and with g_{GABA} = 10 μS/cm^2 corresponding to a 60-pA tonic I_{GABA} (A_3). *B*: GC spikes form networks simulated as in *A*, with E_{GABA} in model FS-BCs set to −54 mV. GC spike rasters from simulations in the absence of tonic g_{GABA} (B_1), with g_{GABA} = 5 μS/cm^2 corresponding to a 30-pA FS-BC tonic I_{GABA} (B_2), and with g_{GABA} = 10 μS/cm^2 corresponding to a 60-pA tonic I_{GABA} (B_3) are illustrated. Spike rasters in *A* and *B* were derived from structurally identical network simulations. *C*: summary plots, on 3 runs in each condition, show the average spontaneous GC firing during 1,000–2,000 ms of the simulations as FS-BC tonic g_{GABA} was increased. *D*: summary of the average evoked GC firing during 2,001–3,500 ms of the simulation following focal afferent activation as a function of model FS-BC tonic g_{GABA}. Simulations were performed with E_{GABA} set at −74 mV or −54 mV (8 independent runs). Simulations in networks with "high activity" levels when E_{GABA} was −74 mV are summarized separately (4 runs at $E_{GABA\text{-}Tonic}$ = −74 mV and 5 runs at $E_{GABA\text{-}Tonic}$ = −54 mV) from networks with low activity at both −74 mV and −54 mV E_{GABA} (5 runs each). *E*: summary of the average evoked GC firing following focal afferent activation as a function of model FS-BC tonic g_{GABA} in networks including mossy fiber sprouting and hilar neuronal loss. Simulations were conducted on 4 structurally identical networks showing high activity with tonic and synaptic E_{GABA} set at −74 mV. Key on *right* applies to *D* and *E*.

seed values that resulted in high-activity networks) including loss of dentate hilar neurons (mossy cells and HIPP cells) and mossy fiber sprouting. As in networks without cell loss, average granule cell firing was increased when FS-BC E_{GABA} was −74 mV and remained low when E_{GABA} was set to −54 mV (Fig. 11*E*). While our measurements of E_{GABA} during exogenous GABA application identified a post-SE depolarizing shift, given findings that the E_{GABA} within a neuron can differ between compartments (Baldi et al. 2010; Romo-Parra et al. 2008), it remains possible that synaptic GABA reversal may differ from the reversal of tonic I_{GABA}. In an additional simulation in which synaptic E_{GABA} was held either at −54 mV or at −74 mV independent of the E_{GABA} of the tonic g_{GABA}, networks with a depolarizing shift in the E_{GABA} of tonic g_{GABA} still consistently demonstrated lower excitability than identical networks with −74 mV tonic E_{GABA} [between-subject analysis for effect of tonic E_{GABA}: $F_{(1,11)} = 32.68$, $P < 0.05$; synaptic E_{GABA}: $F_{(1,11)} = 0.29$, $P > 0.05$; interaction

between tonic and synaptic E_{GABA}: $F_{(1,11)} = 0.46$, $P > 0.05$ by 2-way repeated-measures ANOVA]. Taken together, the simulations show that the depolarization of FS-BC E_{GABA} that occurs after SE can maintain FS-BC excitability despite increases in tonic g_{GABA} and could limit dentate network excitability after SE.

DISCUSSION

The ability of tonic GABAergic inhibition to regulate excitability of projection neurons suggests that tonic I_{GABA} may be modulated to prevent epileptogenesis (Meldrum and Rogawski 2007). Expression and seizure-induced changes in tonic I_{GABA} among dentate perisomatic interneurons critical for feedback inhibition can influence how modulating tonic inhibition will affect dentate function. Our study demonstrates that *1*) $GABA_AR$ δ-subunits, known to underlie tonic I_{GABA}, are expressed in PV+ interneurons in the hilar-granule cell layer border; *2*) FS-BCs express tonic I_{GABA} that is enhanced 1 wk after SE; *3*) increase in $GABA_AR$ δ-subunit expression contributes to post-SE enhancement of FS-BC tonic I_{GABA}; *4*) in contrast to shunting GABAergic inhibition in controls, there is a positive shift in FS-BC E_{GABA} 1 wk after SE, resulting in a depolarizing driving force for I_{GABA}; *5*) corresponding to the post-SE depolarizing shift in FS-BC E_{GABA}, there is a reduction in the expression of the potassium-chloride cotransporter KCC2 in PV+ interneurons 1 wk after SE; and *6*) in computational simulations incorporating tonic g_{GABA} in model FS-BCs, whereas shunting E_{GABA} reduces FS-BC firing and enhances dentate network excitability, depolarizing E_{GABA} reverses decreases in model FS-BC activity and prevents increases in network excitability.

Expression of tonic I_{GABA} in dentate FS-BCs. Perisomatically projecting interneurons expressing PV are critical for precision and timing of network activity (Freund 2003). Since tonic inhibition influences neuronal excitability, gain, and fidelity of information transmission (Duguid et al. 2012; Mitchell and Silver 2003; Song et al. 2011) and is additionally augmented by synaptic spillover during neuronal activity (Glykys and Mody 2007), FS-BC tonic I_{GABA} is ideally suited to regulate feedback inhibition and dentate throughput during behaviorally relevant neuronal activity. The ability of interneuronal tonic I_{GABA} to regulate gamma oscillations (Mann and Mody 2010) and the central role for FS-BCs in dentate gamma oscillations (Bartos et al. 2002) suggest that modulation of FS-BC tonic I_{GABA} by alcohol and neurosteroids, which act on $GABA_ARs$ containing δ-subunits (Stell et al. 2003), may contribute to the impact of these drugs on memory function. Moreover, activity-dependent enhancement of FS-BC tonic I_{GABA} could provide the transient suppression of feedback inhibition needed to induce long-term potentiation in the dentate gyrus (Arima-Yoshida et al. 2011).

There are regional differences in the $GABA_AR$ subunits mediating interneuronal tonic I_{GABA}, with α_5-subunits responsible for tonic I_{GABA} in CA1 interneurons and δ-subunits in CA3 and molecular layer interneurons (Glykys et al. 2007; Mann and Mody 2010; Semyanov et al. 2003). Unlike PV interneurons in the neocortex (Olah et al. 2009), and like molecular layer interneurons in the dentate (Glykys et al. 2007), we find that dentate PV interneurons express $GABA_AR$ δ-subunits. Similar to fast-spiking interneurons in the murine neocortex (Krook-Magnuson et al. 2008), we show that tonic I_{GABA} in dentate FS-BCs is modulated by a $GABA_AR$ δ-subunit-specific agonist. Since dentate interneuronal-like profiles show robust expression of $GABA_AR$ α_1-subunits (Fritschy et al. 1999), and $GABA_ARs$ containing α_1- and δ-subunits can mediate tonic I_{GABA} (Glykys et al. 2007), it is possible that $GABA_ARs$ with α_1- and δ-subunits underlie FS-BC tonic I_{GABA}. Thus, although both granule cell and FS-BC tonic I_{GABA} are mediated by $GABA_AR$ δ-subunits, differential contribution of α_1-subunits to FS-BC and α_4-subunits to granule cell tonic I_{GABA} may provide targets for cell-specific modulation of tonic inhibition.

SE-induced plasticity of FS-BC tonic inhibition. Perisomatic inhibition is pivotal in regulating granule cell excitability in both normal and epileptic dentate gyrus (Coulter and Carlson 2007; Kraushaar and Jonas 2000). Granule cell tonic I_{GABA} is known to be altered after SE (Rajasekaran et al. 2010; Zhan and Nadler 2009; Zhang et al. 2007). Since FS-BC tonic I_{GABA} is increased before the occurrence of behavioral seizures, and not as a compensatory response to changes in the epileptic network, FS-BC tonic I_{GABA} could play a role in development of epilepsy. Indeed, earlier studies have suggested that cellular and synaptic plasticity prior to the onset of spontaneous seizures contribute to epileptogenesis (Brooks-Kayal et al. 1998; Kobayashi et al. 2003; Pathak et al. 2007). Both increases in extracellular GABA due to synaptic spillover or compromised GABA transporter function and changes in $GABA_AR$ expression could enhance tonic I_{GABA} (Farrant and Nusser 2005). However, sIPSC frequency in both FS-BCs (Fig. 6) and granule cells (Kobayashi and Buckmaster 2003) is reduced after SE, indicating that synaptic GABA spillover does not underlie the post-SE increases in FS-BC tonic I_{GABA}. Additionally, even when GABA transporters were blocked, post-SE FS-BCs had larger tonic I_{GABA}, indicating that factors other than compromises in GABA transporter function underlie the increase in tonic I_{GABA}. Our semiquantitative analyses demonstrate increase in the expression of $GABA_AR$ δ-subunit in PV+ interneurons after SE. Although extensive efforts were taken to pair sections from control and experimental animals and to use identical methods during staining and imaging, admittedly quantification of immunofluorescence intensity is associated with limitations including nonlinear antigen-antibody reaction and changes in fluorescence arising from tissue properties and may not accurately reflect protein levels. Crucially, THIP, a $GABA_AR$ δ-subunit-selective agonist under our experimental conditions (Brown et al. 2002; Gupta et al. 2012), causes greater baseline current shift in FS-BCs from post-SE rats, validating the semiquantitative immunofluorescence analysis and confirming that enhanced $GABA_AR$ δ-subunit expression contributes to increases in FS-BC tonic I_{GABA} after SE. Thus the presence and SE-induced plasticity of FS-BC tonic I_{GABA} must be considered when developing seizure therapies targeting tonic inhibition.

Whether tonic I_{GABA} enhances or decreases neuronal excitability depends on complex interactions between GABA driving force and conductance (Song et al. 2011). Several studies have demonstrated that interneuronal E_{GABA} can provide shunting inhibition when E_{GABA} lies between RMP and action potential threshold (Banke and McBain 2006; Song et al. 2011; Vida et al. 2006). Consistent with earlier observations of shunting synaptic E_{GABA} in FS-BCs (Sauer and Bartos 2010; Vida et al. 2006), the difference between FS-BC RMP and

E_{GABA} determined during GABA application in controls was not significant. Methodological differences including use of whole cell recording conditions, younger animals, and CNQX, which unlike structurally related quinoxalinediones depolarizes hippocampal interneurons by nonspecific mechanisms (McBain et al. 1992), may have resulted in more depolarized RMP values in earlier studies (Geiger et al. 1997; Vida et al. 2006). It is important to note that the RMP values in our study are in the same range as the RMP of hippocampal interneurons measured with less invasive cell-attached recordings (Fricker et al. 1999; Verheugen et al. 1999). Moreover, RMP and E_{GABA} values in control FS-BCs in our study are similar to the RMP and IPSC reversal potential reported in hippocampal interneurons from animals over postnatal day 30 (Banke and McBain 2006) and likely result from developmental hyperpolarizing shift in interneuronal RMP and E_{GABA} (Banke and McBain 2006; Sauer and Bartos 2010). Importantly, we show that FS-BC E_{GABA} is depolarized relative to the RMP 1 wk after SE, resulting in a depolarizing GABA driving force, as previously reported in granule cells (Pathak et al. 2007). Curiously, despite post-SE changes in FS-BC I_{GABA} and E_{GABA}, FS-BC RMP remains unchanged. It is possible that changes in non-GABAergic ionic conductances compensate for changes in membrane conductance when tonic g_{GABA} is altered (Brickley et al. 2001). While the trauma of slicing can impact neuronal chloride homeostasis (Dzhala et al. 2012), our use of young adult animals and high-sucrose slicing solution minimizes these effects. Additionally, our inclusion of only morphologically intact neurons, the hyperpolarized FS-BC RMP, and the lack of difference between RMP in control and post-SE FS-BCs suggest that slicing-induced trauma is unlikely to underlie the post-SE depolarization of FS-BC E_{GABA}. FS-BC E_{GABA} undergoes a developmental hyperpolarizing shift believed to result from increases in the expression of the potassium-chloride cotransporter KCC2 (Sauer and Bartos 2010). While cognizant of the limitations of semiquantitative analysis of fluorescence intensity, we find consistent post-SE reduction in the intensity of membrane labeling for KCC2 in FS-BCs, suggesting that a decrease in KCC2 may contribute to the depolarizing shift in FS-BC E_{GABA} after SE. Whether FS-BCs, like granule cells (Pathak et al. 2007), show post-SE activity-dependent changes in the reversal potential for synaptic events remains to be tested.

Impact of tonic I_{GABA} and depolarizing E_{GABA} on FS-BC and network excitability. Using biophysically realistic multicompartmental FS-BC simulations, we determined the tonic conductance that modeled the experimentally observed FS-BC tonic I_{GABA}. Since recordings in slices at 33°C without added GABA or transporter antagonist likely underestimated tonic I_{GABA} amplitudes, our measurements with GABA transporter antagonists may better represent the magnitude of FS-BC tonic I_{GABA} in the biological tissue during neuronal activity. Voltage-clamp simulations identified the range of tonic g_{GABA} (1–10 $\mu S/cm^2$) that was compatible with experimentally derived estimates of FS-BC tonic I_{GABA} (10–60 pA). Changing tonic g_{GABA} across this entire range (50 pA) caused an ~3.3-MΩ shift in R_{in} and a <3% change in input conductance, suggesting that differences in R_{in} and input conductance due to a 10-pA shift in FS-BC tonic I_{GABA} may be difficult to detect experimentally. Increases in tonic g_{GABA} reduced model FS-BC excitability when E_{GABA} was −74 mV and, at similar values of g_{GABA}, enhanced excitability when E_{GABA} was constrained by the depolarized values (−54 mV) observed after SE. As reported previously (Song et al. 2011), increasing tonic g_{GABA} beyond 1 mS/cm^2 in model FS-BCs resulted in shunting inhibition even with depolarizing E_{GABA}. However, the low FS-BC R_{in} and larger driving force (~20 mV) could account for the relatively high g_{GABA} needed to obtain shunting inhibition in our biophysically realistic FS-BC model compared with earlier simulations using single-compartment models with low-leak conductance (Song et al. 2011). Our simulations identify that, together, the post-SE changes in tonic I_{GABA} and E_{GABA} maintain FS-BC excitability during excitatory inputs (Fig. 10). It is possible that the parallel changes in tonic I_{GABA} and reversal potential reflect homeostatic plasticity to maintain FS-BC activity levels in the network (Howard et al. 2007; Turrigiano et al. 1994). In dentate network models with recurrent mossy fiber collaterals, including FS-BCs with simulated tonic I_{GABA} consistently resulted in low evoked granule cell activity when FS-BC E_{GABA} was depolarizing. Curiously, evoked granule cell activity in some but not all network implementations was greatly enhanced and developed into seizurelike recurrent firing when E_{GABA} was −74 mV. Since the average number of cell type-specific connections to each neuron in a given class of cells was not different between the networks, it is likely that the presence of a few highly connected hub cells and formation of feedback excitatory loops (Morgan and Soltesz 2008) may have contributed to the differences in activity patterns between the networks with otherwise identical connectivity statistics. While our simulations predict that post-SE changes in FS-BC inhibition can limit early SE-induced increases in dentate excitability when sprouting is low, structural reorganization and cell loss associated with epileptogenesis could undermine this potential compensatory mechanism. Additionally, maintenance of normal neuronal and network excitability despite altered g_{GABA} and reversal is consistent with recent studies suggesting that multiple combinations of intrinsic parameters can result in similar circuit performance (Marder 2011). However, all parameter combinations may not be identically robust in maintaining normal activity during different network perturbations. Thus, while the observed changes in tonic I_{GABA} and E_{GABA} maintain normal FS-BC and dentate activity during focal afferent activation, these changes may compromise FS-BC responses during certain patterns of network perturbations and may impact generation of network rhythms contributing to memory impairments associated with seizure disorders.

ACKNOWLEDGMENTS

We thank Dr. Jamie Magurie for the gift of $GABA_AR\delta^{-/-}$ mouse brains and Drs. Josh Berlin, Stella Elkabes, and Robert F. Heary for equipment and discussions.

GRANTS

This work is supported by an Epilepsy Foundation Research Grant and National Institute of Neurological Disorders and Stroke Grant NS-069861 to V. Santhakumar.

DISCLOSURES

No conflicts of interest, financial or otherwise, are declared by the author(s). AQ: 8

AUTHOR CONTRIBUTIONS

Author contributions: J.Y., A.P., and T.I. performed experiments; J.Y., A.P., and F.S.E. analyzed data; J.Y., A.P., and V.S. interpreted results of experiments; J.Y., A.P., and F.S.E. prepared figures; J.Y., A.P., F.S.E., T.I., and V.S. approved final version of manuscript; F.S.E. and V.S. edited and revised manuscript; V.S. conception and design of research; V.S. drafted manuscript.

REFERENCES

Arima-Yoshida F, Watabe AM, Manabe T. The mechanisms of the strong inhibitory modulation of long-term potentiation in the rat dentate gyrus. *Eur J Neurosci* 33: 1637–1646, 2011.

Baldi R, Varga C, Tamas G. Differential distribution of KCC2 along the axo-somato-dendritic axis of hippocampal principal cells. *Eur J Neurosci* 32: 1319–1325, 2010.

Banke TG, McBain CJ. GABAergic input onto CA3 hippocampal interneurons remains shunting throughout development. *J Neurosci* 26: 11720–11725, 2006.

Bartos M, Vida I, Frotscher M, Geiger JR, Jonas P. Rapid signaling at inhibitory synapses in a dentate gyrus interneuron network. *J Neurosci* 21: 2687–2698, 2001.

Bartos M, Vida I, Frotscher M, Meyer A, Monyer H, Geiger JR, Jonas P. Fast synaptic inhibition promotes synchronized gamma oscillations in hippocampal interneuron networks. *Proc Natl Acad Sci USA* 99: 13222–13227, 2002.

Ben-Ari Y. Developing networks play a similar melody. *Trends Neurosci* 24: 353–360, 2001.

Bianchi MT, Macdonald RL. Agonist trapping by $GABA_A$ receptor channels. *J Neurosci* 21: 9083–9091, 2001.

Billups D, Attwell D. Control of intracellular chloride concentration and GABA response polarity in rat retinal ON bipolar cells. *J Physiol* 545: 183–198, 2002.

Bragin A, Wilson CL, Almajano J, Mody I, Engel J Jr. High-frequency oscillations after status epilepticus: epileptogenesis and seizure genesis. *Epilepsia* 45: 1017–1023, 2004.

Brickley SG, Revilla V, Cull-Candy SG, Wisden W, Farrant M. Adaptive regulation of neuronal excitability by a voltage-independent potassium conductance. *Nature* 409: 88–92, 2001.

Brooks-Kayal AR, Shumate MD, Jin H, Rikhter TY, Coulter DA. Selective changes in single cell $GABA_A$ receptor subunit expression and function in temporal lobe epilepsy. *Nat Med* 4: 1166–1172, 1998.

Brown N, Kerby J, Bonnert TP, Whiting PJ, Wafford KA. Pharmacological characterization of a novel cell line expressing human $alpha_4beta_3delta$ $GABA_A$ receptors. *Br J Pharmacol* 136: 965–974, 2002.

Buckmaster PS, Yamawaki R, Zhang GF. Axon arbors and synaptic connections of a vulnerable population of interneurons in the dentate gyrus in vivo. *J Comp Neurol* 445: 360–373, 2002.

Buzsaki G. *Rhythms of the Brain*. New York: Oxford Univ. Press, 2006.

Cossart R, Bernard C, Ben-Ari Y. Multiple facets of GABAergic neurons and synapses: multiple fates of GABA signalling in epilepsies. Trends *Neurosci* 28: 108–115, 2005.

Coulter DA. Epilepsy-associated plasticity in gamma-aminobutyric acid receptor expression, function, and inhibitory synaptic properties. *Int Rev Neurobiol* 45: 237–252, 2001.

Coulter DA, Carlson GC. Functional regulation of the dentate gyrus by GABA-mediated inhibition. *Prog Brain Res* 163: 235–243, 2007.

Duguid I, Branco T, London M, Chadderton P, Hausser M. Tonic inhibition enhances fidelity of sensory information transmission in the cerebellar cortex. *J Neurosci* 32: 11132–11143, 2012.

Dyhrfjeld-Johnsen J, Santhakumar V, Morgan RJ, Huerta R, Tsimring L, Soltesz I. Topological determinants of epileptogenesis in large-scale structural and functional models of the dentate gyrus derived from experimental data. *J Neurophysiol* 97: 1566–1587, 2007.

Dzhala V, Valeeva G, Glykys J, Khazipov R, Staley K. Traumatic alterations in GABA signaling disrupt hippocampal network activity in the developing brain. *J Neurosci* 32: 4017–4031, 2012.

Ebihara S, Shirato K, Harata N, Akaike N. Gramicidin-perforated patch recording: GABA response in mammalian neurones with intact intracellular chloride. *J Physiol* 484: 77–86, 1995.

Ekstrand JJ, Pouliot W, Scheerlinck P, Dudek FE. Lithium pilocarpine-induced status epilepticus in postnatal day 20 rats results in greater neuronal injury in ventral versus dorsal hippocampus. *Neuroscience* 192: 699–707, 2011.

Ewell LA, Jones MV. Frequency-tuned distribution of inhibition in the dentate gyrus. *J Neurosci* 30: 12597–12607, 2010.

Farrant M, Nusser Z. Variations on an inhibitory theme: phasic and tonic activation of $GABA_A$ receptors. *Nat Rev Neurosci* 6: 215–229, 2005.

Freund TF. Interneuron Diversity series: Rhythm and mood in perisomatic inhibition. *Trends Neurosci* 26: 489–495, 2003.

Fricker D, Verheugen JA, Miles R. Cell-attached measurements of the firing threshold of rat hippocampal neurones. *J Physiol* 517: 791–804, 1999.

Fritschy JM, Kiener T, Bouilleret V, Loup F. GABAergic neurons and $GABA_A$-receptors in temporal lobe epilepsy. *Neurochem Int* 34: 435–445, 1999.

Geiger JR, Lubke J, Roth A, Frotscher M, Jonas P. Submillisecond AMPA receptor-mediated signaling at a principal neuron-interneuron synapse. *Neuron* 18: 1009–1023, 1997.

Glykys J, Mody I. The main source of ambient GABA responsible for tonic inhibition in the mouse hippocampus. *J Physiol* 582: 1163–1178, 2007.

Glykys J, Peng Z, Chandra D, Homanics GE, Houser CR, Mody I. A new naturally occurring $GABA_A$ receptor subunit partnership with high sensitivity to ethanol. *Nat Neurosci* 10: 40–48, 2007.

Gupta A, Elgammal FS, Proddutur A, Shah S, Santhakumar V. Decrease in tonic inhibition contributes to increase in dentate semilunar granule cell. *J Neurosci* 32: 2523–2537, 2012.

Harney SC, Jones MV. Pre- and postsynaptic properties of somatic and dendritic inhibition in dentate gyrus. *Neuropharmacology* 43: 584–594, 2002.

Hefft S, Jonas P. Asynchronous GABA release generates long-lasting inhibition at a hippocampal interneuron-principal neuron synapse. *Nat Neurosci* 8: 1319–1328, 2005.

Hines ML, Carnevale NT. The NEURON simulation environment. *Neural Comput* 9: 1179–1209, 1997.

Howard AL, Neu A, Morgan RJ, Echegoyen JC, Soltesz I. Opposing modifications in intrinsic currents and synaptic inputs in post-traumatic mossy cells: evidence for single-cell homeostasis in a hyperexcitable network. *J Neurophysiol* 97: 2394–2409, 2007.

Kobayashi M, Buckmaster PS. Reduced inhibition of dentate granule cells in a model of temporal lobe epilepsy. *J Neurosci* 23: 2440–2452, 2003.

Kobayashi M, Wen X, Buckmaster PS. Reduced inhibition and increased output of layer II neurons in the medial entorhinal cortex in a model of temporal lobe epilepsy. *J Neurosci* 23: 8471–8479, 2003.

Kraushaar U, Jonas P. Efficacy and stability of quantal GABA release at a hippocampal interneuron-principal neuron synapse. *J Neurosci* 20: 5594–5607, 2000.

Krook-Magnuson EI, Li P, Paluszkiewicz SM, Huntsman MM. Tonically active inhibition selectively controls feedforward circuits in mouse barrel cortex. *J Neurophysiol* 100: 932–944, 2008.

Mann EO, Mody I. Control of hippocampal gamma oscillation frequency by tonic inhibition and excitation of interneurons. *Nat Neurosci* 13: 205–212, 2010.

Marder E. Variability, compensation, and modulation in neurons and circuits. *Proc Natl Acad Sci USA* 108, *Suppl* 3: 15542–15548, 2011.

Margerison JH, Corsellis JA. Epilepsy and the temporal lobes. A clinical, electroencephalographic and neuropathological study of the brain in epilepsy, with particular reference to the temporal lobes. *Brain* 89: 499–530, 1966.

McBain CJ, Eaton JV, Brown T, Dingledine R. CNQX increases spontaneous inhibitory input to CA3 pyramidal neurones in neonatal rat hippocampal slices. *Brain Res* 592: 255–260, 1992.

Meldrum BS, Rogawski MA. Molecular targets for antiepileptic drug development. *Neurotherapeutics* 4: 18–61, 2007.

Mello LE, Cavalheiro EA, Tan AM, Kupfer WR, Pretorius JK, Babb TL, Finch DM. Circuit mechanisms of seizures in the pilocarpine model of chronic epilepsy: cell loss and mossy fiber sprouting. *Epilepsia* 34: 985–995, 1993.

Mitchell SJ, Silver RA. Shunting inhibition modulates neuronal gain during synaptic excitation. *Neuron* 38: 433–445, 2003.

Morgan RJ, Soltesz I. Nonrandom connectivity of the epileptic dentate gyrus predicts a major role for neuronal hubs in seizures. *Proc Natl Acad Sci USA* 105: 6179–6184, 2008.

Mtchedlishvili Z, Kapur J. High-affinity, slowly desensitizing GABAA receptors mediate tonic inhibition in hippocampal dentate granule cells. *Mol Pharmacol* 69: 564–575, 2006.

Olah S, Fule M, Komlosi G, Varga C, Baldi R, Barzo P, Tamas G. Regulation of cortical microcircuits by unitary GABA-mediated volume transmission. *Nature* 461: 1278–1281, 2009.

Pathak HR, Weissinger F, Terunuma M, Carlson GC, Hsu FC, Moss SJ, Coulter DA. Disrupted dentate granule cell chloride regulation enhances synaptic excitability during development of temporal lobe epilepsy. *J Neurosci* 27: 14012–14022, 2007.

Peng Z, Huang CS, Stell BM, Mody I, Houser CR. Altered expression of the delta subunit of the GABAA receptor in a mouse model of temporal lobe epilepsy. *J Neurosci* 24: 8629–8639, 2004.

Rajasekaran K, Joshi S, Sun C, Mtchedlishvilli Z, Kapur J. Receptors with low affinity for neurosteroids and GABA contribute to tonic inhibition of granule cells in epileptic animals. *Neurobiol Dis* 40: 490–501, 2010.

Raol YS, Budreck EC, Brooks-Kayal AR. Epilepsy after early-life seizures can be independent of hippocampal injury. *Ann Neurol* 53: 503–511, 2003.

Rivera C, Voipio J, Kaila K. Two developmental switches in GABAergic signalling: the K^+-Cl^- cotransporter KCC2 and carbonic anhydrase CAVII. *J Physiol* 562: 27–36, 2005.

Romo-Parra H, Trevino M, Heinemann U, Gutierrez R. GABA actions in hippocampal area CA3 during postnatal development: differential shift from depolarizing to hyperpolarizing in somatic and dendritic compartments. *J Neurophysiol* 99: 1523–1534, 2008.

Rossi DJ, Hamann M, Attwell D. Multiple modes of GABAergic inhibition of rat cerebellar granule cells. *J Physiol* 548: 97–110, 2003.

Santhakumar V. Modeling mossy cell loss and mossy fiber sprouting in epilepsy. In: *Computational Neuroscience in Epilepsy*, edited by Soltesz I, Staley KJ. San Diego, CA: Academic, 2008, p. 89–111.

Santhakumar V, Aradi I, Soltesz I. Role of mossy fiber sprouting and mossy cell loss in hyperexcitability: a network model of the dentate gyrus incorporating cell types and axonal topography. *J Neurophysiol* 93: 437–453, 2005.

Santhakumar V, Bender R, Frotscher M, Ross ST, Hollrigel GS, Toth Z, Soltesz I. Granule cell hyperexcitability in the early post-traumatic rat dentate gyrus: the "irritable mossy cell" hypothesis. *J Physiol* 524: 117–134, 2000.

Santhakumar V, Hanchar HJ, Wallner M, Olsen RW, Otis TS. Contributions of the $GABA_A$ receptor alpha6 subunit to phasic and tonic inhibition revealed by a naturally occurring polymorphism in the alpha6 gene. *J Neurosci* 26: 3357–3364, 2006.

Santhakumar V, Jones RT, Mody I. Developmental regulation and neuroprotective effects of striatal tonic $GABA_A$ currents. *Neuroscience* 167: 644–655, 2010.

Santhakumar V, Ratzliff AD, Jeng J, Toth K, Soltesz I. Long-term hyperexcitability in the hippocampus after experimental head trauma. *Ann Neurol* 50: 708–717, 2001.

Sauer JF, Bartos M. Recruitment of early postnatal parvalbumin-positive hippocampal interneurons by GABAergic excitation. *J Neurosci* 30: 110–115, 2010.

Scimemi A, Semyanov A, Sperk G, Kullmann DM, Walker MC. Multiple and plastic receptors mediate tonic $GABA_A$ receptor currents in the hippocampus. *J Neurosci* 25: 10016–10024, 2005.

Semyanov A, Walker MC, Kullmann DM. GABA uptake regulates cortical excitability via cell type-specific tonic inhibition. *Nat Neurosci* 6: 484–490, 2003.

Song I, Savtchenko L, Semyanov A. Tonic excitation or inhibition is set by $GABA_A$ conductance in hippocampal interneurons. *Nat Commun* 2: 376, 2011.

Stell BM, Brickley SG, Tang CY, Farrant M, Mody I. Neuroactive steroids reduce neuronal excitability by selectively enhancing tonic inhibition mediated by delta subunit-containing $GABA_A$ receptors. *Proc Natl Acad Sci USA* 100: 14439–14444, 2003.

Turrigiano G, Abbott LF, Marder E. Activity-dependent changes in the intrinsic properties of cultured neurons. *Science* 264: 974–977, 1994.

Verheugen JA, Fricker D, Miles R. Noninvasive measurements of the membrane potential and GABAergic action in hippocampal interneurons. *J Neurosci* 19: 2546–2555, 1999.

Vida I, Bartos M, Jonas P. Shunting inhibition improves robustness of gamma oscillations in hippocampal interneuron networks by homogenizing firing rates. *Neuron* 49: 107–117, 2006.

Wei W, Zhang N, Peng Z, Houser CR, Mody I. Perisynaptic localization of delta subunit-containing $GABA_A$ receptors and their activation by GABA spillover in the mouse dentate gyrus. *J Neurosci* 23: 10650–10661, 2003.

West MJ, Slomianka L, Gundersen HJ. Unbiased stereological estimation of the total number of neurons in the subdivisions of the rat hippocampus using the optical fractionator. *Anat Rec* 231: 482–497, 1991.

Zhan RZ, Nadler JV. Enhanced tonic GABA current in normotopic and hilar ectopic dentate granule cells after pilocarpine-induced status epilepticus. *J Neurophysiol* 102: 670–681, 2009.

Zhang N, Wei W, Mody I, Houser CR. Altered localization of $GABA_A$ receptor subunits on dentate granule cell dendrites influences tonic and phasic inhibition in a mouse model of epilepsy. *J Neurosci* 27: 7520–7531, 2007.

Zhang W, Buckmaster PS. Dysfunction of the dentate basket cell circuit in a rat model of temporal lobe epilepsy. *J Neurosci* 29: 7846–7856, 2009.

Zhang W, Huguenard JR, Buckmaster PS. Increased excitatory synaptic input to granule cells from hilar and CA3 regions in a rat model of temporal lobe epilepsy. *J Neurosci* 32: 1183–1196, 2012.

Zhang W, Yamawaki R, Wen X, Uhl J, Diaz J, Prince DA, Buckmaster PS. Surviving hilar somatostatin interneurons enlarge, sprout axons, and form new synapses with granule cells in a mouse model of temporal lobe epilepsy. *J Neurosci* 29: 14247–14256, 2009.

Cellular/Molecular

Decrease in Tonic Inhibition Contributes to Increase in Dentate Semilunar Granule Cell Excitability after Brain Injury

Akshay Gupta,[1] Fatima S. Elgammal,[1]* Archana Proddutur,[1]* Samik Shah,[1] and Vijayalakshmi Santhakumar[1,2]

Departments of [1]Neurology and Neurosciences and [2]Pharmacology and Physiology, New Jersey Medical School, University of Medicine and Dentistry of New Jersey, Newark, New Jersey 07103

Brain injury is an etiological factor for temporal lobe epilepsy and can lead to memory and cognitive impairments. A recently characterized excitatory neuronal class in the dentate molecular layer, semilunar granule cell (SGC), has been proposed to regulate dentate network activity patterns and working memory formation. Although SGCs, like granule cells, project to CA3, their typical sustained firing and associational axon collaterals suggest that they are functionally distinct from granule cells. We find that brain injury results in an enhancement of SGC excitability associated with an increase in input resistance 1 week after trauma. In addition to prolonging miniature and spontaneous IPSC interevent intervals, brain injury significantly reduces the amplitude of tonic GABA currents in SGCs. The postinjury decrease in SGC tonic GABA currents is in direct contrast to the increase observed in granule cells after trauma. Although our observation that SGCs express Prox1 indicates a shared lineage with granule cells, data from control rats show that SGC tonic GABA currents are larger and sIPSC interevent intervals shorter than in granule cells, demonstrating inherent differences in inhibition between these cell types. $GABA_A$ receptor antagonists selectively augmented SGC input resistance in controls but not in head-injured rats. Moreover, post-traumatic differences in SGC firing were abolished in $GABA_A$ receptor blockers. Our data show that cell-type-specific post-traumatic decreases in tonic GABA currents boost SGC excitability after brain injury. Hyperexcitable SGCs could augment dentate throughput to CA3 and contribute substantively to the enhanced risk for epilepsy and memory dysfunction after traumatic brain injury.

Introduction

Brain injury engenders a wide spectrum of neurological complications involving the hippocampus, including an elevated risk for acquired temporal lobe epilepsy and for memory and cognitive dysfunction (McAllister, 1992; Annegers et al., 1998; Herman, 2002; Thompson et al., 2005; Lowenstein, 2009). Although brain injury leads to neuronal damage and enhanced excitability of the dentate gyrus within 1 week after trauma (Lowenstein et al., 1992; Toth et al., 1997), intrinsic excitability of the major glutamatergic neurons remains unchanged (Santhakumar et al., 2000; Howard et al., 2007). However, whether hyperexcitability of a subset of glutamatergic neurons may underlie early postinjury increases in dentate excitability is not known.

Semilunar granule cells (SGCs) are novel excitatory neurons in the dentate inner molecular layer (IML). These have recently been identified as the prime orchestrators of persistent firing in hilar neurons (Larimer and Strowbridge, 2010). Although SGCs, like granule cells, project to CA3, they are unique in the presence of molecular layer axon collaterals (Williams et al., 2007), which could contribute to synaptic excitation of neighboring granule cells. Physiologically, afferent stimulation evokes persistent firing in SGCs, which underlie prolonged synaptic barrages in hilar neurons (Williams et al., 2007). Thus, SGCs are in a pivotal position to regulate dentate feedback circuits and have been proposed to contribute to the integrity of the physiological "dentate gate" (Heinemann et al., 1992) that regulates granule cell throughput (Larimer and Strowbridge, 2010). Since SGCs have dual projection and associational connectivity, and can regulate dentate excitability and hippocampal working memory (Walker et al., 2010), increases in SGC excitability following brain injury could contribute to the development of post-traumatic epilepsy and memory loss.

Granule cell synaptic inhibition undergoes significant changes following brain injury due to loss of hilar interneuronal populations and plasticity of surviving neurons (Toth et al., 1997; Ross and Soltesz, 2000; Santhakumar et al., 2000; Hunt et al., 2011). Moreover, granule cells have persistent "tonic" inhibition mediated by high-affinity, extrasynaptic $GABA_A$ receptors ($GABA_A$Rs) activated by ambient levels of GABA (Stell et al., 2003; Mtchedlishvili and Kapur, 2006). Tonic inhibition can contribute substantially to resting membrane conductance and regulate neuronal gain and excitability (Mitchell and Silver, 2003;

Received Aug. 9, 2011; revised Dec. 7, 2011; accepted Dec. 28, 2011.

Author contributions: V.S. designed research; A.G., F.S.E., A.P., S.S., and V.S. performed research; A.G., F.S.E., A.P., S.S., and V.S. analyzed data; V.S. wrote the paper.

This work was supported by New Jersey Commission for Brain Injury Research Grants 09.003-BIR1 (to V.S.) and 11-3223-BIR-E-0 (to A.G.). We thank Takahiro Ito for technical assistance and Drs. Stella Elkabes and Robert F. Heary for equipment and discussions.

*F.S.E. and A.P. contributed equally to this work.

Correspondence should be addressed to Dr. Vijayalakshmi Santhakumar, Department of Neurology and Neurosciences, UMDNJ/New Jersey Medical School, MSB-H-512, 185 S. Orange Avenue, Newark, NJ 07103. E-mail: santhavi@umdnj.edu.

DOI:10.1523/JNEUROSCI.4141-11.2012

 0270-6474/12/322523-15$15.00/0

Ruiz et al., 2003; Chadderton et al., 2004; Farrant and Nusser, 2005). Receptors underlying granule cell tonic GABA currents are known to be altered in models of acquired epilepsy (Peng et al., 2004; Zhang et al., 2007; Zhan and Nadler, 2009; Rajasekaran et al., 2010), including cortical impact injury (Mtchedlishvili et al., 2010). However, whether the source of inhibitory inputs to SGCs is the same as that of granule cells, whether SGCs have tonic GABA currents, and if brain injury modifies synaptic and tonic inhibition in SGCs, is not known.

This study examines whether concussive brain injury contributes to early changes in the excitability and inhibition of dentate semilunar granule cells, which could underlie increases in dentate excitability observed 1 week after injury.

Materials and Methods

Fluid percussion injury. All procedures were performed under protocols approved by the Institutional Animal Care and Use Committee of the University of Medicine and Dentistry of New Jersey, Newark, New Jersey. Lateral fluid percussion injury (FPI) was performed on young adult (postnatal days 24–26) male, Wistar rats (Charles River) as described previously (Dixon et al., 1987; Lowenstein et al., 1992; Toth et al., 1997; Santhakumar et al., 2000, 2003). Briefly, the rats were placed in a stereotaxic frame under ketamine-xylazine anesthesia. A 2 mm hole was trephined on the left side of the skull 3 mm caudal to bregma and 3.5 mm lateral from the sagittal suture. Two steel screws were placed 1 mm rostral to bregma and 1 mm to the right of the sagittal suture. A Luer-Lok syringe hub with a 2.6 mm inner diameter was placed over the exposed dura and bonded to the skull with cyanoacrylate adhesive. Neo-Predef was applied to the wound, and the animal was returned to its home cage. One day later, animals were anesthetized with isoflurane and attached to a fluid percussion device (Department of Biomedical Engineering, Virginia Commonwealth University, Richmond, VA). A pendulum was dropped to deliver a brief (20 ms) 2.0–2.2 atm impact on the intact dura. This resulted in a moderate level of injury that has been shown to cause a highly reproducible pattern of hilar cell loss (Toth et al., 1997; Santhakumar et al., 2000). For sham injury, the animals were anesthetized and attached to the fluid percussion device, but the pendulum was not dropped.

Slice preparation. One week (5–8 d) after FPI or sham injury (Santhakumar et al., 2001), the rats were anesthetized with isoflurane and decapitated. Horizontal brain slices (300 μm for patch-clamp and 400 μm for field experiments) were prepared in ice-cold sucrose artificial CSF (sucrose-aCSF) containing the following (in mM): 85 NaCl, 75 sucrose, 24 $NaHCO_3$, 25 glucose, 4 $MgCl_2$, 2.5 KCl, 1.25 NaH_2PO_4, and 0.5 $CaCl_2$ using a Leica VT1200S Vibratome. The slices were sagittally bisected, and the slices from the left hemisphere (ipsilateral to the side of injury) were incubated at 32 ± 1°C for 30 min in a submerged holding chamber containing an equal volume of sucrose-aCSF and recording aCSF, and subsequently were held at room temperature. The recording aCSF contained the following (in mM): 126 NaCl, 2.5 KCl, 2 $CaCl_2$, 2 $MgCl_2$, 1.25 NaH_2PO_4, 26 $NaHCO_3$, and 10 D-glucose. All solutions were saturated with 95% O_2 and 5% CO_2 and maintained at a pH of 7.4 for 1–6 h.

In vitro *electrophysiology.* For patch-clamp recordings, slices (300 μm) were transferred to a submerged recording chamber and perfused with oxygenated aCSF at 33 ± 1°C. Whole-cell voltage-clamp and current-clamp recordings from dentate granule cells and neurons in the IML were performed using infrared differential interference contrast visualization techniques (Stuart et al., 1993; Santhakumar et al., 2006) with a Nikon Eclipse FN-1 microscope, using a 40× water-immersion objective. Recordings were obtained using MultiClamp 700B (Molecular Devices). Data were low-pass filtered at 3 kHz, digitized using DigiData 1440A, and acquired using pClamp10 at 10 kHz sampling frequency. Tonic and synaptic GABA currents were recorded in perfusing aCSF with no added GABA. Except when indicated (see Fig. 9), no GABA transporter antagonists were included in the recording solution. Voltage-clamp recordings of inward GABA currents were obtained using microelectrodes (5–7 MΩ) containing the following (in mM): 125 CsCl, 5 NaCl, 10 HEPES, 2 $MgCl_2$, 0.1 EGTA, 2 Na-ATP, and 0.5 Na-GTP, titrated to a pH 7.25 with CsOH. Biocytin (0.2%) was included in the internal solution for *post hoc* cell identification, and the glutamate receptor antagonist kynurenic acid (3 mM KyA, Tocris Bioscience) was included in the external solution to isolate GABA currents. In experiments where spontaneous and miniature IPSCs (mIPSCs) were recorded as outward currents from a holding potential of 0 mV, the internal solution consisted of the following (in mM): 125 Cs-methanesulfonate, 5 NaCl, 10 HEPES, 0.2 EGTA, 2 Mg-ATP, 0.2 Na-GTP, and 5 QX-314 with biocytin (0.2%). Among neurons recorded in the IML, only cells showing the widespread dendritic morphology and axon projecting to the hilus (Williams et al., 2007) were analyzed and included in the study. Recordings were discontinued if series resistance increased by >20%. In some experiments, selective $GABA_A$R agonists with a preference for δ-subunit-containing $GABA_A$Rs, 4,5,6,7-tetrahydroisoxazolo[5,4-c]pyridin-3-ol (THIP, 1 μM), or α-tetrahydrodeoxycorticosterone (THDOC, 20 nM) (Brown et al., 2002; Stell et al., 2003) were included in the external solution. The GABA transporter-1 inhibitor 1-[2-([(diphenylmethylene)imino]oxy)ethyl]-1,2,5,6-tetrahydro-3-pyridinecarboxylic acid (NO-711) was used to test the contribution of GABA uptake mechanisms to changes in tonic GABA currents in Figure 9. All salts were purchased from Sigma-Aldrich. Tonic GABA current, the steady-state current blocked by the $GABA_A$R antagonist bicuculline methiodide (BMI, 100 μM, Sigma-Aldrich)

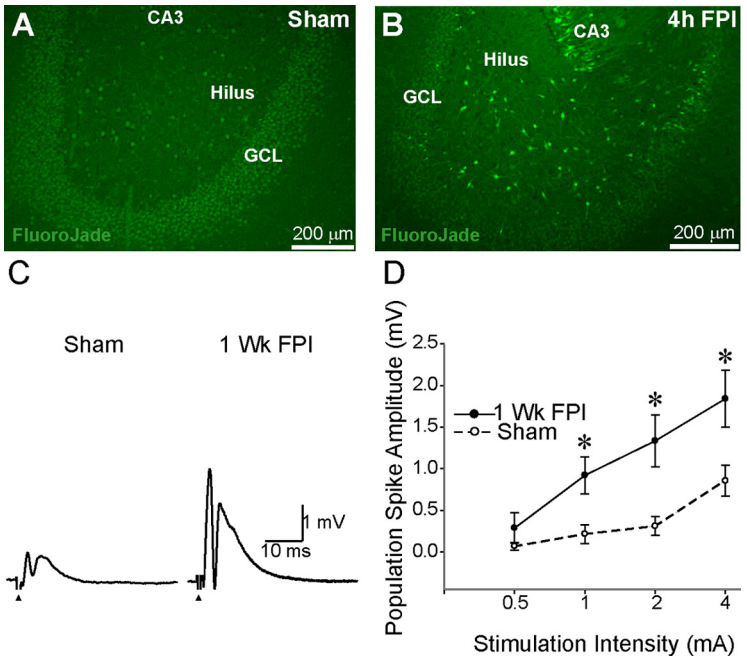

Figure 1. Dentate hilar cell death and increased excitability after concussive brain injury. ***A***, Representative Fluoro-Jade C-stained section from a rat perfused 4 h after sham injury shows no fluorescently labeled neurons, illustrating the absence of dying neurons in sham-injured controls. ***B***, Fluoro-Jade C-stained section from a rat perfused 4 h after FPI shows numerous labeled dying neurons in the hilus. ***C***, Representative traces of granule cell layer field responses evoked by perforant path stimulation in slices from a sham-injured (left) and head-injured (right) rat obtained 1 week after FPI illustrates the larger population spike amplitude in the injured dentate gyrus compared with sham injury. Traces are an average of four trials in response to a 4 mA stimulus to the perforant path. Arrows indicate location of stimulus artifact that was truncated. ***D***, Summary data demonstrate the postinjury increase in afferent-evoked excitability of the dentate gyrus at various stimulation intensities. Error bars indicate SEM. *$p < 0.05$, unpaired Student's *t* test. Wk, Week; GCL, granule cell layer.

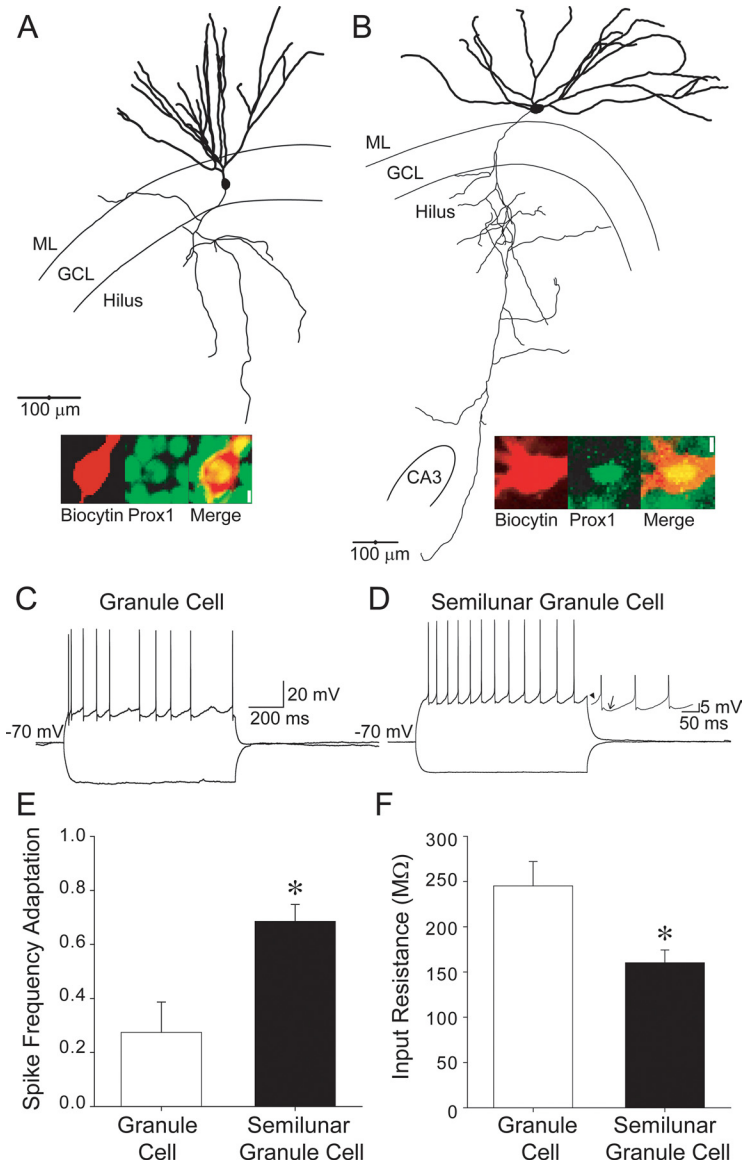

Figure 2. Features that distinguish granule cells from semilunar granule cells. ***A***, Illustration of a fully reconstructed granule cell shows the typical location of the somata in the granule cell layer (GCL) and compact dendritic spread in the molecular layer (ML). The axon (mossy fiber, thin line) is seen projecting in the hilus, toward CA3. Inset, Confocal image shows labeling for biocytin (left), Prox1 (middle), and the merged image (right), illustrating colabeling. Scale bar, 5 μm. ***B***, Reconstruction of a biocytin-filled semilunar granule cell shows the location of somata in the ML and demonstrates the wider dendritic span compared with the granule cell in ***A***. Note the high degree of branching of the SGC axon (thin line) in the hilus and projection to CA3. Inset, Confocal image of the somata of the SGC in ***B*** shows labeling for biocytin (left), Prox1 (middle), and the merged image (right), illustrating colabeling. Scale bar, 5 μm. ***C***, Membrane voltage traces from the granule cell in ***A*** show the highly adapting firing pattern in response to +200 pA current injection and hyperpolarization during a −120 pA current injection. ***D***, Current-clamp recordings from the semilunar granule cell in ***B*** illustrate the continuous firing with low adaptation during a +200 pA depolarizing current injection from a holding potential of −70 mV. Note that the hyperpolarization in response to a −120 pA current injection is smaller than in the granule cell in ***C***. Inset, Expanded membrane voltage trace shows the slow ramp depolarization (arrowhead) and large, slow afterhyperpolarization (arrow) that are distinctive of SGCs. ***E***, Summary histogram shows lower spike frequency adaptation ratio (i.e., higher adaptation) in granule cells compared with SGCs. ***F***, Summary plot illustrates the low input resistance of SGCs compared with granule cells. *$p < 0.05$, Student's t test.

or gabazine (SR95531, 10 μM, Sigma-Aldrich), was measured as described previously (Santhakumar et al., 2006; Glykys and Mody, 2007) using custom macros in IgorPro7.0 software (WaveMetrics).

Membrane voltage recordings were performed using pipettes containing the following (mM): 126 K-gluconate, 4 KCl, 10 HEPES, 4 Mg-ATP, 0.3 Na-GTP, 10 PO-creatinine with 0.2% biocytin. For experiments examining the firing rate and input resistance, cells were held at −70 mV with small current injections. The test pulse consisted of 1 s current injections from −200 pA in steps of 40 pA. The threshold for the first action potential was determined by calculating the first time derivative (dV/dt) of the voltage trace and setting 30 mV/ms as the threshold level for action potential initiation. The membrane voltage at the time when dV/dt value crossed 30 mV/ms was measured as the action potential threshold (Cooper et al., 2003; Howard et al., 2007). Spike frequency adaptation ratio was calculated as the ratio of the interspike interval between the first two and last two spikes in response to a +200 pA current injection for 1 s. In SGCs, the input resistance was determined from the slope of linear fits to the steady-state voltage responses during current injections in the range of −200–0 pA (in 40 pA steps). Input resistance measured from the steady-state voltage responses to −120 pA current injections was used to compare intrinsic properties of granule cells and SGCs. The membrane time constant was fitted to the initial part of the voltage response during −120 pA current injections.

Field recordings were performed in an interface recording chamber (BSC2, Automate Scientific) perfused with aCSF. Brain slices (400 μm) rested on a filter paper and were stabilized with platinum wire weights. The tissue was continuously superfused with humidified 95% O_2/5% CO_2 and the temperature of the perfusing solution was maintained at 34°C using a proportional control heating unit (PTC03, Automate Scientific). Field recordings of evoked population spikes in the granule cell layer of the dentate gyrus were obtained using patch pipettes filled with recording aCSF. To evoke the field responses, constant current stimuli (0.5–4 mA, 50 μs) were applied at 0.1 Hz through a bipolar 90 μm tungsten stimulating electrode placed in the perforant path at the junction of the dorsal blade and the crest and coupled to a high-voltage stimulus isolator (A365R, WPI). Recordings were obtained using an AxoPatch200B amplifier, filtered at 4 kHz using a Bessel filter, and digitized at 10 kHz with a DigiData 1440A analog-to-digital interface (Molecular Devices). The field responses in the granule cell layer were measured at five predetermined points in each slice (Santhakumar et al., 2000, 2001), including the tips of the dorsal and the ventral blades, the middle of the dorsal and ventral blades, and the middle of the crest, and the largest response was studied further.

Anatomical methods. Following physiological recordings, slices were fixed in 0.1 M phosphate buffer containing 4% paraformaldehyde at 4°C for 2 d. For *post hoc* immunohistochemistry, thick slices (300 μm) were incubated overnight at room temperature with antibodies against Prox1 (AB5475, 1:1000, polyclonal rabbit; Millipore) (Szabadics et al., 2010) or parvalbumin (PV-28, 1.5:1000, polyclonal rabbit, Swant) (Földy et al., 2007) in 0.3% Triton X-100 and 2% normal goat serum containing PBS. Immunoreactions were revealed using Alexa Fluor 488-conjugated secondary goat antibodies against rabbit IgG and biocytin staining was revealed using Alexa Fluor 594-conjugated streptavidin. Sections were visualized and imaged using a Zeiss LSM 510 confocal microscope with a 0.5 numerical aperture 20×

objective. Cell reconstructions and morphological analyses were performed with Neurolucida V.10.02 (MBF Bioscience) using confocal image stacks.

Fluoro-Jade C staining was performed on sections from rats perfusion fixed with 4% paraformaldehyde 4 h after sham or head injury. Hippocampal sections (40 μm) were mounted on gelatinized slides and air dried. Slides were immersed in 100% alcohol, 70% ethanol, and water for 2 min each followed by a 15 min incubation in 0.06% potassium permanganate before being stained with 0.001% Fluoro-Jade C in 0.1% acetic acid in the dark for 30 min. NeuN staining was performed in sections from rats perfused 1 week after sham or head injury. Sections were incubated overnight at room temperature with anti-NeuN antibody (MAB377, 1:10,000, mouse monoclonal, Millipore) in 0.3% Triton and 2% normal goat serum in PBS. Sections were reacted with Alexa Fluor 594-conjugated goat anti-mouse secondary to reveal staining. Controls in which primary antibody was omitted were routinely included. Quantification was performed on randomly selected sections from septal and temporal poles and midlevels of the hippocampus on the injured side. Cell counts were performed using the Optical Fractionator probe of Stereo Investigator V.10.02 (MBF Bioscience) using an Olympus BX51 microscope and a 100× oil objective. In each section, the hilus was outlined by a contour traced using a 10× objective. The following sampling parameters were set at 100×: counting frame, 50 × 50 μm; dissector height, 15 μm; and top guard zone, 10 μm. Approximately 25 sites per contour, selected using randomized systematic sampling protocols, were sampled. In each section, the cell count was estimated based on planimetric volume calculations in Stereo Investigator (West et al., 1991; West, 1993).

Analysis and statistics. Individual sIPSCs were detected using custom software in IgorPro7.0 (Santhakumar et al., 2006, 2010). Events were visualized, and any "noise" that spuriously met trigger specifications was rejected. Cumulative probability plots of sIPSC parameters were constructed using IgorPro by pooling equal number of sIPSCs from each cell. Statistical analysis was performed by paired and unpaired Student's *t* test (Microsoft Excel 2007) or Kolmogorov–Smirnov (K–S) test (in IgorPro7.0) for data that were not distributed normally. Additionally, two-way repeated-measure ANOVA (SysStat) was used to test for statistical differences between the firing of sham-injured and FPI SGC in response to increasing current injections. Significance was set to $p < 0.05$. Data are shown as mean ± SEM or median and interquartile range (IQR) where appropriate.

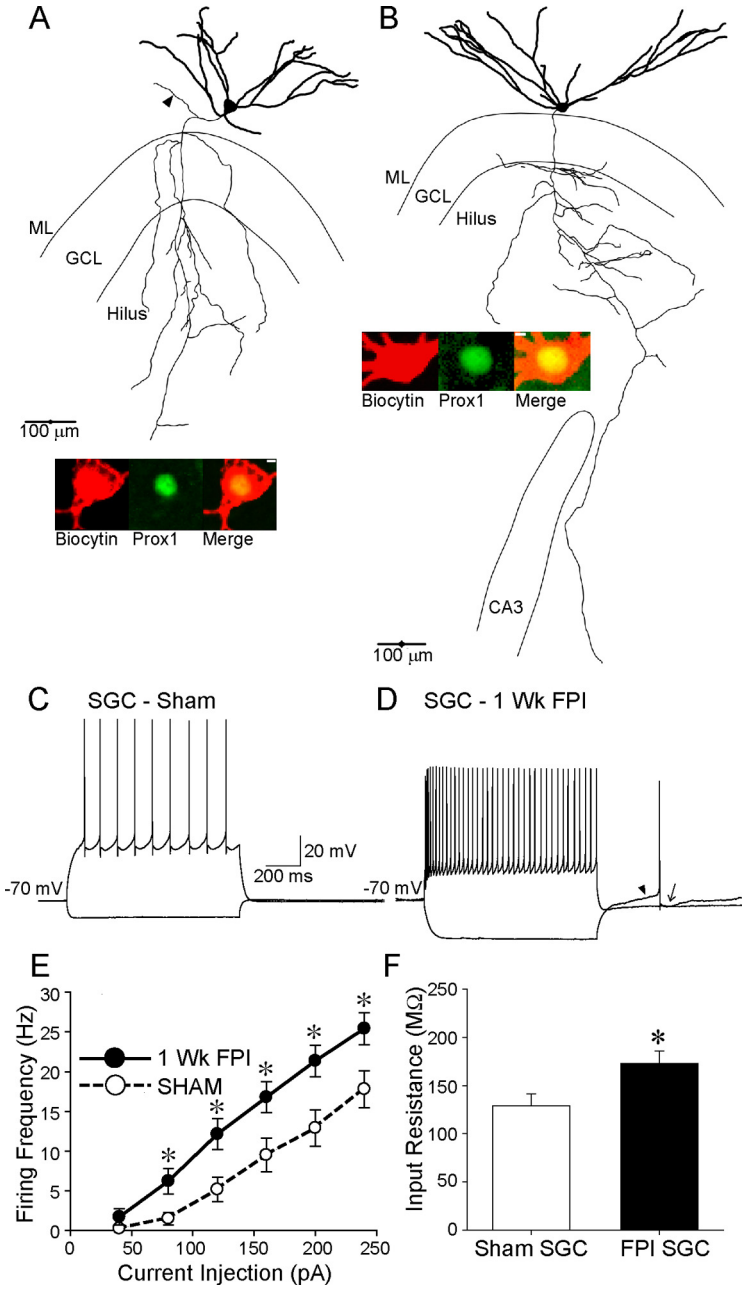

Figure 3. Increase in excitability of semilunar granule cells after brain injury. ***A***, ***B***, Biocytin-filled and reconstructed semilunar granule cells in experiments performed 1 week after sham injury (***A***) and head injury (***B***) show the SGC soma in the molecular layer (ML) and widespread dendrites (thick lines). Axons (thin lines) of both control and injured SGCs are seen projecting toward CA3. Note the axon collateral in the inner molecular layer (arrowhead) of the control SGC in ***A***. Insets, Confocal images of biocytin (left) and Prox1 labeling (middle) of the SGC soma. The merged images (right) demonstrate Prox1 labeling in SGCs from both sham-injured and FPI rats. Scale bar, 5 μm. ***C***, Example membrane voltage traces from the sham-injured SGC in ***A*** show the nonadapting firing in response to a +200 pA current injection and hyperpolarization during a −120 pA current injection. ***D***, Representative recordings in the FPI SGC in ***B*** illustrate the higher firing frequency for the same +200 pA depolarizing current injection as in ***C***. Additionally, the hyperpolarization in response to a −120 pA current injection is larger than in the sham-injured SGC (***C***). Note that the characteristic slow ramp depolarization (arrowhead) and large slow afterhyperpolarization (arrow) are observed in the FPI SGC. ***E***, Summary plot of firing rates of sham-injured and FPI SGCs during 1 s depolarizing current steps shows the enhanced firing frequency in FPI SGC. ***F***, Histograms show that FPI SGCs have higher input resistance than controls. Sham-injured SGC data are derived from the same group of cells as in Figure 2. *$p < 0.05$, Student's *t* test. GCL, Granule cell layer; Wk, week.

Results

Hilar neuronal degeneration and increased dentate excitability 1 week after lateral fluid percussion injury

Concussive brain injury is known to result in instantaneous damage to neurons in the dentate hilus and an increase in dentate excitability as early as 1 week after injury (Lowenstein et al., 1992; Toth et al., 1997; Santhakumar et al., 2000). The severity of injury correlates well with the extent of neuronal damage and the risk for developing temporal lobe epilepsy (Coulter et al., 1996; Toth et al., 1997; Thompson et al., 2005; Kharatishvili et al., 2006). In

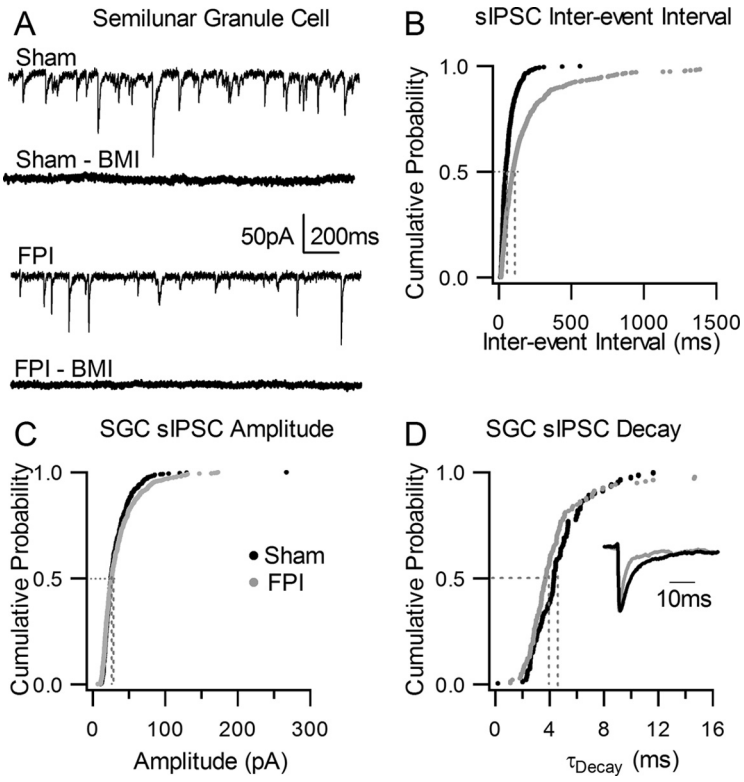

Figure 4. Decrease in SGC spontaneous IPSC frequency after FPI. ***A***, Representative traces of voltage-clamp recordings from sham-injured SGCs (top two traces) and FPI SGCs (bottom two traces) show the higher sIPSC frequency in sham-injured SGC (top trace) and the complete block of synaptic events in BMI (100 μM) in the same cell. Note the decrease sIPSC frequency in the recording from an FPI SGC (bottom trace) and subsequent block of synaptic events in BMI (100 μM). ***B–D***, Cumulative probability plots of interevent interval (***B***), amplitude (***C***), and weighted decay time constant (***D***) of sIPSCs recorded in kynurenic acid (3 mM) in sham-injured SGCs (black) and FPI SGCs (gray). Labels in ***C*** apply to ***B*** and ***D*** as well. Vertical dashed lines indicate median of the distribution at $p = 0.5$. ***D***, Inset, Overlay of normalized average sIPSC traces from a sham-injured SGC (black) and an FPI SGC (gray) illustrate the more rapid decay of sIPSCs after brain injury. The same number of individual events was selected from each cell to develop the cumulative distribution (sham injured: $n = 6$ cells; FPI: $n = 6$ cells).

this study, we used a moderate injury strength of 2.0–2.2 atm pressure, which has been shown to result in reproducible neuronal loss largely restricted to the dentate hilus (Toth et al., 1997) and increase in the ability to evoke limbic seizures (Santhakumar et al., 2001). As illustrated by representative Fluoro-Jade C-stained hippocampal sections from rats perfused 4 h after sham injury or FPI (Fig. 1*A*,*B*), degenerating neurons labeled by Fluoro-Jade C were observed in the hilus of head-injured rats (214.8 ± 64.3 hilar neurons/section in 12 sections from three rats) and not in sham-injured controls (0 ± 0 hilar neurons/section in 9 sections from three rats, $p < 0.05$ *t* test vs FPI). These data are consistent with rapid neuronal degeneration in the dentate hilus following mechanical injury to neurons during impact (Toth et al., 1997). Additionally, NeuN staining for neuronal nuclei was performed to verify the presence of hilar neuronal loss at later time points. Comparison of sections prepared 1 week after sham or head injury revealed a significant decrease in NeuN-stained neurons in the dentate hilus 1 week after FPI (sham injured: 306.8 ± 33.2 hilar neurons/section, a total of 444 cells counted in 12 sections from 3 rats; FPI: 204.3 ± 30.8 hilar neurons/section, based on 364 cells counted in 14 sections from 3 rats, 33.5 ± 9.6% decrease, $p < 0.05$, *t* test). To assess the early post-traumatic changes in dentate excitability, we examined field recordings of afferent-evoked granule cell population responses 1 week after FPI. The amplitude of the granule cell population spike evoked by perforant path stimulation was larger in slices from head-injured rats compared with age-matched sham-injured controls (Fig. 1*C*). Summary data in Figure 1*D* demonstrate the postinjury increase in dentate-evoked population response at various stimulation intensities (sham injured: $n = 9$ slices from 5 rats; FPI: $n = 8$ slices from 3 rats) and confirm that our system reliably replicates the post-traumatic increase in dentate excitability, which has been observed after moderate concussive head trauma and proposed to augment limbic epileptogenicity after brain injury (Lowenstein et al., 1992; Toth et al., 1997; Santhakumar et al., 2001).

Early post-traumatic hyperexcitability of semilunar granule cells

Since post-traumatic increase in dentate excitability is well established 1 week after injury, we focused on this early time point in the current study. Although increases in excitability of granule cells or mossy cells are potential direct mechanisms to account for post-traumatic increases in dentate field excitability, little postinjury change in firing has been found in these two dentate glutamatergic neurons (Santhakumar et al., 2000; Howard et al., 2007). We examined whether the excitability of SGCs, a population of neurons originally described by Ramón y Cajal (1995) and recently characterized as glutamatergic dentate projection neurons (Williams et al., 2007), is altered after brain injury.

To ascertain whether we could reliably distinguish granule cells from SGCs, we recorded and filled granule cells in the granule cell layer and presumed SGCs in the IML. Similar to observations in naive rats (Williams et al., 2007), dendrites of SGCs from sham-injured rats had a wider span compared with the relatively compact dendritic spread of granule cells (Fig. 2*A*,*B*; maximum dendritic spread in μm, granule cell: 289.0 ± 24.0, $n = 8$; SGC: 509.6 ± 40.1, $n = 11$, $p < 0.05$, *t* test). The angle of dendritic spread, the maximum angle subtended by the dendrites at the soma, was also significantly larger in SGCs, confirming that SGCs are morphologically distinct from granule cells (angle of dendritic spread in degrees, granule cell: 55.4 ± 5.4, $n = 8$; SGC: 115.9 ± 6.9, $n = 11$, $p < 0.05$, *t* test). Consistent with previous findings (Williams et al., 2007), 3 of 10 SGCs had associational axon collaterals in the granule cell layer or IML (Fig. 3*A*, arrowhead). SGCs also exhibited extensive axonal branching in the subgranular region of the hilus and four of eight fully reconstructed SGCs had axons projecting all the way to CA3 (Fig. 2*B*). The morphological similarities between SGCs and granule cells have led to the suggestion that SGCs may be a class of granule cells distinguished by their location. Nuclear expression of the homeodomain transcription factor Prox1 has been used as a specific marker to identify granule cells both in the granule cell layer and in ectopic locations (Jessberger et al., 2008; Lavado et al., 2010; Szabadics et al., 2010). As expected, all eight biocytin-filled and recorded granule cells examined expressed Prox1 (Fig. 2*A*). Since the presence or absence of Prox1 could provide insights into SGC

lineage, we tested morphologically identified SGCs for Prox1 immunolabeling. As illustrated by insets in Figures 2*B* and 3, *A* and *B*, biocytin-filled SGCs demonstrated nuclear labeling for Prox1 (all eight cells tested), indicating a shared lineage with granule cells.

In addition to morphological differences, granule cells and SGCs demonstrate certain distinct physiological characteristics (Williams et al., 2007). In response to depolarizing current steps from a holding potential of −70 mV, both SGCs and granule cells responded with continuous firing (Fig. 2*C*,*D*). The prolonged granule cell firing in response to current injection, while consistent with earlier whole-cell recordings (Staley et al., 1992; Lübke et al., 1998; Santhakumar et al., 2000), differs from the highly adapting firing observed by Williams et al. (2007). Despite continuous firing in both SGCs and granule cells, firing rates in SGCs demonstrated considerably higher adaptation ratios, indicating lower spike-frequency adaptation, than in granule cells (Fig. 2*E*; adaptation ratio, granule cell: 0.3 ± 0.1, $n = 8$; SGC: 0.7 ± 0.1, $n = 11$, $p < 0.05$, *t* test). SGCs also displayed a characteristic slow ramp potential before each action potential and were followed by a distinctive slow afterhyperpolarization (Fig. 2*D*, inset), as reported by Williams et al. (2007). Moreover, the input resistance (R_{in}) of SGCs was significantly lower than that of granule cells (Fig. 2*F*; in MΩ, granule cell: 254.2 ± 26.9, $n = 8$; SGC: 160.1 ± 14.3, $n = 13$, $p < 0.05$, *t* test), as has been reported previously (Williams et al., 2007). Similarly, the membrane time constant of SGCs was lower than in granule cells (in ms, granule cell: 20.7 ± 2.3, $n = 8$; SGC: 15.0 ± 1.6, $n = 13$, $p < 0.05$, *t* test). These data show that regardless of the common neurochemical marker and axonal projection, SGCs and granule cells can be reliably distinguished based on somatodendritic morphology and active and passive physiological properties.

Next, we compared the intrinsic properties of sham-injured SGCs with FPI SGCs from rats 1 week after head injury. Neurons recorded in the IML were filled during recordings and processed for biocytin immunohistology. Only SGCs identified based on somatodendritic morphology and axonal projection to the hilus were analyzed further (Fig. 3*A*,*B*). Like sham-injured SGCs, FPI SGCs could be identified by the presence of the ramp depolarization before the action potential and pronounced slow afterhyperpolarization (Fig. 3*D*). We examined the mean SGC firing frequency in response to 1 s current injections from a holding potential of −70 mV. As illustrated in Figure 3*C–E*, firing frequency of FPI SGCs was significantly greater than that of sham-injured SGCs (difference between sham-injured SCG and FPI SGC firing was significant; $F_{(1,22)} = 6.9$, $p < 0.05$ by two-way repeated-measures ANOVA, $n = 12$ sham-injured SGCs and 14 FPI SGCs). However, there was no apparent depolarizing shift in the resting membrane potential (in mV, sham-injured SGC: −86.1 ± 2.15, $n = 13$ cells; FPI SGC: −90.5 ± 4.0, $n = 14$ cells, $p > 0.05$, *t* test) or reduction in action potential threshold (in mV, sham-injured SGC: −39.9 ± 2.8, $n = 13$ cells; FPI SGC: −39.8 ± 3.5, $n = 14$ cells, $p > 0.05$, *t* test) between sham-injured and FPI SGCs (values were not corrected for junctional potentials). FPI SGCs showed lower adaptation ratios, indicating greater spike-frequency adaptation, during firing compared with sham-injured SGCs (adaptation ratio: sham-injured SGC: 0.71 ± 0.1, $n = 12$ cells; FPI SGC: 0.45 ± 0.0, $n = 14$ cells, $p < 0.05$, *t* test), suggesting that there may be postinjury changes in intrinsic membrane currents in SGCs. Notably, as illustrated by the membrane voltage traces in Figure 3, *C* and *D*, FPI SGCs showed greater hyperpolarization in response to a −120 pA current injection compared with sham-injured SGCs. Accordingly, the input resistance of FPI SGCs was greater than in sham-injured SGCs (Fig. 3*F*; R_{in} measured as the slope of linear fits to the average voltage response during the last 200 ms of 1 s current injections from −200 to −40 pA, sham-injured SGC: 132.2 ± 12.3 MΩ, $n = 13$ cells; FPI SGC: 173.0 ± 12.8 MΩ, $n = 13$ cells, $p < 0.05$, *t* test). Our data constitute the first demonstration of changes in SGC excitability in a model of neurological disease.

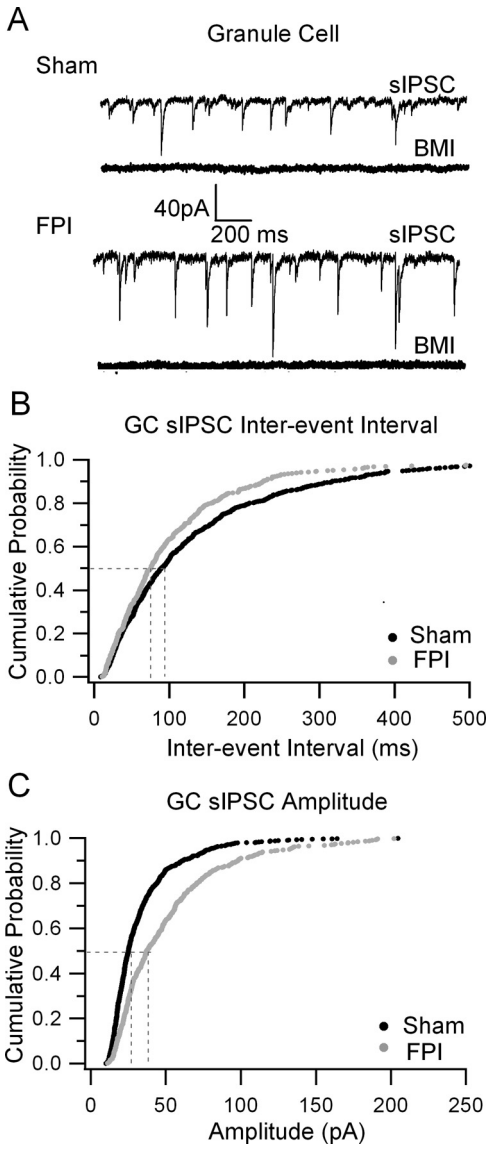

Figure 5. Increase in granule cell sIPSC frequency and amplitude after brain injury. ***A***, Example current traces of individual sIPSCs in sham-injured (top two traces) and FPI (bottom two traces) granule cells illustrate the lower frequency and amplitude in sham-injured granule cells compared with FPI granule cells. The block of synaptic events in BMI (100 μM) is illustrated in the respective lower traces. ***B***, ***C***, Cumulative probability plots of granule cell sIPSC interevent interval (***B***) and amplitude (***C***) in sham-injured SGCs (black) and FPI SGCs (gray). Vertical dashed lines indicate median of the distribution at $p = 0.5$. Identical number of events from each cell were used in the analysis (control: $n = 12$ cells; FPI: $n = 7$ cells). Recordings were performed in 3 mM kynurenic acid.

Post-traumatic changes in SGC synaptic inhibition

As might be predicted based on loss of hilar interneurons and plasticity of the surviving interneurons following brain injury (Lowenstein et al., 1992; Toth et al., 1997; Ross and Soltesz, 2000; Santhakumar et al., 2000; Hunt et al., 2011), synaptic inhibition

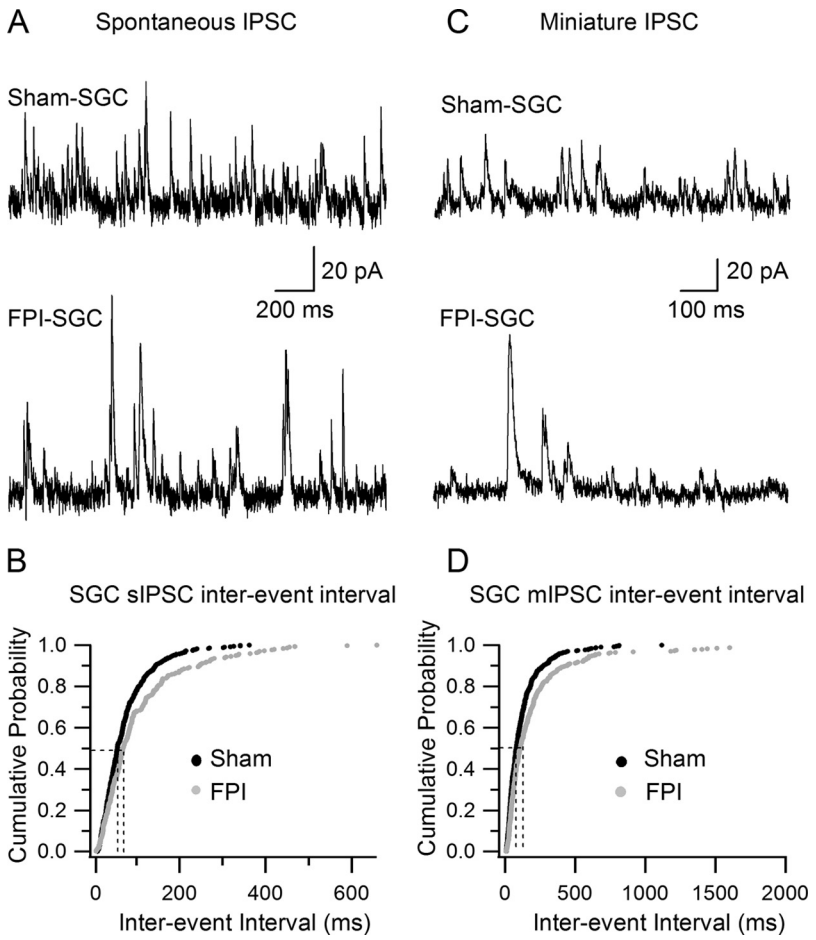

Figure 6. Decrease in spontaneous and miniature IPSC frequency in SGCs after FPI. ***A***, Representative traces of voltage-clamp recordings from SGCs held at 0 mV show the higher sIPSC frequency in sham-injured SGC (top) and a decrease in sIPSC frequency in the recording from an FPI SGC (bottom). ***B***, Cumulative probability plots of sIPSC interevent interval in sham-injured (black) and FPI (gray) SGCs. Vertical dashed lines indicate median of the distribution at $p = 0.5$. ***C***, Voltage-clamp recording of miniature IPSCs in sham-injured SGC (top) and FPI SGC (bottom). ***D***, Cumulative probability plots of mIPSC interevent interval in sham-injured (black) and FPI SGCs (gray). Vertical dashed lines indicate median of the distribution at $p = 0.5$.

of granule cells and mossy cells undergo profound post-traumatic modifications (Santhakumar et al., 2001; Howard et al., 2007; Mtchedlishvili et al., 2010). Curiously, despite postinjury hilar interneuronal loss and a corresponding decrease in action potential-independent mIPSCs, the frequency of spontaneous IPSCs in granule cells and mossy cells is elevated following FPI (Santhakumar et al., 2001; Howard et al., 2007). Increased excitability of certain interneurons and enhanced excitatory drive to surviving interneurons after brain injury may contribute to an increase in sIPSC frequency following brain injury (Ross and Soltesz, 2000; Santhakumar et al., 2001; Hunt et al., 2011). Since the dendritic distribution of SGCs corresponds with the axonal distribution of hilar interneurons vulnerable to postinjury loss (Lowenstein et al., 1992; Toth et al., 1997), we examined whether brain injury altered sIPSC parameters in SGCs. Recordings were performed in the presence of the glutamate receptor antagonist kynurenic acid (3 mM) to block excitatory synaptic currents and isolate IPSCs. Complete block of synaptic events following perfusion of BMI (100 μM) was used to confirm that the synaptic events were mediated by $GABA_A$Rs (Fig. 4*A*, top and bottom, traces labeled BMI). One week after FPI, the interevent interval of sIPSC in SGCs was prolonged compared with that in sham-injured SGCs (Fig. 4*A*,*B*; in ms, sham-injured SGC: 64.2 ± 2.5, median = 45.9, IQR = 26.5–82.1, $n = 6$ cells; FPI SGC: 207.9 ± 17.3, median = 95.2, IQR = 46.0–198.5, $n = 6$ cells, $p < 0.05$, K–S test) indicating a decrease in sIPSC frequency. However, there was no change in either the sIPSC amplitude (Fig. 4*C*; in pA, sham-injured SGC: 31.2 ± 9.1, median = 24.9, IQR = 18.4–38.4, $n = 6$ cells; FPI SGC: 34.5 ± 10.4, median = 25.7, IQR = 17.8–41.9, $n = 6$ cells, $p > 0.05$, K–S test) or the 20–80% rise time in FPI SGCs (in ms, sham-injured SGC: 0.2 ± 0.0, $n = 6$ cells; FPI SGC: 0.2 ± 0.0, $n = 6$ cells, $p > 0.05$, t test). The amplitude-weighted decay time constant (τ_{decay}) of sIPSCs showed a small but statistically significant decrease in FPI SGCs (Fig. 4*D*; in ms, sham-injured SGC: median = 4.2, IQR = 3.3–5.3; FPI SGC: median = 3.5, IQR = 2.8–4.7, $n = 6$ cells each, $p < 0.05$, K–S test). Since previous studies have demonstrated loss of several major hilar neuronal populations, including those expressing somatostatin, parvalbumin, cholecystokinin, and substance P receptor after FPI (Lowenstein et al., 1992; Toth et al., 1997; Santhakumar et al., 2000), the observed decrease in SGC sIPSC frequency may be due to the postinjury loss of hilar interneurons and a resulting reduction in inhibitory drive to SGCs.

Our data demonstrating post-traumatic prolongation of sIPSC interevent interval in SGCs are in direct contrast to the early decrease in sIPSC interevent interval in granule cells and mossy cells (Ross and Soltesz, 2000; Santhakumar et al., 2001; Howard et al., 2007). What accounts for the post-traumatic increase in sIPSC interevent interval in SGCs instead of the decrease in granule cells? Could differences in experimental conditions, such as the inclusion of glutamate receptor antagonists during recordings, be responsible? Indeed, previous experiments have shown that the application of glutamate receptor antagonists leads to a greater reduction in sIPSC frequency in granule cells from head-injured rats (FPI granule cells) compared with sham-injured controls (Santhakumar et al., 2001). Under our experimental conditions, we found that in contrast to SGCs, sIPSC interevent interval in granule cells was reduced after FPI (Fig. 5*A*,*B*; in ms, sham-injured granule cell: 138.1 ± 41.5, median = 89.1, IQR = 44.0–171.8, $n = 12$ cells; FPI granule cell: 110.2 ± 45.8, median = 75.5, IQR = 39.9–136.5, $n = 7$ cells, $p < 0.05$, K–S test). These data are consistent with earlier experiments in granule cells performed in the absence of glutamate receptor antagonists (Ross and Soltesz, 2000; Santhakumar et al., 2001). The amplitude of sIPSCs in granule cells was also significantly increased after head injury (Fig. 5*C*; in pA, sham-injured granule cell: 32.9 ± 7.0, median = 25.0, IQR = 17.9–38.4, $n = 12$ cells; FPI granule cell: 50.0 ± 10.9, $n = 7$ cells, median = 37.1, IQR = 243–62.3, $p < 0.05$, K–S test). However, τ_{decay} of granule cell sIPSCs was not altered after head injury (in ms, sham-injured granule cell: 4.7 ± 0.8, median = 4.1, IQR = 3.0–5.5, $n = 12$ cells; FPI granule cell: 5.4 ± 3.7, median =

3.9, IQR = 2.8–5.07, $n = 7$ cells, $p > 0.05$, K–S test). As in SGCs, synaptic events were fully blocked by BMI (100 μM; Fig. 5*A*, traces labeled BMI). The striking agreement of our sIPSC data from granule cells with results of earlier studies in granule cells and mossy cells (Ross and Soltesz, 2000; Santhakumar et al., 2001; Howard et al., 2007), and the diametrically opposite change observed in SGCs under identical experimental conditions, demonstrate the cell-type specificity of posttraumatic decrease in synaptic inhibition in SGCs.

To determine whether brain injury resulted in changes in synaptic inhibitory input to SGCs even under conditions in which glutamate receptors were not blocked, we recorded sIPSCs at a holding potential of 0 mV, close to the reversal potential for glutamatergic synaptic events (Fig. 6*A*,*B*). The inward synaptic currents recorded at 0 mV were fully blocked by SR95531 (10 μM), indicating that we could effectively isolate $GABA_A$R-mediated synaptic events (data not shown). Similar to our observations in glutamate antagonists (Fig. 4), there was an increase in sIPSC interevent interval in SGCs 1 week after FPI (Fig. 6*A*,*B*; in ms, sham-injured SGC: 72.0 ± 2.6, median = 54.6, IQR = 33.0–92.1, $n = 5$ cells; FPI SGC: 103.1 ± 6, median = 68.1, IQR = 38.8–126.8, $n = 3$ cells, $p < 0.05$, K–S test, 100 events from each cell were included in the analysis), indicating a decrease in SGC sIPSC frequency after FPI. SGC sIPSC amplitude showed a small but statistically significant increase after brain injury (Fig. 6*A*; in pA, sham-injured SGC: 26.0 ± 0.7, median = 21.5, IQR = 15.1–31.6, $n = 5$ cells; FPI SGC: 26.6 ± 0.8, median = 24.1, IQR = 18.0–32.2, $n = 3$ cells, $p < 0.05$, K–S test). Once again, these data confirmed the postinjury decrease in SGC sIPSCs and revealed the striking contrast to the enhanced granule cell sIPSC frequency observed in earlier studies (Santhakumar et al., 2001).

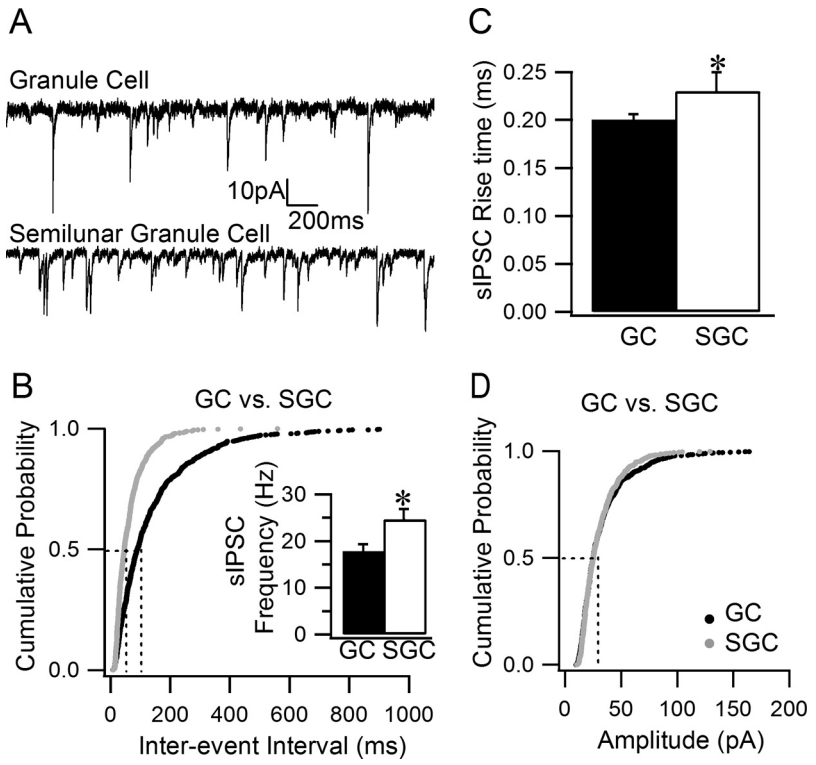

Figure 7. Intrinsic diversity in SGC and granule cell synaptic inhibition. ***A***, Representative voltage-clamp recordings ($V_{hold} = -70$ mV) of individual sIPSCs in a granule cell (top) and an SGC (bottom) from a sham-injured rat. Note the lower sIPSC frequency in the granule cell compared with the SGC. ***B***, Cumulative probability plots compare the sIPSC interevent interval granule cells (black) and SGCs (gray) in control rats recorded in 3 mM kynurenic acid. Inset, Summary histogram of sIPSC frequency in granule cells (GCs) and SGCs. ***C***, Summary histogram of the 20 – 80% rise time in control granule cells and SGCs. ***D***, Cumulative probability plots of sIPSC amplitude in granule cells (black) and SGCs (gray). Vertical dashed lines indicate median of the distribution at $p = 0.5$. Identical number of events from each cell were used in the analysis (GC: $n = 12$ cells; SGC: $n = 6$ cells). Labels in ***D*** apply to ***B*** and ***D***. sIPSC data were derived from the same control group of cells as in Figures 4 and 5. *$p < 0.05$, Student's *t* test.

Previous studies have demonstrated that neuronal loss after moderate FPI is confined to the dentate hilus and that most major hilar interneuronal populations are lost to a similar extent after FPI (Toth et al., 1997; Santhakumar et al., 2000). Therefore, we considered the possibility that the loss of hilar neurons may contribute to postinjury decreases in inhibitory synaptic input to SGC. To directly test for injury-induced changes in SGC inhibitory inputs, we examined whether the action potential-independent mIPSCs in SGCs are altered after FPI. Voltage-clamp recordings of outward inhibitory synaptic currents ($V_{hold} = 0$ mV) in the presence of the sodium channel blocker TTX (1 μM) demonstrated an increase in SGC mIPSC interevent interval after brain injury (Fig. 6*C*,*D*; in ms, sham-injured SGC: 123.2 ± 6.1, median = 78.2, IQR = 39.9–150.1, $n = 4$ cells; FPI SGC: 213.0 ± 18.4, median = 107.8, IQR = 50.1–217.18, $n = 5$ cells, $p < 0.05$, K–S test; 100 events from each cell were included in the analysis). The amplitude of mIPSCs in SGCs was also enhanced after FPI (in pA, sham-injured SGC: 26.0 ± 0.6, median = 23.1, IQR = 17–32.1, $n = 4$ cells; FPI SGC: 29.2 ± 0.5, median = 27.2, IQR = 21.3–34.8, $n = 5$ cells, $p < 0.05$, K–S test). The postinjury increase in mIPSC interevent interval is similar to findings in granule cells and mossy cells after FPI (Toth et al., 1997; Howard et al., 2007), and is consistent with a decrease in inhibitory inputs to SGCs. Since our data (Fig. 1) and previous studies (Toth et al., 1997; Santhakumar et al., 2000) have demonstrated that the neuronal loss after moderate FPI is restricted to the hilus, our findings suggest that loss of hilar interneurons could underlie the postinjury decrease in SGC mIPSC frequency. Although the decrease in mIPSC frequency is consistent across SGCs (our data), granule cells (Toth et al., 1997), and mossy cells (Howard et al., 2007), the distinctive decrease in sIPSC frequency in SGCs (current study) compared with the increase in granule cells (Santhakumar et al., 2001) and mossy cells (Howard et al., 2007) suggests that different classes of interneurons may contribute to synaptic inhibition in SGCs and granule cells after head injury.

Cell-type-specific differences in SGC and granule cell synaptic inhibition

Could inherent, cell-type-specific differences in inhibitory input to SGCs and granule cells contribute to the opposite posttraumatic changes in sIPSC interevent interval in the two cell types? Previous studies have identified that GABAergic basket cells expressing the calcium-binding protein parvalbumin (PV) are instrumental in providing perisomatic inhibition to granule cells (Kraushaar and Jonas, 2000; Hefft and Jonas, 2005). The predominant axonal distribution of PV+ basket cells is to the granule cell layer (Hefft and Jonas, 2005). A salient feature of PV+ interneurons in the granule

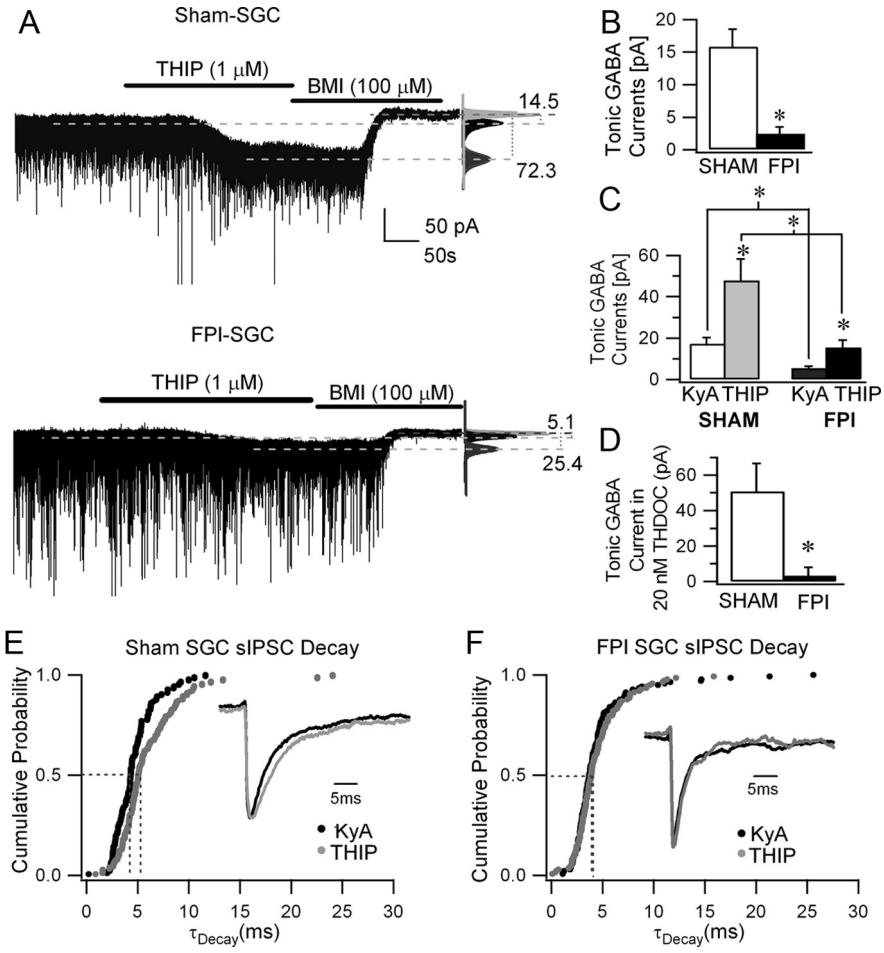

Figure 8. Decrease in SGC tonic GABA currents after brain injury. ***A***, Representative voltage-clamp recordings ($V_{hold} = -70$ mV) from a sham-injured (top) and FPI SGC (bottom) 1 week after injury illustrate the magnitude of tonic GABA current blocked by a saturating concentration of BMI (100 μM). Right, Gaussian fits to all-points histograms derived from 30 s recording periods in control conditions in the presence of 3 mM kynurenic acid, after the addition of THIP (1 μM) and during BMI perfusion used to determine tonic current amplitude. The dashed lines indicate the Gaussian means and the difference currents are noted. ***B***, Summary histogram of the tonic GABA currents in sham-injured and FPI SGC in kynurenic acid. ***C***, Histogram of tonic GABA currents in control aCSF with KyA and following addition of THIP in recordings from both sham-injured and FPI SGCs. ***D***, Summary data of tonic GABA current amplitude measured in THDOC (20 nM) in sham-injured and FPI SGCs. ***E***, ***F***, Cumulative probability plots comparing the sIPSC-weighted decay time constants in aCSF with KyA (black) and following the addition of THIP (gray) in recordings from sham-injured (***E***) and FPI (***F***) SGCs. Vertical dashed lines indicate median of the distribution at $p = 0.5$. Insets, Overlay of normalized average sIPSC traces from a sham-injured SGC (***E***, inset) and an FPI SGC (***F***, inset) during recordings in aCSF with KyA (black) and from the same cell following the addition of THIP (gray). The same number of individual events were selected from each cell to develop the cumulative distribution (sham injured: $n = 3$ cells; FPI: $n = 4$ cells). *$p < 0.05$, paired and unpaired Student's *t* test.

cell layer is that, unlike hilar interneurons, they are relatively resistant to cell loss following brain injury (Toth et al., 1997). During immunohistochemical staining, we found that granule cells filled with biocytin during recordings were typically surrounded by a dense mesh of axons labeled for PV in sections from both sham-injured and head-injured rats (data not shown). On the other hand, SGCs were located in the molecular layer, which showed a relatively sparse labeling for parvalbumin in sections from both sham-injured and FPI rats (data not shown). These observations suggest that, compared with granule cells, SGCs may receive fewer somatic inputs from PV+ basket cells.

To determine whether intrinsic differences in synaptic inhibitory input to SGCs and granule cells may contribute to the divergent postinjury responses, we compared the sIPSC parameters of SGCs and granule cells from sham-injured control rats (in recordings performed with Cs-Cl-based internal solutions in the presence of 3 mM kynurenic acid). Curiously, our data show that the sIPSC interevent interval in sham-injured SGCs was shorter than in sham-injured granule cells (Fig. 7*A*,*B*; in ms, SGC: 64.2 ± 2.5, $n = 6$ cells; granule cell: 138.1 ± 41.5, $n = 12$ cells, $p < 0.05$, K–S test), contributing to a higher sIPSC frequency in SGCs (Fig. 7*B*, inset; in Hz, SGC: 24.6 ± 2.3, $n = 6$ cells; granule cell: 17.8 ± 1.6, $n = 12$ cells, $p < 0.05$, *t* test). Additionally, sIPSC rise time was significantly slower in SGCs (Fig. 7*C*; in ms, SGC: 0.23 ± 0.01, $n = 6$ cells; granule cell: 0.20 ± 0.01, $n = 12$ cells, $p < 0.05$ *t* test), suggesting that SGCs received a greater proportion of IPSCs from dendritically projecting interneurons compared with granule cells. While the largest amplitude events in granule cells were larger than in SGCs, the difference in sIPSC amplitude between SGCs and granule cells was not statistically significant (Fig. 7*D*; in pA, SGC: 31.2 ± 9.07, median = 24.9, IQR = 18.4–38.4, $n = 6$ cells; granule cell: 32.9 ± 7.0, median = 25.0, IQR = 17.9–38.4, $n = 12$ cells, $p > 0.05$, K–S test). Similarly, there was no difference in the sIPSC τ_{decay} between SGCs and granule cells (in ms, SGC: median = 4.2, IQR = 3.3–5.3; granule cell: median = 4.1, IQR = 3.0–5.5, $n = 12$ cells, $p > 0.05$, K–S test). Together, the higher sIPSC frequency in control SGCs and the postinjury decrease in spontaneous and miniature IPSC frequency indicate that SGCs receive greater inhibitory input from populations of hilar interneurons vulnerable to injury-induced cell loss compared with granule cells. These findings revealed unexpected, and hitherto unknown, differences in inhibition between SGCs and granule cells.

Brain injury decreases SGC tonic GABA currents

Apart from the classical synaptic inhibitory currents, granule cells express tonic GABA currents mediated by extrasynaptic and perisynaptic $GABA_AR$ containing $\alpha4$ and δ subunits (Stell et al., 2003; Wei et al., 2003; Peng et al., 2004; Mtchedlishvili and Kapur, 2006). Given the similarities between SGCs and granule cells, and the evidence for injury-induced changes in granule cell tonic inhibition (Mtchedlishvili et al., 2010), we examined SGCs for the presence and postinjury changes in tonic GABA currents. In morphologically identified SGCs, application of a saturating concentration of the $GABA_AR$ antagonist BMI (100 μM) decreased the holding current, indicating the presence of tonic GABA currents (Fig. 8*A*). The magnitude of tonic GABA currents in SGCs was significantly decreased after FPI (Fig. 8*A*,*B*; in pA, sham-injured SGC: 16.7 ± 1.7, $n = 8$ cells; FPI SGC: 4.1 ± 0.9, $n = 9$ cells, $p < 0.05$, *t* test). Even when the tonic GABA currents were normalized by cell membrane capacitance to eliminate confounding effects due to differences in cell size, tonic GABA

currents in SGCs from head-injured rats were lower than in sham-injured controls (in pA/pF, sham-injured SGC: 0.18 ± 0.04, $n = 8$ cells; FPI SGC: 0.07 ± 0.02, $n = 9$ cells, $p < 0.05$, t test). Tonic GABA currents were measured at physiological temperature in the absence of added GABA or GABA transporter inhibitors. In a subset of experiments in which SGC tonic GABA currents were measured without prior application of the GABA modulator THIP, tonic GABA currents in SGCs still showed a significant decrease after FPI (in pA, sham-injured SGC: 15.8 ± 1.5, $n = 3$ cells; FPI SGC: 2.4 ± 1.1, $n = 4$ cells, $p < 0.05$, t test). Since comparison of baseline tonic GABA currents in kynurenic acid, measured in experiments without and with subsequent perfusion of THIP, revealed no statistical difference in either sham-injured SGCs (tonic GABA currents in pA, in kynurenic acid without THIP: 15.8 ± 1.5, $n = 3$ cells; in experiments including THIP modulation: 17.2 ± 3, $n = 5$ cells, $p > 0.05$, t test) or FPI SGCs (tonic GABA currents in kynurenic acid in pA, without THIP: 2.4 ± 1.1, $n = 3$ cells; in experiments including THIP modulation: 5.4 ± 1.1, $n = 5$ cells, $p > 0.05$, t test), the data were pooled (Fig. 8*B*). As illustrated in Figure 8*A,C*, THIP (1 μM) increased the baseline holding current and thereby potentiated tonic GABA currents (tonic GABA currents in pA, sham-injured SGC 17.2 ± 3 in kynurenic acid and 47.9 ± 10.5 in THIP, $n = 5$ cells, $p < 0.05$, t test; FPI SGC 5.4 ± 1.1 in kynurenic acid and 15.5 ± 3.7 in THIP, $n = 5$ cells, $p < 0.05$, t test), demonstrating the role of $GABA_AR$ δ subunits in SGC tonic GABA currents. The magnitude of SGC tonic GABA currents measured in the presence of THIP was also decreased after brain injury (Fig. 8*C*). However, the extent to which THIP enhanced SGC tonic GABA currents was not altered after FPI (increase with THIP, sham-injured SGC: 310.6 ± 78.6%, $n = 5$ cells; FPI SGC: 294.0 ± 77.8%, $n = 5$ cells, $p > 0.05$, t test). Because the lack of an immunological marker to differentiate between granule cells and SGCs renders it difficult to directly quantify injury-induced changes in $GABA_AR$ δ subunit expression in SGCs, we performed additional physiological experiments in morphologically identified SGCs to determine whether $GABA_AR$ currents mediated by δ subunits are altered after FPI. We found that tonic GABA currents recorded in the presence of THDOC (20 nM), a relatively specific neurosteroid agonist of $GABA_AR$ δ subunits in nM concentrations (Stell et al., 2003), were significantly lower in SGCs from head-injured rats compared with sham-injured controls (Fig. 8*D*; in pA, sham-injured SGC: 50.9 ± 15.6, $n = 3$ cells; FPI SGC: 5.1 ± 3.8, $n = 4$ cells, $p < 0.05$, t test). The consistently lower tonic GABA current amplitude in SGCs from head-injured rats in the presence of both THDOC and THIP, and the lack of difference in THIP modulation of tonic GABA currents between sham-injured and FPI SGCs together suggest that decreases in $GABA_ARs$ containing δ subunits contribute, in part, to the postinjury decrease in tonic GABA currents in SGCs.

As demonstrated earlier (Fig. 4*D*), the sIPSC τ_{decay} is slower in control SGCs compared with FPI SGCs. Previous studies in granule cells have shown that $GABA_AR$ δ subunits can be located perisynaptically and contribute to a slow component of synaptic decay (Wei et al., 2003). Since the more rapid sIPSC τ_{decay} following injury paralleled the decrease in tonic GABA currents (Fig. 8*A,B*), we examined whether brain injury reduces the contribution of $GABA_AR$ with δ subunits to sIPSC decay in SGCs. In sham-injured SGCs, THIP (1 μM) slowed sIPSC τ_{decay}, indicating a role for $GABA_AR$ δ subunits in the time course of sIPSCs (Fig. 8*E*; sIPSC τ_{decay} in ms, in KyA: 4.5 ± 1.13, median = 4.24, IQR = 3.01–5.29; in THIP: 6.1 ± 2.0, median = 5.10, IQR = 4.15–7.56, $n = 3$ cells, $p < 0.05$, K–S test). However, as illustrated by the cumulative probability distribution plots of sIPSC τ_{decay} (Fig. 8*F*), THIP failed to alter sIPSC τ_{decay} in FPI SGCs (sIPSC τ_{decay} in ms, in KyA: 4.57 ± 1.7, median = 3.68, IQR = 2.86–4.77; in THIP: 4.9 ± 2.8, median = 3.86, IQR = 2.98–5.28, $n = 4$, cells $p > 0.05$, test). These results are consistent with a post-traumatic decrease in contribution of $GABA_AR$ with δ subunits to sIPSC decay in SGCs.

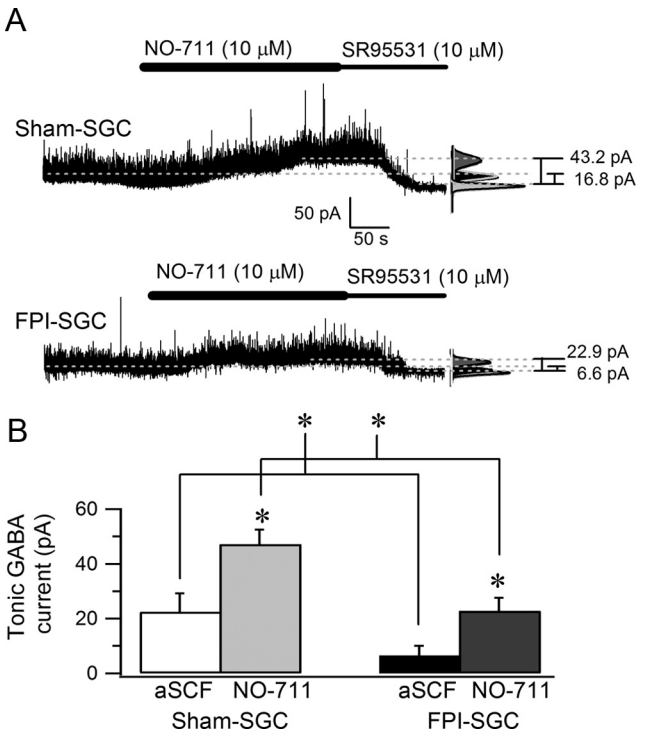

Figure 9. Postinjury decrease in SGC tonic GABA currents is maintained in the presence of GABA transporter blocker. ***A***, Representative voltage-clamp recordings ($V_{hold} = 0$ mV) from a sham-injured (top) and FPI SGC (bottom) 1 week after injury illustrate the magnitude of tonic GABA current blocked by SR95531 (gabazine, 10 μM). Right, Gaussian fits to all-points histograms derived from 30 s recording periods in aCSF after addition of NO-711 (10 μM) and during SR95531 perfusion used to determine tonic current amplitude. The dashed lines indicate the Gaussian means and the difference currents are noted. ***B***, Summary histogram of SGC tonic GABA currents in aCSF and after addition of NO-711 in recordings from both sham-injured and FPI SGCs. *$p < 0.05$, paired and unpaired Student's t test.

Next we examined whether changes in GABA uptake might contribute to the postinjury decrease in SGC tonic GABA currents. Tonic GABA currents were recorded as baseline inward currents ($V_{hold} = 0$ mV, in the absence of glutamate antagonists or added GABA) blocked by a saturating concentration of SR95531 (gabazine, 10 μM). As illustrated in Figure 9*A,B*, the amplitude of tonic GABA currents was considerably reduced in SGCs from head-injured rats compared with sham-injured controls (in pA, sham-injured SGC: 22.5 ± 6.7, $n = 8$ cells; FPI SGC: 6.6 ± 3.6, $n = 5$ cells, $p < 0.05$, t test). In all recordings, the GAT-1 (GABA transporter-1) antagonist NO-711 (10 μM) enhanced SGC tonic GABA currents. Even when differences in GABA transport were abolished, tonic GABA currents measured in NO-711 were larger in sham-injured SGCs than in FPI SGCs (Fig. 9*B*; in pA, sham-injured SGC: 47.2 ± 5.3, $n = 8$ cells; FPI SGC: 22.9 ± 4.9, $n = 5$ cells, $p < 0.05$, t test). Moreover, the extent to which NO-711 enhanced tonic GABA currents was not different between sham-injured and FPI SGCs (enhancement by NO-711, sham-injured SGC: 271.2 ± 61.5%, $n = 8$ cells; FPI SGC: 258.1 ± 11.0%, $n = 5$ cells, $p > 0.05$, t test), suggesting that changes in GABA transporter function are unlikely to underlie the postin-

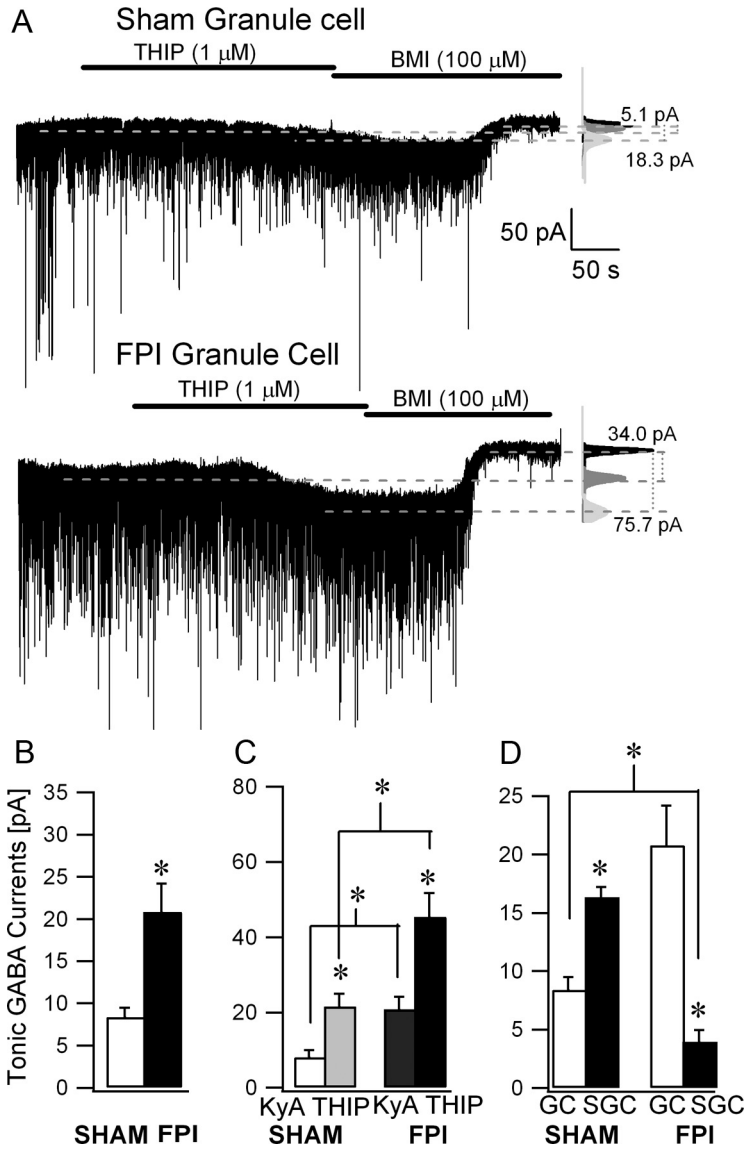

Figure 10. Granule cell tonic GABA currents are increased after brain injury. ***A***, Example voltage-clamp recordings (V_{hold} = −70 mV) from granule cells from a sham-injured (top) and FPI (bottom) rat obtained 1 week after injury show the presence of tonic GABA current blocked by a saturating concentration of BMI (100 μM). Right, Gaussian fits to all-points histograms derived from 30 s recording periods in KyA after adding THIP (1 μM) and during BMI perfusion. The dashed lines indicate the Gaussian means and the difference currents are noted. Note the larger amplitude of tonic GABA currents in FPI granule cells. ***B***, Summary plot of tonic GABA currents in sham-injured and FPI-granule cells in KyA. ***C***, Histogram of tonic GABA currents in control aCSF with KyA and following addition of THIP in recordings from both sham-injured and FPI granule cells. ***D***, Comparison of tonic GABA current amplitudes between granule cells (GCs) and SGCs in sham-injured and FPI rats. Histograms are based on tonic GABA currents recorded in KyA from the same group of cells as in Figures 8 and 10, ***A*** and ***B***. *$p < 0.05$, paired and unpaired Student's *t* test.

injury indicate that granule cell tonic GABA currents are elevated on the side contralateral to injury (Mtchedlishvili et al., 2010). However, granule cell tonic GABA currents were not enhanced 1–6 months after severe fluid percussion injury (Pavlov et al., 2011). We examined whether brain injury leads to early changes in granule cell tonic GABA currents when the dentate network shows increases in perforant path-evoked excitability. Unlike SGCs, tonic GABA currents in granule cells were enhanced 1 week after FPI (Fig. 10*A*,*B*; in pA, sham-injured granule cell: 8.4 ± 1.1, $n = 9$ cells; FPI granule cell: 20.8 ± 3.4, $n = 6$ cells, $p < 0.05$, *t* test). The increase in granule cell tonic GABA currents was statistically significant even when normalized to the cell capacitance (in pA/pF, sham-injured granule cell: 0.15 ± 0.03, $n = 9$ cells; FPI granule cell: 0.6 ± 0.24, $n = 6$ cells, $p < 0.05$, *t* test). Additionally, THIP (1 μM) enhanced tonic GABA currents in granule cells from both sham-injured and FPI rats (Fig. 10*C*; in pA, sham-injured granule cell: 8.1 ± 1.9 in KyA and 21.6 ± 3.4 in THIP, $n = 6$ cells; FPI granule cell: 20.8 ± 3.4 in KyA and 45.4 ± 6.4 in THIP, $n = 6$ cells). Potentiation of tonic GABA currents by THIP was not different between granule cells from sham-injured and FPI rats (tonic current amplitude in KyA, sham-injured granule cell: 285.22 ± 46.39%, $n = 6$ cells; FPI granule cell: 243.42 ± 44.5%, $n = 6$ cells, $p > 0.05$, *t* test), suggesting that increases in $GABA_AR$ containing δ subunits may underlie the enhancement of granule cell tonic GABA currents after brain injury. Interestingly, comparison of tonic GABA currents between SGCs and granule cells in control rats revealed that tonic GABA current amplitudes in SGCs were considerably larger than those in granule cells (Fig. 10*D*; in pA, granule cell: 8.4 ± 1.1, $n = 9$ cells; SGC: 16.3 ± 0.9, $n = 6$ cells, $p < 0.05$, *t* test). Moreover, after injury, tonic GABA currents in FPI SGCs were reduced even when compared with sham-injured granule cells (Fig. 10*D*). Significantly, the results reveal differences in magnitude and in the direction of postinjury plasticity of tonic GABA currents between SGCs and granule cells and demonstrate cell-type-specific reduction in SGC tonic inhibition after brain injury.

jury decrease in SGC tonic GABA currents. Together, our data support the inference that, in addition to reduced synaptic GABA spillover as a consequence of postinjury decrease in sIPSC frequency, decreases in $GABA_AR$ δ subunits contribute to lower tonic GABA currents in SGCs after head injury.

Although our data show that brain trauma results in diametrically opposite changes in synaptic inhibition in granule cells and SGCs, it is possible that early changes in tonic GABA currents after brain injury are a result of a global decrease in tonic inhibition, independent of cell type. Studies in rodent models of acquired epilepsy have demonstrated long-term increases in granule cell tonic GABA currents (Zhan and Nadler, 2009). Results of a recent study conducted 3 months after cortical-impact

Post-traumatic decrease in tonic inhibition augments SGC excitability

Since the receptors underlying tonic GABA currents contribute to membrane conductance and regulate neuronal excitability (Stell et al., 2003; Chadderton et al., 2004), we examined whether the post-traumatic reduction in SGC tonic GABA conductance may underlie the increase in SGC input resistance and excitability after brain injury (Fig. 3*C*–*F*). In recordings from sham-injured SGCs, the $GABA_A$ receptor antagonist SR95531 (20 μM) in-

creased SGC input resistance measured as the slope of linear fits to the voltage response to the last 200 ms of 1 s hyperpolarizing current injections from −200 to −40 pA (R_{in} in SR95531 as percentage of R_{in} in aCSF: 117.2 ± 3.4%, $n = 8$ cells, $p < 0.05$ by paired Student's t test), indicating that GABA conductance contributes substantively to the low input resistance in sham-injured SGCs (Fig. 11*A*, top, *B*). Consistent with our prediction based on the post-traumatic decrease in tonic GABA currents, and in contrast to sham-injured SGCs, SR95531 did not alter the input resistance of FPI SGCs (Fig. 11*A*, bottom; R_{in} in gabazine as percentage of R_{in} in aCSF: 101.2 ± 5.5%, $n = 10$ cells, $p > 0.05$ by paired Student's t test). The postinjury loss of gabazine (SR95531) modulation of SGC input resistance (Fig. 11*B*) indicates that a decrease in $GABA_AR$ conductance underlies the increase in SGC input resistance after brain injury. Most crucially, there was no difference in the firing elicited by positive current injections in SGCs from sham-injured and head-injured rats in the presence of gabazine (Fig. 11*C*; difference between sham-injured and FPI SGC firing was not significant, $F_{(1,12)} = 0.07$, $p = 0.8$ by two-way repeated-measures ANOVA, $n = 6$ sham-injured and 10 FPI SGCs). Together, these data indicate that the post-traumatic changes in GABAergic inhibition contribute to cell-specific enhancement of SGC excitability after brain injury.

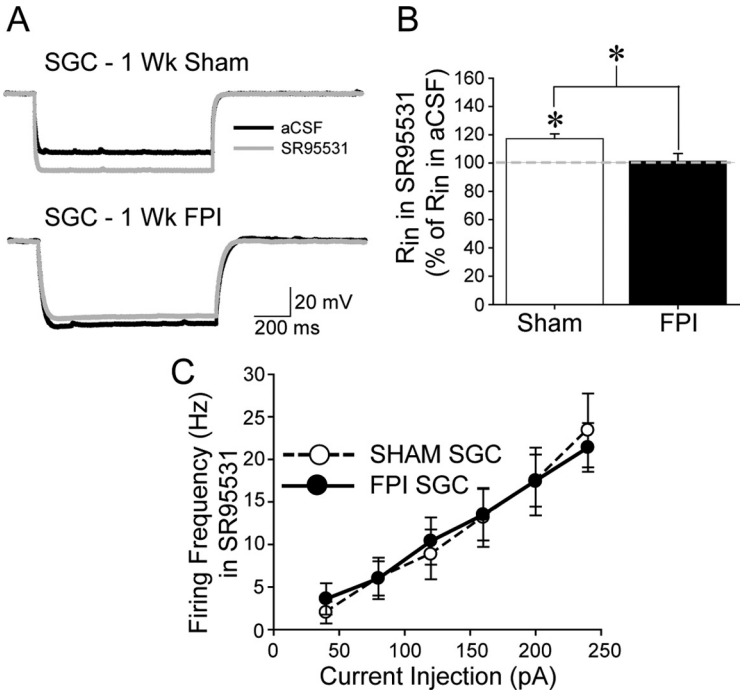

Figure 11. $GABA_A$ receptor antagonists enhance SGC input resistance in sham-injured controls but not after FPI. ***A***, Membrane voltage responses to a −120 pA current injection recorded in a control and an FPI SGC illustrate that SR95531 (20 μm) increased the hyperpolarizing response in sham-injured SGCs (top) but failed to alter the response of FPI SGCs (bottom). ***B***, Summary plot of the effect of SR95531 on SGC R_{in}, expressed as a percentage of R_{in} in control aCSF, shows that SR95531 enhanced R_{in} control SGC but failed to alter R_{in} in FPI SGC. ***C***, Plot of SGC firing rates recorded in the presence of SR95531 (20 μm) reveals the action potential frequency during 1 s depolarizing current steps was not different in sham-injured and FPI SGCs. *$p < 0.05$ paired and unpaired Student's t test. Wk, Week.

Discussion

In seeking to identify cellular mechanisms underlying post-traumatic limbic hyperexcitability, this study has demonstrated altered excitability and tonic inhibition in glutamatergic SGCs following brain injury. Simultaneously, the data revealed that granule cells and SGCs have fundamental differences in inhibition. First, in relation to brain trauma, there is early postinjury increase in excitability of SGCs, which is unique among dentate excitatory neurons. In SGCs, there are cell-specific reductions in synaptic and tonic GABA currents 1 week after brain injury. By comparison, in granule cells, synaptic and tonic GABA currents increase 1 week after brain injury. Crucially, the post-traumatic decrease in GABAergic inhibition enhances SGC input resistance and excitability after FPI. These data establish for the first time the involvement of SGCs in neurological disease and demonstrate neuronal hyperexcitability resulting from decrease in tonic GABA currents in a model of acquired epilepsy. Second, concerning native properties, SGCs express Prox1, a specific marker for granule cells, indicating the common origin of the two types of cells. Regardless of the shared dendritic location, SGCs receive more frequent and slower rising sIPSCs than granule cells, indicating differences in GABAergic innervation. Compared with granule cells, SGCs have larger tonic GABA currents, which contribute to their passive membrane properties. $GABA_AR$ with δ subunits contribute to both tonic and synaptic inhibition in SGCs. Overall, we show that differences in GABAergic inhibition are a critical distinguishing feature between SGCs and granule cells and that GABAergic plasticity selectively enhances SGC excitability after brain injury.

Role of hyperexcitable SGCs in the injured brain: hub, short circuit, or both?

Brain injury leads to distinctive pathological changes in the hippocampus and results in epilepsy and cognitive disorders (Coulter et al., 1996; Toth et al., 1997; Santhakumar et al., 2001; D'Ambrosio et al., 2005; Cohen et al., 2007; Kharatishvili and Pitkänen, 2010). Here we demonstrate that SGCs, novel glutamatergic IML neurons, are more excitable 1 week after brain injury. Since SGCs contribute to sustained depolarization of hilar interneurons or "up-states," which have been proposed as a cellular substrate for working memory (Larimer and Strowbridge, 2010), post-traumatic changes in SGC physiology may underlie memory and cognitive impairments following brain injury (Lyeth et al., 1990; Schwarzbach et al., 2006).

What are the potential implications of enhanced SGC excitability after brain injury? While SGC axonal projection constitutes a parallel output from dentate to CA3, the prolonged, input-specific inhibition of granule cells during sustained SGC firing indicates that SGCs augment the dentate gate through activation of hilar feedback interneurons (Larimer and Strowbridge, 2010). Although it is possible that the increase in SGC excitability represents a homeostatic response to enhance the dentate gate, the post-traumatic loss of hilar interneurons that constitute the feedback circuit (Lowenstein et al., 1992; Toth et al., 1997) will more likely diminish the contribution of SGCs to feedback inhibition in the injured brain. A potential consequence of the injury-induced network changes is that the direct SGC projections to CA3 may "short-circuit" the dentate gate and impart the en-

hanced excitability to CA3. An alternative, albeit not mutually exclusive, possibility is that the SGC IML associational collaterals may excite neighboring granule cells, forming a local focus of hyperexcitability after trauma. SGC innervation of surviving mossy cells (Williams et al., 2007) may also contribute to septotemporal spread of excitability (Ratzliff et al., 2004). Given the typical sustained SGC firing, the possibility that SGCs drive early postinjury increases in dentate excitability is compatible with the contribution of polysynaptic network activity to the increase in duration of granule cell and mossy cell firing after brain injury (Santhakumar et al., 2000). Furthermore, it remains to be seen whether SGCs undergo structural plasticity of hilar and molecular layer axon collaterals analogous to the aberrant recurrent mossy fiber sprouting after brain injury (Golarai et al., 2001; Santhakumar et al., 2001; Kharatishvili et al., 2006). While the relatively sparse distribution of SGCs pose a potential caveat to its ability to transform network activity, computational analyses predict that a few highly connected neurons could serve as "hubs" that shape network behavior in epilepsy (Morgan and Soltesz, 2008). Together, SGCs are ideally situated to enhance local excitability, compromise specificity of the dentate gate, directly activate hippocampal neurons, and thereby play a causal role in early increases in evoked population responses in the dentate gyrus after brain injury.

Differential synaptic inhibition of granule cells and SGCs: insights from injury

Our demonstration that SGCs express Prox1 and likely share the granule cell niche of adult neurogenesis (Jessberger et al., 2008; Lavado et al., 2010; Karalay and Jessberger, 2011) may explain the numerous similarities between the cell types. However, the differences in sIPSC frequency between SGCs and granule cells in control rats, and the opposite changes in sIPSC frequency observed after FPI, indicate inherent differences in the source of their inhibitory inputs. Given our current understanding, the postinjury decrease of spontaneous and miniature IPSC frequency in SGCs is consistent with post-traumatic hilar interneuronal loss (Lowenstein et al., 1992; Toth et al., 1997). In contrast to SGCs, granule cells from head-injured rats have more frequent sIPSCs but fewer mIPSCs (Toth et al., 1997; Santhakumar et al., 2001), indicating that granule cells may be innervated by neurons that survive and are more excitable after injury. We suggest that SGCs are less likely to be innervated by PV+ interneurons with axons in the granule cell layer. Since PV+ basket cells generate robust, perisomatic inhibition of granule cells (Hefft and Jonas, 2005), are relatively resilient (Toth et al., 1997), and possibly more excitable (Ross and Soltesz, 2000) after brain injury, they are a potential source of increases in granule cell sIPSC frequency after brain injury. Moreover, because basket cells are central to maintaining sparse granule cell activity (Kraushaar and Jonas, 2000), a paucity of PV+ basket cell inputs to SGCs, consequent to its location in the IML, may be permissive to the characteristic persistent firing in SGCs (Larimer and Strowbridge, 2010). Location-dependent distinctions in synaptic physiology have recently been demonstrated among ectopic CA3 granule cells (Szabadics et al., 2010). Whether lower PV+ basket cell innervation of SGCs underlies the absence of post-traumatic increases in SGC sIPSC frequency remains to be tested. Nonetheless, potential differences in PV+ basket cell innervation do not explain the inherent higher frequency and slower rise time of SGC sIPSCs compared with granule cells. The most plausible explanation for our data is that, compared to granule cells, SGCs receive a greater inhibitory input from vulnerable populations of hilar interneurons that project to the distal dendrites.

Tonic inhibition and SGC excitability

As in granule cells (Stell et al., 2003; Wei et al., 2003; Peng et al., 2004), we find that SGC tonic inhibition is mediated by $GABA_AR$ with δ subunits. The post-traumatic decrease in SGC tonic GABA currents occurs simultaneously with unchanged THIP modulation and reduction in SGC sIPSC frequency, indicating that both decreases in $GABA_AR$ δ subunits and reduced synaptic spillover (Glykys and Mody, 2007) may contribute to the decrease. Our data show that robust tonic GABAergic inhibition is an essential component of the resting membrane conductance of SGCs, and suggest that $GABA_AR$ conductance may underlie the low input resistance of SGCs. Post-traumatic increase in SGC excitability, occurring as a consequence of reduced SGC tonic inhibition, is consistent with the capacity of shunting inhibitory conductance to regulate excitability and offset neuronal firing (Brickley et al., 1996; Mitchell and Silver, 2003). More importantly, tonic inhibition can contribute to multiplicative scaling of neuronal activity during noisy physiological synaptic input, as would occur *in vivo*, and has been proposed to aid in pattern separation (Mitchell and Silver, 2003; Silver, 2010). Consequently, post-traumatic decrease in tonic inhibition may compromise the ability of SGCs to participate in input discrimination and contribute to memory and cognitive disabilities following brain injury. Although decrease in tonic inhibition can lower seizure thresholds (Maguire et al., 2005), granule cell tonic GABA current is enhanced or unchanged in acquired epilepsy (Zhang et al., 2007; Zhan and Nadler, 2009; Mtchedlishvili et al., 2010). How enhanced tonic GABA currents influence seizure thresholds is unclear since, while increased GABA conductance may limit excitability, depolarizing shifts in GABA reversal (Bonislawski et al., 2007; Pathak et al., 2007) tend to augment excitability. In contrast, cell-specific postinjury decrease in tonic GABA conductance could enhance excitability regardless of changes in GABA reversal. Thus, our data demonstrate that brain injury leads to early and selective decrease in SGC tonic GABA currents, resulting in post-traumatic enhancement in SGC excitability, and indicate that SGCs and tonic GABA currents may contribute to abnormal dentate circuit function after brain injury.

In summary, our results have identified intrinsic differences in inhibitory control of granule cells and semilunar granule cells that may contribute to functional distinctions between the two apparently similar dentate projection neurons and, thereby, extend our fundamental understanding of the dentate circuit involved in working memory. Our study reveals that SGCs are a potential source of increase in dentate excitability after brain injury, and suggests that SGCs may play a causal role in post-traumatic epileptogenesis and memory dysfunction that could be generalized to acquired temporal lobe epilepsy with diverse etiologies.

References

Annegers JF, Hauser WA, Coan SP, Rocca WA (1998) A population-based study of seizures after traumatic brain injuries. N Engl J Med 338:20–24.

Bonislawski DP, Schwarzbach EP, Cohen AS (2007) Brain injury impairs dentate gyrus inhibitory efficacy. Neurobiol Dis 25:163–169.

Brickley SG, Cull-Candy SG, Farrant M (1996) Development of a tonic form of synaptic inhibition in rat cerebellar granule cells resulting from persistent activation of GABAA receptors. J Physiol 497:753–759.

Brown N, Kerby J, Bonnert TP, Whiting PJ, Wafford KA (2002) Pharmacological characterization of a novel cell line expressing human alpha(4)beta(3)delta GABA(A) receptors. Br J Pharmacol 136:965–974.

Chadderton P, Margrie TW, Häusser M (2004) Integration of quanta in cerebellar granule cells during sensory processing. Nature 428:856–860.

Cohen AS, Pfister BJ, Schwarzbach E, Grady MS, Goforth PB, Satin LS (2007)

Injury-induced alterations in CNS electrophysiology. Prog Brain Res 161:143–169.

Cooper DC, Moore SJ, Staff NP, Spruston N (2003) Psychostimulant-induced plasticity of intrinsic neuronal excitability in ventral subiculum. J Neurosci 23:9937–9946.

Coulter DA, Rafiq A, Shumate M, Gong QZ, DeLorenzo RJ, Lyeth BG (1996) Brain injury-induced enhanced limbic epileptogenesis: anatomical and physiological parallels to an animal model of temporal lobe epilepsy. Epilepsy Res 26:81–91.

D'Ambrosio R, Fender JS, Fairbanks JP, Simon EA, Born DE, Doyle DL, Miller JW (2005) Progression from frontal-parietal to mesial-temporal epilepsy after fluid percussion injury in the rat. Brain 128:174–188.

Dixon CE, Lyeth BG, Povlishock JT, Findling RL, Hamm RJ, Marmarou A, Young HF, Hayes RL (1987) A fluid percussion model of experimental brain injury in the rat. J Neurosurg 67:110–119.

Farrant M, Nusser Z (2005) Variations on an inhibitory theme: phasic and tonic activation of GABA(A) receptors. Nat Rev Neurosci 6:215–229.

Földy C, Lee SY, Szabadics J, Neu A, Soltesz I (2007) Cell type-specific gating of perisomatic inhibition by cholecystokinin. Nat Neurosci 10:1128–1130.

Glykys J, Mody I (2007) The main source of ambient GABA responsible for tonic inhibition in the mouse hippocampus. J Physiol 582:1163–1178.

Golarai G, Greenwood AC, Feeney DM, Connor JA (2001) Physiological and structural evidence for hippocampal involvement in persistent seizure susceptibility after traumatic brain injury. J Neurosci 21:8523–8537.

Hefft S, Jonas P (2005) Asynchronous GABA release generates long-lasting inhibition at a hippocampal interneuron-principal neuron synapse. Nat Neurosci 8:1319–1328.

Heinemann U, Beck H, Dreier JP, Ficker E, Stabel J, Zhang CL (1992) The dentate gyrus as a regulated gate for the propagation of epileptiform activity. Epilepsy Res [Suppl] 7:273–280.

Herman ST (2002) Epilepsy after brain insult: targeting epileptogenesis. Neurology 59 [9 Suppl 5]:S21–S26.

Howard AL, Neu A, Morgan RJ, Echegoyen JC, Soltesz I (2007) Opposing modifications in intrinsic currents and synaptic inputs in post-traumatic mossy cells: evidence for single-cell homeostasis in a hyperexcitable network. J Neurophysiol 97:2394–2409.

Hunt RF, Scheff SW, Smith BN (2011) Synaptic reorganization of inhibitory hilar interneuron circuitry after traumatic brain injury in mice. J Neurosci 31:6880–6890.

Jessberger S, Toni N, Clemenson GD Jr, Ray J, Gage FH (2008) Directed differentiation of hippocampal stem/progenitor cells in the adult brain. Nat Neurosci 11:888–893.

Karalay O, Jessberger S (2011) Translating niche-derived signals into neurogenesis: the function of Prox1 in the adult hippocampus. Cell Cycle 10:2239–2240.

Kharatishvili I, Pitkänen A (2010) Posttraumatic epilepsy. Curr Opin Neurol 23:183–188.

Kharatishvili I, Nissinen JP, McIntosh TK, Pitkänen A (2006) A model of posttraumatic epilepsy induced by lateral fluid-percussion brain injury in rats. Neuroscience 140:685–697.

Kraushaar U, Jonas P (2000) Efficacy and stability of quantal GABA release at a hippocampal interneuron-principal neuron synapse. J Neurosci 20:5594–5607.

Larimer P, Strowbridge BW (2010) Representing information in cell assemblies: persistent activity mediated by semilunar granule cells. Nat Neurosci 13:213–222.

Lavado A, Lagutin OV, Chow LM, Baker SJ, Oliver G (2010) Prox1 is required for granule cell maturation and intermediate progenitor maintenance during brain neurogenesis. PLoS Biol 8:e1000460.

Lowenstein DH (2009) Epilepsy after head injury: an overview. Epilepsia 50 [Suppl 2]:4–9.

Lowenstein DH, Thomas MJ, Smith DH, McIntosh TK (1992) Selective vulnerability of dentate hilar neurons following traumatic brain injury: a potential mechanistic link between head trauma and disorders of the hippocampus. J Neurosci 12:4846–4853.

Lübke J, Frotscher M, Spruston N (1998) Specialized electrophysiological properties of anatomically identified neurons in the hilar region of the rat fascia dentata. J Neurophysiol 79:1518–1534.

Lyeth BG, Jenkins LW, Hamm RJ, Dixon CE, Phillips LL, Clifton GL, Young HF, Hayes RL (1990) Prolonged memory impairment in the absence of hippocampal cell death following traumatic brain injury in the rat. Brain Res 526:249–258.

Maguire JL, Stell BM, Rafizadeh M, Mody I (2005) Ovarian cycle-linked changes in GABA(A) receptors mediating tonic inhibition alter seizure susceptibility and anxiety. Nat Neurosci 8:797–804.

McAllister TW (1992) Neuropsychiatric sequelae of head injuries. Psychiatr Clin North Am 15:395–413.

Mitchell SJ, Silver RA (2003) Shunting inhibition modulates neuronal gain during synaptic excitation. Neuron 38:433–445.

Morgan RJ, Soltesz I (2008) Nonrandom connectivity of the epileptic dentate gyrus predicts a major role for neuronal hubs in seizures. Proc Natl Acad Sci U S A 105:6179–6184.

Mtchedlishvili Z, Kapur J (2006) High-affinity, slowly desensitizing GABAA receptors mediate tonic inhibition in hippocampal dentate granule cells. Mol Pharmacol 69:564–575.

Mtchedlishvili Z, Lepsveridze E, Xu H, Kharlamov EA, Lu B, Kelly KM (2010) Increase of GABAA receptor-mediated tonic inhibition in dentate granule cells after traumatic brain injury. Neurobiol Dis 38:464–475.

Pathak HR, Weissinger F, Terunuma M, Carlson GC, Hsu FC, Moss SJ, Coulter DA (2007) Disrupted dentate granule cell chloride regulation enhances synaptic excitability during development of temporal lobe epilepsy. J Neurosci 27:14012–14022.

Pavlov I, Huusko N, Drexel M, Kirchmair E, Sperk G, Pitkänen A, Walker MC (2011) Progressive loss of phasic, but not tonic, GABAA receptor-mediated inhibition in dentate granule cells in a model of post-traumatic epilepsy in rats. Neuroscience 194:208–219.

Peng Z, Huang CS, Stell BM, Mody I, Houser CR (2004) Altered expression of the Δ subunit of the $GABA_A$ receptor in a mouse model of temporal lobe epilepsy. J Neurosci 24:8629–8639.

Rajasekaran K, Joshi S, Sun C, Mtchedlishvilli Z, Kapur J (2010) Receptors with low affinity for neurosteroids and GABA contribute to tonic inhibition of granule cells in epileptic animals. Neurobiol Dis 40:490–501.

Ramón y Cajal S (1995) Histology of the nervous system of man and vertebrates. New York: Oxford UP.

Ratzliff AH, Howard AL, Santhakumar V, Osapay I, Soltesz I (2004) Rapid deletion of mossy cells does not result in a hyperexcitable dentate gyrus: implications for epileptogenesis. J Neurosci 24:2259–2269.

Ross ST, Soltesz I (2000) Selective depolarization of interneurons in the early posttraumatic dentate gyrus: involvement of the Na(+)/K(+)-ATPase. J Neurophysiol 83:2916–2930.

Ruiz A, Fabian-Fine R, Scott R, Walker MC, Rusakov DA, Kullmann DM (2003) GABAA receptors at hippocampal mossy fibers. Neuron 39:961–973.

Santhakumar V, Bender R, Frotscher M, Ross ST, Hollrigel GS, Toth Z, Soltesz I (2000) Granule cell hyperexcitability in the early post-traumatic rat dentate gyrus: the "irritable mossy cell" hypothesis. J Physiol 524:117–134.

Santhakumar V, Ratzliff AD, Jeng J, Toth Z, Soltesz I (2001) Long-term hyperexcitability in the hippocampus after experimental head trauma. Ann Neurol 50:708–717.

Santhakumar V, Voipio J, Kaila K, Soltesz I (2003) Post-traumatic hyperexcitability is not caused by impaired buffering of extracellular potassium. J Neurosci 23:5865–5876.

Santhakumar V, Hanchar HJ, Wallner M, Olsen RW, Otis TS (2006) Contributions of the $GABA_A$ receptor $\alpha 6$ subunit to phasic and tonic inhibition revealed by a naturally occurring polymorphism in the $\alpha 6$ gene. J Neurosci 26:3357–3364.

Santhakumar V, Jones RT, Mody I (2010) Developmental regulation and neuroprotective effects of striatal tonic GABAA currents. Neuroscience 167:644–655.

Schwarzbach E, Bonislawski DP, Xiong G, Cohen AS (2006) Mechanisms underlying the inability to induce area CA1 LTP in the mouse after traumatic brain injury. Hippocampus 16:541–550.

Silver RA (2010) Neuronal arithmetic. Nat Rev Neurosci 11:474–489.

Staley KJ, Otis TS, Mody I (1992) Membrane properties of dentate gyrus granule cells: comparison of sharp microelectrode and whole-cell recordings. J Neurophysiol 67:1346–1358.

Stell BM, Brickley SG, Tang CY, Farrant M, Mody I (2003) Neuroactive steroids reduce neuronal excitability by selectively enhancing tonic inhibition mediated by delta subunit-containing GABAA receptors. Proc Natl Acad Sci U S A 100:14439–14444.

Stuart GJ, Dodt HU, Sakmann B (1993) Patch-clamp recordings from the

soma and dendrites of neurons in brain slices using infrared video microscopy. Pflugers Arch 423:511–518.

Szabadics J, Varga C, Brunner J, Chen K, Soltesz I (2010) Granule cells in the CA3 area. J Neurosci 30:8296–8307.

Thompson HJ, Lifshitz J, Marklund N, Grady MS, Graham DI, Hovda DA, McIntosh TK (2005) Lateral fluid percussion brain injury: a 15-year review and evaluation. J Neurotrauma 22:42–75.

Toth Z, Hollrigel GS, Gorcs T, Soltesz I (1997) Instantaneous perturbation of dentate interneuronal networks by a pressure wave-transient delivered to the neocortex. J Neurosci 17:8106–8117.

Walker MC, Pavlov I, Kullmann DM (2010) A 'sustain pedal' in the hippocampus? Nat Neurosci 13:146–148.

Wei W, Zhang N, Peng Z, Houser CR, Mody I (2003) Perisynaptic localization of Δ subunit-containing $GABA_A$ receptors and their activation by GABA spillover in the mouse dentate gyrus. J Neurosci 23:10650–10661.

West MJ (1993) New stereological methods for counting neurons. Neurobiol Aging 14:275–285.

West MJ, Slomianka L, Gundersen HJ (1991) Unbiased stereological estimation of the total number of neurons in the subdivisions of the rat hippocampus using the optical fractionator. Anat Rec 231:482–497.

Williams PA, Larimer P, Gao Y, Strowbridge BW (2007) Semilunar granule cells: glutamatergic neurons in the rat dentate gyrus with axon collaterals in the inner molecular layer. J Neurosci 27:13756–13761.

Zhan RZ, Nadler JV (2009) Enhanced tonic GABA current in normotopic and hilar ectopic dentate granule cells after pilocarpine-induced status epilepticus. J Neurophysiol 102:670–681.

Zhang N, Wei W, Mody I, Houser CR (2007) Altered localization of $GABA_A$ receptor subunits on dentate granule cell dendrites influences tonic and phasic inhibition in a mouse model of epilepsy. J Neurosci 27:7520–7531.

American Epilepsy Society

Our Mission

The American Epilepsy Society promotes research and education for professionals dedicated to the prevention, treatment and cure of epilepsy.

Abstract Search

(Abst. 2.047), 2011

Decrease in Tonic GABA Currents and Enhanced Excitability of Dentate Semilunar Granule Cells after Traumatic Brain Injury

Authors: A. Gupta, A. Proddutur, F. S. Elgammal, T. Ito, V. Santhakumar
Instit: University of Medicine and Dentistry

Content:
RATIONALE:
Brain injury is an etiological factor for temporal lobe epilepsy and can lead to memory and cognitive impairments. Although it has been established that brain injury leads to early and persistent changes in dentate excitability, the mechanisms underlying these changes are yet to be fully elucidated. In classic dentate projection neurons, granule cells, tonic GABA currents modulate neuronal excitability and are altered in animal models of epilepsy. However, whether brain injury leads to early changes in tonic GABA currents in granule cells is not known. Additionally, recent studies have characterized a novel class of projection neurons, semilunar granule cells (SGC) which, like granule cells, project to CA3 but have distinctive dendritic structure and physiology (Williams et al., 2007). Since SGCs have molecular layer axon collaterals and form an alternate dentate output, changes in SGC physiology following brain injury will influence overall dentate excitability and output. This study examined whether concussive brain injury alters granule cell and SGC synaptic and tonic GABA currents and SGC excitability.
METHODS:
This study used lateral fluid percussion injury (FPI) in young adult rats to model brain injury in vivo. Whole-cell patch-clamp recording data from hippocampal slices in FPI and sham-injured rats were compared. Biocytin immunocytology was used for post-hoc cell identification.
RESULTS:
One week after FPI, the amplitude of granule cell tonic GABA currents, measured as the baseline currents blocked by the GABAa receptor antagonist bicuculline (100 ?M), was significantly increased compared to sham-injured controls (in pA, CON: 8.4±1.1, n=11; FPI: 20.8±3.4, n=6, $p < 0.01$). The post-injury increase in granule cell tonic GABA currents returned to control levels 3 months after injury (in pA, CON: 9.4±3.1, n=6; FPI: 6.5±1.7, n=5, $p > 0.05$). Recordings from granule cells and SGCs in control rats showed that the two cell types differed in synaptic and tonic inhibitory current parameters. Spontaneous inhibitory synaptic currents (sIPSCs) in SGCs were smaller in amplitude but more frequent than in granule cells. The magnitude of tonic GABA currents in SGCs was significantly larger than in granule cells. The GABAa receptor antagonist, gabazine, enhanced the input resistance of SGCs indicating that tonic GABA currents contribute to the characteristic low input resistance that distinguishes SGCs from granule cells. In contrast to granule cells, the amplitude of tonic GABA currents in SGCs from head-injured rats was reduced one week after FPI. Additionally, after FPI, SGCs showed an increase in input resistance and firing in response to depolarizing current injections.
CONCLUSIONS:
These data are the first demonstration of early and opposite changes in tonic GABA currents in granule cells and SGCs after brain injury. Our results show post-injury increase in SGC excitability and suggest that SGCs may

provide a focus for early dentate hyperexcitability after brain trauma.

Back to search results

Print this Page

Presentation Abstract

Program#/Poster#: 159.12/BB7

Presentation Title: Differential changes in GABAergic tone of dentate granule cells and semilunar granule cells after brain injury

Location: Hall A-C

Presentation time: Sunday, Nov 13, 2011, 11:00 AM -12:00 PM

Authors: ***A. GUPTA**, A. PRODDUTUR, F. ELGAMMAL, T. ITO, V. SANTHAKUMAR;
UMDNJ, Newark, NJ

Abstract: Concussive brain injury leads to cellular and synaptic changes in the dentate gyrus resulting in early dentate hyperexcitability and prolonged increases in epileptogenicity. While head injury leads to dentate hilar cell loss, granule cells and molecular layer neurons are relatively spared after brain injury. The molecular layer includes feed-forward GABAergic interneurons which regulate the dynamic range of granule cell excitability and a recently characterized class of excitatory neurons, semilunar granule cells (SGCs). SGCs have persistent firing patterns and molecular layer axon collaterals (Williams et al., 2007) making them candidates for feed-forward excitation in the dentate gyrus. Tonic GABA currents which regulate neuronal excitability are present in granule cells and molecular layer neurons and are known to be altered in neurological diseases such as epilepsy. This study was conducted to identify changes in tonic GABA currents in dentate granule cells and molecular layer neurons after brain injury.

Whole-cell patch clamp recordings were obtained from granule cells and dentate molecular layer neurons in hippocampal slices from juvenile rats subjected to lateral fluid percussion injury (FPI) and sham-operated controls (Santhakumar et al., 2001). The magnitude of tonic GABA currents in granule cells was enhanced one week after FPI. The selective agonist of $GABA_A$ receptors with δ subunits, THIP, caused similar increases in granule cell tonic GABA currents in both head-injured and control rats. The early increase in granule cell tonic GABA currents returned to control levels

three months after injury. In control rats, tonic GABA currents in morphologically identified SGCs were significantly greater than in granule cells. Tonic GABA currents in SGCs were enhanced by THIP indicating the contribution of $GABA_A$ receptors containing δ subunits. In contrast to the post-injury changes in granule cells, the amplitude of tonic GABA currents in SGCs from head-injured rats was significantly reduced one week after FPI. Additionally, the input resistance and intrinsic excitability of morphologically and physiologically identified SGCs was enhanced one week after head injury. Unlike SGCs, the magnitude of tonic GABA currents in molecular layer interneurons was not decreased after FPI.
The data demonstrate hitherto unknown differences in GABAergic tone between granule cells and SGCs. The observed post-traumatic decrease tonic GABAergic conductance and increase in intrinsic excitability of SGCs could contribute to dentate hyperexcitability after traumatic brain injury.

Disclosures: **A. Gupta:** None. **A. Proddutur:** None. **F. Elgammal:** None. **T. Ito:** None. **V. Santhakumar:** None.

Keyword(s): INHIBITION

SEIZURE

TRAUMATIC BRAIN INJURY

Support: NJCBIR 09.003.BI R1 to VS

[Authors]. [Abstract Title]. Program No. XXX.XX. 2011 Neuroscience Meeting Planner. Washington, DC: Society for Neuroscience, 2011. Online.

Badrinath Roysam (University of Houston - Houston, TX, USA)

Viji Santhakumar (University of Medicine and Dentistry of New Jersey - Newark, NJ, USA)

Session 5, Sunday 3:45 PM (20 min. talk)

Morphologically distinctive dentate projection neurons show unique developmental profile and post-traumatic plasticity

Elgammal FS, Gupta A, Chika-Nwosuh O, Swietek B, Kella K and Santhakumar V

Moderate forms of concussive brain trauma increase the risk of multiple organic pathologies, including spontaneously occurring seizures and memory dysfunction. Our investigation of post-traumatic plasticity among molecular layer neurons, revealed a class of neurons with somata in the inner molecular layer and axonal projections to CA3, which an earlier study had identified as glutamatergic semilunar granule cells (SGCs), distinguished from dentate granule cells by morphological and physiological features (Williams et al.,2007). The most striking morphological difference between SGCs and granule cells is the wide dendritic span of the SGCs compared to granule cells. Our earlier studies in one month old rats have used this morphological classification to demonstrate that SGCs receive significantly greater synaptic and tonic GABAergic inhibition compared to granule cells (Gupta et al., 2012). Likewise, SGCs also receive significantly greater excitatory synaptic inputs than granule cells. Within a week after concussive brain injury, SGCs and granule cells demonstrate contrasting changes in inhibitory tone, with a post-injury increase in tonic and synaptic GABA currents in dentate granule cells as opposed to a decrease in both parameters in SGCs after brain injury. Moreover, intrinsic excitability of SGCs is enhanced after brain injury (Gupta et al., 2012) which was unique among dentate excitatory neurons. Interestingly, while the frequency inhibitory synaptic currents in granule cells remained unchanged between one and four month old uninjured rats, there was a significant decrease in synaptic inhibition in SGCs during the same time period indicating that SGCs show developmental plasticity into early adulthood. We propose that location and morphological characteristics contribute, in part, to the differences in synaptic inputs and post-traumatic plasticity between SGCs and granule cells. Using the open source, L-Measure software we are analysing morphometric data from 3D Neurolucida reconstructions of a set of SGCs and granule cells recorded during slice physiology experiments. In addition to the expected differences in somatic size, location, and maximum dendritic spread we compare several morphometric characteristics of dendrites and axons between SGCs and granule cells in uninjured brain slices. We find that compared to granule cells, SGCs have a greater total axonal length with significantly higher branching in the dentate hilus. The implications of SGC morphology to its distinctive synaptic physiology and post-traumatic and developmental plasticity and network function will be discussed.

Kenneth Smith (Mitre Corporation)

Robert F. Smith (George Mason University - Fairfax, VA, USA)

Robert G. Smith (University of Pennsylvania - Philadephia, PA, USA)

Jeff Sprenger (MBF Bioscience, Inc - Burlington, VT, USA)

Armen Stepanyants (Northeastern University - Boston, MA, USA)